^{99}Mo Production at a High-Current Accelerator-based Neutron Source



Doctoral Thesis
for
the Award of the Doctoral Degree
of the Faculty of Mathematics and Natural Sciences
Institute for Nuclear Physics
of the University of Cologne

submitted by

Doruntin Shabani

September 28, 2026

FH AACHEN
UNIVERSITY OF APPLIED SCIENCES

Abstract

Molybdenum-99 is the parent radionuclide of technetium-99m, which is used in diagnostic nuclear medicine extensively. Since the large-scale production depends on a limited number of research reactors, alternative and complementary production methods are of growing interest. This thesis investigates the feasibility of producing ^{99}Mo by neutron capture on natural molybdenum through the $^{98}\mathrm{Mo}(n,\gamma)^{99}\mathrm{Mo}$ reaction at a high-current accelerator-based neutron source. The work focuses on a target–moderator–reflector assembly and examines how neutron transport, moderation, reflection, and irradiation geometry influence the achievable activity and specific activity.

The study combines PHITS neutron transport simulations, activation calculations, and experimental neutron activation benchmarks. Activities measured by gamma-ray spectrometry for bare and cadmium-covered activation foils were compared with simulation-based predictions. Two calculation approaches were considered: a flux analysis method based on thermal, epithermal, and fast flux components, and a flux folding method using energy-dependent neutron spectra and nuclear data. The benchmark results showed that the simulation framework can reproduce the measured activation behaviour with sufficient accuracy for the subsequent design study, while also indicating the increased sensitivity of epithermal activation to resonance effects.

A systematic parameter study was then performed for different moderator materials, reflector materials, reflector thicknesses, irradiation plate positions, and molybdenum plate thicknesses. The results show that the ^{99}Mo yield is governed mainly by the epithermal neutron flux and by the balance between neutron activation and self-shielding in the molybdenum plates. Among the investigated configurations, a water moderator combined with a magnesium oxide reflector was identified as the most practical option when both neutronic performance and engineering constraints are considered. For an optimized configuration with a 3 cm axial molybdenum plate, three lateral plates, and a six-day irradiation, the calculated production level is on the order of 2400 Ci of ^{99}Mo, while remaining within the range of low-specific-activity generator concepts.

Overall, the thesis shows that accelerator-driven neutron capture can provide a technically plausible route for low-specific-activity ^{99}Mo production, provided that neutron spectrum shaping, target geometry, and self-shielding are carefully treated. Further experimental work on thick molybdenum targets will be important for refining the model and moving toward an engineering design.

Table of Contents

List of Tables **VII**

List of Figures **IX**

1 Introduction **1**
1.1 Motivation 1
1.2 Molybdenum-99 Production Techniques 4
1.2.1 Fission of Uranium-235 4
1.2.2 Neutron Capture of Molybdenum-98 6
1.2.3 Direct Cyclotron Production from Molybdenum-100 8
1.2.4 Photo-fission of Uranium-238 11
1.2.5 Photonuclear Reaction of Molybdenum-100 13
1.3 High Brilliance Neutron Source 15
1.4 Research Objective 17
1.5 Thesis Outline 17

2 Physics Background **19**
2.1 Neutron Sources 20
2.1.1 Reactor-based Sources 20
2.1.2 Radioisotopic Sources 20
2.1.3 Accelerator-driven Sources 21
2.2 Neutron Transport Phenomena 22
2.2.1 Neutron Interactions with Matter 22
2.2.2 Moderation and Slowing Down 23
2.2.3 Leakage and Reflectors 24
2.2.4 Neutron Flux 25
2.3 Neutron Activation 27
2.3.1 Fundamental Activation Integral 27
2.3.2 Thermal Neutron Activation 27
2.3.3 Epithermal Neutron Activation and Resonances 28
2.3.4 Cadmium Filtering 29
2.3.5 Neutron Self-shielding 30
2.4 Gamma-ray Spectrometry 30

3 Methodology **33**
3.1 Simulation Tools and Nuclear Data Libraries . . . 33
3.1.1 PHITS Code . . . 33
3.1.2 DCHAIN Code . . . 35
3.1.3 Nuclear Data Libraries . . . 37
3.2 Activity Determination Methods . . . 38
3.2.1 Experimental . . . 38
3.2.1.1 Detector System . . . 39
3.2.1.2 Calibration Procedures . . . 40
3.2.1.3 Data Processing and Corrections . . . 41
3.2.2 Simulation . . . 43
3.2.2.1 Flux Analysis Method . . . 43
3.2.2.2 Flux Folding Method (PHITS–DCHAIN) . . . 46

4 Validation of Activity Determination Methods **49**
4.1 Experimental Setup . . . 49
4.1.1 Irradiation Setup and Neutron Source . . . 49
4.1.2 Activation Foils . . . 50
4.1.2.1 Bare Foil Irradiations . . . 51
4.1.2.2 Cd-Covered Foil Irradiations . . . 51
4.1.3 Gamma Spectrometry and Activity Calculation . . . 53
4.2 Simulation Setup . . . 54
4.3 Results and Discussion . . . 56
4.3.1 Gamma Spectra and Peak Identification . . . 57
4.3.2 Bare Foil Irradiations . . . 59
4.3.3 Cadmium-Covered Foil Irradiation . . . 61
4.3.4 Assessment of the Epithermal Neutron Spectrum . . . 63
4.4 Conclusions . . . 65

5 Parameter Study for the Production of Molybdenum-99 **67**
5.1 Introduction . . . 67
5.2 Study Setup . . . 68
5.2.1 Simulation . . . 68
5.2.2 Target–Moderator–Reflector (TMR) Concept . . . 69
5.2.3 Proton Beam and Target Design . . . 70
5.2.4 Moderator and Reflector Candidates . . . 70
5.2.5 Irradiation Plate and Positioning . . . 71
5.2.6 Parameter Variation . . . 72
5.3 Results and Discussion . . . 72
5.3.1 Neutron Spectra within the Mo Plates . . . 73
5.3.2 Irradiation Plate Positioning and Moderator Effects . . . 74
5.3.3 Reflector Material and Thickness Effects . . . 76

5.3.4 Effect of Axial Plate Thickness on Activity and Specific Activity 78
5.3.5 Optimized Reference Configuration 80
5.4 Additional Design Studies 80
5.4.1 Enriched Molybdenum-98 Irradiation Plates 80
5.4.2 Dissolved Sodium Molybdate Concept 82
5.4.3 Direct Proton Irradiation of Molybdenum 83
5.4.4 Composite Reflector Configurations 84
5.4.5 Self-Shielding Experiment 85
5.5 Conclusions and Outlook 88

6 Conclusion **91**

7 References **95**

8 Teilpublikationen **103**

9 Declaration on the use of AI-based and language-support tools **104**

A Uncertainty Propagation **105**
A.1 Uncertainty Propagation for Experimental Activities 105
A.1.1 Gaussian propagation of uncertainty 105
A.1.2 Uncertainties of individual input quantities 105
A.1.2.1 Net peak counts 105
A.1.2.2 Decay constant 105
A.1.3 Activity from gamma spectrometry 106
A.1.3.1 Uncertainty of activity 106
A.1.4 Uncertainty propagation for Molybdenum-99 106
A.2 Propagation to simulated activity 107

B Experimental Counts and Activity Results **109**

C Activity Distribution Maps for the TMR Parameter Study **110**

D Automation Workflow for PHITS Simulations and Data Analysis **135**
D.1 Development of the Reference PHITS Input File 135
D.2 Parameterization of the Geometry 136
D.3 Generation of PHITS Input Files 136
D.4 Treatment of Molybdenum Plate Positions 137
D.5 Generated Directory Structure 138
D.6 Generation of Cluster Batch Files 139
D.7 Parsing of PHITS Output Files 140
D.8 Calculation of Neutron Flux Components 141
D.9 Epithermal Spectrum Correction 141

D.10 Flux-Weighted Fast Cross Section 142
D.11 Calculation of Molybdenum-99 Activity 143
D.12 Summation of Plate Activities 143
D.13 Visualization and Comparison of Configurations 144
D.14 Summary 144

List of Tables

1.1 Operating research reactors relevant to current or planned medical radioisotope production [7–13]. 4
1.2 Future reactor projects relevant to medical isotope production [14–17]. 5
1.3 Principal characteristics of reactor-fission-based ^{99}Mo production. . . 5
1.4 Principal characteristics of neutron-capture-based ^{99}Mo production. . 8
1.5 Principal characteristics of direct cyclotron production of ^{99m}Tc via the $^{100}\mathrm{Mo}(p, 2n)$ reaction. 10
1.6 Principal characteristics of photo-fission-based ^{99}Mo production. . . 12
1.7 Principal characteristics of photonuclear ^{99}Mo production via the $^{100}\mathrm{Mo}(\gamma, n)$ reaction. 14

2.1 Typical properties of common radioisotopic neutron sources, adapted from [25, 26]. 21
2.2 Slowing-down and thermal absorption properties of selected moderator materials. 24
2.3 Reference properties of selected reflector materials. 25

3.1 Fitted parameters for the logarithmic efficiency model. 40

4.1 Summary of activation foils used in the benchmark experiments, grouped by irradiation condition. For isotopes appearing more than once within the same irradiation condition, entries labeled "– 1" correspond to the first irradiation campaign, while unlabeled entries correspond to the extended multi-monitor campaign. Foil masses were measured prior to irradiation using a laboratory balance, with an estimated relative uncertainty of $\pm 1\%$. 52
4.2 Irradiation, decay, and measurement parameters for the activation foils used in the benchmark experiments. The listed γ-line intensities correspond to absolute emission probabilities. 53
4.3 Nuclear data for the investigated (n, γ) reactions. Values are given with absolute uncertainties ($\pm 1\sigma$), derived from the relative uncertainties provided in the database [55]. 55

5.1 Major radionuclides produced during direct proton irradiation of a Mo target. 83

B.1 Net peak counts and activities for bare foil irradiations. Foils labelled "–1" correspond to the initial Au–In foil set, while unlabeled foils correspond to the extended multi-monitor foil set. 109
B.2 Net peak counts and activities for Cd-covered foil irradiations. Foils labelled "–1" correspond to the initial Au–In foil set, while unlabeled foils correspond to the extended multi-monitor foil set. 109

List of Figures

1.1 Overview of principal ^{99}Mo and ^{99m}Tc production routes and their corresponding specific activity classifications. HSA: high specific activity and LSA: low specific activity classifications refer to production routes where applicable. 3

1.2 Energy-dependent neutron-capture cross section data for the $^{98}\mathrm{Mo}(n,\gamma)^{99}$Mo reaction from the JENDL-4.0 evaluated nuclear data library [19], accessed through JANIS Web [20]. 7

1.3 Representative excitation function of the $^{100}\mathrm{Mo}(p,2n)^{99m}$Tc reaction from the TENDL evaluated nuclear data library [22], accessed through JANIS Web [20] illustrating the dependence of reaction cross section on proton energy. The optimal production window is typically located between approximately 16 and 24 MeV. 9

1.4 Representative photo-fission cross section of ^{238}U from the ENDF/B-VIII.1 evaluated nuclear data library [23], accessed through JANIS Web [20], as a function of photon energy. 11

1.5 Representative cross section of the $^{100}\mathrm{Mo}(\gamma,n)^{99}$Mo reaction from the ENDF/B-VIII.1 evaluated data library [23], accessed through JANIS Web [20], as a function of photon energy showing the giant dipole resonance region relevant for photonuclear production. 13

1.6 Overview of the High Brilliance neutron Source (HBS) concept including the linear accelerator system (1), target–moderator–reflector (TMR) assemblies (2, 3, 4), and representative instrument halls (5, 6, 7). The schematic illustrates the accelerator-driven neutron production concept and the extraction of neutron beams to multiple instrument stations. 15

2.1 Simplified workflow linking neutron generation to experimentally reconstructed activities. (Layout drafted with AI-assisted graphics tools and finalized by the author.) 19

2.2 Microscopic neutron capture cross section of ^{113}Cd from the ENDF/B-VIII.1 evaluated data library [23], accessed through JANIS Web [20], as a function of neutron energy. 29

3.1 Recommended physics models and data libraries for use in PHITS obtained from [29]. 34

3.2 Concept of the coupled PHITS–DCHAIN calculation workflow obtained from [35]. 36
3.3 BEGe detector system used for gamma-ray spectrometry measurements. The detector was housed in a lead shield (A), and the principal counting geometry was defined by a source-to-endcap distance of 19 cm (B). 39
3.4 Energy dependence of the FEP efficiency for the two counting geometries. The lines represent the fit of the data with Eq. 3.2. 41
3.5 Illustration of the flux folding procedure. The energy-dependent neutron capture cross section for ^{197}Au(n,γ)^{198}Au reaction, its multi-group representation, and the corresponding neutron flux spectrum within the gold foil with a thickness of 0.0025 cm are shown. The reaction rate is obtained by folding the flux with the cross section over all energy groups. 47

4.1 Geometrical model of the irradiation facility used for the neutron activation experiments and corresponding simulations. The figure shows a top view of the paraffin moderator with the embedded plexiglass tubes and a vertical cross-section along the symmetry axis of the central tube containing the AmBe neutron source and surrounding materials. 50
4.2 Polyethylene holder with (A) bare W sample and (B) Cd-covered W sample. 51
4.3 AmBe neutron energy spectrum used in this work. [57] 54
4.4 Simulated neutron energy spectrum within the Au – 1 foil for bare and Cd-covered irradiations. 56
4.5 Representative γ-ray spectra obtained for selected activation foils in the extended multiple-monitor study for a) bare foil irradiation and b) Cd-covered irradiation. 57
4.6 Enlarged bare-foil γ-ray spectrum for the ^{198}Au isotope used for activity determination. 58
4.7 Enlarged bare-foil γ-ray spectrum for the ^{116m}In isotope used for activity determination. 58
4.8 Experimental and simulated activities at the EOI for the bare foils. . . 60
4.9 Ratios of simulated to experimentally measured activities for bare foil irradiations. 61
4.10 Experimental and simulated activities at the end of irradiation for Cd-covered foils. 62
4.11 Ratios of simulated to experimentally measured activities for Cd-covered foil irradiation. 63

4.12 Representative determination of the epithermal shape factor α using the Cd-covered multi-monitor k_0-factors method. The value of α is obtained from the slope of the fitted linear regression. 64

5.1 Section view in the $x = 0$ plane of the HBS-type TMR reference geometry, showing the Ta target and the surrounding moderator and reflector. 69

5.2 Geometrical model of the layered Ta–water–Ta target used in the simulations. The target has a surface area of 12×24 cm^2 and consists of a 0.6 cm Ta layer, a 1.0 cm water layer, and a 0.25 cm Ta back layer, for a total thickness of 1.85 cm. 70

5.3 Geometric model of the (a) arrangement of the four irradiation plates (A–D) around the Ta target and (b) aluminum casing (Al casing) enclosing the assembly and defining the moderator volume. 71

5.4 Overview of the automated workflow used for the parameter study. 73

5.5 Simulated neutron energy spectra within the Mo plates positioned at a distance of 3 cm from the Al casing, with a 5 cm H_2O moderator and 10 cm Pb reflector. 74

5.6 Calculated ^{99}Mo activity in Plate A for various moderators as a function of plate distance from the Al casing and moderator thickness, with a 5 cm Pb reflector. 75

5.7 Total ^{99}Mo activity from all plates after 6 days of irradiation as a function of reflector thickness for different reflector materials (Pb, MgO, Be), shown separately for each moderator (H_2O, D_2O, ZrH_2, Be). For each moderator-–reflector thickness combination, the plate distance and moderator thickness correspond to the highest activity configuration identified in the preceding analysis. 77

5.8 ^{99}Mo activity and specific activity for the MgO–H_2O system as a function of axial plate (Plate A) thickness after 6 days of irradiation. . 79

5.9 Comparison of ^{99}Mo activities calculated using the FAM and FFM for natural and enriched ^{98}Mo targets as a function of target thickness. Results are shown for a 12×12 cm^2 irradiation plate positioned 1.35 cm from the target. 81

5.10 Calculated total ^{99}Mo activity for composite reflector configurations consisting of an inner MgO layer and an outer Pb layer, shown as a function of the MgO and Pb thickness. The activity corresponds to the sum over the investigated irradiation regions. 84

5.11 The Cyclone 30XP cyclotron facility at the INM-5, used for radionuclide production and target irradiation [74]. 85

5.12 Comparison of the preliminary self-shielding experiment and the corresponding PHITS simulation model. The irradiation setup consisted of a Be neutron-production target, a polyethylene moderator assembly, and embedded Au and Mo activation foils. The simulation geometry was developed to reproduce the experimental configuration as accurately as possible for activation calculations. 86
5.13 Comparison of experimentally measured activation foil activities with activities predicted using the FAM and FFM. The left panel shows results obtained using the default PHITS proton-induced reaction models for neutron production in Be, whereas the right panel shows results obtained using evaluated nuclear data. 87

1 Introduction

Molybdenum-99 (^{99}Mo) and its daughter radionuclide technetium-99m (^{99m}Tc) are among the most important radionuclides used in modern nuclear medicine. Its short half-life and suitable gamma emission for imaging make ^{99m}Tc well suited for use for many diagnostic nuclear medicine procedures worldwide. Maintaining a reliable supply of ^{99}Mo therefore remains an essential requirement for healthcare systems and radiopharmaceutical production.
For ^{99}Mo production, the choice of production route depends on nuclear-reaction yields, neutron-field characteristics, irradiation conditions, target processing, and the available production infrastructure. The main production routes include uranium-fission production of ^{99}Mo, neutron-capture production via $^{98}\mathrm{Mo}(n,\gamma)^{99}\mathrm{Mo}$, photonuclear production of ^{99}Mo, and direct accelerator-based production of ^{99m}Tc. For medical supply, the most relevant differences between these routes are the obtainable activity, product specific activity, processing requirements, radioactive waste generation, and compatibility with existing production and distribution chains.
Accelerator-driven neutron sources are therefore being considered as complementary to reactor systems for isotope production, because they can generate neutron fields without relying on a critical reactor core. In particular, High-Current Accelerator-driven Neutron Sources (HiCANS) provide compact, non-critical neutron-source concepts that are primarily developed for neutron-scattering, imaging, and analytical applications, but may also be evaluated for radionuclide production.
This chapter introduces the motivation for the investigation of accelerator-driven ^{99}Mo production, reviews principal production techniques relevant to this work, introduces the High Brilliance neutron Source (HBS) concept, and states the research objectives and thesis structure.

1.1 Motivation

Technetium-99m (^{99m}Tc) is the most widely used radionuclide in diagnostic nuclear medicine and is employed in approximately 80% of all nuclear medicine procedures worldwide, corresponding to roughly 30 million examinations annually [1, 2]. The radionuclide is obtained from the decay of molybdenum-99 (^{99}Mo), which is distributed through $^{99}\mathrm{Mo}/^{99m}\mathrm{Tc}$ generator systems and subsequently eluted in hospitals and radiopharmacies. Due to the short half-lives of ^{99}Mo ($t_{1/2} \approx$ 66 h) and ^{99m}Tc ($t_{1/2} \approx 6$ h), the supply chain is time-critical and vulnerable to

interruptions. Any disruption in production, processing, or transportation can rapidly lead to shortages and delayed diagnostic procedures [1]. Germany alone performs approximately 60,000 ^{99m}Tc-based procedures per week, corresponding to a demand of roughly 2,400 Ci of ^{99}Mo activity at the end of irradiation (EOI) [3].

At present, most global ^{99}Mo production relies on the fission of uranium targets in a limited number of ageing research reactors [1]. While this approach remains highly efficient and produces high specific activity (HSA) ^{99}Mo, it is associated with significant radioactive waste generation, complex radiochemical separation procedures, high infrastructure costs, and proliferation concerns related to uranium handling. Furthermore, production is concentrated in relatively few reactors, several of which are approaching the end of their operational lifetimes. Planned maintenance outages and unexpected shutdowns have repeatedly caused worldwide shortages of medical isotopes over the past decades [2, 3].

These limitations have motivated the investigation of reactor-independent or reactor-complementary routes, including neutron-capture production of ^{99}Mo, photonuclear production of ^{99}Mo, and direct cyclotron production of ^{99m}Tc. For routine medical supply, however, a production route depends on achievable yield and specific activity, processing requirements, radionuclidic impurities, radioactive waste generation, and distribution constraints.

In the present work, the route of interest is neutron capture on Mo via the $^{98}\mathrm{Mo}(n,\gamma)^{99}\mathrm{Mo}$ reaction, which provides a direct non-fission pathway to ^{99}Mo. Since natural Mo contains a substantial fraction of ^{98}Mo, irradiation of natural Mo can produce ^{99}Mo without uranium targets and without fission-product separation. Compared with uranium-fission production, this route avoids the generation of fission products in the target and can therefore simplify some aspects of target handling and post-irradiation processing.

A key limitation of the neutron-capture route is the comparatively low specific activity of the produced ^{99}Mo. In this carrier-added production route, only a small fraction of the molybdenum target atoms are converted to ^{99}Mo, so the product remains mixed with a much larger amount of stable molybdenum. The thermal neutron-capture cross section of ^{98}Mo is relatively small, while the resonance integral in the epithermal region is substantially larger. Therefore, meaningful ^{99}Mo production is strongly enhanced by neutron fields with a strong epithermal component. Optimising neutron spectrum, especially the balance between thermalisation and conservation of epithermal neutrons, becomes a central challenge for accelerator-driven neutron-source concepts intended for ^{99}Mo production.

Recent developments in HiCANS facilities have created new possibilities for such production schemes. These facilities use high-current proton accelerators and compact target–moderator–reflector (TMR) assemblies to generate intense neutron fields without relying on a critical reactor core. One example is the proposed High Brilliance neutron Source (HBS) concept at Forschungszentrum Jülich, where a 70 MeV

high-current proton beam impinges on a tantalum (Ta) target to produce neutrons via proton-induced reactions [4]. Although the HBS concept was developed mainly for neutron scattering, imaging, and analytical applications, the same neutron production principle can also be examined for activation-based radionuclide production.

The neutron spectrum and flux distribution inside such a TMR assembly depend strongly on the choice of moderator material, reflector material, irradiation geometry, and target configuration. In particular, the achievable ^{99}Mo activity through the $^{98}\mathrm{Mo}(n,\gamma)^{99}\mathrm{Mo}$ reaction is sensitive to the epithermal neutron flux and to neutron self-shielding effects inside thick molybdenum irradiation plates. As a result, a systematic investigation of moderator and reflector configurations is required to assess whether an HBS-type TMR assembly could produce ^{99}Mo activities of practical relevance.

This thesis investigates the feasibility of producing ^{99}Mo via neutron capture on natural molybdenum in an HBS-type TMR assembly. The focus lies on how neutron transport, moderation, reflection, and irradiation geometry influence the achievable activity and specific activity of ^{99}Mo, while considering practical engineering constraints associated with realistic neutron source designs. Beyond assessing feasibility in principle, the calculated activities are compared with the estimated demand of ^{99}Mo activity in Germany in order to evaluate whether the production levels are of a relevant order of magnitude. Radiochemical processing, regulatory approval, and detailed facility design are outside the scope of this work.

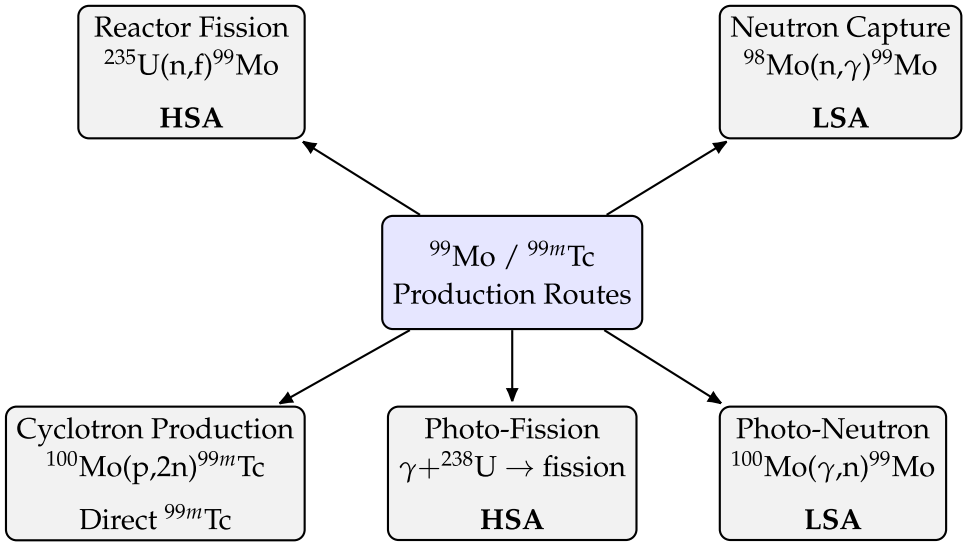


Figure 1.1: Overview of principal ^{99}Mo and ^{99m}Tc production routes and their corresponding specific activity classifications. HSA: high specific activity and LSA: low specific activity classifications refer to production routes where applicable.

1.2 Molybdenum-99 Production Techniques

The production of ^{99}Mo and ^{99m}Tc can be achieved through several nuclear reaction pathways, each with different implications for product specific activity, infrastructure requirements, radioactive waste generation, and distribution logistics. The routes discussed in this section include uranium-fission production of ^{99}Mo, neutron-capture production via $^{98}\mathrm{Mo}(n,\gamma)^{99}\mathrm{Mo}$, direct cyclotron production of ^{99m}Tc, photon-induced fission of uranium, and photonuclear production via $^{100}\mathrm{Mo}(\gamma,n)^{99}\mathrm{Mo}$. Figure 1.1 summarizes these pathways. The remainder of this section outlines the main advantages and limitations of each route, with emphasis on reactor-independent options and the role of neutron spectrum optimization for the $^{98}\mathrm{Mo}(n,\gamma)^{99}\mathrm{Mo}$ pathway.

1.2.1 Fission of Uranium-235

High-flux research reactors remain the dominant infrastructure for large-scale ^{99}Mo production, mainly through neutron-induced fission of uranium targets. In a typical research reactor, the fission of ^{235}U releases on average approximately 2.5 fast neutrons per fission event with energies in the MeV range [5]. These neutrons are subsequently moderated within the reactor core, resulting in a neutron spectrum consisting of thermal, epithermal, and fast components. Thermal neutrons at room temperature have characteristic energies of approximately 0.025 eV.
Research reactors are capable of delivering very high neutron fluxes, typically exceeding 10^{14} cm^{-2} s^{-1}, enabling efficient neutron-capture and fission-based isotope production reactions. For medical isotope applications, the dominant production route remains the fission of uranium targets for the generation of ^{99}Mo, which subsequently decays to ^{99m}Tc. This approach produces high-specific-activity (HSA) ^{99}Mo, typically on the order of $\sim 10^4$ Ci g^{-1}, making it suitable for conventional ^{99}Mo/^{99m}Tc generator systems used in nuclear medicine [6].

Table 1.1: Operating research reactors relevant to current or planned medical radioisotope production [7–13].

Reactor	**Country**	**Role**
SAFARI-1	South Africa	Medical isotope production
HFR	Netherlands	Medical isotopes and irradiation services
BR2	Belgium	Medical isotopes & materials research
OPAL	Australia	Nuclear medicine & neutron research
WWR-c	Russia	Medical isotopes production
RA-3	Argentina	Medical isotopes production
FRM II	Germany	Research & planned isotope production

In addition to isotope production, research reactors are generally operated as multi-purpose facilities supporting neutron experiments, materials testing, fuel irradiation studies, and basic nuclear research. This broad functionality maximizes the scientific and industrial return on the large infrastructure investments associated with reactor operation. Table 1.1 lists a selection of operating research reactors currently contributing to the global medical isotope supply infrastructure.
Despite these advantages, reactor-based isotope production presents important limitations. The fission process generates significant quantities of long-lived radioactive waste and introduces proliferation concerns associated with the handling and processing of enriched uranium targets. Furthermore, global ^{99}Mo production remains concentrated within a relatively small number of ageing research reactors, making the supply chain vulnerable to unplanned outages, maintenance shutdowns, and regulatory interruptions [2, 3, 13]. Several major supply disruptions observed during the past decades have demonstrated the fragility of this centralized production model and highlighted the dependence of nuclear medicine on a limited reactor fleet.

Table 1.2: Future reactor projects relevant to medical isotope production [14–17].

Project	**Country**	**Status**	**Estimated Cost**
PALLAS	Netherlands	Under construction	∼€2.0–3.0 B
JHR	France	Under construction	∼€2.5 B
MPR	South Africa	Design phase	∼€750 M
RA-10	Argentina	Under construction	∼€500 M

Several major reactor projects, shown in Table 1.2, are currently under construction or in advanced planning stages with the aim of replacing ageing infrastructure and expanding future irradiation capacity.

Table 1.3: Principal characteristics of reactor-fission-based ^{99}Mo production.

Aspect	**Characteristic**
Nuclear reaction	$^{235}\mathrm{U}(n,f)^{99}\mathrm{Mo}$
Target material	Highly enriched or low enriched ^{235}U
Final product	^{99}Mo
Typical neutron flux	$\sim 10^{13}$–10^{15} cm^{-2}/s^{-1}
Specific activity	High (carrier-free)
Radioactive waste generation	High
Infrastructure options	High flux research reactor
Main technical challenge	Reactor availability, processing, waste management

Modern research reactors require major capital investment, with total project costs frequently ranging from several hundred million to multiple billions of euros depending on reactor power, irradiation capabilities, and associated radiochemical infrastructure. In addition to these costs, licensing, construction, and commissioning programmes typically extend over many years and may exceed a decade before full operational deployment. At the same time, many existing production reactors are approaching the end of their operational lifetimes, increasing concerns regarding long-term supply reliability. The combination of ageing infrastructure, centralized production capacity, long construction schedules, and high investment requirements has intensified international interest in complementary production methods based on accelerator technologies. The main features of reactor-fission-based ^{99}Mo production are collected in Table 1.3.
Reactor-based production therefore remains difficult to replace because it combines high neutron fluxes with HSA ^{99}Mo suitable for established generator systems. Its main vulnerability is not the nuclear reaction itself, but the dependence on a small number of expensive, highly regulated, and ageing irradiation facilities. This vulnerability provides the main motivation for considering accelerator-driven routes as complementary production options rather than direct replacements for the existing reactor supply chain.

1.2.2 Neutron Capture of Molybdenum-98

An alternative non-fission route for producing ^{99}Mo is neutron capture on molybdenum according to

$$^{98}\mathrm{Mo}(n,\gamma)^{99}\mathrm{Mo} \tag{1.1}$$

In this reaction, a neutron is absorbed by a ^{98}Mo nucleus, producing radioactive ^{99}Mo, which subsequently decays to ^{99m}Tc. Since natural molybdenum contains approximately 24.14% ^{98}Mo [18], irradiation can be performed using either natural molybdenum or isotopically enriched targets. Unlike the fission-based production route, neutron capture on molybdenum does not require fissile material and therefore avoids the generation of large quantities of fission products and transuranic radioactive waste.
The neutron-capture route is typically performed in thermal or epithermal neutron fields produced either by research reactors or accelerator-driven neutron sources. Compared to the neutron-induced fission cross section of ^{235}U, the neutron-capture cross section of ^{98}Mo is relatively small in the thermal energy region. The LSA arises because the reaction is carrier-added: only a small fraction of the molybdenum target atoms are converted to ^{99}Mo, while the product remains mixed with stable molybdenum carrier.

The neutron-energy spectrum plays a central role in this reaction. Although the thermal capture cross section of ^{98}Mo is comparatively modest, Figure 1.2 shows several pronounced resonance peaks in the epithermal energy region. These resonances increase the importance of the spectral neutron flux, rather than only the total neutron flux, for evaluating ^{99}Mo production. For accelerator-driven systems, the target–moderator–reflector (TMR) configuration is therefore a key design variable because it determines the neutron spectrum and flux at the irradiation position.

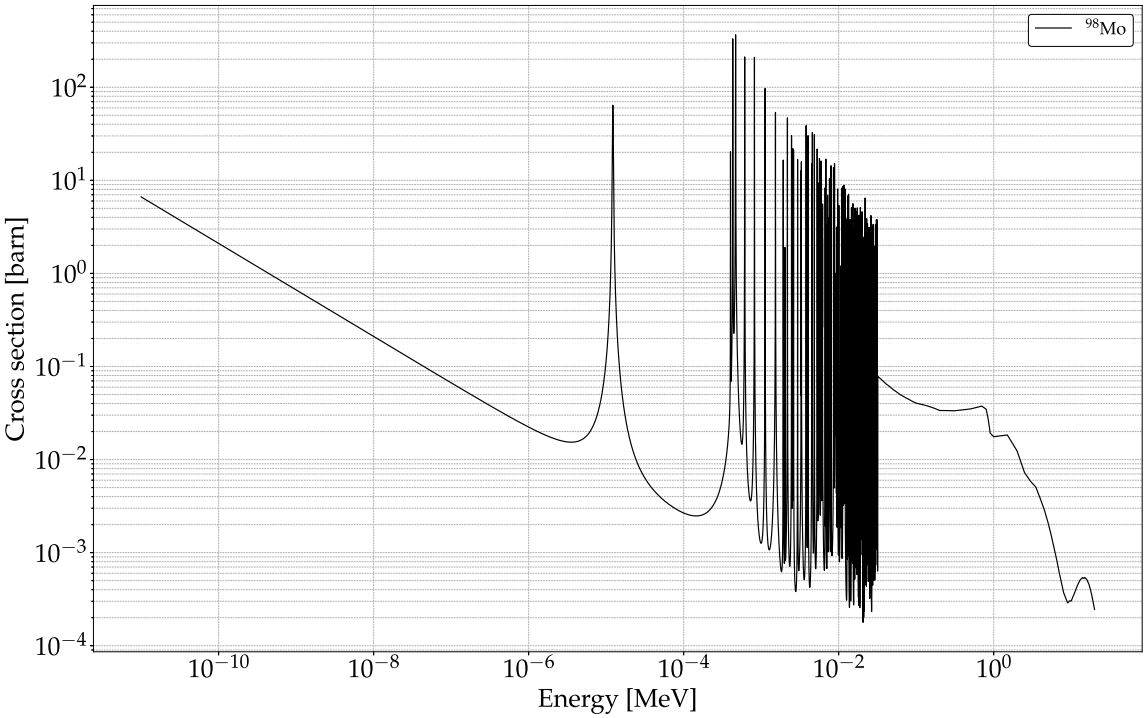


Figure 1.2: Energy-dependent neutron-capture cross section data for the ^{98}Mo$(n,\gamma)^{99}$Mo reaction from the JENDL-4.0 evaluated nuclear data library [19], accessed through JANIS Web [20].

The main advantage of neutron capture on molybdenum is that ^{99}Mo can be produced without uranium targets. As a result, the production route avoids fission-product generation, reduces proliferation-related concerns, and simplifies several aspects of target handling and post-irradiation processing. The use of molybdenum targets also offers a more direct target chemistry and may support target recovery or recycling strategies.
The main limitation is the low specific activity of the product. In this carrier-added route, only a small fraction of the molybdenum target atoms are converted to ^{99}Mo, so the product remains mixed with a much larger amount of stable molybdenum. This reduces compatibility with conventional alumina-based technetium generator systems developed for HSA fission-produced ^{99}Mo. Alternative generator con-

cepts based on high-capacity sorbent materials and chromatographic separation techniques have therefore been developed for LSA applications [6, 13, 21].
For this route, production performance is governed mainly by the neutron flux, the epithermal spectral component, and neutron self-shielding inside the molybdenum target. These factors make the neutron-capture pathway particularly suitable for the TMR optimisation studies performed in this thesis.
Table 1.4 highlights the features of the neutron-capture route that are most relevant for the TMR studies in this thesis.

Table 1.4: Principal characteristics of neutron-capture-based ^{99}Mo production.

Aspect	**Characteristic**
Nuclear reaction	$^{98}\mathrm{Mo}(n,\gamma)^{99}\mathrm{Mo}$
Target material	Natural or enriched molybdenum
Specific activity	Low (LSA)
Neutron spectrum importance	Strong epithermal contribution
Radioactive waste generation	Low
Uranium requirement	None
Infrastructure options	Reactor or accelerator-driven source
Main technical challenge	Optimization of the neutron spectrum

In the context of this thesis, the relevance of HiCANS technology lies in the possibility of generating neutron fields in a compact, non-critical TMR assembly. Unlike a reactor core, such a source allows the moderator, reflector, and irradiation geometry to be treated as design parameters. The suitability of an accelerator-driven neutron source for ^{99}Mo production therefore depends on whether these parameters can provide sufficient epithermal flux at the molybdenum target while limiting losses from leakage, absorption, and self-shielding.

1.2.3 Direct Cyclotron Production from Molybdenum-100

An alternative accelerator-driven approach for medical isotope production is the direct cyclotron production of ^{99m}Tc through the reaction

$$^{100}\mathrm{Mo}(p,2n)^{99m}\mathrm{Tc} \tag{1.2}$$

In this reaction, protons interact with enriched ^{100}Mo targets, resulting in the emission of two neutrons and the formation of ^{99m}Tc. Proton energies in the range of approximately 16–24 MeV are typically used in order to maximize production yield while limiting the formation of undesired radionuclidic impurities. Unlike other production pathways, this method generates ^{99m}Tc directly and therefore bypasses the intermediate production of ^{99}Mo.

The direct production route has attracted considerable interest because it eliminates the need for uranium targets, reactor infrastructure, and large-scale fission-product processing. Furthermore, many medical and industrial cyclotrons already operate within the energy range required for the reaction, making the approach potentially compatible with existing accelerator infrastructure.

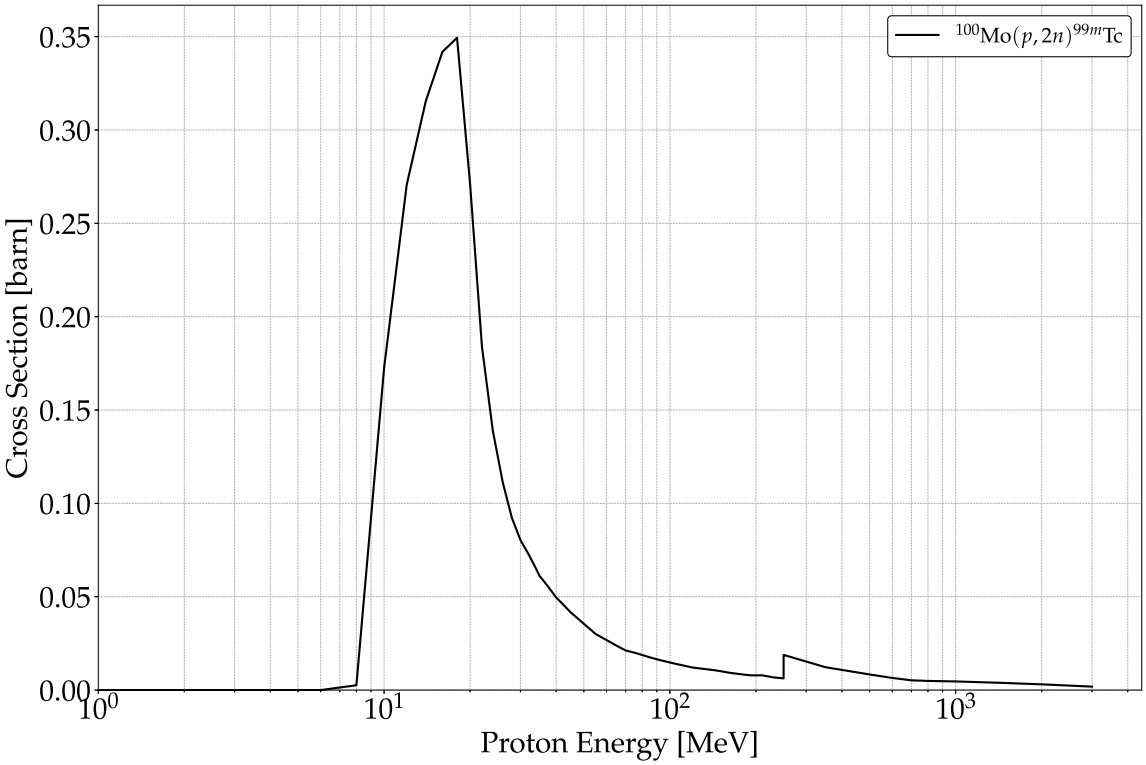


Figure 1.3: Representative excitation function of the ^{100}Mo$(p,2n)^{99m}$Tc reaction from the TENDL evaluated nuclear data library [22], accessed through JANIS Web [20] illustrating the dependence of reaction cross section on proton energy. The optimal production window is typically located between approximately 16 and 24 MeV.

The production yield of the reaction depends strongly on the incident proton energy. At lower proton energies, the reaction cross section remains relatively small, whereas excessive proton energies increase the probability of competing nuclear reactions leading to unwanted technetium isotopes. Consequently, careful optimization of the proton beam energy window is required in order to achieve acceptable radionuclidic purity for clinical applications.
As illustrated in Figure 1.3, the reaction cross section exhibits a pronounced maximum within a limited proton-energy range. Operating within this energy window is essential for maximizing ^{99m}Tc production while simultaneously minimizing the generation of radionuclidic contaminants originating from competing reaction

channels. Beam-energy degradation inside thick targets must therefore be carefully considered during target design and irradiation optimization.
The main distinction of this route is that it produces ^{99m}Tc directly, rather than producing ^{99}Mo for subsequent generator-based distribution. This removes the need for uranium targets and large-scale fission product separation, and it can make use of cyclotron infrastructure already available in some medical or industrial settings. The route is therefore most relevant for local or regional supply models rather than for centralized ^{99}Mo distribution.
The same direct production feature also defines the main limitation. Because ^{99m}Tc has a half-life of approximately 6 h, the product must be processed, quality-controlled, transported, and used within a short time window. Production capacity is therefore limited by the number and location of suitable cyclotrons, the achievable beam current and irradiation time, and the logistics of nearby hospitals or radiopharmacies. In addition, enriched ^{100}Mo targets are expensive and require efficient recovery and recycling.
Product quality depends strongly on the selected proton energy window, target thickness, beam current conditions, irradiation time, and chemical processing. These parameters must be controlled to maximize ^{99m}Tc yield while limiting the formation of unwanted technetium isotopes and other radionuclidic impurities.
The main characteristics of direct cyclotron production of ^{99m}Tc are listed in Table 1.5.

Table 1.5: Principal characteristics of direct cyclotron production of ^{99m}Tc via the $^{100}\mathrm{Mo}(p, 2n)$ reaction.

Aspect	**Characteristic**
Nuclear reaction	$^{100}\mathrm{Mo}(p, 2n)^{99m}\mathrm{Tc}$
Target material	Enriched ^{100}Mo
Final product	Direct ^{99m}Tc production
Required accelerator	Medium-energy cyclotron
Typical proton energy	$\sim$16–24 MeV
Product quality	Direct ^{99m}Tc
Radioactive waste generation	Low
Main technical challenge	Regional distribution limitations

Development programmes, including large-scale work at institutions such as TRIUMF in Canada, have demonstrated that cyclotron-based production can provide ^{99m}Tc quantities suitable for regional nuclear medicine use. Its role is therefore best understood as regional supplementation of the ^{99m}Tc supply, especially in areas where suitable cyclotron infrastructure and short distribution distances are available. In contrast to ^{99}Mo generator supply, this route depends less on centralized isotope production but more strongly on local production scheduling, rapid processing, and distribution logistics.

1.2.4 Photo-fission of Uranium-238

Another proposed route for the production of ^{99}Mo is the photon-induced fission of uranium targets using high-energy bremsstrahlung radiation generated by electron accelerators. In this approach, energetic electrons impinge on a high-Z converter target (lead or tungsten), producing an intense bremsstrahlung photon spectrum that subsequently induces fission reactions in uranium according to

$$^{238}\mathrm{U}(\gamma, f) \tag{1.3}$$

The resulting fission products include ^{99}Mo together with a wide range of additional radioactive isotopes similar to those generated in conventional reactor-based U fission. Since the process relies on accelerator-generated photons rather than a critical reactor core, photo-fission systems are often considered a reactor-independent route for producing HSA ^{99}Mo.

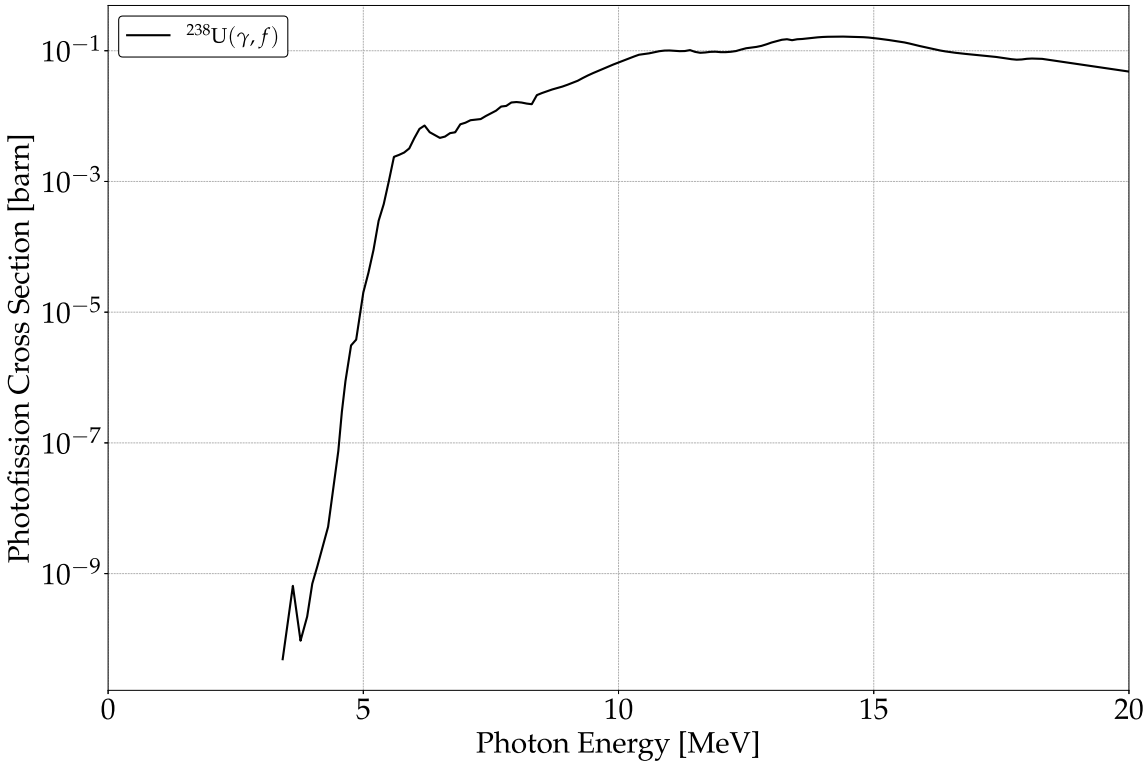


Figure 1.4: Representative photo-fission cross section of ^{238}U from the ENDF/B-VIII.1 evaluated nuclear data library [23], accessed through JANIS Web [20], as a function of photon energy.

The efficiency of the photo-fission process depends strongly on the bremsstrahlung photon spectrum and the giant dipole resonance region of uranium. Photon energies in the range of approximately 10–20 MeV contribute most effectively to the fission

probability. Consequently, electron accelerator energy, converter material, and target geometry all play important roles in determining the achievable isotope production yield.
As illustrated in Figure 1.4, the photo-fission cross section increases significantly within the giant dipole resonance region. Efficient isotope production therefore requires bremsstrahlung spectra containing sufficient photon intensity within this energy range. The broad energy distribution of bremsstrahlung photons, however, also reduces the overall photon-utilization efficiency compared with direct charged-particle reactions.
The main benefit of photo-fission is that it can produce HSA ^{99}Mo without using a critical reactor core. The product is therefore more compatible with established ^{99}Mo/^{99m}Tc generator systems than LSA Mo-based routes. However, this benefit is achieved through a fission process, so uranium target handling, fission product separation, and radioactive waste management remain central parts of the production concept. A summary of the main technical characteristics of photo-fission-based ^{99}Mo production is given in Table 1.6.

Table 1.6: Principal characteristics of photo-fission-based ^{99}Mo production.

Aspect	**Characteristic**
Nuclear reaction	$^{238}\mathrm{U}(\gamma, f)$
Target material	Uranium
Specific activity	High (HSA)
Primary radiation source	Bremsstrahlung photons
Required accelerator	High-power electron accelerator
Radioactive waste generation	High
Compatibility with Tc generators	Excellent
Main technical challenge	Thermal management

The main technical difficulty is the conversion of electron beam power into useful fission yield. Bremsstrahlung production is inefficient, and a large fraction of the accelerator power is deposited as heat in the converter and uranium target. Industrial-scale operation therefore requires high-power electron accelerators, robust target cooling, and radiochemical infrastructure capable of separating ^{99}Mo from a complex fission-product mixture.
Photo-fission has therefore been investigated as a reactor-independent route to high-specific-activity ^{99}Mo, but not as a route that eliminates the main chemical and waste-management issues of uranium fission. Its relevance is strongest where the objective is to avoid reactor criticality while retaining generator-compatible ^{99}Mo. For the present thesis, photo-fission mainly serves as a comparison case: it demonstrates that accelerator-based production can still involve fission chemistry, whereas the neutron-capture route investigated here avoids uranium targets entirely.

1.2.5 Photonuclear Reaction of Molybdenum-100

A non-fission accelerator-driven route for producing ^{99}Mo is the photonuclear reaction

$$^{100}\mathrm{Mo}(\gamma, n)^{99}\mathrm{Mo} \tag{1.4}$$

In this process, high-energy bremsstrahlung photons generated by an electron accelerator interact with enriched ^{100}Mo targets, resulting in neutron emission and the formation of ^{99}Mo. Since the reaction does not involve uranium, the method avoids the generation of large quantities of fission products and eliminates many of the proliferation concerns associated with uranium-based isotope production.

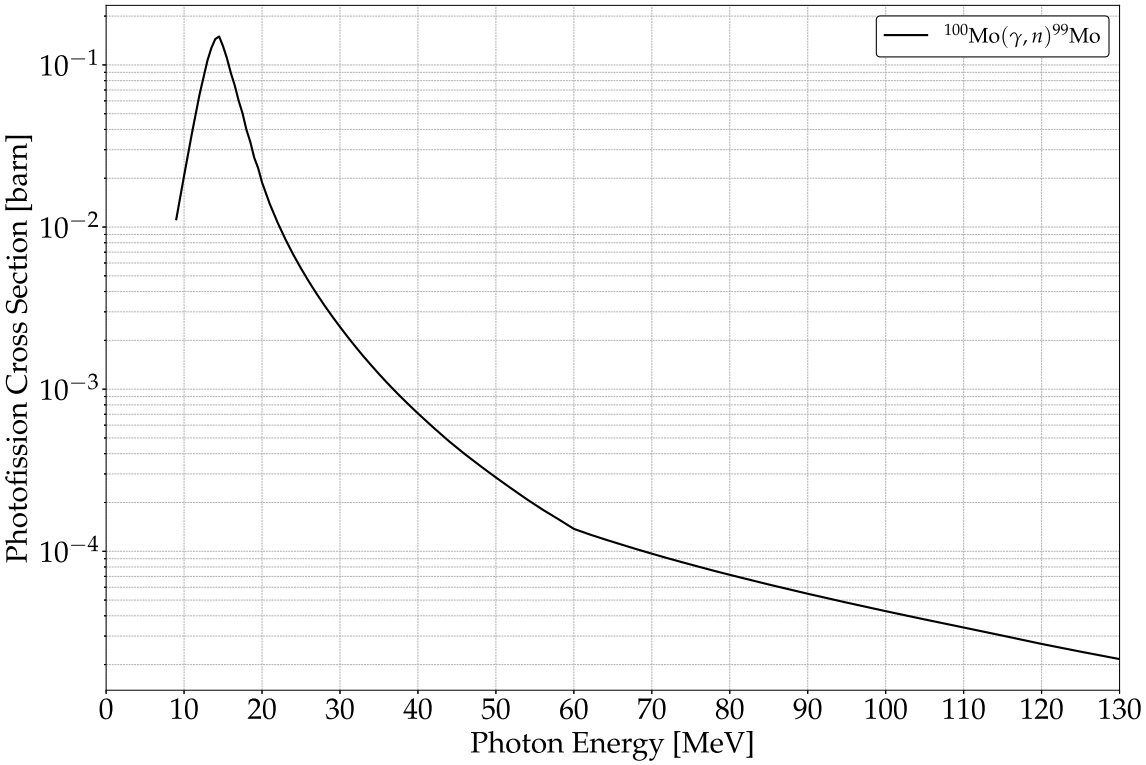


Figure 1.5: Representative cross section of the ^{100}Mo$(\gamma, n)^{99}$Mo reaction from the ENDF/B-VIII.1 evaluated data library [23], accessed through JANIS Web [20], as a function of photon energy showing the giant dipole resonance region relevant for photonuclear production.

Photonuclear production is typically performed using high-power electron linacs operating in combination with high-Z converter materials such as tungsten (W) or tantalum (Ta). Energetic electrons impinge on the converter target and generate a continuous bremsstrahlung photon spectrum, part of which subsequently induces the (γ, n) reaction in the molybdenum target.

The reaction probability depends strongly on photon energy and is closely related to the giant dipole resonance region of ^{100}Mo. Efficient production therefore requires sufficient photon intensity within the relevant energy range, typically around 10–20 MeV. Consequently, electron-beam energy, converter design, and target geometry strongly influence the achievable production yield.
As illustrated in Figure 1.5, the reaction cross section increases significantly within the giant dipole resonance region before decreasing again at higher photon energies. Efficient isotope production therefore depends on maximizing the overlap between the bremsstrahlung photon spectrum and the energy range corresponding to the largest reaction probability.
The photonuclear route shares one important feature with neutron-capture production: ^{99}Mo is produced in a molybdenum target without using uranium. This reduces the fission-product waste stream and avoids fissile target material. However, the product is still LSA ^{99}Mo because it is formed within the bulk molybdenum target and remains mixed with stable molybdenum carrier.

Table 1.7: Principal characteristics of photonuclear ^{99}Mo production via the $^{100}\mathrm{Mo}(\gamma, n)$ reaction.

Aspect	**Characteristic**
Nuclear reaction	$^{100}\mathrm{Mo}(\gamma, n)^{99}\mathrm{Mo}$
Target material	Enriched ^{100}Mo
Specific activity	Low (LSA)
Primary radiation source	Bremsstrahlung photons
Required accelerator	High-power electron accelerator
Radioactive waste generation	Low
Uranium requirement	None
Main technical challenge	Thermal management

The main performance limitation is the low efficiency of the photonuclear process. Only the part of the bremsstrahlung spectrum overlapping the giant dipole resonance contributes effectively to the $^{100}\mathrm{Mo}(\gamma, n)^{99}\mathrm{Mo}$ reaction, while much of the electron beam power is deposited as heat in the converter and target assemblies. For this reason, production yield is governed not only by the nuclear cross section, but also by converter design, electron beam power, target geometry, and thermal management. The principal characteristics of photonuclear ^{99}Mo production via $^{100}\mathrm{Mo}(\gamma, n)$ are summarized in Table 1.7.
Commercial and research interest in photonuclear production has increased in recent years due to the growing demand for reactor-independent isotope production technologies. For example, NorthStar Medical Radioisotopes has pursued non-uranium ^{99}Mo production concepts based on neutron capture in ^{98}Mo and photon-induced transmutation of ^{100}Mo, together with generator technology designed for

LSA ^{99}Mo [13].
Photonuclear production is therefore most relevant as a uranium-free accelerator route to ^{99}Mo, but its practical use is limited by the LSA product and the thermal demands of high-power bremsstrahlung production. Compared with neutron capture, it avoids the need for an intense neutron field but introduces the additional requirement of an electron accelerator, converter target, and photon-to-neutron reaction geometry. In this work, the route provides a useful comparison to $^{98}\mathrm{Mo}(n,\gamma)^{99}\mathrm{Mo}$ because both methods avoid uranium targets but produce LSA ^{99}Mo.

1.3 High Brilliance Neutron Source

The present work focuses on accelerator-driven neutron production based on the High Brilliance neutron Source (HBS) concept developed at Forschungszentrum Jülich. The HBS belongs to the class of High-Current Accelerator-driven Neutron Sources (HiCANS), in which compact high-current accelerators are used to generate neutron beams without a critical reactor core.

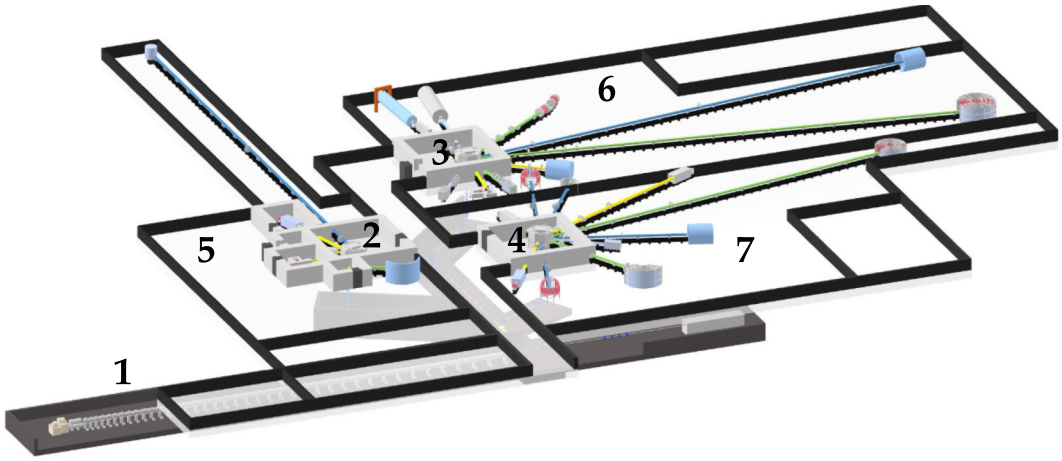


Figure 1.6: Overview of the High Brilliance neutron Source (HBS) concept including the linear accelerator system (1), target–moderator–reflector (TMR) assemblies (2, 3, 4), and representative instrument halls (5, 6, 7). The schematic illustrates the accelerator-driven neutron production concept and the extraction of neutron beams to multiple instrument stations.

In the HBS concept, a high-current proton beam impinges on a heavy metal target and produces neutrons through proton-induced nuclear reactions. The generated neutrons are then moderated and reflected within a compact target–moderator–reflector (TMR) assembly to obtain neutron spectra suitable for applications such as neutron scattering, imaging, and neutron analytics.

The reference HBS design is based on a pulsed proton beam with an energy of approximately 70 MeV and a duty cycle of up to 20%. A Ta target is typically used due to its favorable thermal and mechanical properties under high-power irradiation conditions. The generated fast neutrons are then moderated using hydrogen-rich moderator materials and redirected toward experimental or irradiation positions using reflector structures surrounding the TMR assembly.
Figure 1.6 illustrates the general layout of the HBS concept, including the accelerator, target stations, and instrument areas. Since neutron generation is coupled directly to accelerator operation, the time structure and intensity of the neutron source can be controlled through the proton beam parameters.
One of the central features of the HBS concept is the compact TMR geometry, which strongly influences the resulting neutron spectrum and flux distribution. The moderator material, reflector material, target geometry, and irradiation position determine the relative contributions of thermal, epithermal, and fast neutrons within the system. The neutron field can therefore be adapted to different applications by changing the spectral characteristics at the beam extraction or irradiation position. For neutron-capture-based ^{99}Mo production, the epithermal neutron component is of particular importance because the resonance integral of the $^{98}\mathrm{Mo}(n,\gamma)^{99}\mathrm{Mo}$ reaction contributes significantly to the activation rate. The HBS-type TMR geometry is therefore relevant for this work because moderator and reflector configurations can be studied as design variables that control the neutron spectrum at the molybdenum irradiation position.
Compared to conventional reactor facilities, HiCANS concepts such as the HBS offer several potential advantages:

- absence of a critical reactor core
- modular accelerator and target-station operation
- compact facility layout compared with reactor-based neutron sources
- flexible control of beam timing and operating conditions
- potential compatibility with decentralized isotope production concepts
- less complex licensing requirements due to the absence of reactor criticality

At the same time, accelerator-driven neutron sources generally provide lower neutron fluxes than large high-performance research reactors. Achieving isotope production rates of practical relevance therefore requires careful optimisation of neutron transport, moderation efficiency, reflector performance, and irradiation geometry.
In addition to neutron production performance, practical engineering constraints are important in HiCANS designs. Target thermal loads, radiation damage, cooling

requirements, shielding design, and the available irradiation volume all influence whether a compact accelerator-driven source can be used for isotope production.
The present work investigates whether optimised TMR configurations can produce ^{99}Mo activities of practical relevance through the $^{98}\mathrm{Mo}(n,\gamma)^{99}\mathrm{Mo}$ reaction, subject to realistic source, geometry and irradiation volume constraints. Particular emphasis is placed on how moderator and reflector configurations influence the neutron spectrum, activation behaviour, total activity, and specific activity in molybdenum irradiation targets.

1.4 Research Objective

The objective of this thesis is to evaluate the neutron transport and activation feasibility of producing ^{99}Mo via the $^{98}\mathrm{Mo}(n,\gamma)^{99}\mathrm{Mo}$ reaction in an HBS-type target–moderator–reflector assembly.
The work combines neutron transport simulations, activation calculations, and experimental benchmarking to quantify how moderation, reflection, and irradiation geometry influence the achievable ^{99}Mo activity and specific activity.
The specific objectives are:

- to benchmark simulation-based activation methods against neutron activation experiments
- to investigate neutron spectra and flux distributions in HBS-type TMR systems
- to evaluate the influence of moderator and reflector materials on ^{99}Mo production
- to analyze the effects of irradiation geometry and self-shielding in Mo plates
- to identify practically plausible TMR configurations for accelerator-driven ^{99}Mo production

1.5 Thesis Outline

The remainder of this thesis is structured as follows:

- Chapter 2 introduces the physical principles relevant to neutron production, neutron transport, neutron activation, and gamma spectrometry.
- Chapter 3 presents the simulation tools, nuclear data libraries, experimental procedures, and activity determination methods used throughout this work.

- Chapter 4 validates the simulation-based activation workflow by comparing calculated activities with neutron activation benchmark experiments performed using bare and cadmium-covered activation foils.
- Chapter 5 presents a systematic parameter study of accelerator-driven ^{99}Mo production in an HBS-type target–moderator–reflector assembly, focusing on the influence of moderator materials, reflector configurations, and irradiation geometries on activity and specific activity.
- Finally, Chapter 6 summarizes the main findings of this work and discusses possible directions for future research and technical development.

2 Physics Background

This chapter defines the physical quantities and modelling assumptions used to connect simulated neutron fields with measured activation products in this thesis. Figure 2.1 provides an overview of the workflow linking neutron generation to experimentally reconstructed activities.

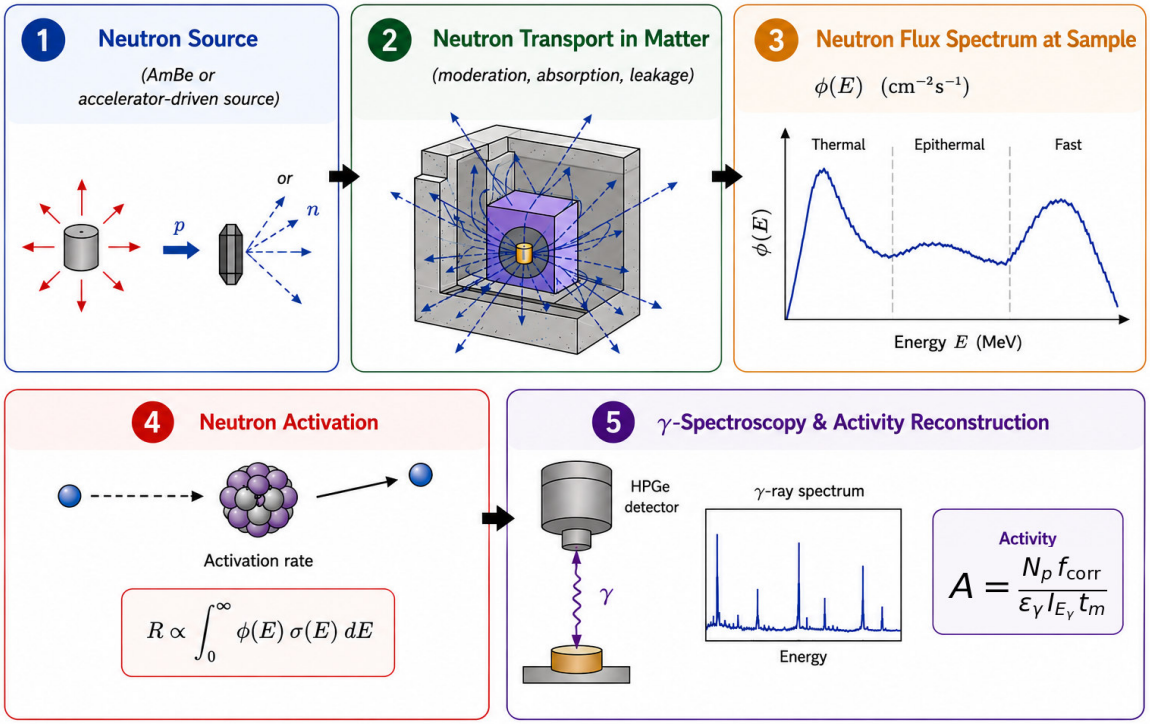


Figure 2.1: Simplified workflow linking neutron generation to experimentally reconstructed activities. (Layout drafted with AI-assisted graphics tools and finalized by the author.)

The workflow begins with neutron generation, followed by transport, moderation, and spectral shaping in the irradiation geometry. The neutron flux spectrum at the sample position is then used to calculate activation rates and activity build-up. The final step is the reconstruction of experimental activities from γ-spectrometry measurements. The definitions introduced here are therefore limited to the quantities needed for the benchmark experiments and the target–moderator–reflector simulations.

2.1 Neutron Sources

The source term determines the initial energy, angular, and intensity distribution of the neutron field before it is modified by surrounding materials. Different source types differ in production mechanism, neutron yield, energy spectrum, angular distribution, and operational complexity. These differences directly influence moderation, leakage, activation rates, and the design of irradiation geometries.
In this work, the source description is needed for two different purposes: the benchmark experiments and the accelerator-driven TMR simulations. Reactor sources are discussed only as a reference case because much of the activation formalism used for thermal and epithermal neutron fields was developed for reactor irradiation conditions.

2.1.1 Reactor-based Sources

In research reactors, fast neutrons are produced mainly by fission of ^{235}U with typical energies of a few MeV. These neutrons are slowed down by scattering in the moderator and surrounding core structures, producing a spectrum that is commonly divided into thermal, epithermal, and fast components [5].
The thermal part is associated with neutrons close to equilibrium with the moderator, the epithermal region corresponds to the slowing-down spectrum, and the fast part is associated with the original fission spectrum and incompletely moderated neutrons. This classification is important because neutron capture reactions are often treated differently in each energy region. In particular, thermal activation is commonly described using tabulated cross sections corresponding to a neutron energy of 25 meV ($v = 2200\ \mathrm{m\,s^{-1}}$), while epithermal activation is described using resonance integrals [24].
Although a reactor is not used as the primary neutron source in this work, reactor-based activation theory provides the reference formalism for the flux-based reaction-rate model used later.

2.1.2 Radioisotopic Sources

Radioisotopic neutron sources generate neutrons either through spontaneous fission or through (α, n) reactions involving α-emitting radionuclides and light target nuclei. They are compact, continuously emitting sources and are widely used for detector testing, calibration, and laboratory-scale activation benchmarks [25, 26].
The most common (α, n) sources combine an α emitter such as ^{241}Am, ^{239}Pu, or ^{238}Pu with Be. In an AmBe source, the dominant neutron-producing reaction is

$$\alpha + {}^{9}\mathrm{Be} \rightarrow {}^{12}\mathrm{C} + n + 5.71\ \mathrm{MeV} \tag{2.1}$$

with only a small fraction of emitted α particles inducing this reaction, while most are stopped in the source matrix [25].

The emitted neutron spectrum is continuous and extends to several MeV. In this study, an AmBe source was used for benchmark experiments because its neutron emission field is well characterised and can be reproduced in simulation. Typical properties of common radioisotopic neutron sources are summarised in Table 2.1. The listed average energies represent mean energies of broad neutron spectra rather than monoenergetic emissions.

Table 2.1: Typical properties of common radioisotopic neutron sources, adapted from [25, 26].

Source	Reaction	Average neutron energy	Typical yield
AmBe	(α, n)	4.2–5.0 MeV	10^6–10^8 s^{-1}
PuBe	(α, n)	4.2–5.0 MeV	10^6–10^8 s^{-1}
AmLi	(α, n)	$\sim$0.3 MeV	10^5–10^7 s^{-1}
^{252}Cf	Spontaneous fission	$\sim$2.1 MeV	10^6–10^9 s^{-1}

2.1.3 Accelerator-driven Sources

Accelerator-driven neutron sources generate neutrons by bombarding a target with charged particles, usually protons or deuterons. Since neutron production is externally driven, the source strength and time structure can be controlled by the accelerator parameters.

At proton energies from several hundred MeV to the GeV range, neutron production is dominated by spallation in heavy targets such as lead (Pb), tungsten (W), and tantalum (Ta). Spallation produces many neutrons per incident proton, but requires large facilities, extensive shielding, and high beam power infrastructure [27]. At lower proton energies, in the range of several tens of MeV, neutron production occurs mainly through proton-induced reactions commonly denoted as (p, xn). These systems generally produce fewer neutrons per proton than spallation sources, but they are more compact and easier to adapt to specific applications.

A lower energy example relevant to this thesis is the High Brilliance Neutron Source (HBS) concept, in which 70 MeV pulsed proton beams are incident on a tantalum target to generate fast neutrons. The neutron field is then modified by the moderator and reflector materials in the TMR assembly, resulting in irradiation positions with different spectral and flux characteristics.

2.2 Neutron Transport Phenomena

For the activation calculations in this thesis, neutron transport determines the energy-dependent flux inside the irradiation sample rather than only the source yield. Because neutrons are electrically neutral, they do not lose energy continuously through Coulomb interactions. Instead, they undergo discrete scattering and absorption events, making neutron trajectories stochastic [5, 25]. For activation analyses, the central output is the neutron flux spectrum in the sample volume, which determines reaction rates through convolution with energy-dependent cross sections.

2.2.1 Neutron Interactions with Matter

The probability that a neutron undergoes a particular interaction is described by the microscopic cross section $\sigma_x(E)$, where x denotes the interaction type. For a material with atomic number density N, the macroscopic cross section is

$$\Sigma_x(E) = N\sigma_x(E) \tag{2.2}$$

with units of inverse length. The total macroscopic cross section is

$$\Sigma_t(E) = \sum_x \Sigma_x(E) \tag{2.3}$$

and the corresponding mean free path is

$$\ell(E) = \frac{1}{\Sigma_t(E)} \tag{2.4}$$

For an uncollided monoenergetic neutron beam in a homogeneous medium, the intensity decreases according to

$$I(x) = I_0 e^{-\Sigma_t x} \tag{2.5}$$

where x is the path length. This expression is useful for illustrating the attenuation behavior of neutrons in shielding materials, although in practical activation geometries the flux is often dominated by scattered neutrons rather than by the uncollided component.
Neutron interactions are commonly divided into scattering and absorption. Elastic scattering changes neutron direction and transfers kinetic energy to the target nucleus, making it the main mechanism for neutron moderation. Inelastic scattering excites the target nucleus and is accompanied by energy loss of the neutron and subsequent γ emission. Absorption removes neutrons from the flux through reactions such as radiative capture (n, γ), charged-particle emission (n, p) or (n, α), and fission [5, 25].

Many capture cross sections show strong energy dependence, especially in the epithermal region, where resonance absorption can occur due to compound nucleus formation. This behaviour is particularly important for activation calculations because narrow resonance structures can dominate reaction rates even when the thermal cross section is small [28].

2.2.2 Moderation and Slowing Down

Moderation is the process by which fast neutrons lose energy primarily through elastic scattering until they approach thermal equilibrium with the medium. For elastic scattering on a stationary nucleus of mass number A, the minimum neutron energy after collision is

$$E'_{\min} = \alpha E \tag{2.6}$$

where

$$\alpha = \left(\frac{A-1}{A+1}\right)^2 \tag{2.7}$$

A useful measure of moderation efficiency is the *average* logarithmic energy decrement,

$$\xi = \left\langle \ln\left(\frac{E}{E'}\right) \right\rangle \tag{2.8}$$

which represents the mean logarithmic reduction of neutron energy per collision. For isotropic elastic scattering in the centre-of-mass system, ξ can be written as

$$\xi = 1 + \frac{\alpha \ln \alpha}{1-\alpha} \tag{2.9}$$

The approximate number of collisions needed to slow a neutron from E_0 to E is then

$$n \simeq \frac{\ln(E_0/E)}{\xi} \tag{2.10}$$

These expressions are standard reactor physics results for neutron slowing down in moderators and are given in [5].
For compounds or mixtures, an effective logarithmic decrement can be estimated as a scattering-weighted average,

$$\xi_{\text{eff}} = \frac{\sum_i N_i \sigma_{s,i} \xi_i}{\sum_i N_i \sigma_{s,i}} \tag{2.11}$$

where N_i, $\sigma_{s,i}$, and ξ_i are the atomic number density, scattering cross section, and logarithmic energy decrement of constituent nuclide i.
A useful moderator must slow neutrons efficiently while absorbing as few neutrons as possible. Table 2.2 compares selected nuclei and compounds relevant to this work.

For elemental entries, the listed absorption values are thermal microscopic absorption cross sections at 0.0253 eV. For compounds, the values are approximate formula-unit reference values obtained from the constituent absorption cross sections and are used only for qualitative comparison. The absorption cross sections listed are thermal microscopic absorption cross sections at 0.0253 eV and are therefore used only as reference values. For non-thermal spectra, an effective absorption cross section must be obtained by spectrum-averaging $\sigma_a(E)$. The listed collision numbers n correspond to slowing down from 2 MeV to 0.025 eV using Eq. (2.10).

Table 2.2: Slowing-down and thermal absorption properties of selected moderator materials.

Material	ξ	n	σ_a **[barn]**
H	1.000	18	0.332
D	0.725	25	0.0005
Be	0.207	88	0.0076
O	0.120	152	0.0002
Zr	0.022	827	0.185
H_2O	∼0.92	∼20	∼0.66
D_2O	∼0.59	∼31	∼0.001
ZrH_2	∼0.77	∼24	∼0.85

Moderators containing hydrogen, such as H_2O and ZrH_2, provide compact moderation because hydrogen transfers a large fraction of neutron energy per collision. Heavy water and beryllium have lower energy loss per collision but much smaller absorption probabilities, which can improve neutron economy.
At thermal energies, bound-atom effects can become important. Scattering in materials such as water or zirconium hydride is not always well described by a free-gas approximation because molecular and lattice binding affect the angular and energy distribution of scattered neutrons. Modern transport calculations therefore use thermal scattering law data, commonly denoted $S(\alpha, \beta)$, for materials where bound scattering significantly affects the thermal spectrum.

2.2.3 Leakage and Reflectors

In finite systems, some neutrons escape the geometry without further interaction. This loss mechanism is called leakage and reduces the neutron population available for moderation and activation. Reflectors reduce leakage by scattering outward-moving neutrons back into the active region.
Reflector performance depends on material density, scattering probability, absorption probability, thickness, and the energy spectrum in the reflector. Increasing reflector thickness generally reduces leakage, but the benefit eventually saturates once most recoverable neutrons have already been scattered back.

Table 2.3 compares different reflector materials. The listed microscopic cross sections are thermal reference values only. In practice, reflector performance must be interpreted using energy-dependent macroscopic cross sections and the actual neutron spectrum.

Table 2.3: Reference properties of selected reflector materials.

Material	**Density (g/cm^3)**	σ_s **(barn)**	σ_a **(barn)**
Be	1.85	∼6.1	∼0.0076
MgO	3.58	∼7.4	∼0.063
Pb	11.34	∼11	∼0.17

Beryllium is an effective reflector because it combines low absorption with better scattering properties. Magnesium oxide provides moderate reflection with good thermal and mechanical stability. Lead is included because, in accelerator-driven systems, fast-neutron leakage is important and high-density, high-Z materials can help reduce leakage in fast-spectrum regions. At sufficiently high neutron energies, threshold reactions such as $(n, 2n)$ will also contribute to neutron multiplication, although this is a fast-neutron effect and is negligible after the spectrum has thermalised [25, 28].

2.2.4 Neutron Flux

The neutron flux used in activation analysis is the scalar neutron flux. It represents the total neutron path length per unit volume and per unit time and has units of $\mathrm{cm}^{-2}\,\mathrm{s}^{-1}$. For a monoenergetic neutron population with number density n and speed v, the scalar flux is

$$\phi = nv \tag{2.12}$$

This scalar quantity should be distinguished from the neutron current, which describes directional transport across a surface. The scalar flux is the relevant quantity for activation calculations because reaction rates are proportional to the total neutron path length available for interactions within the material.
In realistic irradiation fields, neutrons are distributed over energy. The neutron field is therefore described by the energy-dependent scalar flux $\phi(E)$, where $\phi(E)\,dE$ is the flux contribution from neutrons with energies between E and $E + dE$. The total flux is

$$\phi = \int_0^\infty \phi(E)\,dE \tag{2.13}$$

For the analyses in this thesis, the spectrum is divided into thermal, epithermal, and fast regions using fixed energy boundaries. These boundaries are analysis conventions rather than universal physical limits:

- **Thermal region:** $0 < E < E_{Cd}$, with $E_{Cd} = 0.5$ eV
- **Epithermal region:** $E_{Cd} < E < E_{fast}$, with $E_{fast} = 0.1$ MeV
- **Fast region:** $E_{fast} < E < 20$ MeV

The corresponding region-integrated fluxes are

$$\phi_{th} = \int_{0}^{E_{Cd}} \phi(E)\, dE \tag{2.14}$$

$$\phi_{epi,tot} = \int_{E_{Cd}}^{E_{fast}} \phi(E)\, dE \tag{2.15}$$

$$\phi_{fast} = \int_{E_{fast}}^{20\,\mathrm{MeV}} \phi(E)\, dE \tag{2.16}$$

The quantities ϕ_{th}, $\phi_{epi,tot}$, and ϕ_{fast} defined above are region-integrated fluxes obtained directly from the neutron spectrum. They should be distinguished from the conventional flux parameters used in resonance integral activation formalisms. In the Høgdahl convention, the thermal contribution is written using the 2200 m/s thermal flux ϕ_0, while the epithermal contribution is written using the epithermal flux parameter ϕ_e associated with an assumed $1/E$ slowing-down spectrum [24]. For an ideal $1/E$ epithermal spectrum between E_{Cd} and E_{fast},

$$\phi_{epi,tot} = \phi_e \ln\left(\frac{E_{fast}}{E_{Cd}}\right) \tag{2.17}$$

so that

$$\phi_e = \frac{\phi_{epi,tot}}{\ln\left(E_{fast}/E_{Cd}\right)} \tag{2.18}$$

When tabulated 2200 m/s cross sections or resonance integrals are used, the corresponding flux parameter must therefore be defined consistently with the adopted convention. If the simulated energy-dependent flux spectrum is used directly, the activation rate can instead be evaluated from the full spectral integral.

2.3 Neutron Activation

Neutron activation describes the production of radioactive nuclei through neutron-induced reactions, most commonly radiative capture (n, γ). The reaction rate is governed by the interaction between the neutron flux spectrum and the energy-dependent cross section of the target nucleus.

2.3.1 Fundamental Activation Integral

If the neutron flux can be considered homogeneous within the sample, the reaction rate per target atom is

$$r = \int_0^\infty \phi(E)\,\sigma(E)\,dE \tag{2.19}$$

where $\phi(E)$ is the energy-dependent scalar flux and $\sigma(E)$ is the microscopic reaction cross section. If $\phi(E)$ is expressed in $\mathrm{cm^{-2}\,s^{-1}}$ and $\sigma(E)$ is expressed in barns, the factor 10^{-24} $\mathrm{cm^2/barn}$ must be included. If SI units are used throughout, one barn corresponds to 10^{-28} $\mathrm{m^2}$.
For a sample containing N_T target atoms, the total reaction rate is

$$R = N_T r \tag{2.20}$$

with

$$N_T = \frac{m}{M} N_A h \tag{2.21}$$

where m is the sample mass, M is the molar mass, N_A is Avogadro's number, and h is the isotopic abundance of the target nuclide.

2.3.2 Thermal Neutron Activation

In the thermal region, neutrons are close to equilibrium with the moderator and are often described by a Maxwellian distribution. For many capture reactions, the cross section approximately follows a $1/v$ dependence,

$$\sigma(v) = \frac{\sigma_0 v_0}{v} \tag{2.22}$$

where σ_0 is the tabulated cross section at the reference velocity $v_0 = 2200\ \mathrm{m\,s^{-1}}$.
If the reaction follows $1/v$ behaviour and the thermal flux is expressed using the corresponding 2200 m/s convention, the thermal contribution can be approximated as

$$r_{th} \approx \sigma_0 \phi_0 \tag{2.23}$$

Here, ϕ_0 is the conventional 2200 m/s thermal flux used consistently with the tabulated cross section σ_0. This quantity should not be confused with the region-integrated subcadmium flux ϕ_{th} defined in Section 2.2.4.

2.3.3 Epithermal Neutron Activation and Resonances

In the epithermal region, neutrons are slowing down from higher energies and the neutron flux is often approximated by a $1/E$ dependence. In this energy range, neutron capture cross sections exhibit pronounced resonance structures associated with the formation of a compound nucleus at discrete energies. These resonances can dominate the activation rate even when the thermal cross section is relatively small.

Near a resonance energy E_r, the capture cross section can be described by the Breit–Wigner expression

$$\sigma_\gamma(E) = \frac{\lambda_r^2 g}{4\pi} \frac{\Gamma_n \Gamma_\gamma}{(E - E_r)^2 + \frac{\Gamma^2}{4}} \tag{2.24}$$

where λ_r is the neutron wavelength at the resonance energy, g is the statistical spin factor, and Γ_n, Γ_γ, and Γ are the neutron, radiative, and total resonance widths, respectively.

For an ideal slowing-down spectrum of the form $\phi(E) \propto 1/E$, the epithermal contribution to the activation rate is represented by the resonance integral

$$I_0 = \int_{E_{Cd}}^{E_{fast}} \frac{\sigma(E)}{E}\, dE \tag{2.25}$$

which condenses the energy-dependent behaviour of the cross section into a single parameter.

In real systems, however, the epithermal spectrum deviates from the ideal $1/E$ behaviour due to factors such as geometry, moderation conditions, and neutron leakage. This deviation is commonly described by a modified spectrum of the form

$$\phi(E) \propto \frac{1}{E^{1+\alpha}} \tag{2.26}$$

where the parameter α characterizes the deviation from the ideal slowing-down spectrum. For $\alpha = 0$, the ideal $1/E$ spectrum is recovered.

The deviation from the ideal spectrum alters the contribution of resonances to the activation rate and therefore requires a corrected resonance integral, denoted here

as $I_\gamma(\alpha)$. This quantity represents the effective resonance contribution under the actual spectral conditions, with

$$I_\gamma(0) = I_0 \tag{2.27}$$

The epithermal contribution to the activation rate can then be written as

$$r_{epi} \approx I_\gamma(\alpha)\, \phi_{epi} \tag{2.28}$$

where ϕ_{epi} is the epithermal neutron flux defined consistently with the resonance-integral formalism.

2.3.4 Cadmium Filtering

Cadmium covers are commonly used to suppress the thermal component of an irradiation field. Because ^{113}Cd has a very large neutron-capture cross section at thermal energies, a sufficiently thick cadmium cover strongly attenuates low-energy neutrons.

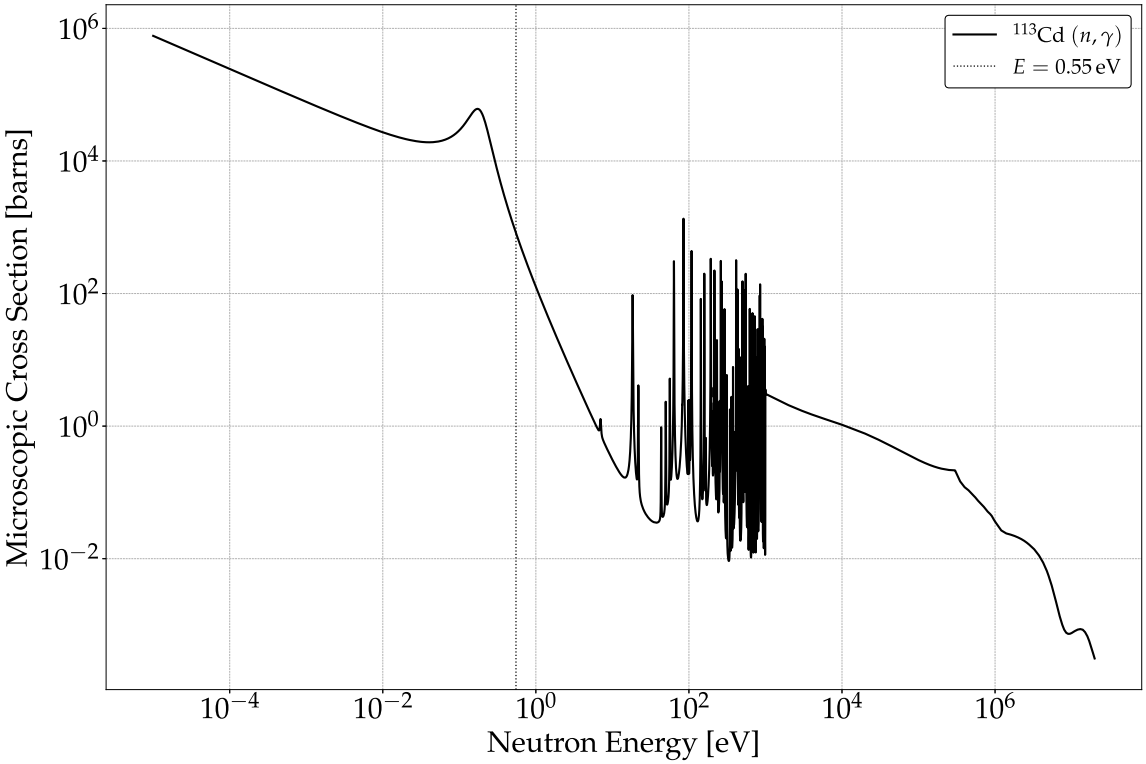


Figure 2.2: Microscopic neutron capture cross section of ^{113}Cd from the ENDF/B-VIII.1 evaluated data library [23], accessed through JANIS Web [20], as a function of neutron energy.

The effective cadmium cut-off is not a sharp physical boundary and depends on cover thickness and irradiation geometry; however, a value of $E_{Cd} \approx 0.5$ eV is commonly adopted for activation analysis calculations.
As shown in Figure 2.2, the neutron capture cross section of ^{113}Cd is extremely large in the thermal energy region and decreases rapidly above the cadmium cut-off energy. Consequently, neutrons with energies below approximately 0.5 eV are strongly attenuated by the cadmium cover, while higher-energy epithermal neutrons are transmitted to a much greater extent.
Under cadmium-covered conditions, the thermal contribution is strongly reduced, so the remaining activation is mainly sensitive to epi-cadmium neutrons and resonance capture. Residual thermal transmission, fast-neutron reactions, and sample self-shielding may still need to be considered depending on the foil, cover thickness, and irradiation field.

2.3.5 Neutron Self-shielding

In activation analysis, the neutron flux inside a sample is not always equal to the unperturbed flux in the surrounding medium. Absorption and scattering within the sample perturb the local neutron field and can reduce the volume-averaged flux available for activation. This effect is referred to as neutron self-shielding.
The exponential attenuation expression in Eq. 2.5 illustrates the basic removal of uncollided neutrons in a homogeneous material. However, it is not sufficient for activation modelling in realistic irradiation fields, where the neutron spectrum is energy-dependent and the flux also contains scattered neutrons.
Self-shielding is especially important in energy regions where the capture cross section contains strong resonances. At resonance energies, neutrons can be absorbed preferentially near the surface of the sample, reducing the neutron flux at those energies deeper inside the material. The effective resonance contribution to the activation rate is therefore lower than it would be in an infinitely dilute sample.
The magnitude of self-shielding depends on sample composition, thickness, geometry, and the incident neutron spectrum. In analytical activation formalisms, it is often represented by correction factors relating the effective flux in the sample to the unperturbed flux. In Monte Carlo transport calculations, self-shielding can be treated explicitly when the sample geometry, material composition, and energy-dependent cross sections are modelled with sufficient detail.

2.4 Gamma-ray Spectrometry

After neutron activation, the produced radionuclides decay and may emit characteristic γ rays. Gamma-ray spectrometry is used in this work to identify activation products and to determine their activities from the measured full-energy peaks.

High-purity germanium (HPGe) detectors are used because their energy resolution allows closely spaced γ lines to be separated and multiple radionuclides to be identified in the same spectrum. The measured spectrum contains full-energy peaks superimposed on a continuum background arising mainly from Compton scattering and ambient background radiation.
For a selected γ line, the activity at a defined reference time can be obtained from the net full-energy peak area as

$$A_{\mathrm{ref}} = \frac{N_{\mathrm{p}}}{\varepsilon_{\gamma}\, I_{E_{\gamma}}\, t_{m}}\, f_{\mathrm{corr}} \tag{2.29}$$

where N_{p} is the net peak area, ε_{γ} is the full-energy peak efficiency at the corresponding energy, $I_{E_{\gamma}}$ is the emission probability of the selected γ line, and t_m is the live measurement time. The correction factor f_{corr} converts the measured peak area to the chosen reference time and includes decay before counting, decay during counting, dead-time losses, γ self-absorption, and coincidence summation where applicable.
The reconstructed activities are then used to determine experimental reaction rates and to benchmark the simulation-based activation predictions described in the following chapter.

3 Methodology

This chapter describes the tools, data, and procedures used to model neutron transport and activation and to determine induced activities from both measurements and simulations. It first introduces the Monte Carlo (MC) transport code PHITS and the activation and decay-chain code DCHAIN, together with the nuclear data libraries used throughout this work. It then presents the experimental workflow used to reconstruct activities from measured γ-ray spectra. Finally, it outlines the two simulation-based activity prediction approaches applied in this work: the flux analysis method (FAM) and the flux folding method (FFM).

3.1 Simulation Tools and Nuclear Data Libraries

MC particle transport simulations are widely used to model radiation transport and interactions in complex geometries. In MC simulations, the histories of many individual particles are sampled and tracked through matter, including processes such as scattering, absorption, and nuclear reactions. The probability of each interaction is determined from evaluated nuclear data, most importantly energy-dependent cross sections. By repeating this sampling over a large number of particle histories, the MC method provides statistical estimates of quantities such as neutron flux spectra, reaction rates, and energy deposition.
For activation studies, the predicted neutron flux spectrum in the sample is combined with activation and decay calculations to determine nuclide production and the resulting activities as a function of irradiation and cooling time. In this work, MC simulations were used to determine neutron flux spectra in the investigated systems, which were then used as input to the activity calculations described in Section 3.2.2.

3.1.1 PHITS Code

MC transport calculations were performed using the Particle and Heavy Ion Transport code System (PHITS) [29], a general-purpose transport code developed through a collaboration of institutes in Japan and managed by the Japan Atomic Energy Agency (JAEA). PHITS can simulate the transport and interaction of a wide range of particles, including heavy ions, protons, neutrons, electrons, and photons, over

broad energy ranges. This is achieved using a combination of evaluated nuclear data libraries and nuclear reaction models at higher energies.
A PHITS simulation is defined by an input file in which the user specifies transport settings together with geometry, material compositions, and particle source terms. Simulation results are obtained using tally estimator functions that score quantities such as energy deposition, particle flux, energy spectra, and production yields. The input components most relevant for this work are summarized below.
Parameter section (transport and physics settings) – The parameter section specifies physical and numerical settings controlling particle transport. This includes the choice of physics models and transport options, as well as run parameters that determine statistical precision (e.g., the number of particle histories). PHITS provides different recommended combinations of models and data libraries for nuclear reactions, as shown in Fig. 3.1. The choice of transport settings and physics treatment influences both the physical composition of the neutron field (e.g., moderation and reaction probabilities) and the statistical uncertainty of the scored spectra. PHITS also supports parallel execution using MPI (Message Passing Interface) [30, 31] for distributed-memory parallelism, and OpenMP (Open Multi-Processing) [32, 33] for shared-memory multithreading parallelism. Both of these were used where needed to obtain sufficient statistics.

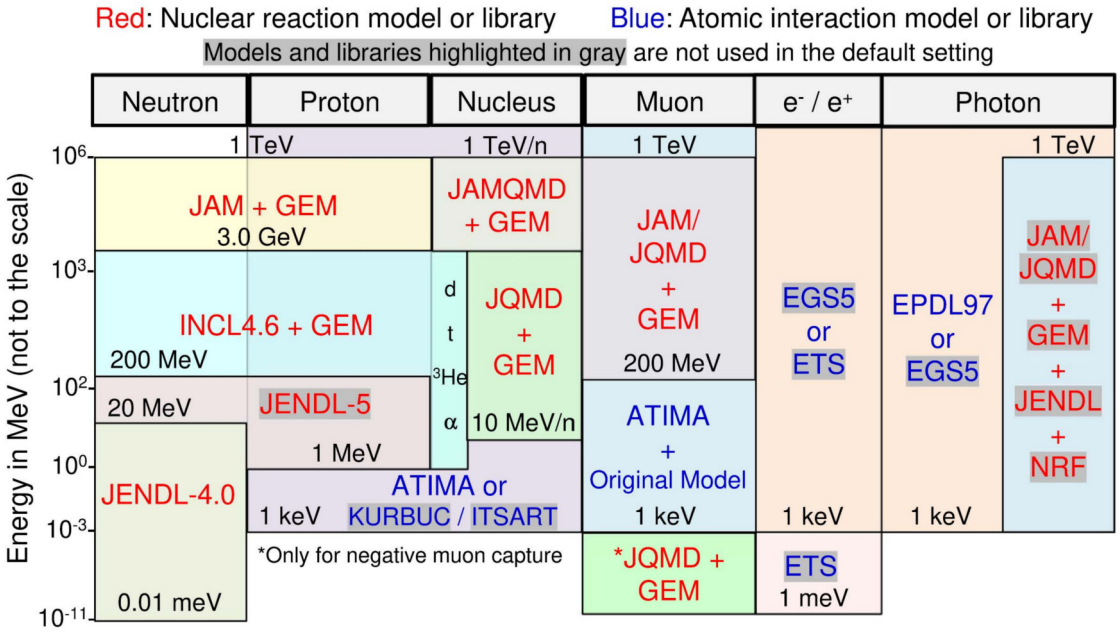


Figure 3.1: Recommended physics models and data libraries for use in PHITS obtained from [29].

Source description – The source description specifies the initial conditions for simulated particle histories, including particle type, energy distribution, and spatial

and angular emission characteristics. These settings determine the normalization and spectral characteristics of the primary radiation field and therefore strongly influence the scored neutron flux spectra and derived reaction rates. In this work, the source definitions were selected to represent the relevant neutron production conditions of each investigated system.

Material description – Material definitions specify elemental or isotopic composition and density for each region in the model. Together with the nuclear and atomic data used by PHITS, these definitions determine interaction probabilities and therefore control moderation behaviour, absorption, and spectral shaping. For neutron transport, the material definition is also where the user links materials to specific evaluated data treatments, for example by assigning thermal scattering law data $S(\alpha, \beta)$ for moderators such as water when appropriate (Section 3.1.3). Material specification is particularly relevant for activation because absorption and resonance effects in moderators, structural components, and the samples themselves can significantly modify the neutron spectrum at the irradiation position.

Geometry description – The geometry description defines the three-dimensional arrangement of all components and boundaries in the simulated setup. PHITS supports general geometry (GG) and combinatorial geometry (CG). For moderated and shielded systems, the local neutron spectrum is sensitive to distance, interface, and irradiation position. Therefore, geometric precision is important for reliable activation predictions.

Scoring of simulation results (tallies) – Tallies are estimator functions used to score quantities of interest during the transport calculation, such as track-length flux, energy spectra, and production yields. In neutron activation applications, tallies are used to obtain neutron flux spectra in regions of interest. These spectra are then converted into reaction rates and activities. PHITS also provides tallies (e.g., `[T-Product]` and `[T-Yield]`) related directly to activation. These can estimate nuclide production in a scoring region. In this work, the main workflow is based on neutron flux spectra (primarily from `[T-Track]`) combined with subsequent activation calculations (Section 3.2.2). This choice was made to maintain control over the activation modelling assumptions and to use a consistent analysis approach across all investigated configurations. Consequently, tally definitions (scoring region, energy binning, and number of histories) directly affect the resolution and uncertainty of the neutron spectra and the resulting activities.

3.1.2 DCHAIN Code

DCHAIN [34] is an activation and decay-chain code that calculates the time-dependent evolution of radionuclide inventories during irradiation and subsequent cooling. While it is applicable to general radiation fields, its development and many applications are closely linked to activation problems in accelerator facilities. Activation calculations in this work were performed using PHITS version 3.22

together with the coupled DCHAIN-PHITS implementation distributed in the same release.

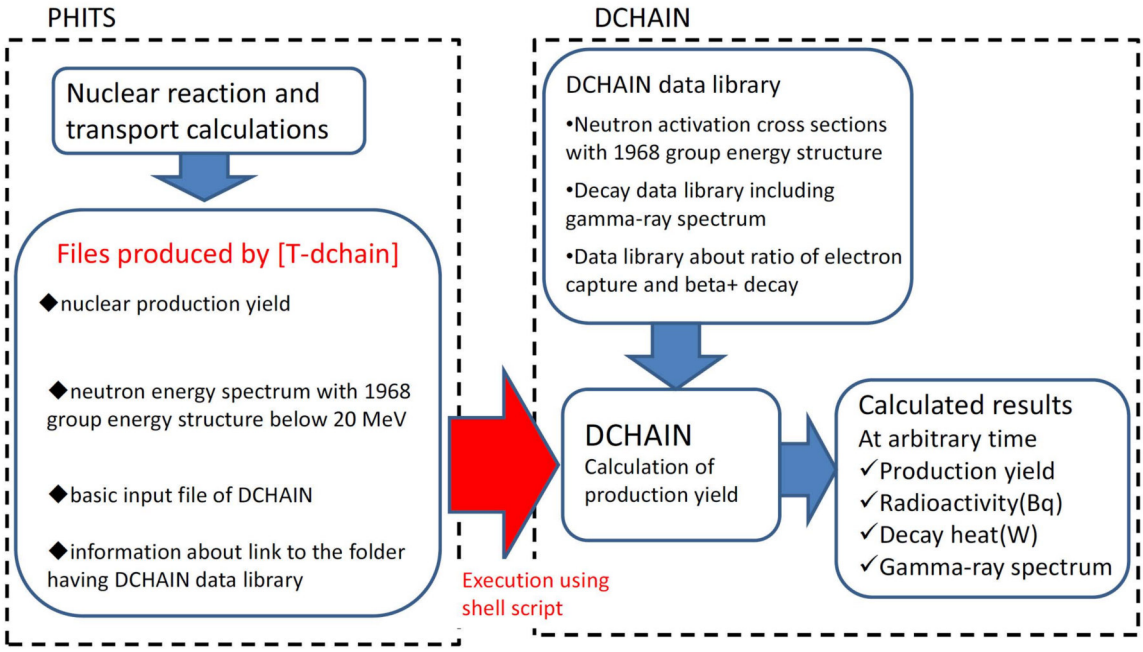


Figure 3.2: Concept of the coupled PHITS–DCHAIN calculation workflow obtained from [35].

The coupling between particle transport and activation (Fig. 3.2) is implemented via the PHITS tally `[T-Dchain]`, which generates the DCHAIN input and auxiliary files required for the time-dependent inventory calculation.
Conceptually, the coupled workflow separates the neutron-induced transmutation below 20 MeV and the nuclide production from reactions induced by particles above 20 MeV. On the transport side, `[T-Dchain]` produces a neutron spectrum file based on `[T-Track]` and a nuclide production yield file based on `[T-Yield]`, in addition to the DCHAIN input file. The `[T-Track]` output provides neutron energy spectra below 20 MeV in a 1968-group structure, while `[T-Yield]` provides nuclide production yields from reactions induced by protons, heavy ions, mesons, and neutrons with energies above 20 MeV.
The time evolution of nuclide inventories in DCHAIN is based on Bateman-type chain formalisms [36] and includes contributions from radioactive decay, neutron reactions below 20 MeV, and production/depletion from higher-energy nuclear interactions represented through the transport-derived yield terms [34]. The irradiation history is defined explicitly for the activation calculation as a sequence of irradiation and cooling steps with associated relative intensity factors. The time variation specified in the particle transport source definition is independent of the time structure used in the activation calculation; therefore, the irradiation schedule must be defined separately in the `[T-Dchain]` tally.

DCHAIN employs internal decay and neutron reaction cross-section libraries and allows the user to select between different evaluated datasets and hybrid combinations. In addition, modern versions propagate statistical uncertainties derived from simulated neutron spectra and nuclide yields through to inventories and derived activation quantities [34]. Typical outputs include time-dependent nuclide inventories and activities, as well as derived quantities such as decay heat, photon spectra, and photon effective dose rates for user-defined regions and output times.

3.1.3 Nuclear Data Libraries

Nuclear data libraries provide the evaluated interaction and decay information required for radiation transport and activation calculations, most importantly energy-dependent reaction cross sections, secondary-particle production data, and radioactive decay data. In transport simulations, these data determine microscopic interaction probabilities and thereby influence macroscopic observables such as moderation, attenuation, and reaction rates. For activation calculations, neutron-induced transmutation data and decay data are additionally required to predict nuclide inventories and activities as a function of irradiation and cooling time.

In general, nuclear data can be distinguished between experimental compilations and evaluated libraries. Evaluated libraries combine measurements with nuclear reaction modelling and consistency checks to provide complete datasets suitable for simulations.

Neutron transport calculations performed with PHITS used evaluated nuclear data from the JENDL-4.0 library [19]. PHITS combines evaluated nuclear data for low-energy neutron-induced reactions with nuclear reaction models at higher energies to enable transport simulations over wide energy ranges.

At thermal energies, scattering in bound moderators cannot always be represented adequately by a free-gas treatment, because molecular binding and lattice effects modify the energy and angular distribution of scattered neutrons. Thermal scattering law data $S(\alpha, \beta)$ are therefore used to represent bound-atom scattering in moderators and to improve predictions of thermal neutron spectra. In PHITS, the thermal scattering treatment is assigned through the material definition by linking a moderator to the corresponding dataset. This is relevant for activation analyses because capture reaction rates can be sensitive to the thermal and epithermal spectral shape produced by moderation.

DCHAIN relies primarily on internal neutron reaction cross-section libraries and decay data libraries. The neutron reaction cross sections are used to convert neutron spectra into transmutation rates, while decay data are used to construct decay chains and compute time-dependent inventories and derived quantities such as activities, decay heat, and photon spectra.

In this work, the neutron reaction cross section library in DCHAIN was selected via `inxslib=100`, corresponding to the hybrid library composed (in order) of JENDL/AD-2017 [37], JENDL-4.0, ENDF/B-VIII.0 [38], JEFF-3.3 [39], and FENDL/A-3.0 [40]. Hybrid libraries are constructed by including all reactions from the highest-priority library and then adding reactions from subsequent libraries only when they are absent from earlier ones.
The decay data library was selected via `idcylib=5`, corresponding to a hybrid library that prioritizes JENDL/DDF-2015 [41] and supplements missing nuclides from ENDF/B-VIII.0 [38].
This simulation environment was kept fixed throughout the work to ensure comparability between simulated configurations and to avoid systematic differences arising from code or library changes between simulation campaigns.

3.2 Activity Determination Methods

Experimentally determined activities provide the reference values against which simulation-based activity predictions are assessed. Activated samples were measured by high-resolution γ-spectrometry, and activities at the end of irradiation (EOI) were reconstructed from peak areas using calibrated detector efficiencies and standard decay corrections. These experimental activities were used as benchmark values to validate and interpret the activity predictions obtained from MC neutron transport simulations.
For the simulations, neutron flux spectra were converted into reaction rates and combined with the same irradiation and decay formalism to predict activities at EOI. Two approaches were used for this conversion: the flux analysis method (FAM) and the flux folding method (FFM). The following sections first describe the experimental reconstruction procedure and then present the simulation-based methods used in the following chapters.

3.2.1 Experimental

Experimental activity reconstruction was based on γ-spectrometry of activated samples using a broad-energy high-purity germanium detector system. For each sample, the activity was reconstructed from the net counts of a selected full-energy peak, corrected for detector efficiency and radioactive decay between EOI and the start of the measurement.
Quantitative γ-spectrometry requires a well-defined counting geometry, an energy calibration, and an absolute full-energy peak (FEP) efficiency calibration. In addition, consistent peak evaluation is required to obtain background-corrected net peak areas and to control systematic effects such as peak interferences and coincidence summing.

3.2.1.1 Detector System

Measurements were performed using a broad-energy high-purity germanium (BEGe) detector system (Mirion Technologies). The detector was operated inside a 10 cm thick lead shield to reduce background radiation. Energy deposited by a γ ray produces electron–hole pairs in the germanium crystal. The resulting charge pulse is proportional to the deposited energy and is processed to generate a pulse-height spectrum.
The signals from the BEGe detector were processed with a charge-sensitive preamplifier integrated into the detector cryostat, followed by a digital signal-processing (DSP) unit, and recorded with a digital MCA controlled by GENIE 2000 spectroscopy software [42].
According to the manufacturer's specifications, the detector provides an energy resolution of $\leq$ 0.65 keV full width at half maximum (FWHM) at the 122.1 keV γ-ray line of ^{57}Co and $\leq$ 1.80 keV FWHM at the 1.33 MeV γ-ray line of ^{60}Co. The specified relative efficiency is 34%. These characteristics make the detector suitable for high-resolution gamma-ray spectrometry and the identification of closely spaced photopeaks.

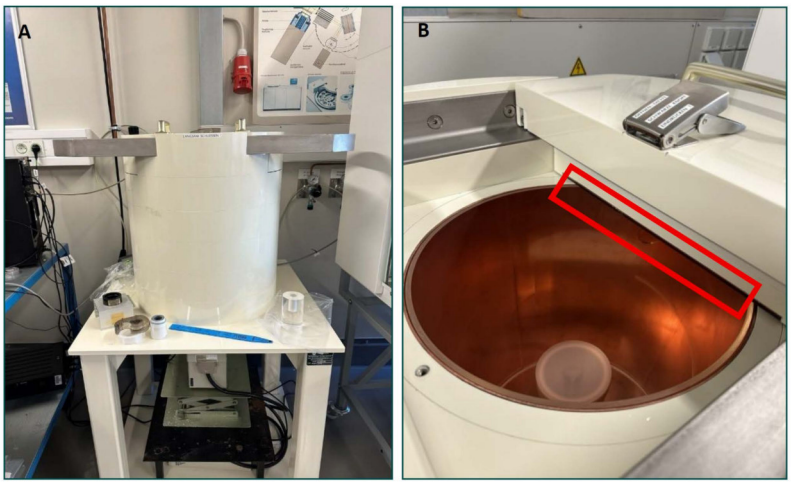


Figure 3.3: BEGe detector system used for gamma-ray spectrometry measurements. The detector was housed in a lead shield (A), and the principal counting geometry was defined by a source-to-endcap distance of 19 cm (B).

The detector was housed in a 10 cm thick low-background lead shield consisting of 80 mm and 20 mm layers of low-activity lead.
Two counting geometries were used: a distance of 19 cm from the detector endcap and a close geometry with the sample placed directly on the endcap (0 cm). The 19 cm geometry was used as the principal configuration because most samples were foil-type and therefore represent extended sources rather than ideal point

sources. A larger distance reduces sensitivity to positioning and source extension. Measurements at 0 cm were performed for small foils to increase counting efficiency, and a separate efficiency calibration was applied for this geometry. The detector setup and the definition of the counting distance are shown in Fig. 3.3.
Spectra were acquired and analysed using GENIE 2000 [42], which was used for peak identification, background subtraction, and peak fitting. The resulting net peak areas constitute the primary experimental input for the activity reconstruction described below.
The produced radionuclides were identified by matching the measured γ-ray energies to reference γ-line energies listed in [43].

3.2.1.2 Calibration Procedures

Energy calibration assigns each channel of the recorded spectrum to a γ-ray energy. Absolute FEP efficiency calibration converts net peak areas into emission rates. Because absolute efficiency depends strongly on the source-to-detector distance, the efficiency calibration was performed separately for the two counting geometries used in this study.
Energy calibration – Energy calibration was established using reference sources with well-known γ-ray energies, in particular ^{137}Cs (662.3 keV) and ^{60}Co (1,174.3 keV and 1,333.6 keV). A linear channel-to-energy relationship was used:

$$E(\text{keV}) = a + b \cdot \text{channel} \tag{3.1}$$

where the fitted coefficients were $a = -0.01519$ and $b = 0.2497$ and apply to both measurement geometries.
Efficiency calibration – The absolute FEP efficiency $\varepsilon(E_\gamma)$ was determined using an ^{152}Eu point source with an activity of 40.1 ± 0.8 kBq. Efficiency curves were obtained separately for the 19 cm and 0 cm counting geometries as shown in Fig. 3.4. For the 0 cm geometry, losses due to true coincidence summing (TCS) were corrected using the method described in [44]. For the main analysis peaks with high counting statistics, the TCS-corrected and uncorrected activities agreed within the statistical and efficiency calibration uncertainties.

Table 3.1: Fitted parameters for the logarithmic efficiency model.

Distance	a_0	a_1	a_2	a_3	a_4
0 cm	-1.216×10^2	8.137×10^1	-2.030×10^1	2.212	-8.987×10^{-2}
19 cm	-1.189×10^2	7.630×10^1	-1.884×10^1	2.030	-8.167×10^{-2}

The FEP efficiency was parameterised using the logarithmic polynomial model

$$\ln(\varepsilon(E_\gamma)) = \sum_{i=0}^{4} a_i \left(\ln(E_\gamma)\right)^i \tag{3.2}$$

where E_γ is given in keV. The coefficients a_i returned by the fit are given in Table 3.1 for the two counting geometries.

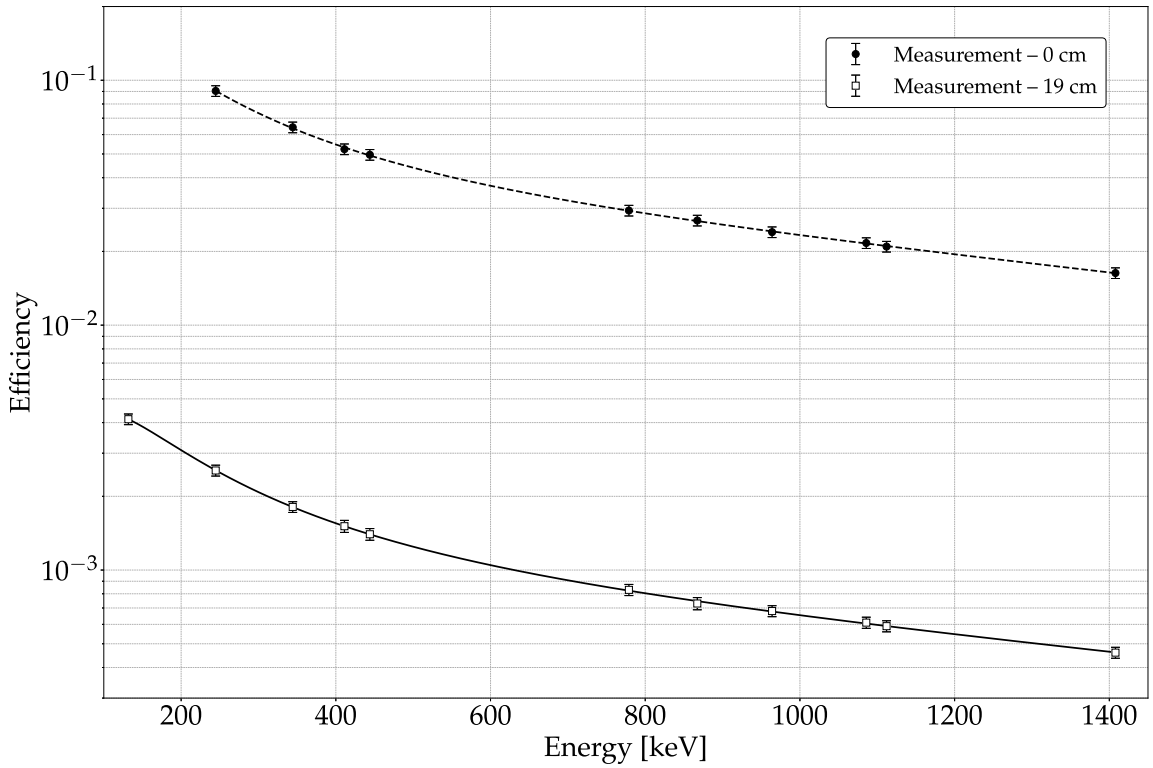


Figure 3.4: Energy dependence of the FEP efficiency for the two counting geometries. The lines represent the fit of the data with Eq. 3.2.

3.2.1.3 Data Processing and Corrections

After each irradiation, induced activities were determined from the measured γ-ray spectra by extracting net full-energy peak areas and converting them into activities at EOI. Net peak areas N_p were obtained in GENIE 2000 via peak fitting with background subtraction. For each radionuclide, a γ line with high emission probability and free of spectral interference was selected.

Activity at EOI – For a peak at energy E_γ, the activity at EOI is obtained from the net peak area using the FEP efficiency $\varepsilon_\gamma = \varepsilon(E_\gamma)$ and the absolute emission probability I_{E_γ} of the selected transition [25]. Using the live counting time t_m, the delay time between EOI and the start of counting t_d, and decay constant λ, the activity reconstruction is

$$A_{\mathrm{EOI}} = \frac{N_p}{\varepsilon_\gamma \, I_{E_\gamma} \, t_m \, C \, D} \tag{3.3}$$

with

$$C = \frac{1 - e^{-\lambda t_m}}{\lambda\, t_m} \tag{3.4}$$

and

$$D = e^{-\lambda t_d} \tag{3.5}$$

Here D corrects for decay between EOI and the start of counting, while C corrects for decay during counting. The times t_m and t_d were taken from measurement logs, and I_γ and $t_{1/2}$ (hence λ) were obtained from evaluated decay data [43]. Equation (3.3) is equivalent to

$$A_{\mathrm{EOI}} = \frac{N_p \lambda}{\varepsilon_\gamma I_{E_\gamma} (1 - e^{-\lambda t_m}) e^{-\lambda t_d}} \tag{3.6}$$

Irradiation saturation and production rate – When relating A_{EOI} to a constant production rate during irradiation of duration t_{irr}, the saturation factor

$$S = 1 - e^{-\lambda t_{\mathrm{irr}}} \tag{3.7}$$

is used, giving the corresponding production rate

$$R = \frac{A_{\mathrm{EOI}}}{S} \tag{3.8}$$

^{99}Mo activity from the mixed 140 keV peak – For ^{99}Mo, the 140.5 keV peak contains contributions from both ^{99}Mo and its daughter $^{99\mathrm{m}}$Tc and therefore requires a parent–daughter treatment. Following [45], the specific count rate of the mixed peak is

$$A_{sp}(^{99}\mathrm{Mo} + {}^{99\mathrm{m}}\mathrm{Tc}) = \frac{N_p}{t_m\, w} \left[\frac{\lambda_2 K_1 - \lambda_1 K_2}{\lambda_2 - \lambda_1} + \left(\frac{\gamma_1}{\gamma_2 F_{12}} \right) K_1 \right] \tag{3.9}$$

where subscripts 1 and 2 refer to ^{99}Mo and $^{99\mathrm{m}}$Tc, respectively, w is the mass of the molybdenum sample, F_{12} is the fraction of the mother isotope decaying into the daughter isotope, and γ_1 and γ_2 denote the emission probabilities used in the formalism of [45]. The factors

$$K_i = S_i\, D_i\, C_i \qquad (i = 1, 2) \tag{3.10}$$

combine saturation (S_i), decay (D_i), and counting (C_i) corrections. The parent-only contribution is obtained from

$$A_{sp}(^{99}\mathrm{Mo}) = \frac{\gamma_1}{\gamma_2 F_{12}}\, A_{sp}(^{99}\mathrm{Mo} + {}^{99\mathrm{m}}\mathrm{Tc}) \tag{3.11}$$

The activity at EOI is then

$$A_{\mathrm{EOI}}(^{99}\mathrm{Mo}) = A_{sp}(^{99}\mathrm{Mo}) \cdot w \cdot \frac{1}{\varepsilon_{140}\gamma_1} \tag{3.12}$$

where ε_{140} is the full-energy peak efficiency at 140.5 keV and γ_1 is the absolute 140.5 keV emission probability of ^{99}Mo used in the parent–daughter correction. No additional decay corrections are applied because the time dependence is already included through K_i in Eq. (3.9).

Uncertainty propagation – Uncertainties on experimentally reconstructed activities arise primarily from counting statistics, efficiency calibration, peak fitting, and evaluated decay data. A full uncertainty propagation based on Gaussian error propagation is provided in Appendix A.1.

3.2.2 Simulation

Simulation-based activity prediction in this work is based on MC neutron transport calculations performed with PHITS. Neutron flux spectra in the regions of interest were obtained by scoring energy-dependent neutron spectra with tally estimators and were then converted into reaction rates and activities at EOI. Two approaches were used: the flux analysis method (FAM) and the flux folding method (FFM) implemented using the coupled PHITS–DCHAIN workflow. Both approaches use the same irradiation and decay timing formalism. They differ primarily in how the neutron spectrum is combined with cross-section data.

3.2.2.1 Flux Analysis Method

FAM predicts activities by combining the simulated neutron flux spectrum with integral activation parameters. Instead of performing a full energy-dependent folding of flux and cross section, the neutron flux is separated into thermal, epithermal, and fast components, which are treated using corresponding integral quantities.

The neutron energy spectrum within the sample was obtained using the `[T-Track]` tally in PHITS and integrated over predefined energy intervals to obtain fluxes for the thermal, epithermal, and fast regions. The energy ranges used in this work are thermal (1 meV to 0.5 eV), epithermal (0.5 eV to 0.1 MeV), and fast (0.1 MeV to 20 MeV).

Reaction rate and activity – The neutron capture reaction rate is approximated as

$$R \approx N\left(\sigma_{\mathrm{th}}\,\phi_{\mathrm{th}} + I_\gamma(\alpha)\,\phi_{\mathrm{epi}} + \sigma_{\mathrm{fast}}\,\phi_{\mathrm{fast}}\right) \tag{3.13}$$

where N is the number of target atoms, σ_{th} is the thermal capture cross section, $I_\gamma(\alpha)$ is the resonance integral corrected for the epithermal spectrum shape, and σ_{fast} is the effective fast-region capture cross section [46]. The number of target atoms is

$$N = \frac{m}{M}\,N_{\mathrm{A}}\,h \tag{3.14}$$

where m is the sample mass, M is the molar mass, N_A is Avogadro's number, and h is the isotopic abundance. The activity at EOI follows from

$$A_{EOI} = R\left(1 - e^{-\lambda t_{irr}}\right) \tag{3.15}$$

with decay constant λ and irradiation time t_{irr}.
Thermal region – In the thermal region, neutrons are approximately in equilibrium with the surrounding medium and the capture cross section often follows a $1/v$ dependence. The thermal contribution is therefore described using the thermal cross section σ_{th} [47].
Epithermal region – In the epithermal region, the neutron flux is commonly approximated by a power-law dependence [24, 48]

$$\phi(E) \propto \frac{1}{E^{1+\alpha}} \tag{3.16}$$

where α characterizes deviations from the ideal $1/E$ spectrum. The parameter α was determined from the simulated neutron spectrum by fitting

$$\ln\left(\frac{\phi(E)}{\Delta E}\right) = -(1+\alpha)\,\ln(E) \tag{3.17}$$

within the epithermal energy range.
The total epithermal flux is given by:

$$\phi_{epi,tot} = \int_{E_{min}}^{E_{max}} \phi(E)\,dE \tag{3.18}$$

where E_{min} and E_{max} are 0.5 eV and 0.1 MeV, respectively, and was obtained directly from the simulated spectrum. For consistency with the resonance integral formalism, the epithermal flux per unit lethargy is expressed as

$$\phi_{epi} = \frac{\phi_{epi,tot}}{\ln\left(\frac{E_{max}}{E_{min}}\right)} \tag{3.19}$$

for an ideal $1/E$ spectrum ($\alpha = 0$). This definition provides an epithermal flux parameter consistent with the resonance-integral convention used in Eq. (3.21). For the modified spectrum in Eq. (3.16), integration yields

$$\phi_{epi} = \frac{\phi_{epi,tot}\,\alpha}{E_{min}^{-\alpha} - E_{max}^{-\alpha}} \tag{3.20}$$

The resonance integral is tabulated for an ideal $1/E$ spectrum and must therefore be corrected when the spectrum deviates from this assumption. In this work, the α-dependent resonance integral was evaluated using [24, 47] as

$$I_\gamma(\alpha) = \left[\frac{I_\gamma - 0.426\,\sigma_{\text{th}}}{E_r^\alpha} + \frac{0.426\,\sigma_{\text{th}}}{(2\alpha+1)\,E_{Cd}^\alpha}\right] E_0^\alpha \tag{3.21}$$

where I_γ is the tabulated resonance integral, E_r is the effective resonance energy, E_{Cd} is the cadmium cut-off energy (0.5 eV), and $E_0 = 1\,\text{eV}$ is the reference energy.
Fast region – The contribution of fast neutrons is included using an effective cross section obtained by spectrum-weighted averaging over the fast energy region

$$\sigma_{\text{fast}} = \frac{\int_{E_{\text{min}}}^{E_{\text{max}}} \sigma(E)\,\phi(E)\,dE}{\int_{E_{\text{min}}}^{E_{\text{max}}} \phi(E)\,dE} \tag{3.22}$$

where E_{min} and E_{max} are 0.1 MeV and 20 MeV, respectively.
The FAM provides a computationally efficient approximation to activation by combining region-integrated neutron fluxes with integral nuclear data for the thermal, epithermal, and fast regions.
Neutron self-shielding effects – Equation (3.15) relates the activity to the reaction rate obtained from region-integrated flux components and effective nuclear data, but it does not include an explicit self-shielding correction factor. In an epithermal neutron field, a sample with a strong resonance capture cross section perturbs the local neutron flux inside the material by absorption and scattering, leading to a reduced flux at resonance energies [49]. A common definition of the resonance-neutrons self-shielding factor is the ratio between the reaction rate per target atom in the real sample and that in an equivalent, infinitely diluted sample [49, 50]. Similarly, thermal-neutron self-shielding can be defined as the analogous ratio evaluated over the thermal spectrum [51]. More generally, Monte Carlo approaches determine self-shielding correction factors by comparing reaction-rate integrals obtained using the perturbed neutron spectrum inside the real sample with those obtained using an unperturbed spectrum [52].
In this study, neutron flux spectra are scored directly within the sample volume using the `[T-Track]` tally. Therefore, the spectrum used in the activation calculation already includes the flux depression and spectral distortions caused by the sample itself. This is consistent with the general Monte Carlo definition of self-shielding as a flux perturbation within the sample relative to an unperturbed reference [49, 50, 52].
Nevertheless, in the FAM approach the flux is reduced to three broad energy integrals (thermal, epithermal, fast) and combined with integral quantities such as $I_\gamma(\alpha)$. This coarse energy condensation does not resolve narrow resonance structures explicitly and therefore does not capture, in a detailed way, how resonance-specific

flux depressions modify the effective capture rate [49, 50]. Consequently, while scoring the flux in the sample accounts for the overall magnitude of self-shielding, residual bias may remain in FAM when strong, narrow resonances dominate the activation. In such cases, the flux-folding approach (FFM), which uses a fine multi-group representation of the neutron spectrum, provides a more detailed treatment of resonance behaviour.

3.2.2.2 Flux Folding Method (PHITS–DCHAIN)

FFM determines induced activity by folding the simulated neutron flux spectrum with energy-dependent nuclear reaction cross sections within the coupled PHITS–DCHAIN framework.
The PHITS simulation provides the neutron flux spectrum below 20 MeV and nuclide production yields from higher-energy interactions. The coupling is performed using the `[T-Dchain]` tally, which provides DCHAIN with the 1968-group neutron flux spectrum below 20 MeV and nuclide production yields from interactions above 20 MeV.
Within DCHAIN, reaction rates are obtained by combining the multi-group neutron flux with corresponding group-wise reaction cross sections. The effective microscopic reaction cross section for nuclide k is calculated as a flux-weighted average

$$\sigma_{\mathrm{tr},k} = \frac{\sum_g \sigma^g_{\mathrm{tr},k}\, \phi_g(t)}{\sum_g \phi_g(t)} \tag{3.23}$$

where $\sigma^g_{\mathrm{tr},k}$ is the group-wise cross section and $\phi_g(t)$ is the neutron flux in energy group g. This is the discrete multi-group representation of

$$R = N \int_0^\infty \phi(E)\, \sigma(E)\, dE \tag{3.24}$$

and therefore constitutes a direct flux folding of the neutron spectrum with energy-dependent cross section data.
Figure 3.5 illustrates this procedure by showing the energy-dependent cross section together with its multi-group representation and a representative neutron flux spectrum.
The time-dependent inventory $N_i(t)$ of nuclide i is obtained by solving the system of coupled differential equations describing production, decay, and transmutation [34]

$$\frac{dN_i(t)}{dt} = Y_i(t) - \left(\lambda_i + \sigma_{\mathrm{tr},i}\, \phi(t)\right) N_i(t) + \sum_j f_{j\to i} \lambda_j N_j(t) + \sum_k g_{k\to i} \sigma_{\mathrm{tr},k} \phi(t) N_k(t) \tag{3.25}$$

where $Y_i(t)$ represents production from high-energy reactions, λ_i is the decay constant, $\phi(t)$ is the total neutron flux, $f_{j\to i}$ are decay branching ratios, and $g_{k\to i}$ are production probabilities from neutron-induced reactions.

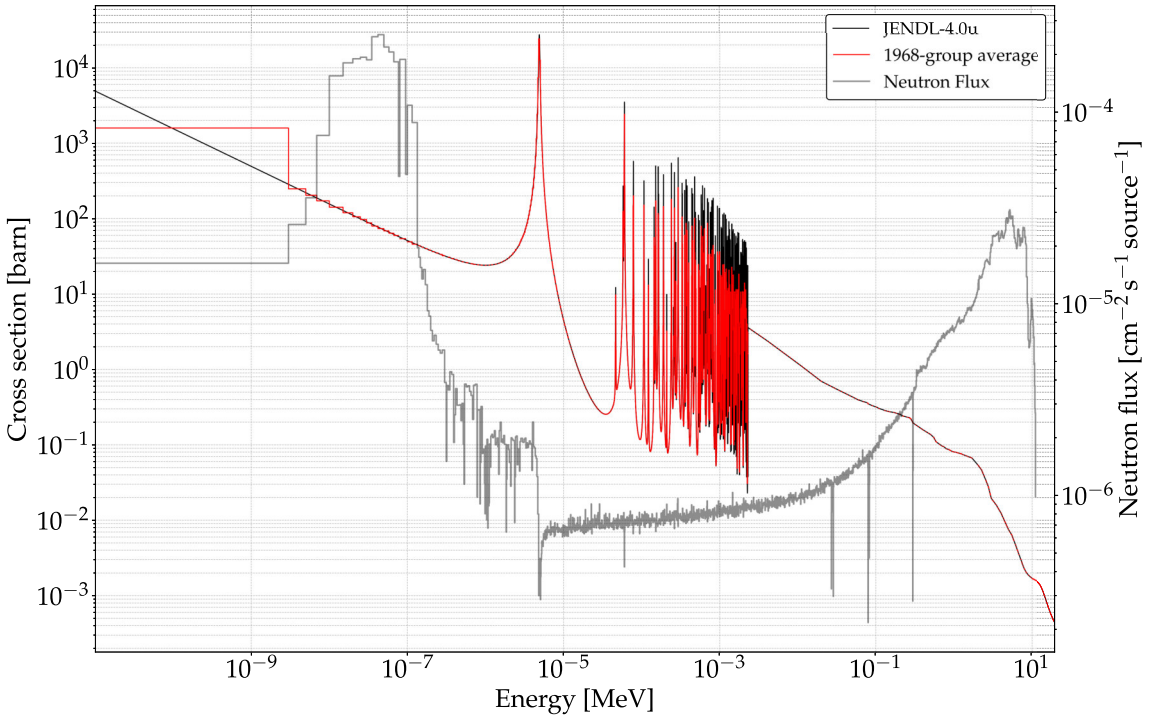


Figure 3.5: Illustration of the flux folding procedure. The energy-dependent neutron capture cross section for ^{197}Au(n,γ)^{198}Au reaction, its multi-group representation, and the corresponding neutron flux spectrum within the gold foil with a thickness of 0.0025 cm are shown. The reaction rate is obtained by folding the flux with the cross section over all energy groups.

By solving Eq. (3.25) over the specified irradiation and cooling schedule, DCHAIN provides time-dependent inventories and derived quantities, including activities at EOI. Compared to the FAM, the FFM avoids thermal, epithermal, and fast spectral approximations and treats energy dependence and decay chains explicitly within the selected multi-group library framework. The FAM provides a computationally efficient alternative that enables quick activity estimates and parameter studies, whereas the FFM offers a more detailed energy-dependent inventory calculation at higher computational cost.

4 Validation of Activity Determination Methods

This chapter presents an experimental validation of the methods used to determine the induced activity from Monte Carlo simulations performed with the PHITS code. The neutron activation experiments were carried out at the irradiation facility of the Aachen University of Applied Sciences, and the measured activities were compared with corresponding simulations. The benchmark experiments were performed in two measurement campaigns using two foil sets irradiated under two conditions, bare and cadmium-covered (Cd-covered). This chapter benchmarks the activity prediction workflow described in Section 3.2 by comparing measured foil activities with PHITS-based predictions using the flux analysis method (FAM) and flux folding method (FFM). The simulations are evaluated using all the model parameters, such that the comparison tests the neutron source model, the neutron transport, and the two different activity calculation approaches. The deviations from the benchmark results and their systematic behavior are analysed in the following sections.

4.1 Experimental Setup

This section describes the experimental configuration, including the irradiation setup, the neutron source characteristics, the activation foils and their positioning within the setup, and the gamma spectroscopy measurements used to determine the induced activities.

4.1.1 Irradiation Setup and Neutron Source

The facility consists of a cubic paraffin moderator with sides of 71 cm. The moderator assembly is surrounded by layers of iron, cadmium, and iron (each 0.5 cm thick) to reduce neutron leakage. Five cylindrical plexiglass tubes with an inner diameter of 2 cm, a wall thickness of 0.5 cm, and a length of 49 cm are symmetrically embedded in the paraffin moderator.
The neutron source was an americium–beryllium (AmBe) source, originally calibrated on 2 December 1993 with a neutron emission rate of 2.0×10^7 s^{-1} specified by the supplier. Since the neutron yield of an AmBe source is directly proportional

to the activity of ^{241}Am, the source strength at the time of the experiments was obtained by correcting this value for radioactive decay using the half-life of ^{241}Am ($T_{1/2} = 432.2$ y). The resulting emission rate was 1.9×10^7 s^{-1}, which was used consistently in all simulations and activity calculations presented in this chapter. The supplier's quoted uncertainty of $\pm 10\%$ on the neutron emission rate is treated as a systematic scale uncertainty and was included in the propagated uncertainties of the simulated activities. It was not used to normalise the simulations to the measurements. The source is positioned at the bottom of the central tube, while the activation foils are placed at the same height as the source inside a thin polyethylene holder inserted into one of the lateral tubes. A schematic representation of the irradiation geometry is shown in Fig. 4.1. Based on the mechanical tolerances of the irradiation setup and the mounting procedure, the positional uncertainty of both the source and the foils is estimated to be within ± 2 mm. At this level of moderation, such variations are expected to introduce local flux differences of less than 1%, which are small compared to the dominant uncertainty associated with the neutron source strength.

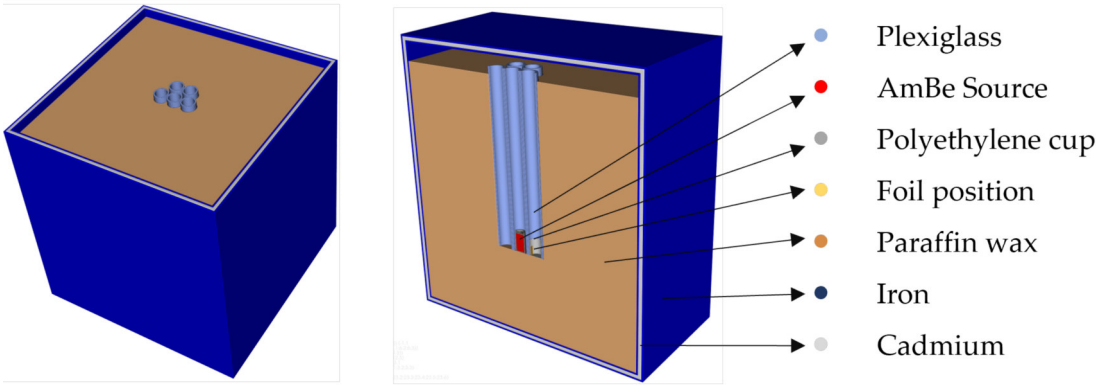


Figure 4.1: Geometrical model of the irradiation facility used for the neutron activation experiments and corresponding simulations. The figure shows a top view of the paraffin moderator with the embedded plexiglass tubes and a vertical cross-section along the symmetry axis of the central tube containing the AmBe neutron source and surrounding materials.

4.1.2 Activation Foils

Two foil sets of irradiations were conducted using foils that served as neutron flux monitors. The foils were selected for their well-known neutron-capture cross sections, simple decay schemes, and characteristic γ-ray emissions suitable for high-resolution gamma spectrometry. A summary of the activation foils used in these experiments, including materials, dimensions, and irradiation conditions, is given in Table 4.1.

4.1.2.1 Bare Foil Irradiations

The benchmark dataset for bare irradiations consists of two foil sets irradiated bare (without Cd-cover) at the same irradiation position in the plexiglass tube. In the initial Au–In benchmark, performed in [53], gold (Au) and indium (In) foils were irradiated to validate the experimental procedure and establish reference activities.

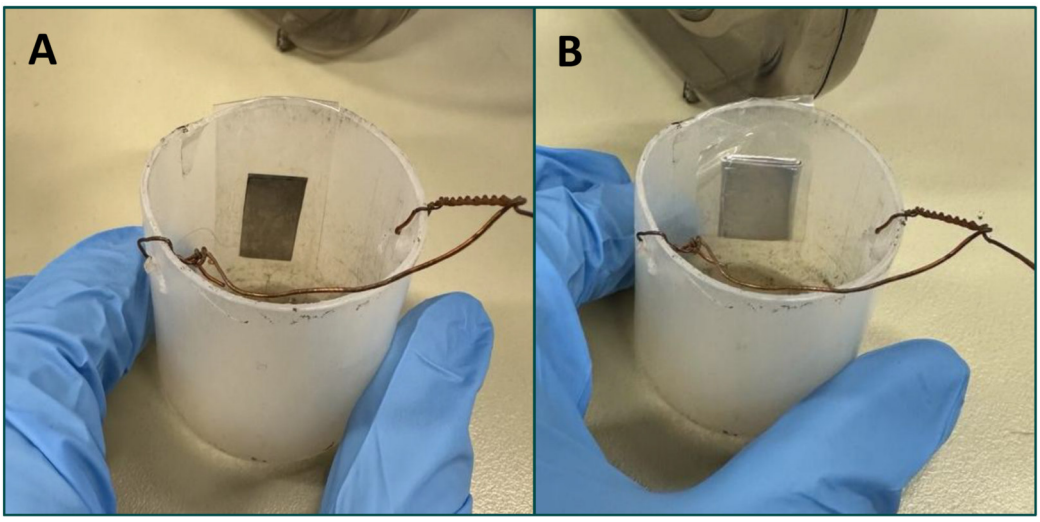


Figure 4.2: Polyethylene holder with (A) bare W sample and (B) Cd-covered W sample.

In the extended multi-monitor benchmark, performed in [54], the dataset was extended by adding molybdenum (Mo), tungsten(W), and manganese (Mn) foils in order to test a wider range of capture cross sections and resonance behaviors. All bare foils were mounted in the polyethylene holder (see Fig. 4.2) and irradiated under identical geometrical conditions, with the foils positioned at the same axial height as the AmBe source in a lateral irradiation channel (see Fig. 4.1).

4.1.2.2 Cd-Covered Foil Irradiations

The Cd-covered benchmark dataset similarly consists of two foil sets, in which the foils were enclosed in Cd to suppress the thermal component of the neutron spectrum. In the initial Cd-covered Au–In benchmark, performed in [53], Au and In foils were irradiated under Cd-covered conditions to enable a direct comparison to the bare irradiated foils.
In the Cd-covered extended multi-monitor benchmark, performed in [54], the extended multi-monitor set (Au, In, Mo, W, and Mn) was irradiated under Cd-covered conditions. For Cd-covered irradiations, the foils were wrapped twice in 0.5 mm thick Cd sheets, resulting in a total thickness of 1 mm, which ensures nearly complete absorption of neutrons below 0.5 eV.

Table 4.1: Summary of activation foils used in the benchmark experiments, grouped by irradiation condition. For isotopes appearing more than once within the same irradiation condition, entries labeled "– 1" correspond to the first irradiation campaign, while unlabeled entries correspond to the extended multi-monitor campaign. Foil masses were measured prior to irradiation using a laboratory balance, with an estimated relative uncertainty of ±1%.

Foil	Isotope of Interest	Purity [%]	Dimensions [mm]	Thickness [mm]	Mass [g]
Bare foils					
Au – 1	^{197}Au	99.95	25×15	0.025	0.1648
In – 1	^{115}In	99.80	5×5	0.025	0.0049
Au	^{197}Au	99.95	10.5×6.0	0.025	0.0277
In	^{115}In	99.80	20.5×10.0	0.025	0.0347
Mo	^{98}Mo	99.90	20.5×10.0	0.050	0.1069
W	^{186}W	99.90	19.0×10.0	0.100	0.4291
Mn	^{55}Mn	99.80	20.0×10.0	0.025	0.0272
Cd-covered foils					
Au – 1	^{197}Au	99.95	25×15	0.025	0.1656
In – 1	^{115}In	99.80	5×5	0.025	0.0052
Au	^{197}Au	99.95	10.5×5.0	0.025	0.0270
In	^{115}In	99.80	19.0×10.0	0.025	0.0348
Mo	^{98}Mo	99.90	20.5×10.0	0.050	0.1066
W	^{186}W	99.90	19.0×10.0	0.100	0.4280
Mn	^{55}Mn	99.80	20.0×10.0	0.025	0.0304

The bare and Cd-covered irradiations were performed separately under identical geometrical conditions to allow direct comparison between measured and simulated activities. The combination of these two experiments, the initial Au–In benchmark and the extended five-monitor study, provides a validation dataset covering a range of neutron capture cross sections and resonance behaviours. These datasets form the experimental basis for the comparison between measured and simulated activities presented in this chapter.

4.1.3 Gamma Spectrometry and Activity Calculation

The activated foils were measured by HPGe γ-spectrometry using the detector system and calibration procedures described in Chapter 3. Most foils were counted at 19 cm source-to-detector distance using the 19 cm efficiency calibration; only the In–1 foils were counted in the 0 cm geometry using the corresponding efficiency curve. Spectra were acquired in live-time mode with dead time below 1% and analysed in GENIE 2000 to extract background-corrected net peak areas.

Table 4.2: Irradiation, decay, and measurement parameters for the activation foils used in the benchmark experiments. The listed γ-line intensities correspond to absolute emission probabilities.

Produced Isotope	Half-life [h]	Irradiation Time [h]	Decay Time [h]	Measurement Time [h]	γ-line [keV]	γ-line Intensity [%]
Bare foils						
^{198}Au – 1	64.56	7.20	68.73	66.75	411.8	95.6
^{116m}In – 1	0.91	2.05	0.08	26.29	416.9	27.2
^{198}Au	64.56	7.58	0.03	13.97	411.8	95.6
^{116m}In	0.91	0.32	0.03	0.42	416.9	27.2
^{99}Mo	65.90	168.00	0.07	192.00	140.5	4.5
^{187}W	23.70	6.00	0.03	16.00	479.5	26.6
^{56}Mn	2.58	8.07	0.13	17.35	846.8	98.9
Cd-covered foils						
^{198}Au – 1	64.56	17.28	25.92	24.95	411.8	95.6
^{116m}In – 1	0.91	3.42	0.10	23.63	416.9	27.2
^{198}Au	64.56	16.05	0.07	7.00	411.8	95.6
^{116m}In	0.91	1.67	0.07	1.33	416.9	27.2
^{99}Mo	65.90	192.90	0.08	144.00	140.5	4.5
^{187}W	23.70	16.83	0.07	69.00	479.5	26.6
^{56}Mn	2.58	18.07	0.08	8.00	846.8	98.9

The irradiation, decay, and measurement parameters are summarised in Table 4.2. For isotopes emitting multiple γ–rays, the transition with the highest emission probability and minimal spectral interference was selected for activity determination. For ^{99}Mo, the activity was determined from the 140.5 keV γ–line, accounting for the parent–daughter contribution from ^{99m}Tc as described in Section 3.2.1.3.
Activities at EOI were reconstructed from net peak areas using the efficiency calibration and decay corrections described in Section 3.2.1. The overall uncertainty of the experimentally determined activities was typically about 10% (see Appendix B).

4.2 Simulation Setup

The Monte Carlo simulations were performed using the PHITS code (version 3.22) under the same experimental conditions as the measurements. Two approaches were evaluated for converting the simulated neutron field to induced activities: the flux analysis method (FAM) and the flux folding method (FFM). No adjustment to experimental results was applied, so the comparison directly tests the neutron source description, neutron transport modelling, and the activity determination procedures. All transport calculations use the code and nuclear data environment defined in Section 3.1.3.

The FAM activity calculation additionally requires thermal cross sections, effective resonance energies, and resonance integrals. The k_0 nuclear data given in Table 4.3 were taken from the evaluated database maintained by the k_0 International Scientific Committee [55], following the standardisation approach described by De Corte [56]. This method additionally relies on the fast neutron cross-sections which were determined using the convolution method described in Chapter 3.

The neutron source was modelled as an isotropic AmBe source. The neutron energy spectrum of the AmBe source used in the simulations was taken from the reference spectrum implemented in PHITS. According to the PHITS documentation, this spectrum, given in Fig. 4.3, is based on the ISO 8529-1 reference for AmBe neutron sources [57]. The spectral distribution was implemented in PHITS using the provided AmBe source definition and normalised to the decay-corrected neutron emission rate of 1.9×10^7 s^{-1}, as described in Section 4.1.

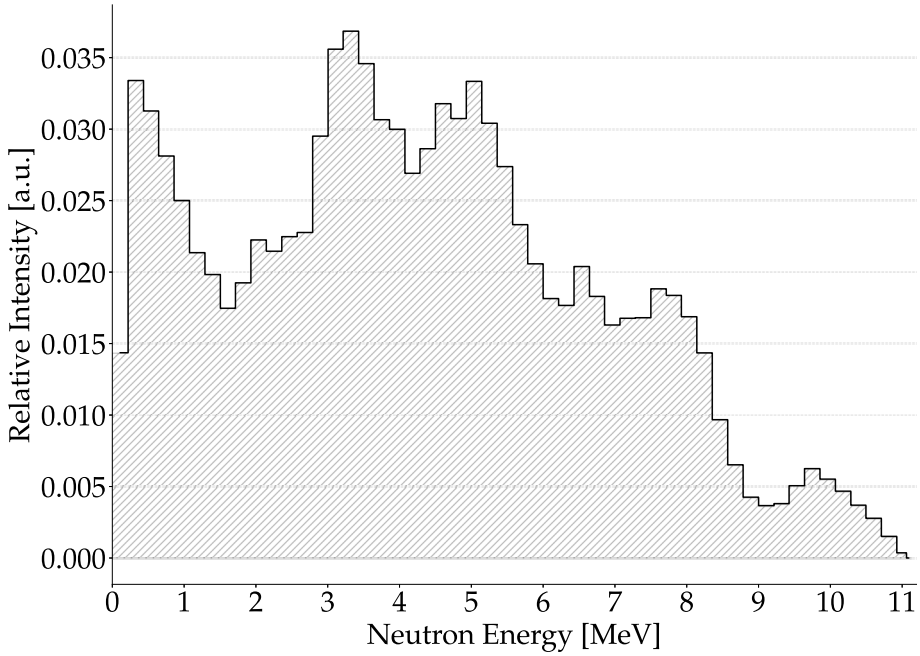


Figure 4.3: AmBe neutron energy spectrum used in this work. [57]

The source strength uncertainty of ±10% was treated as a systematic uncertainty affecting all simulated activities equally. This uncertainty was not used to adjust or normalise the simulations to the experimental results and therefore represents a global scale uncertainty in the benchmark comparison. The γ rays associated with the source were neglected, since the activation considered here is dominated by neutron capture reactions.

Table 4.3: Nuclear data for the investigated (n, γ) reactions. Values are given with absolute uncertainties ($\pm 1\sigma$), derived from the relative uncertainties provided in the database [55].

Reaction	**Thermal Cross Section** σ_{th} [barn]	**Resonance Integral** $I_\gamma(0)$ [barn]	**Effective Resonance Energy** E_r [eV]
$^{197}\text{Au}(n,\gamma)^{198}\text{Au}$	98.7 ± 0.10	1550 ± 28	5.65 ± 0.40
$^{115}\text{In}(n,\gamma)^{116m}\text{In}$	161 ± 3.2	2705 ± 76	1.56 ± 0.03
$^{98}\text{Mo}(n,\gamma)^{99}\text{Mo}$	0.131 ± 0.003	6.96 ± 0.47	241 ± 48
$^{186}\text{W}(n,\gamma)^{187}\text{W}$	41.8 ± 1.2	573 ± 19	20.5 ± 0.2
$^{55}\text{Mn}(n,\gamma)^{56}\text{Mn}$	13.2 ± 0.18	13.9 ± 0.42	468 ± 51

The irradiation geometry used for the simulations was implemented according to the dimensions of the experimental setup, including the paraffin moderator, irradiation channels, foil holders, and activation foil dimensions. Material compositions and densities for the foils, paraffin moderator, cadmium, and structural components were taken from reference data, such as published material definitions from PNNL reports [58].
The foil volumes and densities determine the number of target atoms in the simulation. However, to ensure that the simulated neutron field is combined with the actual number of target atoms present during irradiation, the final activity calculation was performed using the experimentally measured foil masses. This approach is used to avoid inconsistencies due to density or dimensional tolerances.
For both approaches, neutron transport was simulated with 10^9 primary source particles. This resulted in statistical uncertainties below 5% for the flux spectra used in FAM, and below 7% for the spectra used in FFM. These statistical uncertainties are negligible compared to the dominant systematic uncertainties in the benchmark comparison. The overall uncertainty of the simulated activities is dominated by the ±10% uncertainty in the neutron source strength and ±1% uncertainty in the foil masses. Additional sources of uncertainty include nuclear data uncertainties and modelling approximations, which are not explicitly propagated but are considered qualitatively in the discussion of the results. In the FAM the neutron flux was scored using the PHITS [`T-Track`] tally in 100 logarithmically spaced energy bins between 10^{-9} MeV and 20 MeV at the position of each foil. The simulated neutron fluxes were converted to activities using the activation formalism and decay corrections described in Chapter 3. The resulting FAM and FFM activities were compared

directly with the experimentally determined activities in the following section.

4.3 Results and Discussion

In this section, the experimentally measured foil activities are compared with the corresponding PHITS simulation results. The comparison is presented in terms of representative γ-ray spectra, activities at end of irradiation (EOI), and simulated to experimental activity ratios.

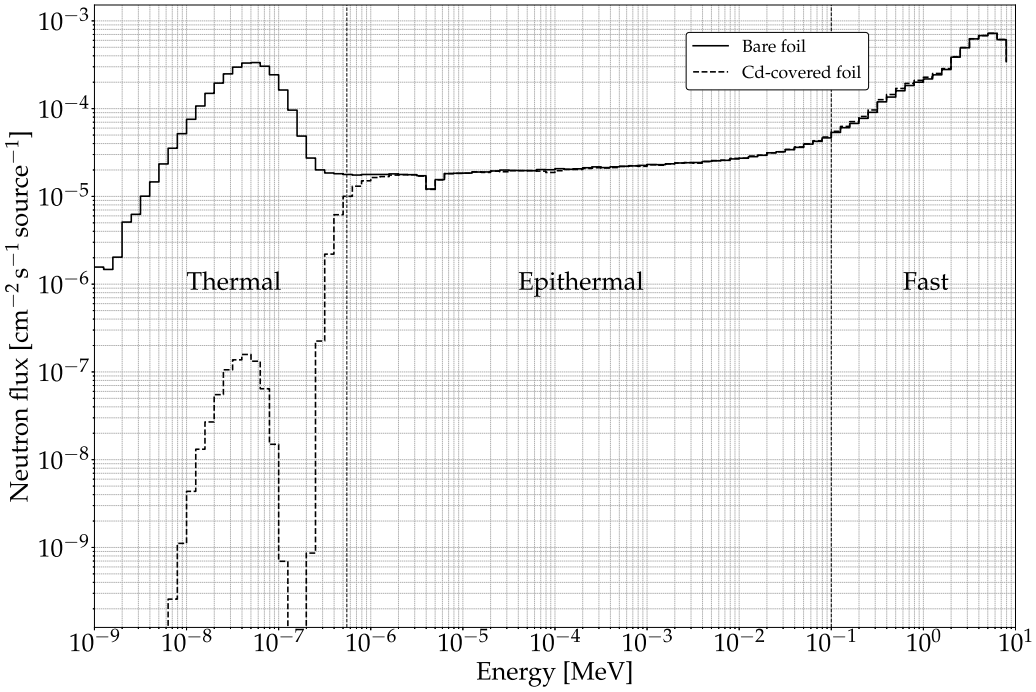


Figure 4.4: Simulated neutron energy spectrum within the Au – 1 foil for bare and Cd-covered irradiations.

Figure 4.4 shows the simulated neutron energy spectrum within the Au – 1 foil for bare and Cd-covered irradiation. As expected, the Cd cover strongly suppresses the thermal neutrons, while the epithermal and fast neutrons remain almost unaffected. A small residual thermal component remains under the Cd-cover because the filter has finite thickness and energy dependent attenuation. This residual contribution is negligible for the calculated activities under Cd-covered irradiation. The spectra shown here are representative for all investigated foils, since the irradiation position and surrounding moderator geometry are identical across the experiments and only the presence of the Cd filter changes the thermal part of the neutron spectrum. Small foil dependent differences occur due to neutron self-shielding, which causes neutron flux depressions at strong resonance energies where the capture cross section is large (at 1.46 eV in the case of Au).

4.3.1 Gamma Spectra and Peak Identification

Representative γ-ray spectra were analysed to confirm the suitability of the selected peaks for activity determination under both bare and Cd-covered conditions, with particular attention to background and potential spectral interferences. For each isotope, the activity was derived from the single γ line listed in Table 4.2, and the resulting experimental activities are summarised in Appendix B.

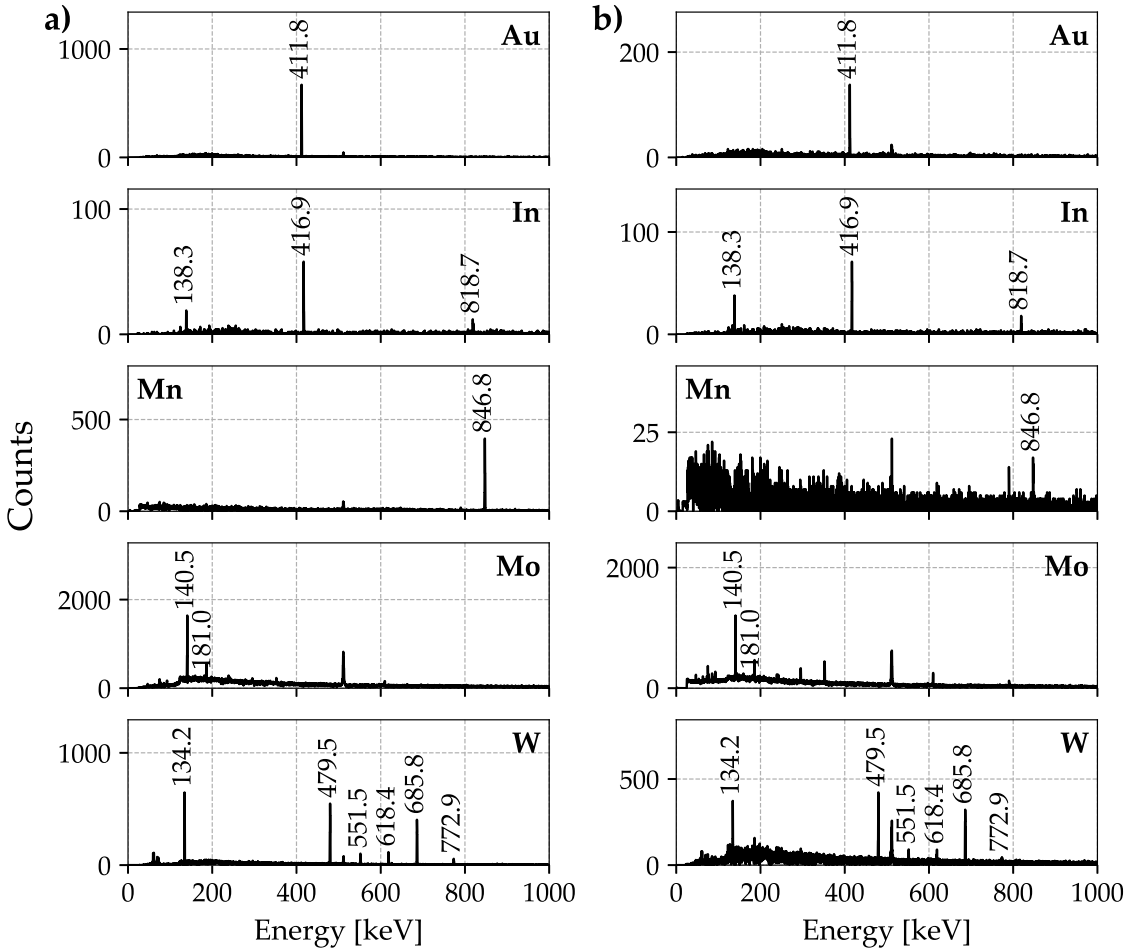


Figure 4.5: Representative γ-ray spectra obtained for selected activation foils in the extended multiple-monitor study for a) bare foil irradiation and b) Cd-covered irradiation.

In the Au spectra, the ^{198}Au 411.8 keV peak is clearly identified and was used for activity determination, with a reduction in peak area for Cd-covered case due to the suppression of the thermal neutron component.

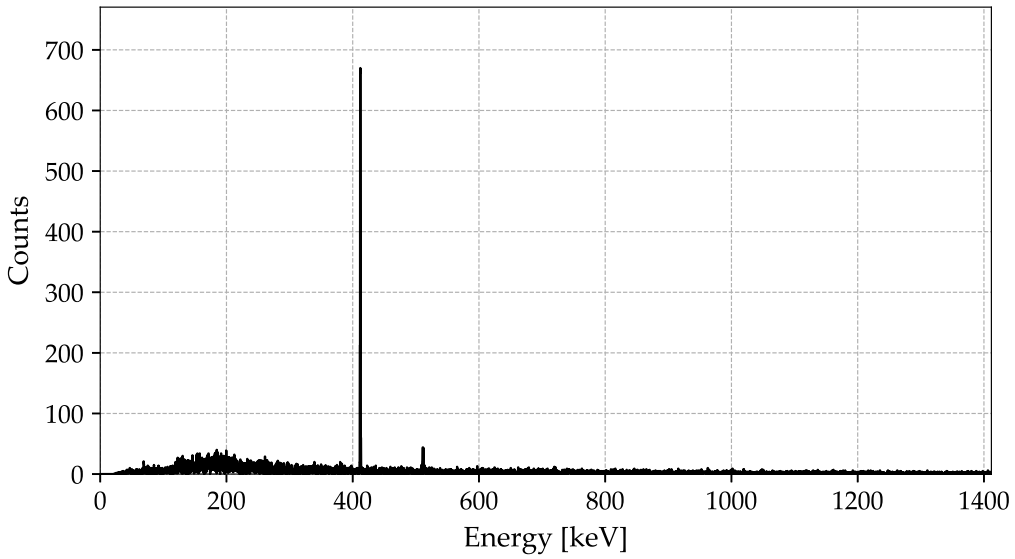


Figure 4.6: Enlarged bare-foil γ-ray spectrum for the ^{198}Au isotope used for activity determination.

In the In spectra, multiple peaks attributed to ^{116m}In are observed, and the 416.9 keV line was selected for activity determination because it provides a well-resolved FEP with a favorable peak-to-background ratio. Although the Cd-covered irradiation yields a lower count rate due to the suppressed thermal neutron component, the longer counting time used for the Cd-covered In foil results in a comparable net peak area in the recorded spectra.

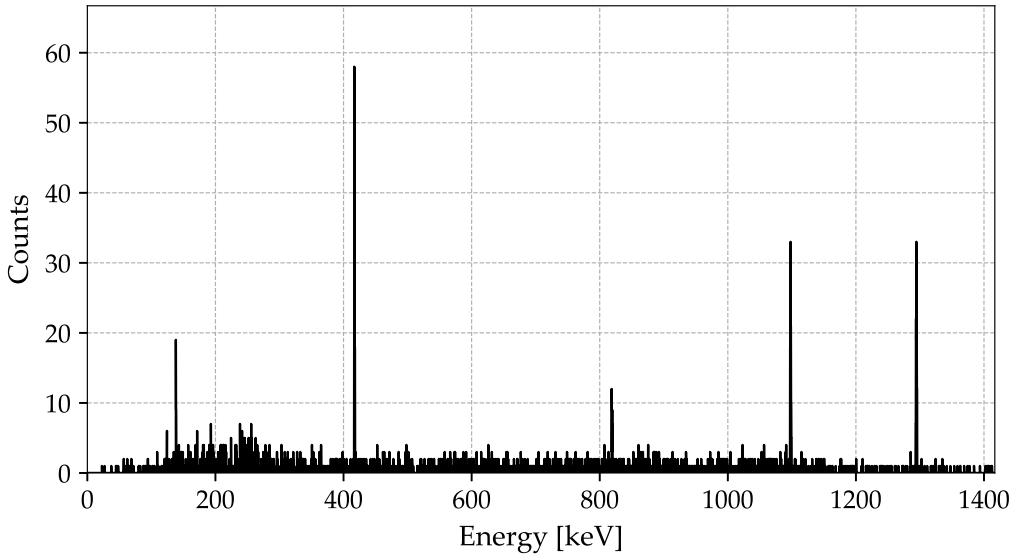


Figure 4.7: Enlarged bare-foil γ-ray spectrum for the ^{116m}In isotope used for activity determination.

For ^{99}Mo, both the 140.5 keV and 181 keV γ lines were observed, and the 140.5 keV peak was used for activity determination because it provides the most reliable peak intensity under the counting conditions. The higher energy ^{99}Mo γ lines, such as 739.5 keV and 777.9 keV, are not clearly visible in the spectra, which is consistent with the lower full-energy peak efficiency of the detector at higher energies and the limited counting statistics.
For ^{187}W, multiple γ lines were observed in the spectra, however for consistency and to avoid additional uncertainty from weaker peaks, the activity was determined using the 479.5 keV line, which provided the clearest peak under the counting conditions.
For ^{56}Mn, the spectra are dominated by the 846.8 keV line, which appears as a single prominent peak with low local background and remains clearly identifiable under Cd-covered irradiation, although with reduced intensity.
For Cd-covered irradiations, a noticeable reduction in peak intensities associated with reactions dominated by thermal neutron capture is observed, consistent with the expected suppression of the thermal neutrons by the Cd filter. For the selected γ lines used in this work, no significant spectral interferences affecting the peak area determination were observed.
The spectra presented here serve as qualitative validation of the experimental measurements. The determination of peak areas, efficiency corrections, and decay corrections was performed according to the procedures described in Chapter 3.

4.3.2 Bare Foil Irradiations

The bare foil irradiations include two experimental datasets in which the foils were exposed to the moderated neutron spectrum. The initial set includes Au and In foils (labelled Au-1 and In-1), while the extended foil set includes a larger set of monitors (Au, In, Mo, W, Mn). Fig. 4.8 compares the measured activities at the end of irradiation (EOI) with the corresponding PHITS results obtained using the FAM and FFM for all bare foil irradiations.
Across the bare irradiations, both approaches reproduce the measured activities within generally acceptable agreement, with most deviations falling in the 10-20% range. For ^{198}Au, the FFM gives the closest agreement, with a deviation of roughly 5%, while the FAM result is about 30% higher than the measurement. For ^{116m}In, the FAM estimates slightly lower activity, whereas the FFM shows a larger underestimation, both within 15%. The irradiation times for both Au foils are similar, so the difference in measured activities is due to the different foil size, thus number of target atoms. For the In foils, the irradiation times differ significantly, therefore the activity is strongly influenced by the irradiation history in addition to the foil size.
For ^{187}W the deviations are larger than for other monitors, FAM result exceeds the measurement by more than 30%, while the FFM value remains within approx-

imately 20%. For ^{56}Mn and ^{99}Mo, both methods show the smallest deviations and reproduce the measured activities within about 10%. The activity of ^{99}Mo remains comparatively low despite the relatively long irradiation time, due to the low neutron capture cross section of ^{98}Mo.

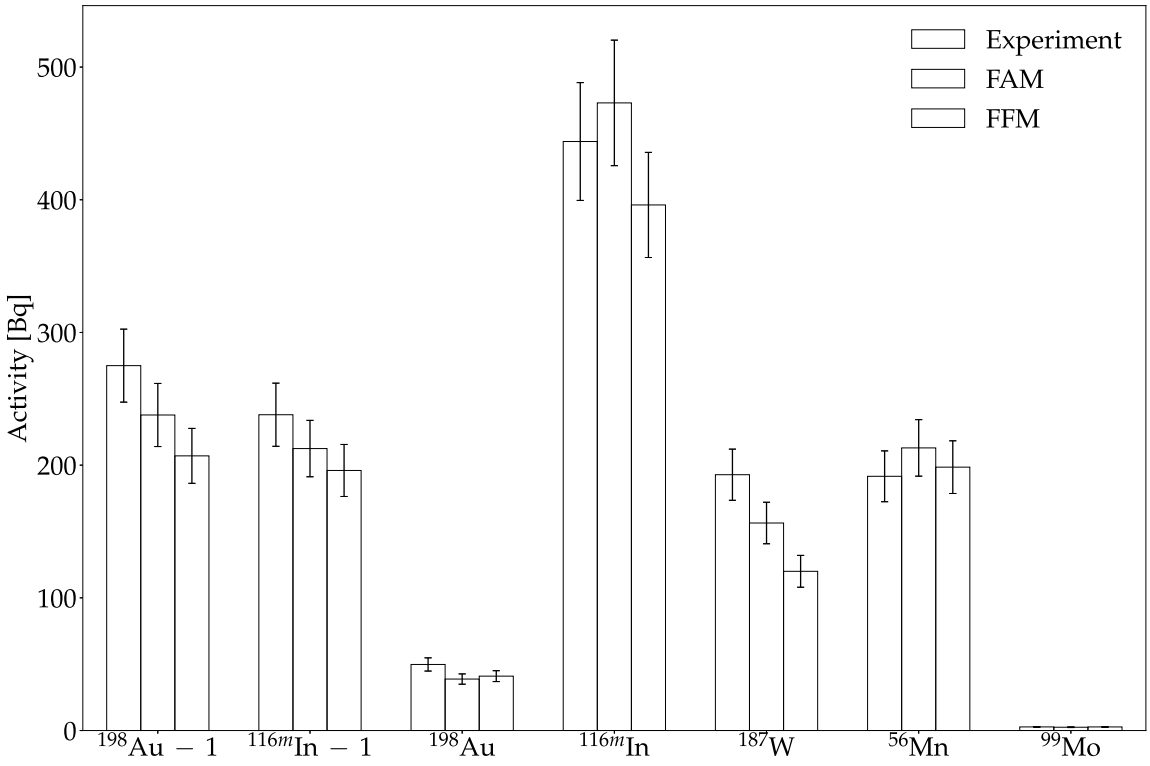


Figure 4.8: Experimental and simulated activities at the EOI for the bare foils.

Overall, the bare foil results demonstrate that the simulations can reproduce the experimental activities with deviations typically in the 10–20% range. This is also shown by the activity ratios shown in Fig. 4.9, where most ratios of simulated to experimental results lie close to 1.0. The FAM exhibits a systematic tendency to overestimate the measured activities, while the FFM generally underestimates the activities across most isotopes.

The difference observed between the two simulation methods is consistent with the methodology of each approach. In the FAM approach, the neutron flux is averaged over a broad energy interval and combined with the resonance integrals, which weight resonance contributions more strongly and can lead to higher predicted activities.

In contrast, the FFM relies on the direct convolution of the discrete neutron energy spectrum with energy dependent cross sections. The finite energy binning of the spectrum and cross-section data can result in an underestimation of narrow resonances, leading to lower predicted activities.

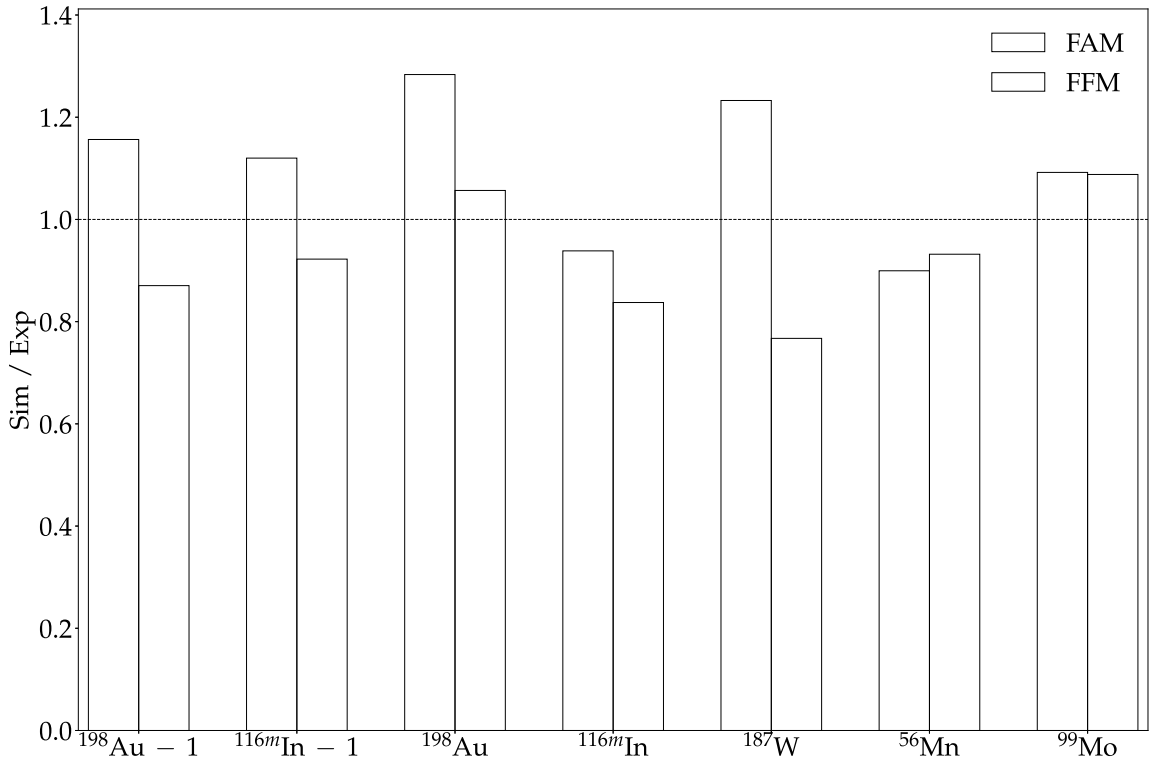


Figure 4.9: Ratios of simulated to experimentally measured activities for bare foil irradiations.

For the bare irradiations, the ratio of simulated to experimental activities lie relatively close to unity for both methods, with mean values of 1.14±0.14 for FAM and 0.93±0.13 for FFM. Overall, this shows a consistent trend in which FAM predicts slightly higher activities than measured, while FFM predicts slightly lower activities than measured, but will a comparable difference across different monitors. Hence, these two methods can be interpreted, in most cases, as providing an upper and a lower limit for the expected activation of the samples.

4.3.3 Cadmium-Covered Foil Irradiation

The Cd-covered foil irradiations test the ability of the simulations to reproduce activation under conditions where the thermal neutron component of the flux is strongly suppressed by the 1 mm Cd filter.
Fig. 4.10 compares the experimentally measured activities at EOI with the corresponding PHITS results obtained using the FAM and FFM for all Cd-covered foils. Compared to bare irradiations, a clear reduction in activation is observed for monitors with strong thermal cross sections as expected. At the same time, the discrepancies between simulation and experiment increase, reflecting the stronger

dependence of the activation on the epithermal spectrum once the thermal spectrum is filtered out.

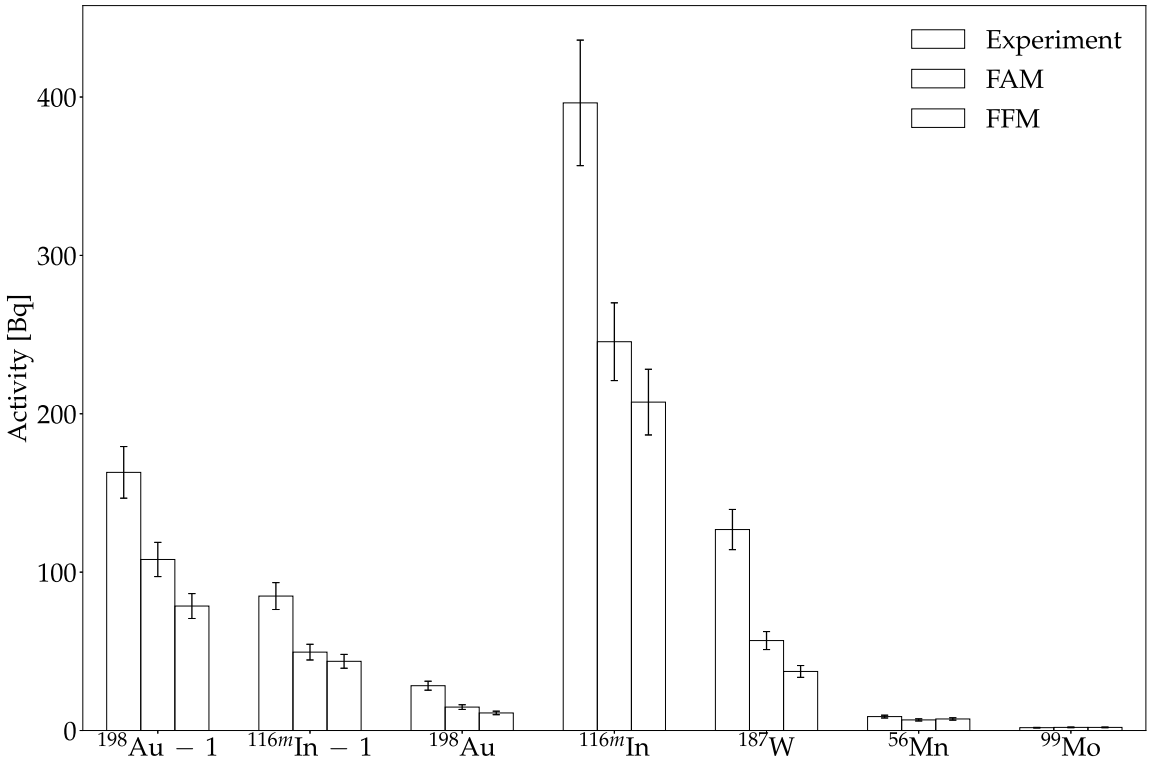


Figure 4.10: Experimental and simulated activities at the end of irradiation for Cd-covered foils.

The FAM substantially overestimates the measured activities, with deviations of approximately 50% for ^{198}Au – 1 and up to about 70% for ^{116m}In – 1. In contrast, the FFM yields lower predicted activities, which are generally closer to the experimental values, although still showing deviations of the order of 20–30%.
The activities in Fig. 4.10 further confirm the trends observed across a wider range of isotopes. For ^{198}Au, the FAM estimates significantly higher activity by nearly a factor of two, while the FFM underestimates it by roughly 25%. A similar behaviour is observed for ^{116m}In, where the FAM result exceeds the measurement by about 60%, whereas the FFM remains within approximately 15–20%. For ^{187}W, the FAM estimation is again substantially higher than the experimental value, while the FFM result lies within about 20%. The activities of ^{56}Mn and ^{99}Mo are reproduced with smaller deviations, typically below 20% for both methods.
The systematic behaviour is also illustrated by the activity ratios that are shown in Fig. 4.11. For the Cd-covered irradiations, the ratios show larger deviations, particularly for the FAM with mean values of 1.66$\pm$0.44, while for the FFM 0.83$\pm$0.20. This increased sensitivity reflects the stronger dependence of the activation on the

epithermal neutron spectrum once the thermal component has been removed by the Cd filter. In this energy region, neutron capture is dominated by resonance absorption, and each activation monitor primarily is activated by the neutron flux around its effective resonance energy. Since the resonance energies differ between the investigated isotopes, the agreement between simulations and experiment becomes isotope dependent. Hence, the isotopes whose activation is dominated by strong epithermal resonances exhibit larger differences between the two calculation methods compared to those with a weaker resonance contribution.

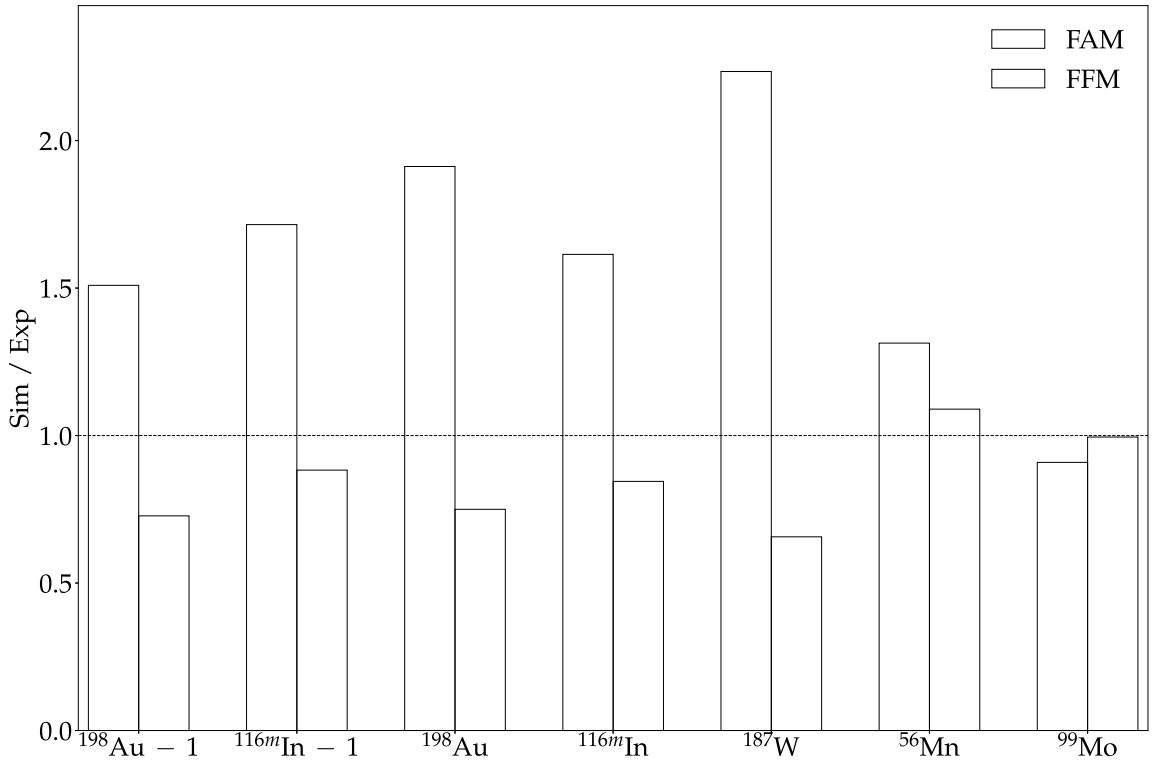


Figure 4.11: Ratios of simulated to experimentally measured activities for Cd-covered foil irradiation.

These deviations indicate that the simplified treatment used by the FAM becomes limited under Cd-covered irradiations and the energy-dependent treatment of the FFM generally underestimates the measured activities. The experimental results fall largely between the two predictions, allowing the two methods to be interpreted as practical upper and lower bounds for the activation yield in this benchmark.

4.3.4 Assessment of the Epithermal Neutron Spectrum

In addition to the activity benchmark presented in this chapter, the measured activation data were also evaluated using several established methods for determining

the epithermal shape factor α [45, 47, 48, 56, 59–62]. The objective of this analysis was to assess whether the neutron spectrum predicted by PHITS could reproduce not only the measured activation rates but also the spectral characteristics of the irradiation facility.
The α-factor describes deviations of the epithermal neutron spectrum from an ideal $1/E$ dependence. It can be estimated from activation ratios of suitable monitor reactions with known resonance parameters and Cd ratios. Therefore, the experimentally determined foil activities were used as input for different analytical α-evaluation methods.
As a representative example, Fig. 4.12 shows the result obtained with the Cd-covered multi-monitor k_0-factor method. In this approach, α is obtained from the slope of the linear fit to the monitor-dependent quantities T_i as a function of the effective resonance energy $\bar{E}_r$ [61].

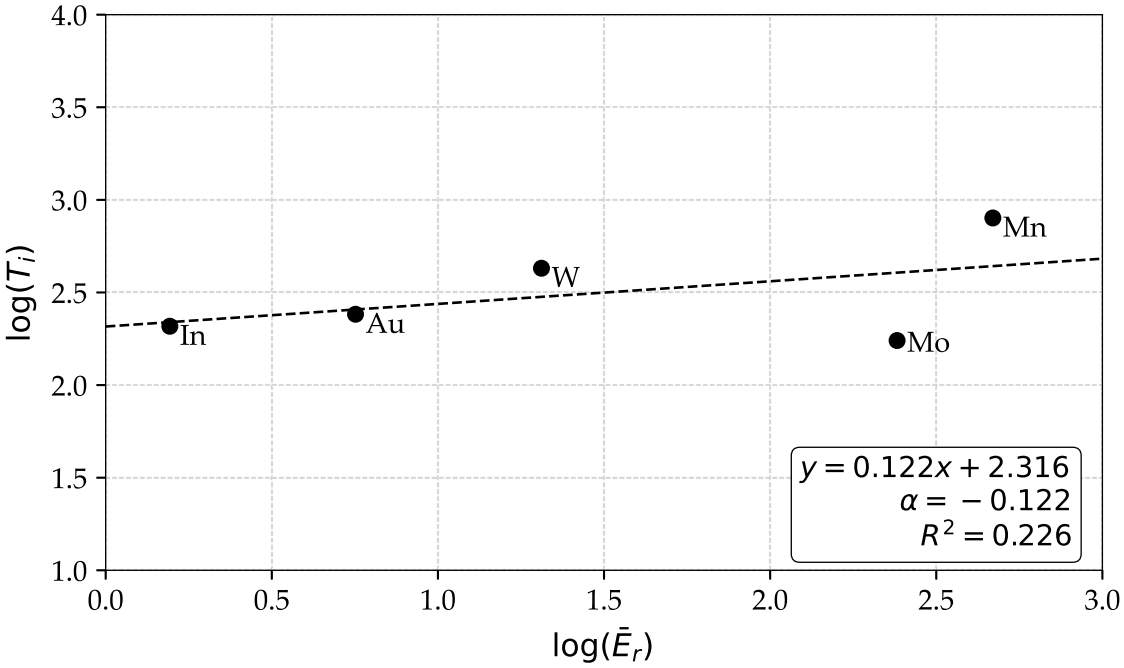


Figure 4.12: Representative determination of the epithermal shape factor α using the Cd-covered multi-monitor k_0-factors method. The value of α is obtained from the slope of the fitted linear regression.

While the comparison of measured and simulated activities showed generally good agreement, the experimentally determined α values varied considerably between the different evaluation methods. For the method shown in Fig. 4.12, an α value of approximately -0.122 was obtained, whereas PHITS predicted values between approximately -0.06 and -0.08. Even larger differences were observed between the individual analytical methods themselves, indicating that the determination of

α was strongly dependent on the selected evaluation method and monitor combination.
These discrepancies indicate that the available benchmark dataset was not sufficient for a reliable determination of the epithermal spectral shape. The main factors contributing to these discrepancies include the selected monitor set, particularly the absence of monitors with higher effective resonance energies, the sensitivity of the result to the Cd transmission correction factor F_{Cd}, the treatment of non-$1/v$ nuclides such as ^{115}In, and possible variations in the counting geometry. A more reliable determination would require a dedicated irradiation campaign with the addition of a monitor with higher effective resonance energy, such as ^{94}Zr (4520 eV), experimentally determined F_{Cd} values for the actual foil-Cd geometry, consistent Westcott corrections or exclusion of unsuitable non-$1/v$ monitors, and fixed counting holders to minimise geometry-related variations.
Since the primary objective of this benchmark was the validation of activation predictions for subsequent optimization studies of the TMR system, further investigation of these discrepancies was considered outside the scope of the present work. A detailed discussion of the α-factor analysis is provided in [54].

4.4 Conclusions

Neutron activation benchmark experiments with bare and Cd-covered foils were analysed and compared with PHITS simulations to validate the activity determination approaches used in this work, the FAM and the FFM. The comparison was performed without renormalisation to the measurements, hence the agreement reflects the combined performance of the AmBe source description, neutron transport modeling, and the activity calculation process.
For bare irradiations, both methods reproduce the measured activities with generally acceptable agreement across all investigated monitors, with mean ratios (A_{sim}/A_{exp}) of 1.14$\pm$0.14 for FAM and 0.93$\pm$0.13 for FFM.
For Cd-covered irradiations, the discrepancies increase, in particular for FAM, with mean ratios of 1.66$\pm$0.44 for FAM and 0.83$\pm$0.20 for FFM. This reduced agreement under Cd cover reflects the increased sensitivity of the activation to the epithermal neutron spectrum. In this case the resonance capture dominates once the thermal neutron component is suppressed. Each monitor is activated by different resonance regions of the epithermal spectrum, therefore the deviations also become more isotope dependent under these conditions.
As a complementary analysis, the experimental activation data were evaluated using several established methods for determining the epithermal shape factor α. Although the simulations successfully reproduced the measured activities, the α-factor analysis remained inconclusive because the different evaluation methods produced substantially different results. Therefore, benchmark conclusions are

based on the comparison between simulated and measured activities.
Overall, within the investigated benchmark configurations, the FAM tends to provide a conservative upper limit and FFM a lower limit for the expected activation, with the experimental activities typically lying between these bounds. The benchmark results support the validity of the PHITS-based activation model within the quoted uncertainties and provide the basis for applying the same approach to more complex systems.
For subsequent ^{99}Mo activity production estimates under bare irradiation conditions, a conservative uncertainty of $\pm$15% is adopted based on the agreement and the distribution observed for the bare foil benchmark.

5 Parameter Study for the Production of Molybdenum-99

The neutron transport and activation tools validated in the previous chapter are used to perform a detailed parameter study of accelerator-based ^{99}Mo production via the $^{98}\mathrm{Mo}(n,\gamma)^{99}\mathrm{Mo}$ reaction. The study focuses on how variations in the target–moderator–reflector (TMR) configuration influence the neutron spectrum and, consequently, the achievable ^{99}Mo activity and specific activity. The aim is to narrow the TMR design to a set of technically feasible configurations that can serve as reference concepts for subsequent engineering design and experimental work.

5.1 Introduction

The reliable supply of ^{99}Mo, the parent nuclide of technetium-99m (^{99m}Tc), remains a key challenge in nuclear medicine. As outlined in Section 1.2, current large-scale production is dominated by reactor-based fission of uranium-235 (^{235}U) in research reactors [1]. This method is associated with significant radioactive waste generation, proliferation concerns, and vulnerability to supply disruptions [2]. These concerns have motivated the development of alternative, non-reactor-based production pathways. Among the non-fission options discussed in Section 1.2, neutron capture on molybdenum with natural isotopic composition via the $^{98}\mathrm{Mo}(n,\gamma)^{99}\mathrm{Mo}$ reaction represents the most direct route to ^{99}Mo. Although this approach inherently yields ^{99}Mo with low specific activity, it offers several advantages: reduced quantities of long-lived radioactive waste, comparatively simple target processing, and can be integrated into accelerator-based neutron source concepts. Particularly, High-Current Accelerator-based Neutron Sources (HiCANS), introduced in Section 2.1.3, provide a promising platform for implementing this route. These neutron sources can deliver neutron flux levels approaching those of medium-scale research reactors in optimized irradiation conditions, without relying on nuclear fission [4].
In this chapter, a parameter study of ^{99}Mo production at an accelerator-driven neutron source modeled after the High Brilliance Source (HBS) concept is presented. Based on the benchmark results in Chapter 4, the flux analysis method (FAM) is used for this parameter scan as a computationally efficient activity estimator. For subsequent ^{99}Mo production estimates under bare irradiation conditions, an uncertainty of approximately $\pm 15\%$ is adopted, consistent with the agreement observed

in the benchmark. The study quantifies how key design parameters, such as moderator and reflector materials, geometric configuration, and Mo plate thickness, affect the total ^{99}Mo activity and the achievable specific activity in the $^{98}\mathrm{Mo}(n,\gamma)^{99}\mathrm{Mo}$ production route. In addition to the primary TMR optimization study, several alternative production concepts and preliminary experimental investigations are presented to assess potential improvements and identify limitations of the proposed production route.

5.2 Study Setup

This section defines the modeling assumptions, the reference geometry used in the study, and the range of design parameters that are varied. The setup is intended to be physically realistic but still generic, so that different moderator, reflector, and irradiation concepts can be compared while keeping basic engineering aspects in mind.

5.2.1 Simulation

The study is based on Monte Carlo particle transport simulations performed with the PHITS code. Neutron spectra were simulated with PHITS (v3.22) using the nuclear data defined in Section 3.1.3. Activities were estimated with the FAM approach described in Section 3.2.2.
PHITS is used to model proton and neutron transport from the primary proton beam interaction in the target through the surrounding moderator and reflector materials. Neutron transport is treated over the full relevant energy range (0 – 70 MeV), allowing simultaneous evaluation of fast (0.1 MeV to 20 MeV), epithermal (0.5 eV to 0.1 MeV), and thermal neutron (1 meV to 0.5 eV) contributions to the $^{98}\mathrm{Mo}(n,\gamma)^{99}\mathrm{Mo}$ reaction. Neutrons with energies above 20 MeV are transported but neglected in the activation calculation, since evaluated (n,γ) cross sections are generally not available above 20 MeV and the capture probability at these energies is expected to be very small. The nuclear data defined in Section 3.1.3 are used throughout the entire simulation campaign.
For each configuration investigated in the parameter study, neutron flux spectra are tallied within the Mo irradiation plates. The fluxes are subsequently separated into thermal, epithermal, and fast components and used as input for the activity calculations described in Section 3.2.2. The resonance integral is calculated from the simulated epithermal spectra, so that spectrum effects are properly taken into account.
All simulations are performed with 10^8 primary proton histories incident on the target, providing sufficient statistical precision to resolve relative differences between configurations. Since the aim of this chapter is to compare design parameters rather

than to perform a detailed uncertainty analysis, all configurations are treated in the same way, and no additional variance reduction techniques are applied.

5.2.2 Target–Moderator–Reflector (TMR) Concept

The investigated system follows the general design principles of accelerator-driven neutron sources, in which a charged particle beam (typically protons or deuterons) impinges on a neutron production target, which can be a heavy metal (Pb, Bi, Pb-Bi, Ta, W) or a low-Z material (Be, Li, or V) depending on the beam energy, producing fast neutrons via (p, xn) reactions [63–65]. In neutron scattering, imaging, and analysis applications, these fast neutrons are moderated to energies suitable for instruments [4, 66]. In the present work, the same basic concept is adapted to provide a neutron spectrum favorable for the (n, γ) reaction on natural Mo plates. The geometry considered in this study is modeled after the TMR concept developed for the HBS [4]. A schematic view of the TMR is shown in Figure 5.1, which serves as the reference configuration for the simulations performed in this chapter.

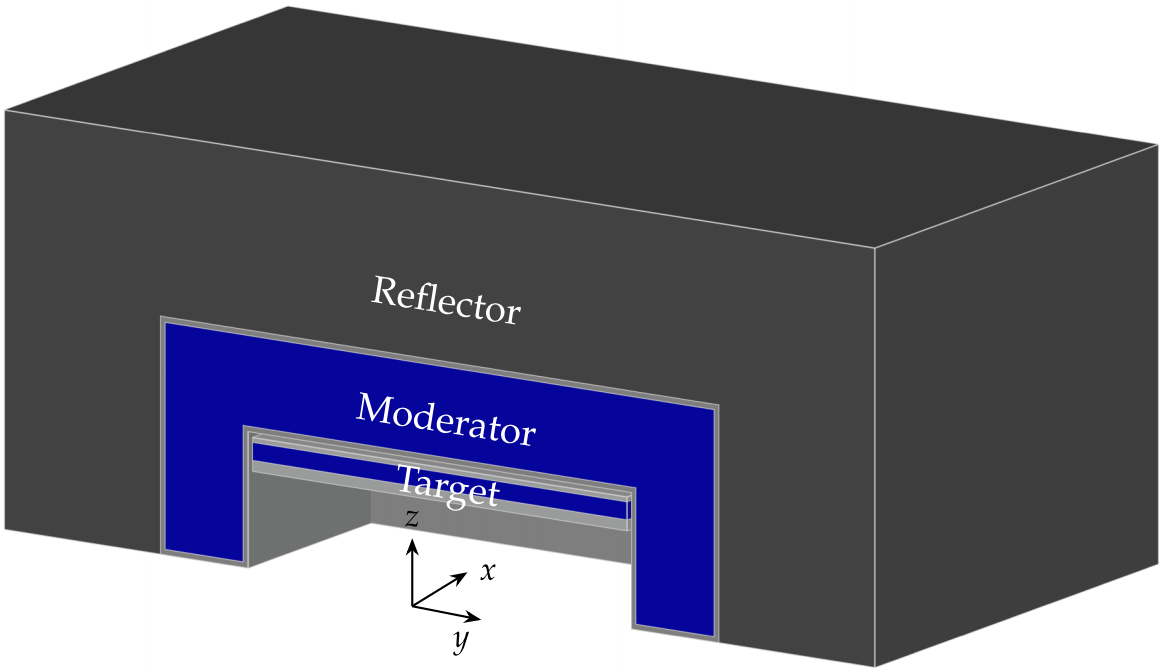


Figure 5.1: Section view in the $x = 0$ plane of the HBS-type TMR reference geometry, showing the Ta target and the surrounding moderator and reflector.

A high-energy proton beam impinges on a tantalum (Ta) target, producing fast neutrons through (p, xn) reactions. These neutrons are subsequently slowed down in a surrounding moderator volume and reflected back toward the irradiation region by a reflector. The Mo irradiation plates are embedded within the moderator,

where they are exposed to a neutron spectrum shaped by the combined effects of moderation and reflection.
This modular TMR configuration conceptually allows the variation of individual components while keeping a consistent overall geometry. In this work, this flexibility is used in the simulations to study how moderator and reflector materials and thicknesses, and the positioning of the irradiation plates, affect the system, without changing the underlying neutron production mechanism.

5.2.3 Proton Beam and Target Design

The proton beam energy was set to 70 MeV with an average beam current of 12 mA, corresponding to the upper operational limits considered for radionuclide production within the HBS design framework [4]. A homogeneous beam distribution over the target surface was assumed for all simulations.
The target consists of a layered tantalum–water–tantalum structure designed to withstand high power densities (up to 3 kW/cm^2) under active cooling. Ta was selected as the target material due to its high melting point, mechanical robustness, and favorable neutron yield in this proton energy range. The water layer serves both as a beam stop and as an initial moderator for fast neutrons produced in the Ta target. A schematic of the target geometry, is shown in Figure 5.2, while the detailed cooling-channel structure is not explicitly modeled in the simulations [67, 68].

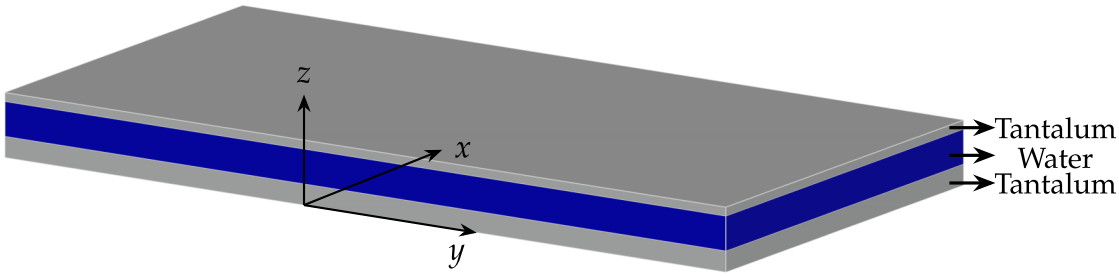


Figure 5.2: Geometrical model of the layered Ta–water–Ta target used in the simulations. The target has a surface area of 12 × 24 cm^2 and consists of a 0.6 cm Ta layer, a 1.0 cm water layer, and a 0.25 cm Ta back layer, for a total thickness of 1.85 cm.

This target design provides a realistic representation of the proposed HBS target while maintaining compatibility with the surrounding moderator and reflector assemblies.

5.2.4 Moderator and Reflector Candidates

Moderator materials were selected based on their neutron slowing-down power, moderating ratio, absorption cross section, and practical implementation consider-

ations, as discussed in Chapter 2. Four candidates were investigated: light water (H_2O), heavy water (D_2O), beryllium (Be), and zirconium hydride (ZrH_2). These materials span a range from strong hydrogenous moderators to low-absorption, high-scattering materials, enabling a broad exploration of possible neutron spectra within the TMR.
Reflector materials were chosen to minimize neutron leakage while remaining compatible with engineering and safety constraints. Three candidates were evaluated: lead (Pb), magnesium oxide (MgO), and beryllium (Be). Pb and MgO are representative reflector materials with favorable scattering properties, whereas Be represents a high-performance reflector from a neutronic perspective, but with known limitations related to irradiation-induced swelling, tritium production, and waste management [69–71]. Hence, in this study, Be is included primarily as a reference case.
The combination of these moderator and reflector candidates enables evaluation of both idealized and practically feasible TMR configurations within a consistent simulation framework.

5.2.5 Irradiation Plate and Positioning

Natural Mo irradiation plates were modeled as rectangular slabs placed within the moderator volume. Four plates were considered in the reference configuration: two plates of 12×24 cm^2 (Plates A and D, each with a mass of approximately 3 kg) and two plates of 12×12 cm^2 (Plates B and C, each with a mass of approximately 1.5 kg). All plates have an initial thickness of 1 cm. A view of the plate arrangement within the TMR assembly is shown in Figure 5.3.

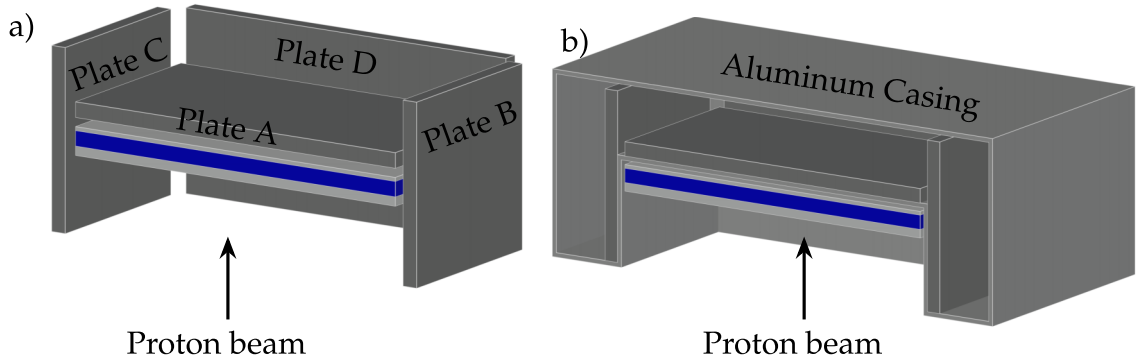


Figure 5.3: Geometric model of the (a) arrangement of the four irradiation plates (A–D) around the Ta target and (b) aluminum casing (Al casing) enclosing the assembly and defining the moderator volume.

Plate A is positioned on-axis, facing the proton beam, and is referred to as the axial plate, while the lateral plates (Plates B, C, and D) are positioned around the target.

This distinction allows direct assessment of geometric effects on neutron flux and activation efficiency. The plates are separated from the Ta target by a 3 mm thick Al casing as shown in Figure 5.3(b).
In addition to the four-plate reference configuration, a reduced single-plate configuration comprising only Plate A was modeled for selected studies. In this case, Plates B, C and D and their associated moderator cavities were removed, and the surrounding moderator volume was adjusted accordingly.
Plate dimensions and spacing were selected to reflect realistic handling and cooling constraints while allowing systematic variation of plate thickness (1–5 cm) to investigate neutron self-shielding effects. The chosen configurations enable direct comparison of single-plate and multi-plate irradiation concepts within the same TMR framework.

5.2.6 Parameter Variation

The study was designed to analyze the influence of material selection and geometric configuration on the ^{99}Mo production. To clearly observe how each parameter affects the activation of the Mo plates, the parameters were varied one at a time while keeping the others constant.
The following parameters were investigated:

- moderator material (H_2O, D_2O, ZrH_2, Be)
- moderator thickness (1–20 cm in 1 cm steps)
- reflector material (Pb, MgO, Be)
- reflector thickness (5–20 cm in 5 cm steps)
- plate position (axial, lateral; Plate–Al casing distance 0–5 cm in 0.5 cm steps)
- plate thickness (1–5 cm in 1 cm steps)

This approach allows us to identify the main effects and parameter dependencies. The selected parameter ranges reflect both neutron physics considerations and practical constraints related to system size, material handling, and engineering feasibility.

5.3 Results and Discussion

In this section we present and discuss the results of the parameter study, which includes approximately 30,000 individual simulations. Initially, we analyze the neutron spectra within the Mo plates obtained for a reference configuration in order to provide a picture of the spectral characteristics in the TMR assembly. To

relate these spectra to ^{99}Mo production, the activity of the Mo plates (for a 6-day irradiation and an average beam current of 12 mA) is then calculated using the expression derived from the FAM and given by Eq. 3.15. This method was chosen because, among the approaches discussed in Section 3.2.2, it offers the shortest computation times while retaining sufficient information for the study. Using the FFM simulations for the entire set of configurations would have required an impractically large amount of computing time and was not applied.
Then, we examine how the ^{99}Mo activities change as individual design parameters are varied. The analysis proceeds in stages, starting with the distance between the irradiation plates and the target, followed by the moderator thickness, moderator material, reflector material, and reflector thickness. Given the large number of configurations, only a selection of representative spectra and activity distributions are shown in this chapter to illustrate the main trends. Additional plots and detailed data for further configurations are provided in Appendix C.

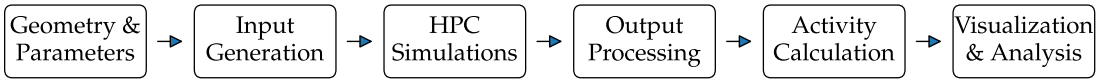


Figure 5.4: Overview of the automated workflow used for the parameter study.

The overall workflow adopted for the automated parameter study is summarized in Fig. 5.4. Following the definition of the geometry and investigated design parameters, the complete simulation campaign was fully automated, including the generation of PHITS input files, execution of the simulations on the HPC cluster, post-processing of the output data, activity calculations, and the subsequent visualization and analysis of the results. Further details on the developed Python scripts and the automation workflow are provided in Appendix D.

5.3.1 Neutron Spectra within the Mo Plates

Before discussing the resulting ^{99}Mo activities, it is useful to examine the neutron energy spectra within the Mo plates for a representative configuration. This provides insight into how plate position and the TMR layout shape the neutron field to which the plates are exposed.
The simulated neutron energy spectra in the Mo plates, given in Fig. 5.5, show a clear dependence on the position of the plates relative to the target. The axial plate consistently experiences higher neutron fluxes across the full energy range, particularly in the epithermal region relevant to produce ^{99}Mo.
This behavior reflects the forward direction of neutron emission from the Ta target under 70 MeV proton irradiation: about 60% of neutrons are emitted in forward direction and about 40% in the backward direction. As a result, the axial plate, which

lies directly in this forward field, receives the highest neutron flux and therefore will have the largest ^{99}Mo activity among the plates for all analysed configurations. In contrast, the lateral plates are located off-axis and are exposed to a less intense neutron flux leading therefore to lower activities.

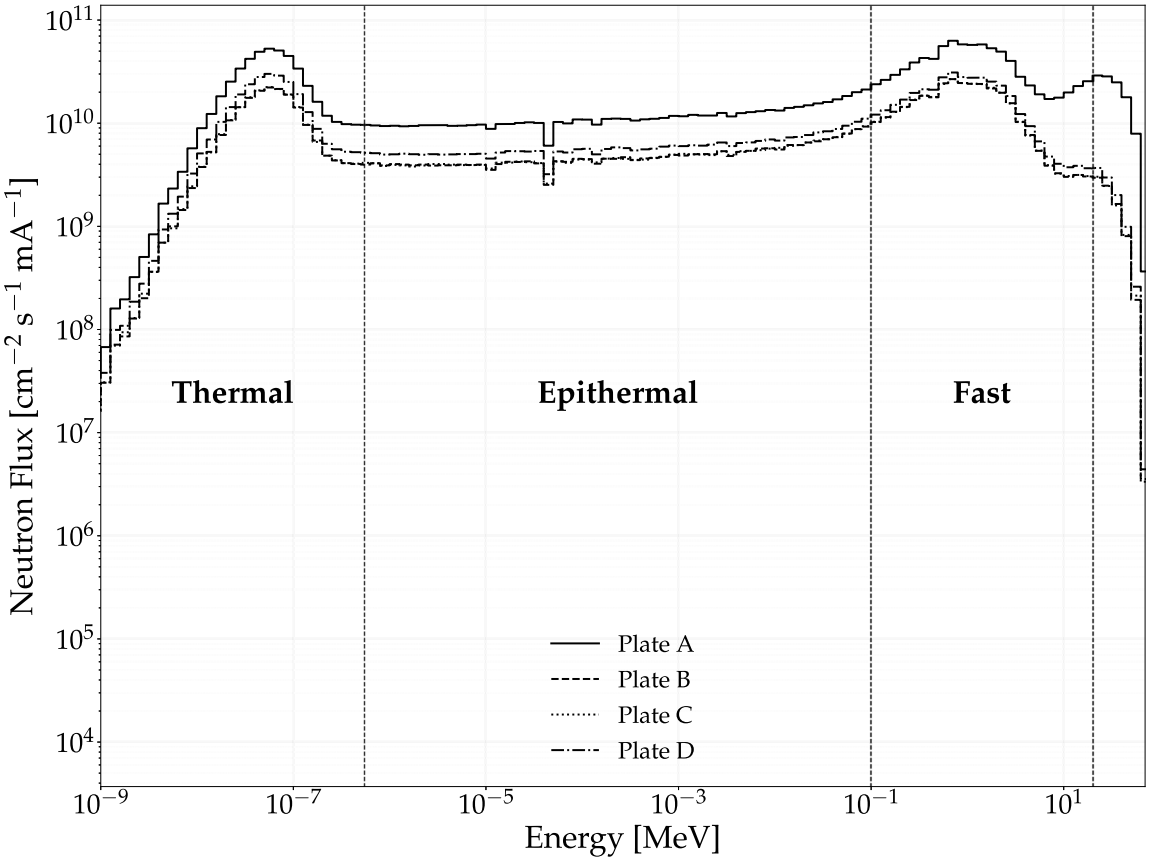


Figure 5.5: Simulated neutron energy spectra within the Mo plates positioned at a distance of 3 cm from the Al casing, with a 5 cm H_2O moderator and 10 cm Pb reflector.

As seen in Figure 5.5, a fraction of neutrons have energies above 20 MeV. These high-energy neutrons are not included in the activity calculation, since the ^{98}Mo$(n,\gamma)^{99}$Mo cross section is generally not tabulated above 20 MeV in evaluated data libraries. Given the very small expected capture probability at these energies, their contribution to the total ^{99}Mo activity has been neglected.

5.3.2 Irradiation Plate Positioning and Moderator Effects

To quantify how the choice of the moderator and the positioning of the irradiation plate influence the ^{99}Mo production, we first examine the activity of the axial plate (Plate A) over a wide range of plate distances and moderator thicknesses. Plate A is

used as a reference, since it is exposed to the highest neutron flux and thus provides the most favorable conditions for observing systematic trends.
In Figure 5.6 the ^{99}Mo activity in the axial plate is compared for different moderator materials as a function of moderator thickness. Two distinct behaviors emerge. For hydrogen-based moderators (H_2O and ZrH_2) the activity reaches a maximum at relatively small moderator thicknesses before saturating or decreasing. In contrast, D_2O and Be show a smooth increase of activity for increasing moderator thickness and the highest value is obtained only for substantially thicker moderators.

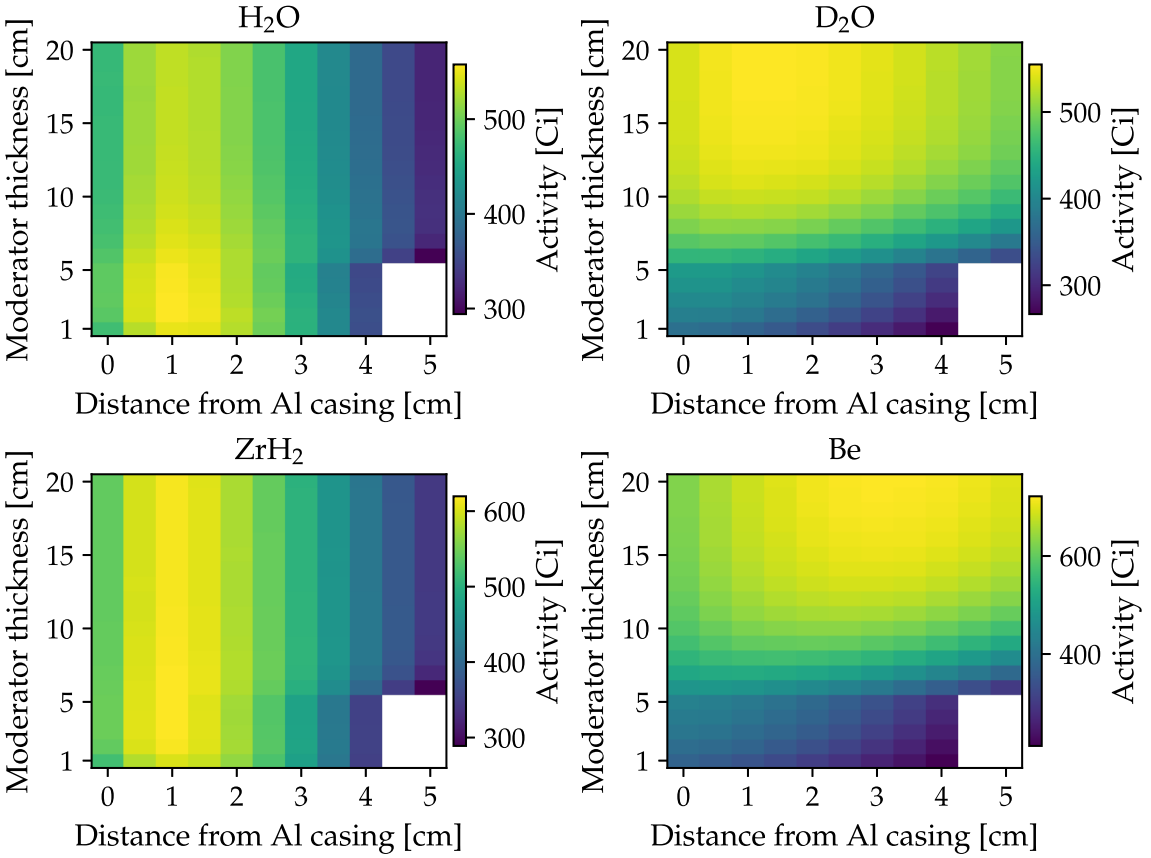


Figure 5.6: Calculated ^{99}Mo activity in Plate A for various moderators as a function of plate distance from the Al casing and moderator thickness, with a 5 cm Pb reflector.

For H_2O and ZrH_2, the strong slowing-down power of hydrogen leads to fast thermalization of the fast neutrons emerging from the target. As a result, even thin moderator layers already produce a significant epithermal component, which is the most relevant energy range for the $^{98}\mathrm{Mo}(n,\gamma)^{99}\mathrm{Mo}$ reaction due to the resonance structure of the cross section. Increasing the moderator thickness further shifts the spectrum toward lower (thermal) energies and increases neutron absorption in the moderator itself, so that the epithermal flux at the plate does not continue to grow.

This explains why the activity distributions for hydrogenous moderators exhibit a relatively sharp maximum at small thicknesses before decreasing. In practice, this behavior favors compact moderator designs when H_2O and ZrH_2 are used.
The behavior of D_2O and Be is noticeably different. Both materials have lower slowing-down power and lower absorption cross sections than H_2O and ZrH_2, so neutrons require longer paths to lose their energy, but are also less likely to be absorbed in the moderator.
Consequently, the ^{99}Mo activity continues to increase over a wider range of moderator thicknesses, as a larger moderator volume is needed to build up a substantial epithermal flux at the plate position. The activity distributions for D_2O and Be therefore rise more slowly but reach their maximum only at much larger thicknesses. This trend reflects the expected spectrum-shaping behavior: hydrogen-based moderators support high activities in relatively compact assemblies, whereas D_2O and Be can achieve comparable or higher activities only in geometries that provide a sufficiently large moderator volume.
In addition to the choice of moderator material, the plate distance from the target also influences the activity. For hydrogen-based moderators, changes in plate distance primarily affect the intensity of the neutron energy spectrum, but do not shift the optimal moderator thickness significantly, since the spectrum is already largely thermalized within a few centimeters. For D_2O and Be, the activity is more sensitive to the effective moderator volume between the target and the plate, so that both moderator thickness and plate distance act together in shaping the epithermal component at the plate position.
For the lateral Plates B, C, and D, the activity maps exhibit the same qualitative dependence on moderator material and thickness as Plate A, but with a notable shift in the optimal plate position. In these cases, the maximum ^{99}Mo activity is reached at smaller distances from the target, i.e. the plates need to be placed closer to the Al casing. This behavior reflects the more rapid geometric attenuation of the neutron flux off-axis: lateral plates intercept fewer forward-directed neutrons and therefore benefit less from additional moderation path length than the axial plate. As the distance from the target increases, the gain in spectrum softening is quickly outweighed by the loss in overall flux, so that the optimum occurs at shorter distances. The corresponding heatmaps for Plates B, C, and D are provided in Appendix C for reference.

5.3.3 Reflector Material and Thickness Effects

We now turn to the role of the reflector in shaping the neutron field. In particular, we investigate how reflector material and thickness influence the total ^{99}Mo activity obtained from all plates for different moderator choices.
Figure 5.7 summarizes the total ^{99}Mo activity for all moderators as a function of reflector type and thickness. Across all moderator types, increasing reflector

thickness initially leads to a clear gain in activity, reflecting the reduction of neutron leakage as more neutrons are scattered back into the moderator and plate region. In most cases, however, the marginal benefit of adding reflector beyond about 10 cm becomes small, and the activity curves tend to level off. This indicates that, once most neutron leakage is suppressed, additional reflector material mainly increases neutron path lengths rather than substantially increasing the flux at the plates.

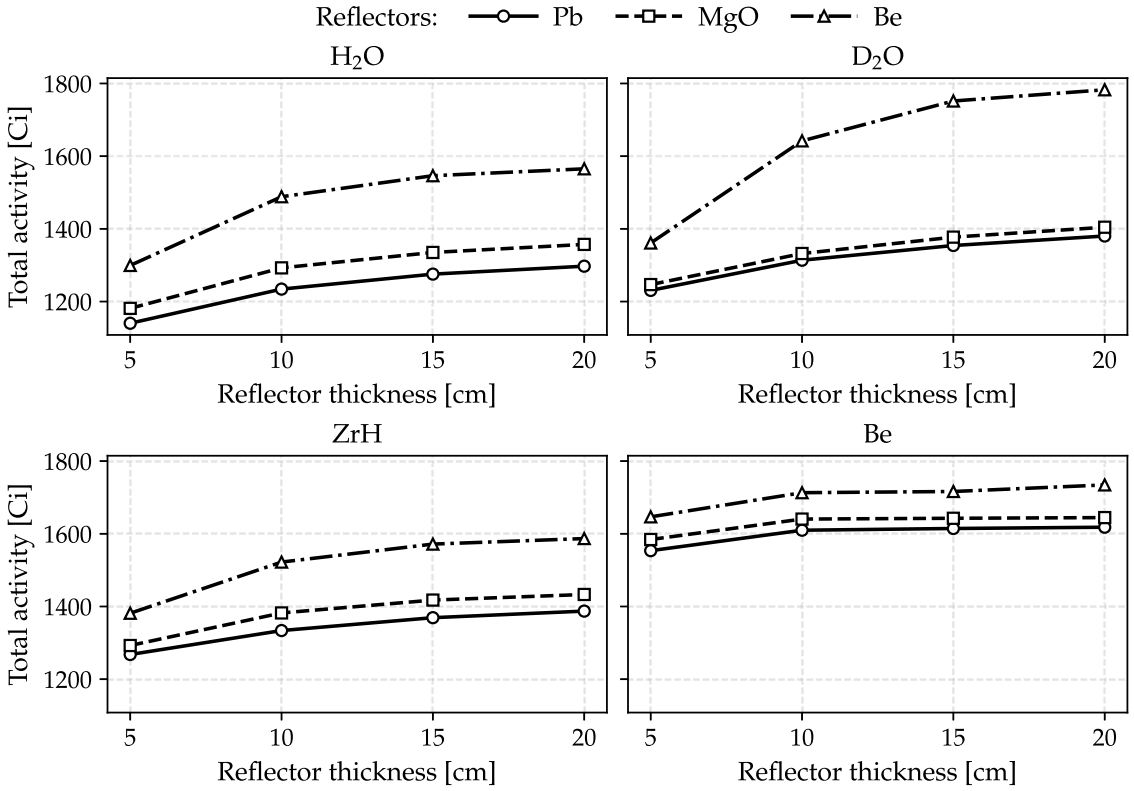


Figure 5.7: Total ^{99}Mo activity from all plates after 6 days of irradiation as a function of reflector thickness for different reflector materials (Pb, MgO, Be), shown separately for each moderator (H_2O, D_2O, ZrH_2, Be). For each moderator-–reflector thickness combination, the plate distance and moderator thickness correspond to the highest activity configuration identified in the preceding analysis.

Among the reflector candidates, Be consistently yields the highest activities for a given moderator, followed by MgO and Pb, in line with their scattering and absorption properties. The combination of a Be reflector with a D_2O moderator stands out in particular, showing noticeable gains even when the reflector thickness is increased beyond 10 cm. It should be noted, however, that this result is partly influenced by the irradiation geometry, in which all plates are kept at the same distance from the Al casing. Allowing different plate positions for each configuration

would have required a much larger number of simulations and substantially more computing time, and was therefore not pursued.
Under the constraint of a fixed plate–casing distance, the Be–D_2O configuration is especially effective at maintaining a high epithermal flux across the plate region. If, instead, plate positions were allowed to vary independently and, for each plate, the distance that maximizes its activity was selected (based on the present parameter scan), the existing data indicate that a Be–Be system (Be moderator and Be reflector) would yield the highest overall activity.
From a practical standpoint, Be is not an attractive reflector material despite its favorable performance. Its use is severely limited by material degradation under neutron irradiation, tritium production, and the resulting challenges in radiation protection and waste management. Neutron exposure leads to swelling and embrittlement of Be, accompanied by tritium release, which complicates operation, handling, and disposal. Pb and MgO offer comparable performance in this context, but MgO is preferable from an engineering perspective: its lower density allows larger reflector volumes within reasonable weight and structural limits, and it avoids the toxicity issues associated with Pb.
The choice of moderator also influences the overall performance across reflector configurations. In the simulations, ZrH_2 generally provides higher activities than H_2O and D_2O for a given reflector, except when combined with Be, where the high performance of the Be-–D_2O combination partially compensates its lower moderating power. However, implementing ZrH_2 as a solid moderator requires a more complex, actively cooled structure, which may offset its advantages. D_2O tends to outperform H_2O but is constrained by cost, availability, and tritium production. Considering these trade-offs, a configuration with an MgO reflector and an H_2O moderator emerges as the most practical baseline option for reliable ^{99}Mo production, balancing performance with material, safety, and engineering considerations.

5.3.4 Effect of Axial Plate Thickness on Activity and Specific Activity

Having established the MgO-–H_2O configuration as a practical reference system, with a moderator thickness of 5 cm and an MgO reflector thickness of 20 cm, we next investigate how the thickness of the axial plate (Plate A) affects both the total activity and the specific activity of ^{99}Mo. This analysis provides an indication on the production potential under different Mo loading scenarios and highlights the trade-off between maximizing total activity and maintaining specific activity.
Figure 5.8 shows the total activity (left) and the specific activity (right) of ^{99}Mo as functions of the Plate A thickness for both the four-plate and single-plate setups. Increasing the thickness of Plate A (i.e. the mass of Plate A) leads to an increase in total activity. Beyond a thickness of about 3 cm, however, the specific activity in

Plate A decreases. This behavior is a direct consequence of neutron self-shielding: as the plate becomes thicker, neutrons are preferentially absorbed in the outer regions, so that the inner volume of the plate is less effectively irradiated. From the perspective of ^{99}Mo/^{99m}Tc generator applications, this decrease in specific activity is critical, since adequate specific activity is required to ensure good generator performance [72]. Within the parameter range studied here, an axial plate thickness of about 3 cm offers the best compromise, providing a high total activity while still maintaining specific activity levels compatible with LSA generator concepts.

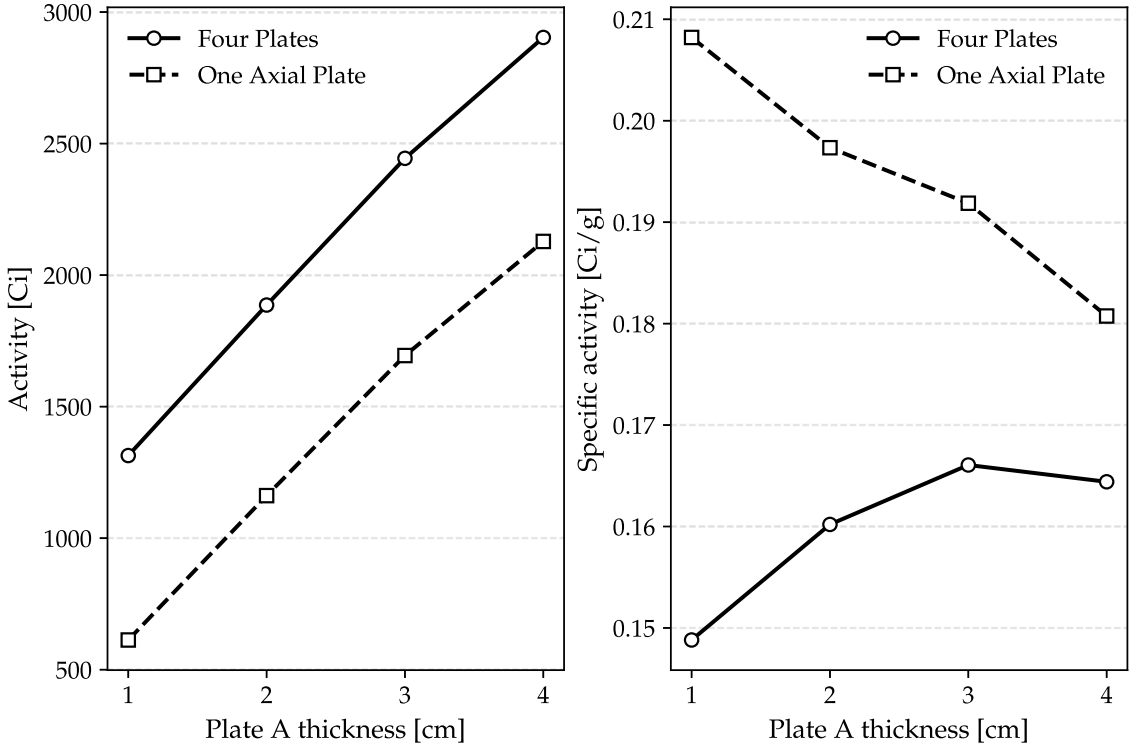


Figure 5.8: ^{99}Mo activity and specific activity for the MgO–H_2O system as a function of axial plate (Plate A) thickness after 6 days of irradiation.

Figure 5.8 also shows the results for an alternative geometry in which only the axial plate is present and its thickness is varied, while the lateral plates are removed. In this case, the total activity increases with increasing Mo plate thickness, since the available neutron flux is concentrated in a single plate. The results indicate that a total activity comparable to that of the four-plate setup can be achieved with a single axial plate, but this would require plate thicknesses exceeding about 4 cm. At such dimensions, neutron self-shielding effects become very strong, and the activity distribution within the plate is highly non-uniform. In this regime, uncertainties associated with self-shielding corrections and resonance absorption become increasingly important and would need to be addressed through dedicated

experimental validation.

5.3.5 Optimized Reference Configuration

Under the optimized MgO–H_2O configuration with a 3 cm thick axial plate, three lateral plates, and a 6-day irradiation time, the simulations indicate a potential production level on the order of 2 400 Ci of ^{99}Mo. This would be sufficient to meet Germany's current weekly demand, while the corresponding specific activity remains within the range for LSA generator designs. Further work should focus on refining self-shielding models, optimizing generator concepts for such specific activities, and addressing practical aspects such as automated plate handling, radiation protection, and long-term operational reliability.
The previous sections identified an MgO–H_2O based TMR configuration as a promising reference design for accelerator-driven ^{99}Mo production. During the development of this concept, several alternative target, moderator, and reflector arrangements were also investigated. Although these configurations were not selected for further optimization, they provide useful insight into the limitations of different production approaches and are summarized in the following section.

5.4 Additional Design Studies

In addition to the parameter variations discussed in the previous sections, several alternative target and moderator concepts were investigated during the development of the TMR system. These studies were performed to evaluate potential routes for increasing the achievable ^{99}Mo activity, improving specific activity, or simplifying the target design. Although none of these concepts were ultimately selected as reference configurations, the results provide useful insight into the limitations and trade-offs associated with accelerator-driven ^{99}Mo production.

5.4.1 Enriched Molybdenum-98 Irradiation Plates

Since natural molybdenum contains only approximately 24.1% ^{98}Mo, the use of isotopically enriched ^{98}Mo targets represents a straightforward strategy for increasing the production yield of the $^{98}\mathrm{Mo}(n,\gamma)^{99}\mathrm{Mo}$ reaction. To evaluate this potential, additional simulations were performed in which natural molybdenum irradiation plates were replaced by fully enriched ^{98}Mo while maintaining the same irradiation conditions.
It should be noted that these simulations were performed using an earlier TMR design in which the tantalum target dimensions were limited to 12×12 cm^2 rather than the final 12×24 cm^2 target geometry adopted in the main parameter study. Consequently, the absolute ^{99}Mo activities reported in this section are not directly

comparable to the activities presented in the preceding sections. The objective of this investigation was instead to assess the relative effect of isotopic enrichment and to compare the behavior of the activity prediction methods for different target thicknesses.

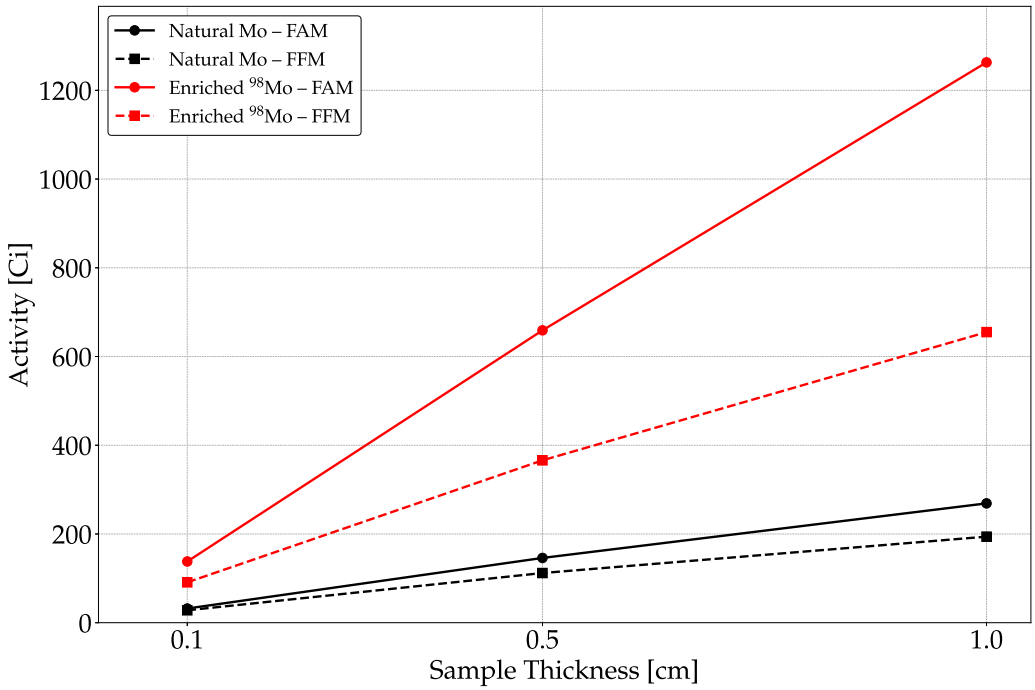


Figure 5.9: Comparison of ^{99}Mo activities calculated using the FAM and FFM for natural and enriched ^{98}Mo targets as a function of target thickness. Results are shown for a 12×12 cm^2 irradiation plate positioned 1.35 cm from the target.

The results shown in Figure 5.9 demonstrate that isotopic enrichment substantially increases the achievable ^{99}Mo activity. For all investigated target thicknesses, the FAM calculations predict activity increases of approximately a factor of 4–5 compared with natural molybdenum. This behavior is consistent with the increased abundance of ^{98}Mo nuclei available for neutron capture.
The FFM calculations also predict significant activity increases for enriched targets; however, the magnitude of the increase is consistently lower than that predicted by the FAM approach. Depending on the target thickness, the FFM results indicate activity increases of approximately a factor of 3–3.5 relative to natural Mo.
Although these calculations were performed for an earlier TMR configuration, the calculated enrichment factors can be used to estimate the potential benefit of isotopic enrichment for the optimized design discussed in the previous sections. Applying these factors to the optimized natural Mo activity obtained for the final MgO-H_2O reflector-moderator configuration suggests that enrichment could increase the EOI

activity of ^{99}Mo to approximately 7200-12000 Ci, depending on whether the FFM or FAM approach is used. These estimates should be regarded only as indicative since they are based on an extrapolation from the earlier TMR geometry and do not fully account for the potentially stronger neutron self-shielding expected in the thicker enriched targets of the optimized design.
An additional difference between the two approaches becomes apparent as the target thickness increases. While both methods predict increasing activity for thicker targets, the FFM results grow less rapidly than the FAM predictions. Consequently, the discrepancy between the two methods becomes larger for thicker molybdenum plates.
This behavior is believed to be related to neutron self-shielding effects that are not fully captured by the simplified FAM approach. As the thickness of the enriched target increases, neutron absorption in the outer layers reduces the neutron flux available to the inner regions of the plate. Since the FFM approach is based on reaction-rate information obtained directly from the transport calculation, it is expected to account more realistically for such attenuation effects. The increasing divergence between the two methods therefore suggests that self-shielding becomes increasingly important for thick enriched molybdenum targets.
These results indicate that isotopic enrichment can significantly improve ^{99}Mo production yields and may represent a viable route toward higher specific activities. At the same time, the observed differences between the activity prediction methods emphasize the importance of accurately treating neutron self-shielding effects when evaluating thick enriched targets.

5.4.2 Dissolved Sodium Molybdate Concept

An alternative target concept investigated in this work was the use of dissolved sodium molybdate (Na_2MoO_4) within the moderator volume. In this approach, the molybdenum target material is distributed throughout the moderator rather than being concentrated in solid irradiation plates. Such a configuration could potentially simplify target handling and provide efficient heat removal through the moderator coolant.
Simulations were performed assuming the maximum practical molybdenum concentration achievable in aqueous solution. For a total molybdenum inventory of approximately 1.8 kg and an irradiation period of six days, the calculated end-of-irradiation activity was approximately 125 Ci of ^{99}Mo, corresponding to a specific activity of approximately 0.07 Ci/g.
Although the concept offers advantages in terms of cooling and mechanical simplicity, both the total activity and the specific activity were substantially lower than those obtained with the solid irradiation plate configurations investigated in this study. Consequently, the dissolved sodium molybdate concept was not considered further as a practical option for large-scale ^{99}Mo production.

5.4.3 Direct Proton Irradiation of Molybdenum

In addition to neutron-capture production, a direct proton irradiation approach was investigated. In this configuration, the Mo plate itself serves as the proton target and is activated directly by the incident proton beam rather than by secondary neutrons produced in a separate target.
For a Mo target mass of approximately 3 kg, the simulations predicted an end-of-irradiation ^{99}Mo activity of approximately 1435 Ci after six days of irradiation. This corresponds to a specific activity of approximately 0.48 Ci/g, which is significantly higher than the values obtained for the neutron-capture configurations investigated in this study.
Table 5.1 summarizes representative radionuclides produced during direct proton irradiation together with their half-lives and activities at the end of irradiation. In addition to the desired ^{99}Mo, significant activities of activation products from Mo, Tc, Nb and Zr isotopes are generated. Several of these radionuclides exhibit activities comparable to or exceeding that of ^{99}Mo immediately after irradiation, while some possess half-lives of several days or longer and therefore remain present during target cooling and subsequent radiochemical processing.

Table 5.1: Major radionuclides produced during direct proton irradiation of a Mo target.

Radionuclide	**Half-life**	**Activity at EOI (Ci)**	**Relative to ^{99}Mo**
^{99}Mo	65.9 h	1435	1.00
^{93m}Mo	6.86 h	3838	2.68
^{90}Mo	5.67 h	1870	1.30
^{96}Tc	4.28 d	2389	1.66
^{95}Tc	20.0 h	2641	1.84
^{94}Tc	4.89 h	1527	1.06
^{89}Zr	78.4 h	1414	0.99
^{90}Nb	14.6 h	3595	2.50
^{96}Nb	23.4 h	430	0.30
^{95}Nb	35.0 d	50.8	0.035
^{92m}Nb	10.2 d	201	0.14

Although direct proton irradiation offers substantially higher specific activities than neutron-capture production, the simultaneous production of numerous radionuclide impurities would considerably complicate the radiochemical processing. In addition, the Mo target must directly absorb the full proton beam power, requiring a dedicated high-power target cooling system capable of removing the deposited

heat while maintaining target integrity.
Since the objective of the present work was the optimization of neutron-capture-based ^{99}Mo production within an HBS-type TMR assembly, rather than the development of a dedicated proton target station, this concept was not investigated further.

5.4.4 Composite Reflector Configurations

In addition to the homogeneous reflector materials discussed, several composite reflector configurations were investigated to determine whether layered reflector arrangements could improve neutron utilization in the TMR assembly. In all investigated configurations, the MgO layer was placed directly outside the moderator, while the Pb layer formed the outer reflector. The thickness of both reflector layers were then varied systematically.
The results shown in Figure 5.10 indicate that introducing a Pb layer in combination with MgO does not improve the resulting ^{99}Mo activity compared with increasing the MgO reflector thickness alone. The highest activities are obtained for configurations with larger MgO thickness, whereas increasing the Pb thickness provides no comparable gain.

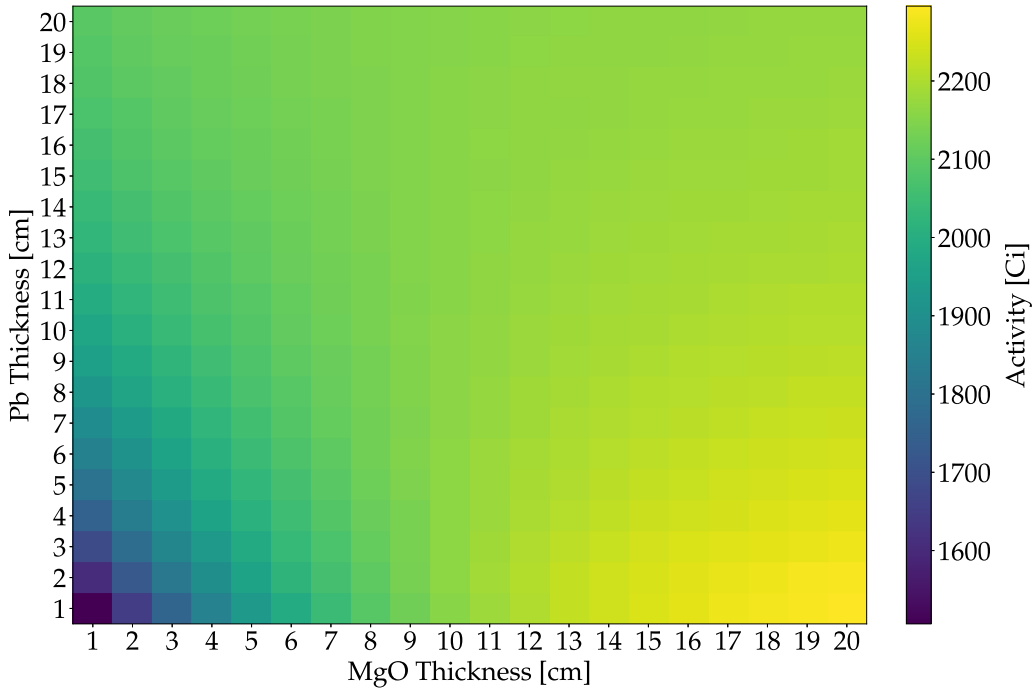


Figure 5.10: Calculated total ^{99}Mo activity for composite reflector configurations consisting of an inner MgO layer and an outer Pb layer, shown as a function of the MgO and Pb thickness. The activity corresponds to the sum over the investigated irradiation regions.

This behavior suggests that, for the present geometry and neutron spectrum, the scattering properties of MgO are more beneficial than the increased density of Pb. The use of Pb in a layered reflector therefore does not provide an advantage over a homogeneous MgO reflector. Consequently, the final optimization was restricted to homogeneous reflector configurations, with MgO selected as the most practical reflector material when both neutronic performance and engineering constraints are considered.

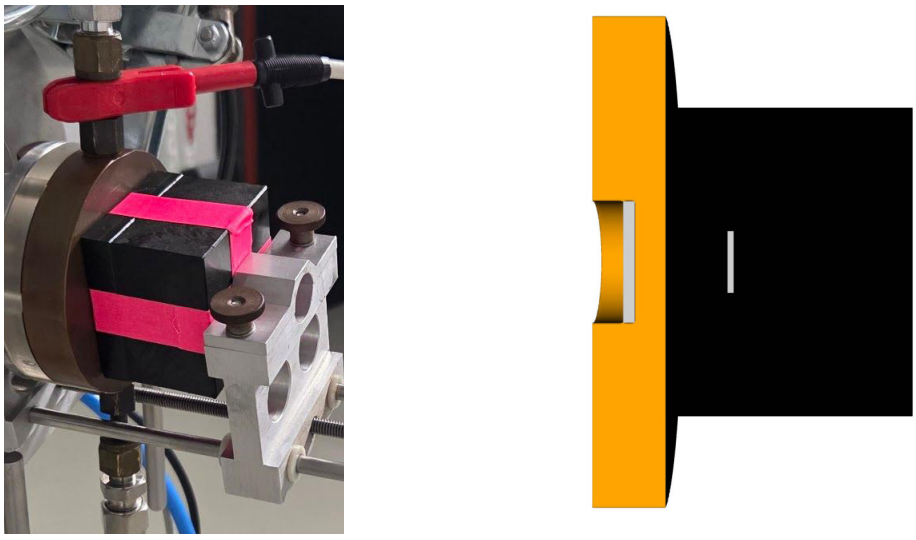
5.4.5 Self-Shielding Experiment

Neutron self-shielding in molybdenum has been identified as a potential source of uncertainty in activation calculations involving thick targets. To investigate this effect experimentally, a dedicated irradiation campaign was initiated at the Nuclear Chemistry division (INM-5) of the Institute of Neurosciences and Medicine (INM) accelerator facility at Forschungszentrum Jülich, using the Cyclone 30XP cyclotron facility [73]. The long-term objective of this work is to quantify neutron attenuation within Mo targets and to provide experimental validation of the activity prediction methods used throughout this study.



Figure 5.11: The Cyclone 30XP cyclotron facility at the INM-5, used for radionuclide production and target irradiation [74].

As a first step, a preliminary irradiation experiment was performed using a simplified activation setup. A 15 MeV proton beam incident on a Be target was used as the neutron source. The irradiation was carried out for 23 minutes at a beam current of 3 μA. Neutrons produced in the Be target were moderated within a polyethylene assembly containing activation foils. A circular Au foil with a radius of 0.5 cm and a thickness of 0.0025 cm and circular Mo foil with the same radius and a thickness of 0.1 cm were positioned inside the moderator assembly to assess the activation response of the foils in the moderated neutron spectrum. The purpose of this initial irradiation was to establish a benchmark configuration before extending the setup to multiple Mo foils positioned at different depths inside the moderator.
Figure 5.12 shows the experimental irradiation setup and the corresponding PHITS model used for the activation calculations. The measured foil activities were subsequently compared with simulation results obtained using both the FAM and FFM.



(a) Experimental irradiation setup at the INM-5 accelerator facility.

(b) PHITS model of the experimental setup showing a Y-cut through the geometry.

Figure 5.12: Comparison of the preliminary self-shielding experiment and the corresponding PHITS simulation model. The irradiation setup consisted of a Be neutron-production target, a polyethylene moderator assembly, and embedded Au and Mo activation foils. The simulation geometry was developed to reproduce the experimental configuration as accurately as possible for activation calculations.

Initial calculations employed the default proton-induced reaction models available in PHITS for neutron production in Be. However, significant discrepancies were observed between the measured and simulated activities. Since accurate prediction of the neutron source term is essential for future self-shielding measurements,

additional investigations were performed to identify the origin of these differences. Particular attention was given to the description of the proton interaction in Be, which represents the neutron source in the experiment. Additional simulations were therefore performed using evaluated proton–Be nuclear data derived from experimental measurements. These data provide a more realistic description of neutron production than the default physics model approach at the investigated proton energy.

As shown in Figure 5.13, the use of evaluated nuclear data resulted in substantially improved agreement between simulation and experiment compared with the default physics-model calculations. The largest improvement was observed for the Au activation foil, where both activity prediction methods reproduced the measured activity considerably more accurately when evaluated nuclear data were employed. Similar improvements were observed for the Mo foil, indicating that the description of neutron production in the Be target represented a major contributor to the discrepancies observed in the initial simulations.

The results demonstrate the importance of using experimentally validated reaction data when modeling low-energy accelerator-driven neutron sources. The improved agreement obtained using evaluated data provides increased confidence in the neutron source description and in the activation calculations performed for future experimental investigations.

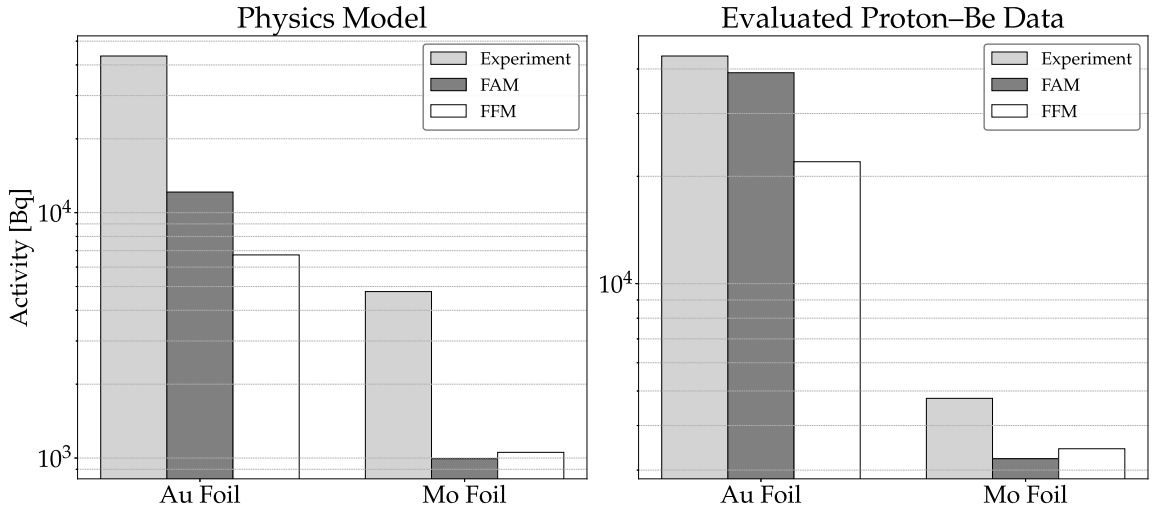


Figure 5.13: Comparison of experimentally measured activation foil activities with activities predicted using the FAM and FFM. The left panel shows results obtained using the default PHITS proton-induced reaction models for neutron production in Be, whereas the right panel shows results obtained using evaluated nuclear data.

The irradiation discussed here represents the first stage of a broader experimen-

tal program aimed at quantifying neutron self-shielding effects in Mo. Future experiments employing multiple Mo foils positioned at different depths within the moderator assembly are planned in order to directly measure neutron attenuation within the target material and provide additional validation of the simulation methodology. Since the experimental campaign is still ongoing, only the preliminary benchmark results are presented here.

5.5 Conclusions and Outlook

This chapter presented a systematic parameter study of accelerator-based ^{99}Mo production via the $^{98}\mathrm{Mo}(n,\gamma)^{99}\mathrm{Mo}$ reaction in an HBS-type target–moderator–reflector (TMR) assembly. Using PHITS simulations with validated neutron transport and activation models, the influence of key design parameters such as moderator and reflector materials and thicknesses, irradiation plate geometry and positioning, and axial plate thickness was quantified in terms of total and specific activity of ^{99}Mo.
The neutron spectra analysis showed that the axial plate consistently experiences the highest neutron flux, particularly in the epithermal neutron energy range relevant for ^{99}Mo production, as a result of the forward direction of neutron emission from the Ta target. Lateral plates sample a softer and less intense neutron field and therefore contribute to lower activities unless placed closer to the target. Moderator studies revealed two distinct regimes: hydrogenous moderators (H_2O, ZrH_2) provide high activities in relatively thin, compact configurations, while D_2O and Be require substantially larger moderator volumes to reach comparable activity levels. Reflector studies demonstrated that increasing reflector thickness reduces neutron leakage and enhances activity up to about 10 cm, beyond which additional gains are modest. Be offers the best performance, followed by MgO and Pb, but its use is disfavored by material degradation, tritium production, and waste management issues.
Taking these performance and engineering constraints into account, a configuration with an H_2O moderator and an MgO reflector was identified as a practical reference system to produce ^{99}Mo at LSA using an accelerator–based neutron source. Within this MgO–H_2O setup, varying the thickness of the axial irradiation plate highlighted the trade-off between total activity and specific activity. Increasing the thickness of this plate initially raises the total activity but eventually leads to a decrease in specific activity due to neutron self-shielding. For the four-plate configuration, an axial plate thickness of about 3 cm was found to offer a good compromise: it provides high total activity while maintaining specific activity levels compatible with LSA generator concepts. Under these conditions and a 6-day irradiation, the simulations indicate a production potential on the order of 2,400 Ci of ^{99}Mo, sufficient to cover Germany's current weekly demand.
The study also explored a single-plate geometry, in which only the axial plate is

present. Although comparable total activities can be achieved by increasing the axial plate thickness beyond approximately 4 cm, the associated self-shielding effects lead to strong activity gradients and increased uncertainty in the activity estimation. Such thick-plate concepts would require dedicated experimental validation and refined self-shielding models before they could be considered viable alternatives to the multiple plate configurations.

In addition to the primary parameter study, several alternative production concepts were evaluated. The use of enriched ^{98}Mo targets demonstrated the potential for substantially increased production yields, although neutron self-shielding effects become increasingly important as target thickness increases. A dissolved sodium molybdate target concept yielded activities and specific activities significantly below those obtained with solid irradiation plates and was therefore not considered a competitive option. Direct proton irradiation of molybdenum produced comparatively high ^{99}Mo activities but was accompanied by the generation of large quantities of additional radionuclides and would require a dedicated high-power target design and cooling system. Composite reflector configurations combining MgO and Pb were also investigated but did not outperform homogeneous MgO reflector systems. These additional studies further support the selection of the MgO–H_2O neutron-capture configuration as the most practical solution within the scope of the present work.

Overall, this parameter study has reduced a broad design space to a small set of technically plausible TMR configurations and identified an MgO–H_2O system with a moderately thick axial plate as a promising baseline for accelerator-driven ^{99}Mo production. A preliminary experimental self-shielding campaign has already been initiated using a proton-driven Be neutron source and activation foil measurements. Initial results demonstrated the importance of accurately describing neutron production through evaluated proton–Be nuclear data and yielded substantially improved agreement between simulation and experiment. Future work should focus on extending these measurements to multiple Mo foils positioned at different moderator depths in order to experimentally quantify neutron attenuation and self-shielding effects. In parallel, further efforts should address improved modeling of self-shielding and resonance absorption in thick Mo plates, as well as the integration of these findings into detailed engineering designs, including generator optimization, plate handling, radiation protection, and long-term operational considerations for HiCANS-type facilities.

6 Conclusion

This thesis investigated neutron activation for the production of ^{99}Mo using accelerator-driven neutron sources and combined neutron-transport simulations with experimental activation benchmarks and gamma-ray spectrometry. The work focused on the influence of target–moderator–reflector (TMR) design parameters on the neutron spectrum and the resulting activation behaviour, with particular emphasis on the role of thermal and epithermal neutrons in the $^{98}\mathrm{Mo}(n,\gamma)^{99}\mathrm{Mo}$ reaction.
The physics background established the theoretical basis linking neutron production, transport, moderation, and activation. Special attention was given to the separation of thermal, epithermal, and fast neutron regions and to the resonance-dominated behaviour of epithermal neutron capture. The role of neutron flux shaping by moderators and reflectors was discussed together with the effects of resonance integrals, cadmium filtering, and neutron self-shielding, which are essential for accurately describing activation in realistic irradiation environments.
A benchmark irradiation setup using an AmBe neutron source was developed to validate the simulation methodology and activation analysis workflow. The experimental activities were reconstructed using gamma-ray spectrometry with HPGe detectors, including corrections for efficiency, decay, and counting geometry. Comparison between measured and simulated activities demonstrated that the coupled neutron-transport and activation methodology provides physically consistent predictions of neutron activation under moderated irradiation conditions.
An additional assessment based on established epithermal shape-factor (α) determination methods was also performed using the benchmark activation data. While the activity predictions showed generally good agreement with the experimental measurements, the resulting α values were strongly dependent on the selected evaluation method and did not provide a consistent basis for validation of the simulated neutron spectrum.
Two complementary activation-analysis approaches were implemented and evaluated. The first approach, referred to as the Flux Analysis Method (FAM), approximated activation using region-integrated neutron fluxes combined with thermal cross sections, resonance integrals, and effective fast-region cross sections. The second approach, referred to as the Flux Folding Method (FFM), used energy-dependent flux spectra and evaluated nuclear data to calculate activation directly through numerical flux folding.
The comparison between both approaches showed that the simplified flux-separated formalism can reproduce the general activation behaviour while requiring signif-

icantly reduced computational effort. However, deviations become more pronounced in cases where strong resonance absorption and spectrum-dependent effects dominate the activation process. In such situations, the multi-group flux-folding approach provides a more detailed representation of the neutron spectrum and resonance behaviour.

The TMR parameter study demonstrated that neutron activation strongly depends on moderator composition, reflector material, irradiation geometry, and target thickness. Hydrogenous moderators produced compact moderation and enhanced thermal neutron fluxes, whereas low-absorption materials preserved neutron economy and maintained stronger epithermal components. Considering both neutronic performance and engineering constraints, an H_2O moderator combined with an MgO reflector was identified as the most practical reference configuration for accelerator-driven ^{99}Mo production, providing a favorable balance between activity yield, engineering feasibility, material availability, and operational considerations.

For the optimized MgO–H_2O configuration, the simulations predicted a production potential of approximately 2400 Ci of ^{99}Mo following a 6-day irradiation period, while maintaining specific activity levels compatible with low-specific-activity generator concepts. The study further demonstrated that increasing target thickness enhances total activity but eventually reduces specific activity due to neutron self-shielding. These results highlight the importance of balancing target mass and neutron utilization when designing activation-based production systems.

Several alternative production concepts were also investigated. Enriched ^{98}Mo targets showed the potential for significantly increased production yields but simultaneously emphasized the growing importance of neutron self-shielding effects in thick targets. Dissolved sodium molybdate targets yielded insufficient activity and specific activity, while direct proton irradiation of molybdenum introduced substantial isotope-production and target-cooling challenges. Composite reflector configurations likewise offered no significant advantage over homogeneous MgO reflector systems. Together, these studies further supported the selection of the MgO–H_2O neutron-capture concept as the most practical solution within the scope of the present work.

To address uncertainties associated with neutron attenuation and self-shielding, a dedicated experimental campaign was initiated at the INM-5 accelerator facility. Preliminary activation measurements performed using a proton-driven Be neutron source demonstrated substantially improved agreement between simulation and experiment when evaluated proton–Be nuclear data were employed instead of default physics models. These results provide increased confidence in the neutron source description and establish a foundation for future experimental investigations of self-shielding effects in Mo.

Overall, this thesis demonstrates that accurate prediction of ^{99}Mo production requires consistent treatment of neutron transport, spectral shaping, resonance ac-

tivation, and activity reconstruction. The combined simulation and experimental approach developed in this work provides a framework for the optimization and validation of accelerator-driven neutron activation systems. Future work should focus on extending the ongoing self-shielding measurements, refining neutron attenuation models for thick Mo targets, and integrating the resulting neutronic data into detailed engineering designs, including generator optimization, target handling, radiation protection, and long-term deployment of HiCANS ^{99}Mo production facilities. Further investigation of the epithermal spectral shape and the observed discrepancies between different α-determination methods may also contribute to improved characterization of the irradiation environment and refinement of future activation models.

7 References

[1] OECD Nuclear Energy Agency. *The Supply of Medical Radioisotopes: 2019 Medical Isotope Demand and Capacity Projection for the 2019–2024 Period*. Paris: OECD Publishing, 2019. DOI: 10.1787/9bffb5f4-en.

[2] American Society of Nuclear Cardiology. *Alert: Significant Mo-99 Shortage Expected in Coming Weeks*. 2025. URL: https://www.asnc.org/news/alert-significant-mo-99-shortage-expected-in-coming-weeks/ (visited on 08/26/2025).

[3] OECD Nuclear Energy Agency. *The Supply of Medical Radioisotopes: 2025 Review*. Tech. rep. OECD-NEA, 2025. URL: https://www.oecd-nea.org/upload/docs/application/pdf/2025-10/7743_medical_radioisotopes_supply_rev.pdf.

[4] T. Brückel and T. Gutberlet, eds. *Opportunities for Research with Neutrons at the Next Generation Facility HBS: Overview of the High Brilliance Neutron Source (HBS) Technical Design Report*. Vol. 9. Schriften des Forschungszentrums Jülich Allgemeines / General. Jülich, Germany: Forschungszentrum Jülich, 2023.

[5] John R. Lamarsh and Anthony J. Baratta. *Introduction to Nuclear Engineering*. 3rd ed. Prentice Hall, 2001.

[6] National Academies of Sciences, Engineering, and Medicine. *Molybdenum-99 for Medical Imaging*. Washington, DC: The National Academies Press, 2016. DOI: 10.17226/23563.

[7] Necsa. *SAFARI-1 Research Reactor*. Accessed: 2026-04-20. 2024. URL: https://www.necsa.co.za/safari-1/.

[8] NRG PALLAS. *High Flux Reactor (HFR) Petten*. Accessed: 2026-04-20. 2024. URL: https://www.nrgpallas.com/high-flux-reactor/.

[9] SCK CEN. *BR2 Research Reactor*. Accessed: 2026-04-20. 2024. URL: https://www.sckcen.be/en/infrastructure/br2-belgian-reactor-2.

[10] ANSTO. *OPAL Reactor Submission*. 2012. URL: https://www.aph.gov.au/parliamentary_business/committees/house_of_representatives_committees?url=pwc/anstonmp/subs/sub01%20-%20ansto%20-%2027%20november%202012.pdf.

[11] MLZ Garching. *FRM II History and Facts*. 2023. URL: https://mlz-garching.de/englisch/about-mlz/facts-und-figures/history.html.

[12] MLZ Garching. *Less Waste from Lower Enriched Uranium Targets*. 2023. URL: https://mlz-garching.de/englisch/news-und-press/news-articles/less-waste-from-lower-enriched-uranium-targets.html.

[13] National Academies of Sciences, Engineering, and Medicine. *Opportunities and Approaches for Supplying Molybdenum-99 and Associated Medical Isotopes to Global Markets: Proceedings of a Symposium*. Washington, DC: The National Academies Press, 2018. ISBN: 978-0-309-46627-1. DOI: 10.17226/24909.

[14] Lexxion. *Research and Economic Activities – PALLAS Reactor Context*. 2023. URL: https://www.lexxion.eu/en/stateaidpost/research-and-economic-activities/.

[15] CEA. *Jules Horowitz Reactor Status Report 2022*. 2022. URL: https://jhrreactor.com/wp-content/uploads/2024/06/Public_JHR_SR_2022.pdf.

[16] Reuters. *South Africa's Nuclear Energy Firm to Tender New Multi-Purpose Research Reactor in 2026*. Accessed: 2026-07-04. Mar. 2026. URL: https://www.reuters.com/business/energy/south-africas-nuclear-energy-firm-tender-new-multi-purpose-research-reactor-2026-03-24/.

[17] IAEA. *RA-10 Multipurpose Research Reactor*. 2023. URL: https://inis.iaea.org/records/yttk9-cbs07.

[18] Juris Meija et al. "Isotopic compositions of the elements 2013 (IUPAC Technical Report)". In: *Pure and Applied Chemistry* 88.3 (2016), pp. 293–306. DOI: 10.1515/pac-2015-0503.

[19] K. Shibata et al. "JENDL-4.0: A new library for nuclear science and engineering". In: *Journal of Nuclear Science and Technology* 48.1 (2011), pp. 1–30. DOI: 10.1080/18811248.2011.9711675.

[20] OECD Nuclear Energy Agency. *JANIS Web Nuclear Data Browser*. Online nuclear data retrieval and visualization tool, accessed 2025-08-26. 2025. URL: https://www.oecd-nea.org/janisweb/.

[21] M. F. Nawar, N. M. Farag, and H. F. Aly. "New strategies for a sustainable ^{99m}Tc supply to meet increasing medical demands: Promising solutions for current problems". In: *Frontiers in Chemistry* 10 (2022), p. 926258. DOI: 10.3389/fchem.2022.926258.

[22] A. J. Koning et al. "TENDL: Complete Nuclear Data Library for Innovative Nuclear Science and Technology". In: *Nuclear Data Sheets* 155 (2019), pp. 1–55. DOI: 10.1016/j.nds.2019.01.002.

[23] National Nuclear Data Center. *ENDF/B-VIII.1 Nuclear Data Library*. Accessed: 2025-08-26. 2024. URL: https://www.nndc.bnl.gov/endf-releases/?version=B-VIII.1/.

[24] M. Blaauw et al. “Estimation of ^{99}Mo production rates from natural molybdenum in research reactors”. In: *Journal of Radioanalytical and Nuclear Chemistry* 310.3 (2016), pp. 1297–1306. DOI: 10.1007/s10967-016-5036-6.

[25] Glenn F. Knoll. *Radiation Detection and Measurement*. 4th ed. Hoboken, NJ: John Wiley & Sons, 2010. ISBN: 9780470131480.

[26] *ISO 8529-1: Neutron Reference Radiations – Part 1: Characteristics and Methods of Production*. International Organization for Standardization. Geneva, Switzerland, 2021.

[27] J. M. Carpenter. “Pulsed Spallation Neutron Sources for Slow Neutron Scattering”. In: *Nuclear Instruments and Methods in Physics Research Section A* 235.1 (1985), pp. 1–18. DOI: 10.1016/0029-554X(77)90560-2.

[28] Kenneth S. Krane. *Introductory Nuclear Physics*. John Wiley & Sons, 1988. ISBN: 0-471-85914-1.

[29] T. Sato et al. “Recent improvements of the Particle and Heavy Ion Transport code System – PHITS version 3.33”. In: *Journal of Nuclear Science and Technology* 61 (2024), pp. 127–135. DOI: 10.1080/00223131.2023.2275736.

[30] MPI Forum. *MPI: A Message-Passing Interface Standard Version 4.0*. Accessed: 2026-04-02. 2021. URL: https://www.mpi-forum.org/docs/mpi-4.0/mpi40-report.pdf.

[31] William Gropp, Ewing Lusk, and Anthony Skjellum. *Using MPI: Portable Parallel Programming with the Message Passing Interface*. MIT Press, 1999.

[32] OpenMP Architecture Review Board. *OpenMP Application Programming Interface Specification Version 5.2*. Accessed: 2026-04-02. 2021. URL: https://www.openmp.org/specifications/.

[33] Barbara Chapman, Gabriele Jost, and Ruud van der Pas. *Using OpenMP: Portable Shared Memory Parallel Programming*. MIT Press, 2008.

[34] H. N. Ratliff et al. “Modernization of the DCHAIN-PHITS activation code with improved decay and cross-section data handling”. In: *Nuclear Instruments and Methods in Physics Research Section B: Beam Interactions with Materials and Atoms* 484 (2020), pp. 29–36. DOI: 10.1016/j.nimb.2020.10.005.

[35] T. Sato et al. *PHITS User’s Manual, Version 3.22*. Tech. rep. Japan Atomic Energy Agency (JAEA), 2023. URL: https://phits.jaea.go.jp.

[36] Harry Bateman. “The Solution of a System of Differential Equations Occurring in the Theory of Radioactive Transformations”. In: *Proceedings of the Cambridge Philosophical Society* 15 (1910), pp. 423–427.

[37] K. Shibata et al. *JENDL Activation Cross Section File 2017 (JENDL/AD-2017)*. Tech. rep. Japan Atomic Energy Agency (JAEA), 2017. URL: https://wwwndc.jaea.go.jp/ftpnd/jendl/jendl-ad-2017.html.

[38] D. A. Brown et al. “ENDF/B-VIII.0: The 8th major release of the nuclear reaction data library with CIELO-project cross sections, new standards and thermal scattering data”. In: *Nuclear Data Sheets* 148 (2018), pp. 1–142. DOI: 10.1016/j.nds.2018.02.001.

[39] A. J. M. Plompen et al. “The Joint Evaluated Fission and Fusion Nuclear Data Library, JEFF-3.3”. In: *European Physical Journal A* 56.7 (2020), p. 181. DOI: 10.1140/epja/s10050-020-00141-9.

[40] International Atomic Energy Agency. *FENDL-3.0: Fusion Evaluated Nuclear Data Library*. Tech. rep. Vienna, Austria: International Atomic Energy Agency, 2017. URL: https://www-nds.iaea.org/fendl30/.

[41] J. Katakura. *JENDL Decay Data File 2015 (JENDL/DDF-2015)*. Tech. rep. Japan Atomic Energy Agency, 2015. URL: https://wwwndc.jaea.go.jp/ftpnd/jendl/jendl-ddf-2015.html.

[42] Canberra Industries, Inc. *Genie 2000 Spectroscopy System: Operations Manual*. Version 3.4. Canberra Industries, Inc. 800 Research Parkway, Meriden, CT 06450, 2013. URL: https://www.mirion.com.

[43] National Nuclear Data Center. *NuDat 3.0 Nuclear Structure and Decay Data Database*. 2020. URL: https://www.nndc.bnl.gov/nudat3/.

[44] S. I. Kafala. “Simple method for true coincidence summing correction”. In: *Journal of Radioanalytical and Nuclear Chemistry* 191.1 (1995), pp. 105–114. DOI: 10.1007/BF02035990.

[45] H. Yücel and M. Karadağ. “Experimental determination of the shape factor α in the $1/E^{1+\alpha}$ epithermal neutron source spectrum by dual monitor method”. In: *Annals of Nuclear ENergy* 31.6 (2004), pp. 681–695. DOI: 10.1016/j.anucene.2003.10.002.

[46] D. Shabani, S. T. Rangaiah, C. Langer, et al. “Benchmarking of the PHITS simulation code using neutron activation experiments for reliable calculations of neutron fields”. In: *Journal of Radioanalytical and Nuclear Chemistry* 334 (2025), pp. 2981–2989. DOI: 10.1007/s10967-025-10020-6.

[47] Van Hung Tran. “Modified method of α determination in the $1/E^{1+\alpha}$ epithermal neutron spectrum of a reactor”. In: *Journal of Radioanalytical and Nuclear Chemistry* 285.2 (2010), pp. 331–336. DOI: 10.1007/s10967-010-0549-x.

[48] Van Hung Tran. “Determination of a factor of epithermal neutron flux in Dalat reactor, Vietnam, based on neutron spectrum calculated using MCNP code”. In: *Journal of Radioanalytical and Nuclear Chemistry* 283.2 (2010), pp. 707–711. DOI: 10.1007/s10967-010-0457-0.

[49] E. Martinho, I. F. Goncalves, and J. Salgado. “Universal curve of epithermal neutron resonance self-shielding factors in foils, wires and spheres”. In: *Applied Radiation and Isotopes* 58 (2003), pp. 371–375. DOI: 10.1016/S0969-8043(02)00313-5.

[50] I. F. Goncalves, E. Martinho, and J. Salgado. “Extension to cylindrical samples of the universal curve of resonance neutron self-shielding factors”. In: *Nuclear Instruments and Methods in Physics Research B* 213 (2004), pp. 186–188. DOI: 10.1016/S0168-583X(03)01550-7.

[51] E. Martinho, J. Salgado, and I. F. Gonçalves. “Universal Curve of the Thermal Neutron Self-Shielding Factor in Foils, Wires, Spheres and Cylinders”. In: *Journal of Radioanalytical and Nuclear Chemistry* 261.3 (2004), pp. 637–643. DOI: 10.1023/B:JRNC.0000037107.17274.16.

[52] Pham Ngoc Son and Bach Nhu Nguyen. “Monte Carlo Simulation of Correction Factors for Neutron Self-Shielding in Neutron Activation Analysis”. In: *Advanced Technologies and Applications of Neutron Activation Analysis*. Ed. by Lylia Alghem Hamidatou. London: IntechOpen, 2018. Chap. 3. DOI: 10.5772/intechopen.76984. URL: https://www.intechopen.com/chapters/61260.

[53] S. T. Rangaiah. “Studying neutron capture reactions in the activation experiments using an Am-Be neutron source”. Master’s Thesis. Aachen, Germany: Aachen University of Applied Sciences, 2022.

[54] N. Taboun. “Neutron flux characterisation of an Am-Be source using flux monitors and Monte-Carlo simulations”. Master’s Thesis. Aachen, Germany: Aachen University of Applied Sciences, 2025.

[55] k_0 International Scientific Committee. *k_0 Nuclear Data for Neutron Activation Analysis*. Accessed via the k_0-NAA Nuclear Data Subcommittee. 2020. URL: https://www.kayzero.com/k0naa/k0naaorg/Nuclear_Data_SC/Nuclear_Data_SC.html (visited on 01/09/2026).

[56] Frans De Corte. “The k_0-Standardization Method: A Move to the Optimization of Neutron Activation Analysis”. Habilitation Thesis. Ghent, Belgium: Ghent University, 1987.

[57] *Neutron Reference Radiations for Calibrating Neutron-Measuring Devices Used for Radiation Protection Purposes – Part 1: Characteristics and Methods of Production*. ISO 8529-1. Geneva, 1989.

[58] R. J. McConn et al. *Compendium of Material Composition Data for Radiation Transport Modeling*. Tech. rep. PNNL-15870. Available online. Richland, WA: Pacific Northwest National Laboratory, 2011. URL: https://www.pnnl.gov/main/publications/external/technical_reports/pnnl-15870.pdf.

[59] F. De Corte et al. “Instantaneous α-Determination without Cd-Cover in the $1/E^{1+\alpha}$ Epithermal Neutron Spectrum”. In: *Journal of Radioanalytical Chemistry* 52.2 (1979), pp. 295–304. DOI: 10.1007/BF02521280.

[60] Haluk Yücel et al. “Characterization of Neutron Flux Spectra in the Irradiation Sites of a 37 GBq ^{241}Am–Be Isotopic Source”. In: *Nuclear Instruments and Methods in Physics Research Section B: Beam Interactions with Materials and Atoms* 338 (2014), pp. 139–144. ISSN: 0168-583X. DOI: 10.1016/j.nimb.2014.08.010.

[61] Ho Manh Dung and Seung Yeon Cho. “A Simple Method for α Determination”. In: *Journal of Radioanalytical and Nuclear Chemistry* 257.3 (Sept. 2003), pp. 573–575. DOI: 10.1023/A:1025444732641.

[62] P. Vermaercke et al. “Neutron Spectrum Calibration Using the Cd-Ratio for Multi-Monitor Method with a Synthetic Multi-Element Standard”. In: *Journal of Radioanalytical and Nuclear Chemistry* 278.3 (2008), pp. 631–636. DOI: 10.1007/s10967-008-1206-5.

[63] K. H. Beckurts and K. Wirtz. *Neutron Physics*. Translated by L. Dresner, Oak Ridge National Laboratory. Berlin, Germany: Springer, 1964.

[64] OECD Nuclear Energy Agency. *Accelerator-Driven Systems (ADS) and Fast Reactors (FR) in Advanced Nuclear Fuel Cycles*. Tech. rep. NEA No. 3109. Paris, France: Organisation for Economic Co-operation and Development, Nuclear Energy Agency (OECD/NEA), 2002. URL: https://www.oecd-nea.org/ndd/reports/2002/nea3109-ads.pdf.

[65] H. Filges and F. Goldenbaum. *Handbook of Spallation Research: Theory, Experiments and Applications*. ISBN: 978-3527406780. Wiley-VCH, 2009.

[66] Stephen Peggs et al. *ESS Technical Design Report*. Tech. rep. Lund, Sweden: European Spallation Source ESS AB, 2013. URL: https://inspirehep.net/literature/1704813.

[67] Qi Ding et al. “An Optimized Microchannel Ta Target for High-Current Accelerator-Driven Neutron Sources”. In: *Nuclear Instruments and Methods in Physics Research Section A: Accelerators, Spectrometers, Detectors and Associated Equipment* 1045 (2023), p. 167508. ISSN: 0168-9002. DOI: 10.1016/j.nima.2022.167508.

[68] J. Baggemann et al. “High Power Target for the High Brilliance Neutron Source”. In: *Nuclear Instruments and Methods in Physics Research Section A: Accelerators, Spectrometers, Detectors and Associated Equipment* 1069 (2024), p. 169912. ISSN: 0168-9002. DOI: 10.1016/j.nima.2024.169912.

[69] V. Chakin et al. “Pores and Cracks in Highly Neutron Irradiated Beryllium”. In: *Journal of Nuclear Materials* 416.1–2 (2011), pp. 3–8. ISSN: 0022-3115. DOI: 10.1016/j.jnucmat.2010.11.098.

[70] D. S. Gelles and H. L. Heinisch. “Neutron Damage in Beryllium”. In: *Journal of Nuclear Materials* 191–194 (1992), pp. 194–198. ISSN: 0022-3115. DOI: 10.1016/S0022-3115(09)80032-9.

[71] M. R. Gilbert and J.-C. Sublet. “Neutron-induced transmutation effects in beryllium”. In: *Nuclear Fusion* 51 (2011), p. 043005. DOI: 10.1088/0029-5515/51/4/043005.

[72] M. Michel, F. Sudbrock, B. Neumaier, et al. “Comparison of standard and modified ^{99}Mo/^{99m}Tc radionuclide generators”. In: *Journal of Radioanalytical and Nuclear Chemistry* 334 (2025), pp. 7255–7263. DOI: 10.1007/s10967-025-10423-5.

[73] Bernd Neumaier and Syed M. Qaim. “Radiochemical Methods in Production of Radionuclides at a Cyclotron”. In: *Journal of Radioanalytical and Nuclear Chemistry* 334 (2025), pp. 9157–9165. DOI: 10.1007/s10967-025-10478-4.

[74] Forschungszentrum Jülich, Institute of Nuclear Medicine (INM-5). *Institute of Nuclear Medicine (INM-5): Scientific Service – Nuclide Production and Targetry*. 2025. URL: https://www.fz-juelich.de/en/inm/inm-5/scientific-service (visited on 06/29/2026).

[75] P. Mastinu et al. “Micro-channel–based high specific power lithium target”. In: *Il Nuovo Cimento C* 38.5 (2015), p. 193. DOI: 10.1393/ncc/i2015-15193-y.

[76] J. Salgado, E. Martinho, and I. F. Gonçalves. “The Calculation of Neutron Self-Shielding Factors of a Group of Isolated Resonances”. In: *Journal of Radioanalytical and Nuclear Chemistry* 260.2 (2004), pp. 317–320. DOI: 10.1023/B:JRNC.0000027103.05680.98.

[77] Forschungszentrum Jülich. *Neutron Scattering: Lecture Notes*. Tech. rep. Accessed: 2025-08-26. Jülich, Germany: Forschungszentrum Jülich GmbH, 2018. URL: https://juser.fz-juelich.de/record/909557.

[78] T. Brückel and T. Gutberlet, eds. *High Brilliance Neutron Source (HBS): Accelerator Design*. Schriften des Forschungszentrums Jülich Allgemeines / General. Technical Design Report booklet. Jülich, Germany: Forschungszentrum Jülich, 2023.

[79] S. Pomme et al. “General activation and decay formulas and their application in neutron activation analysis with k_0 standardisation”. In: *Analytical Chemistry* 68.23 (1996), pp. 4326–4334. DOI: 10.1021/ac9606540.

[80] D. Arnold. *Fundamentals of Gamma Spectrometry*. Procedures Manual for Monitoring of Radioactive Substances in the Environment. Version March 2018. Federal Ministry for the Environment, Nature Conservation and Nuclear Safety (BMU), 2018. URL: https://www.bundesumweltministerium.de/fileadmin/Daten_BMU/Download_PDF/Strahlenschutz/Messanleitungen_2022/gamma_spekt_grundl_v2018-03_en_bf.pdf.

[81] F. De Corte, A. Simonits, and J. Hoste. “The Accuracy and Precision of Experimental α-Determination in the $1/E^{1+\alpha}$ Epithermal Reactor Neutron Spectrum”. In: *Journal of Radioanalytical Chemistry* 67.1 (1981), pp. 51–67.

8 Teilpublikationen

- D. Shabani et al. (2025). “Benchmarking of the PHITS simulation code using neutron activation experiments for reliable calculations of neutron fields”. *J. Radioanal. Nucl. Chem.* DOI: 10.1007/s10967-025-10020-6
- D. Shabani et al. (2026). “Investigating the production of ^{99m}Tc via the ^{98}Mo(n,γ)^{99}Mo reaction at a high-current accelerator-based neutron source”. *Eur. Phys. J. Plus*. DOI: 10.1140/epjp/s13360-026-07931-y
- D. Shabani et al. (2025). “Mo-99 Production via Neutron Capture using a High-Current Accelerator-based Neutron Source”. *Proceedings of the 2025 International Conference on Accelerator Applications (AccApp’25)*, Washington, DC, November 9–12, 2025, pp. 10–12.

9 Declaration on the use of AI-based and language-support tools

I hereby declare that I used AI-based and language-support tools during the preparation of this dissertation. In particular, I used KI:Connect.NRW (`https://chat.kiconnect.nrw/app`), ChatGPT, and DeepL for support in scientific writing, language editing, translation, grammar and style improvement, and the improvement of clarity and readability of selected passages.

The use of these tools was limited to assistance with language, formulation, text revision, and general writing support. The scientific content, research questions, methodological decisions, data collection, data analysis, interpretation of results, conclusions, and final arguments of this dissertation are my own responsibility. All AI- or software-assisted suggestions were critically reviewed, checked, revised, and approved by me before inclusion in the dissertation.

No AI-based tool was used as an author, co-author, or independent source of scientific evidence. Where factual, methodological, or theoretical claims are made in the dissertation, these are based on the cited scientific literature, the conducted analyses, or the research work underlying this dissertation. I take full responsibility for the accuracy, integrity, and originality of the submitted work.

A Uncertainty Propagation

A.1 Uncertainty Propagation for Experimental Activities

A.1.1 Gaussian propagation of uncertainty

All experimentally determined quantities carry uncertainties arising from counting statistics and systematic effects such as detector efficiency, evaluated decay data, and timing parameters. To propagate these uncertainties through the activity calculation, the Gaussian law of propagation of uncertainty was applied, following [53, 54].
For a quantity $u = u(x_1, x_2, \ldots, x_n)$ with independent input variables x_i, the combined variance is

$$\sigma_u^2 = \sum_{i=1}^{n} \left(\frac{\partial u}{\partial x_i} \right)^2 \sigma_{x_i}^2 \tag{A.1}$$

A.1.2 Uncertainties of individual input quantities

A.1.2.1 Net peak counts

The net peak counts N_p were determined from the fitted full-energy peak areas using GENIE 2000. The associated uncertainty ΔN_p was taken directly from the peak analysis output of the software.
The reported uncertainty accounts for the statistical uncertainty of the measured counts as well as the uncertainty associated with background subtraction and peak fitting. Therefore, the uncertainties reported by GENIE 2000 were used directly in the subsequent uncertainty propagation calculations.

A.1.2.2 Decay constant

The decay constant is defined as $\lambda = \ln(2)/t_{1/2}$, with $t_{1/2}$ being the half-life. Propagating the uncertainty in the half-life yields

$$\Delta\lambda = \frac{\ln(2)}{t_{1/2}^2} \Delta t_{1/2} \tag{A.2}$$

A.1.3 Activity from gamma spectrometry

A.1.3.1 Uncertainty of activity

Assuming independent input variables, the combined variance of A_{EOI} is computed from Eq. 3.3 with

$$A_{\mathrm{EOI}} = A_{\mathrm{EOI}}(N_p, \varepsilon_\gamma, I_{E_\gamma}, \lambda, t_m, t_d)$$

For compact reporting, the relative uncertainty can be written as

$$\left(\frac{\Delta A_{\mathrm{EOI}}}{A_{\mathrm{EOI}}}\right)^2 = \left(\frac{\Delta N_p}{N_p}\right)^2 + \left(\frac{\Delta \varepsilon_\gamma}{\varepsilon_\gamma}\right)^2 + \left(\frac{\Delta I_{E_\gamma}}{I_{E_\gamma}}\right)^2 + \left(\frac{\Delta f}{f}\right)^2 \tag{A.3}$$

where

$$f(\lambda, t_m, t_d) = \frac{\lambda}{1 - e^{-\lambda t_m}}\, e^{\lambda t_d} \tag{A.4}$$

The contribution Δf is obtained using Gaussian propagation applied to (λ, t_m, t_d). The dominant experimental contributions arise from detector efficiency calibration, counting statistics, and γ-ray emission probabilities. Depending on the radionuclide and counting statistics, the combined relative uncertainty of experimentally determined activities ranged from a few percent to approximately 10%.

A.1.4 Uncertainty propagation for Molybdenum-99

For the 140.5 keV peak of ^{99}Mo, the uncertainty was propagated directly to the final end-of-irradiation activity. This avoids performing a separate uncertainty propagation for the mixed parent–daughter specific count rate and then applying a second uncertainty term for the same parent–daughter correction factor.
For convenience, define

$$D_\lambda = \lambda_2 - \lambda_1 \tag{A.5}$$

$$B = \frac{\lambda_2 K_1 - \lambda_1 K_2}{D_\lambda} \tag{A.6}$$

$$G = \frac{\gamma_1}{\gamma_2 F_{12}} \tag{A.7}$$

so that Eq. (3.9) can be written as

$$A_{sp}(^{99}\mathrm{Mo} + {}^{99\mathrm{m}}\mathrm{Tc}) = \frac{N_p}{t_m w}\,(B + G K_1) \tag{A.8}$$

The parent-only contribution is

$$A_{sp}(^{99}\mathrm{Mo}) = G A_{sp}(^{99}\mathrm{Mo} + {}^{99\mathrm{m}}\mathrm{Tc}) \tag{A.9}$$

Substituting Eq. (A.8) into Eq. (3.12) gives

$$A_{\mathrm{EOI}}(^{99}\mathrm{Mo}) = \frac{N_p}{t_m \varepsilon_{140}} H \tag{A.10}$$

where

$$H = \frac{B + GK_1}{\gamma_2 F_{12}} \tag{A.11}$$

In this form, the sample mass w has cancelled because A_{sp} is defined per unit mass and the final activity is obtained by multiplying by w. Therefore, w is not included as an independent uncertainty contribution for the final ^{99}Mo activity.
The combined relative uncertainty of the final activity is

$$\left(\frac{\Delta A_{\mathrm{EOI}}}{A_{\mathrm{EOI}}}\right)^2 = \left(\frac{\Delta N_p}{N_p}\right)^2 + \left(\frac{\Delta t_m}{t_m}\right)^2 + \left(\frac{\Delta \varepsilon_{140}}{\varepsilon_{140}}\right)^2 + \left(\frac{\Delta H}{H}\right)^2. \tag{A.12}$$

The uncertainty in H is obtained by Gaussian propagation:

$$(\Delta H)^2 = \sum_j \left(\frac{\partial H}{\partial y_j} \Delta y_j\right)^2, \tag{A.13}$$

with

$$y_j = \{\lambda_1, \lambda_2, K_1, K_2, \gamma_1, \gamma_2, F_{12}\}. \tag{A.14}$$

Thus, the uncertainty associated with the parent–daughter correction is included only once, through the final quantity H, rather than by first propagating the mixed specific count rate and then adding an additional independent $\Delta G/G$ term.
If the uncertainties of K_1 and K_2 are calculated explicitly from their components S_i, D_i, and C_i, then those underlying quantities should not be counted again as independent uncertainty contributions.

A.2 Propagation to simulated activity

For a simulated activity A_{sim} scaling as

$$A_{\mathrm{sim}} \propto Y \cdot N_{\mathrm{target}}$$

the combined relative uncertainty is

$$\left(\frac{\Delta A_{\mathrm{sim}}}{A_{\mathrm{sim}}}\right)^2 = \left(\frac{\Delta Y}{Y}\right)^2 + \left(\frac{\Delta N_{\mathrm{target}}}{N_{\mathrm{target}}}\right)^2 + (\Delta_{\mathrm{MC}})^2 \tag{A.15}$$

Here, Y denotes the neutron source emission rate, which provides the absolute normalization of the simulated neutron flux. N_{target} is the number of target nuclei in the irradiated sample, determined from sample mass, molar mass, and isotopic abundance.
Δ_{MC} represents the relative statistical uncertainty reported by the Monte Carlo simulation for the relevant quantity. This statistical uncertainty propagates directly to the calculated activation.
Using $\Delta Y/Y = 10\%$, $\Delta N_{\text{target}}/N_{\text{target}} = 1\%$, and $\Delta_{\text{MC}} \approx 5\%$, the resulting combined relative uncertainty is approximately 11%.
Thus, an uncertainty of approximately 11% was assigned to the simulated activities. This uncertainty includes source normalization, target-atom normalization, and Monte Carlo statistical uncertainty. No additional cross-section or nuclear-data uncertainty was assigned separately. The reported simulated activities are conditional on the nuclear data libraries used in the PHITS and DCHAIN calculations.

B Experimental Counts and Activity Results

This appendix summarises the experimentally measured net peak counts, the corresponding activities at end of irradiation (EOI), and the simulated activities obtained using the flux analysis method (FAM) and the flux folding method (FFM).

Table B.1: Net peak counts and activities for bare foil irradiations. Foils labelled "–1" correspond to the initial Au–In foil set, while unlabeled foils correspond to the extended multi-monitor foil set.

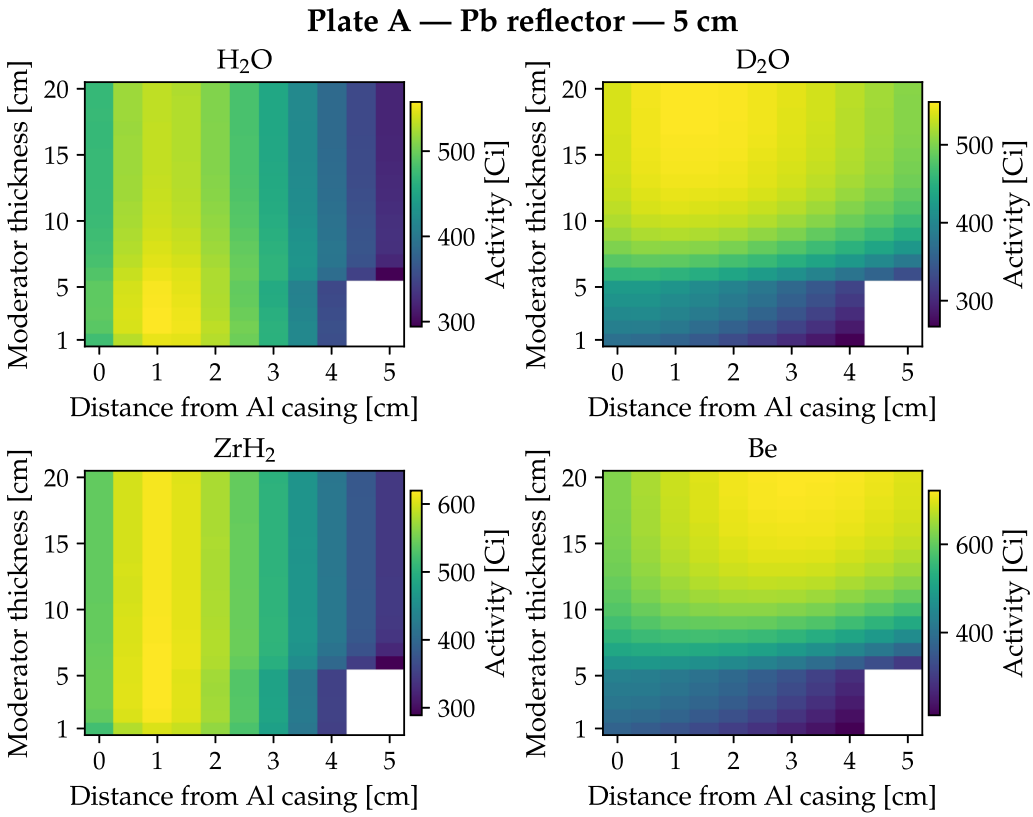
Foil	**γ-line [keV]**	**Net counts**	**Experimental Activity [Bq]**	**FAM Activity [Bq]**	**FFM Activity [Bq]**
Au – 1	411.8	29887 ± 173	237.8 ± 23.8	275.0 ± 30.3	207.0 ± 22.8
In – 1	416.9	12744 ± 113	212.5 ± 21.3	238.0 ± 26.2	196.0 ± 21.6
Au	411.8	2783 ± 53	38.9 ± 4.0	49.8 ± 5.5	41.0 ± 4.5
In	416.9	189 ± 14	473.3 ± 58.8	443.9 ± 48.8	396.1 ± 43.6
Mo	140.5	4408 ± 66	2.51 ± 0.25	2.73 ± 0.30	2.72 ± 0.30
W	479.5	2255 ± 48	142.6 ± 14.6	192.8 ± 21.2	120.0 ± 13.2
Mn	847.0	2081 ± 46	213.2 ± 23.4	191.6 ± 21.1	198.5 ± 21.8

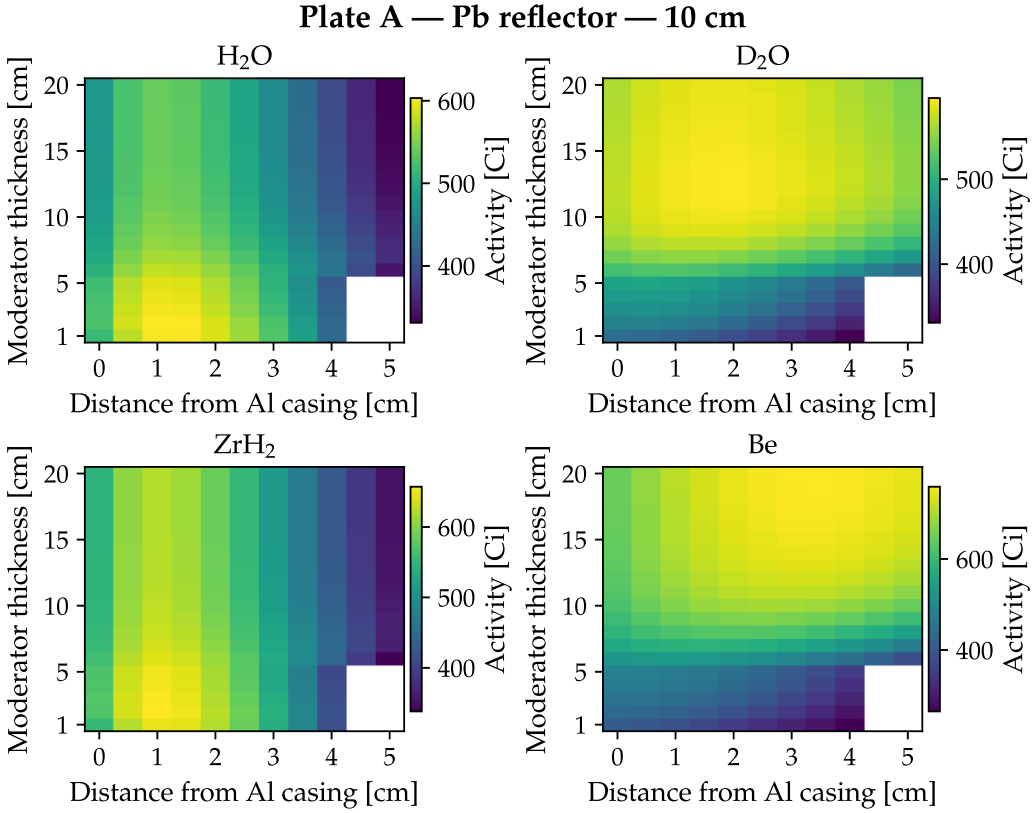
Table B.2: Net peak counts and activities for Cd-covered foil irradiations. Foils labelled "–1" correspond to the initial Au–In foil set, while unlabeled foils correspond to the extended multi-monitor foil set.

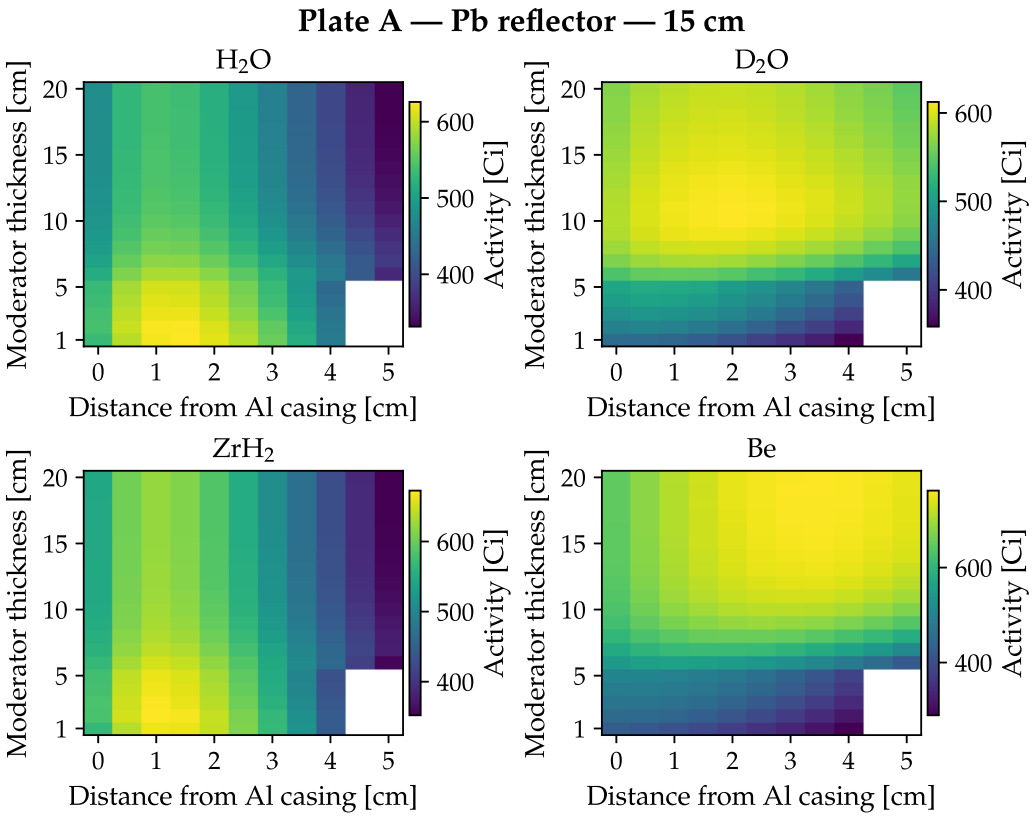
Foil	**γ-line [keV]**	**Net counts**	**Experimental Activity [Bq]**	**FAM Activity [Bq]**	**FFM Activity [Bq]**
Au – 1	411.8	9929 ± 100	108.9 ± 10.9	163.0 ± 17.9	78.6 ± 8.6
In – 1	416.9	2928 ± 54	49.5 ± 5.0	84.9 ± 9.3	43.7 ± 4.8
Au	411.8	533 ± 23	14.8 ± 1.5	28.3 ± 3.1	11.1 ± 1.2
In	416.9	237 ± 15	245.5 ± 24.6	396.3 ± 43.6	207.4 ± 22.8
Mo	140.5	3219 ± 57	1.98 ± 0.20	1.79 ± 0.20	1.96 ± 0.22
W	479.5	2090 ± 46	56.8 ± 5.7	126.9 ± 14.0	37.3 ± 4.1
Mn	847.0	92 ± 10	6.7 ± 1.0	8.8 ± 1.0	7.3 ± 0.8

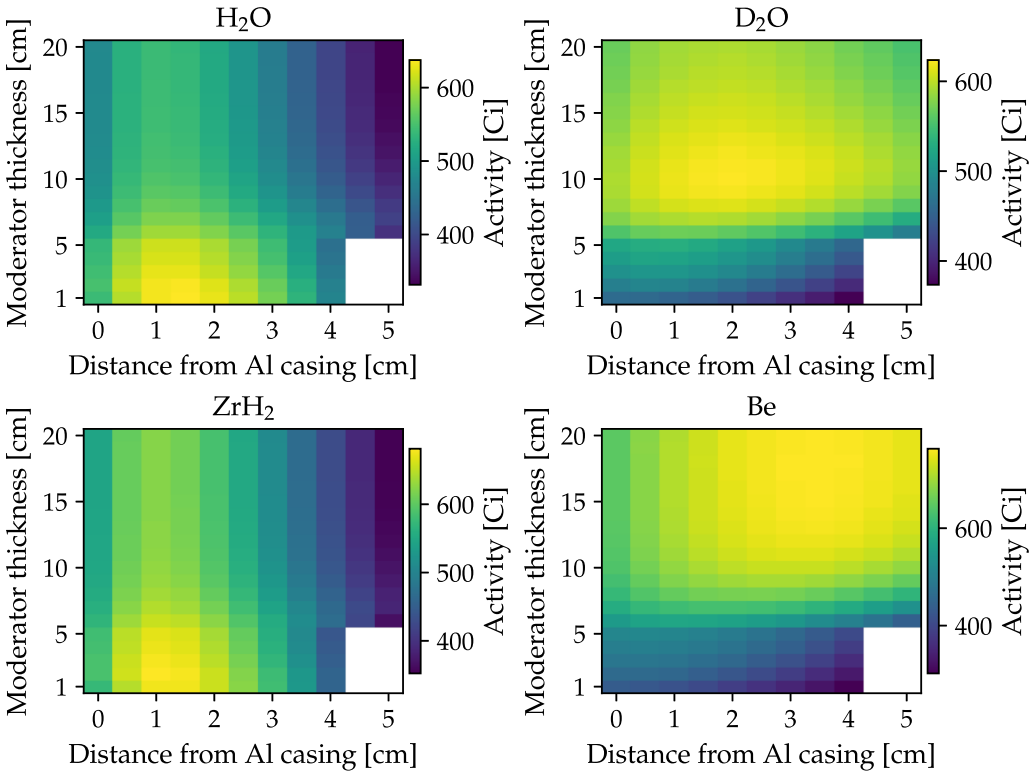
C Activity Distribution Maps for the TMR Parameter Study

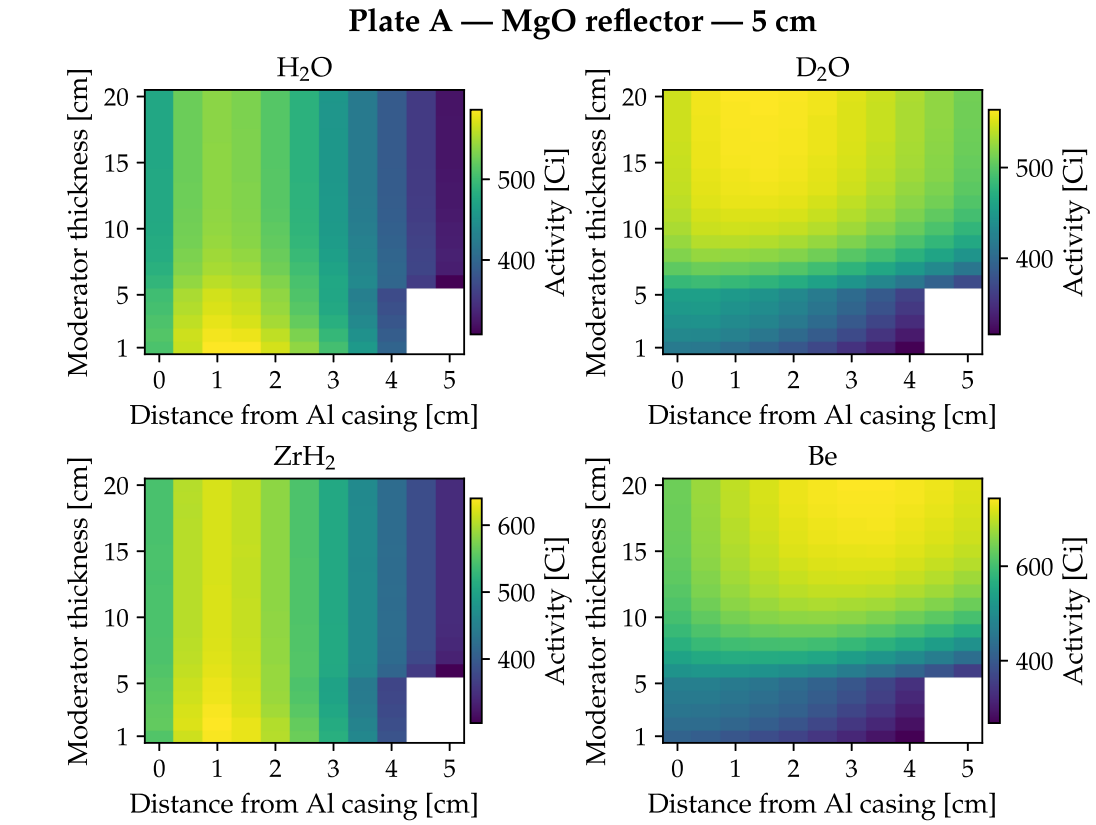
This appendix provides the complete set of two-dimensional ^{99}Mo activity distribution maps obtained in the TMR parameter study. The maps visualise the calculated end-of-irradiation (EOI) ^{99}Mo activity for each investigated configuration as a function of two geometric parameters: the plate distance from the Al casing and the moderator thickness. For each irradiation plate (A–D), results are shown for all investigated moderator materials and for the three reflector candidates (Pb, MgO, Be) with reflector thicknesses of 5, 10, 15, and 20 cm. All activities correspond to the reference irradiation scenario used throughout the parameter scan, i.e. continuous irradiation for 6 days (144 h) with an average proton beam current of 12 mA. In each map, the colour scale represents the calculated ^{99}Mo activity (in Ci) for the corresponding plate under these reference conditions. These maps provide the full parameter scan dataset underlying the representative plots presented in Chapter 5 and allow identification of the highest activity configurations for each plate and material combination.

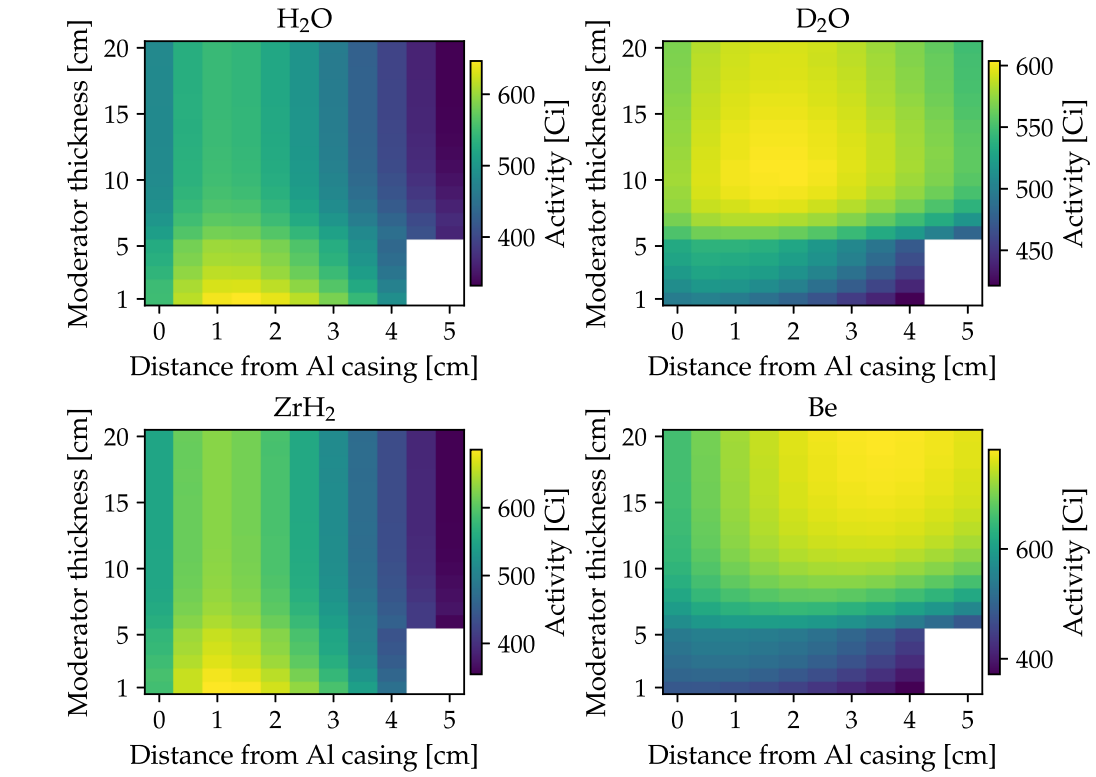

Plate A — Pb reflector — 5 cm
H2O
D2O
ZrH2
Be
Moderator thickness [cm]
Distance from Al casing [cm]
Activity [Ci]

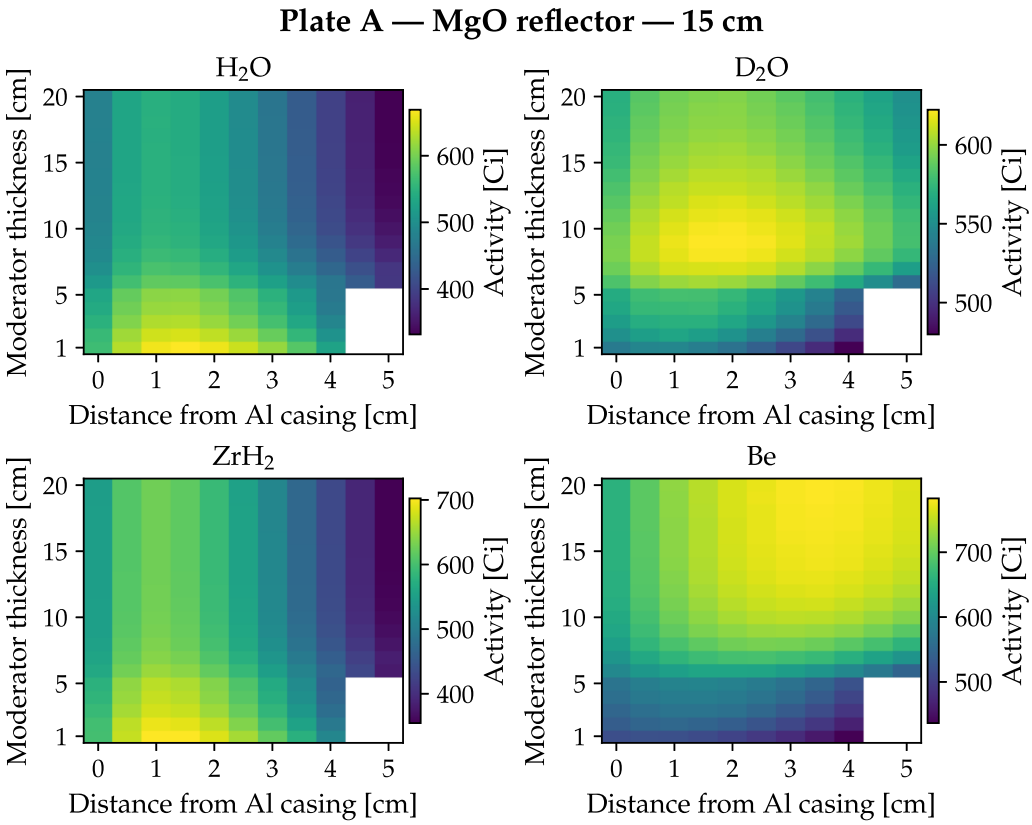

Plate A — Pb reflector — 10 cm
H2O
D2O
ZrH2
Be
Moderator thickness [cm]
Distance from Al casing [cm]
Activity [Ci]

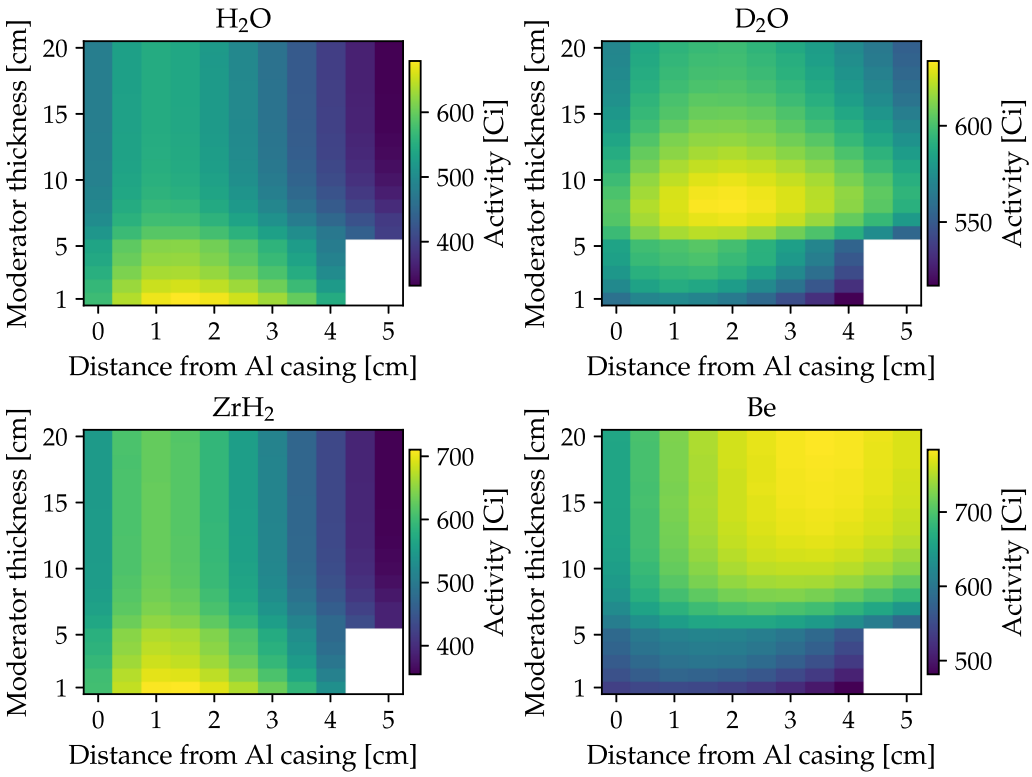

Plate A — Pb reflector — 15 cm
H2O
D2O
ZrH2
Be
Moderator thickness [cm]
Distance from Al casing [cm]
Activity [Ci]
1
5
10
15
20
0
1
2
3
4
5
400
500
600

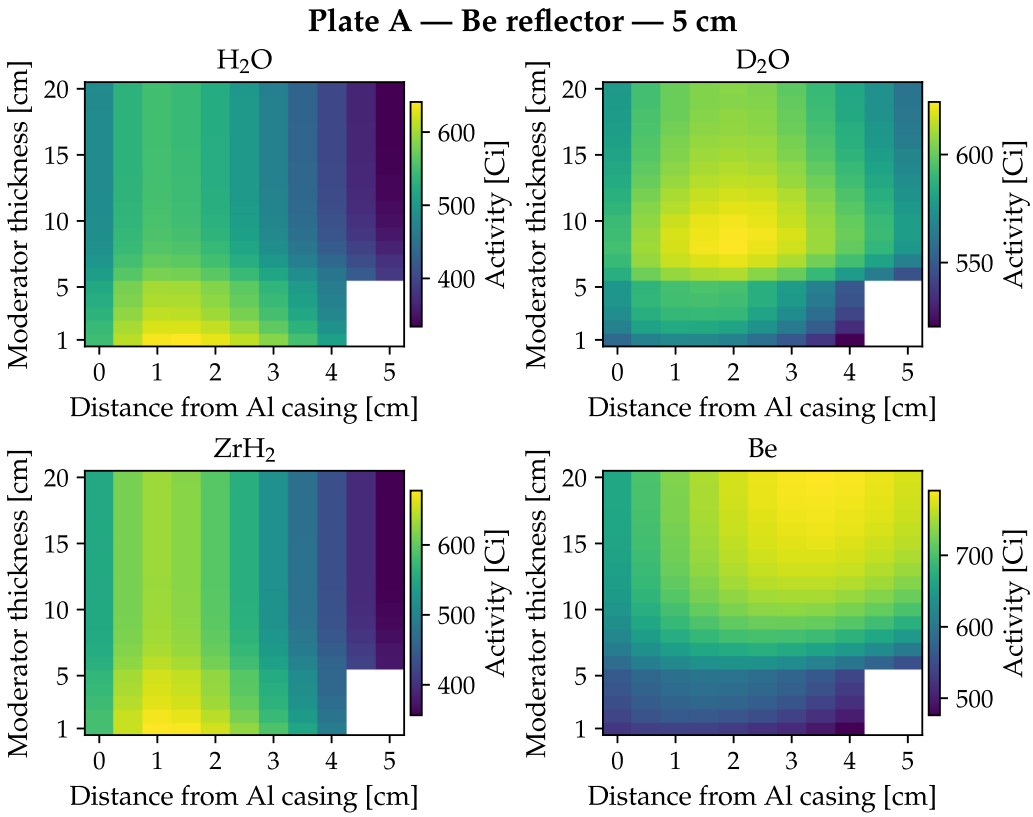

Plate A — Pb reflector — 20 cm
H2O
D2O
ZrH2
Be
Moderator thickness [cm]
Distance from Al casing [cm]
Activity [Ci]
1
5
10
15
20
0
1
2
3
4
5
400
500
600

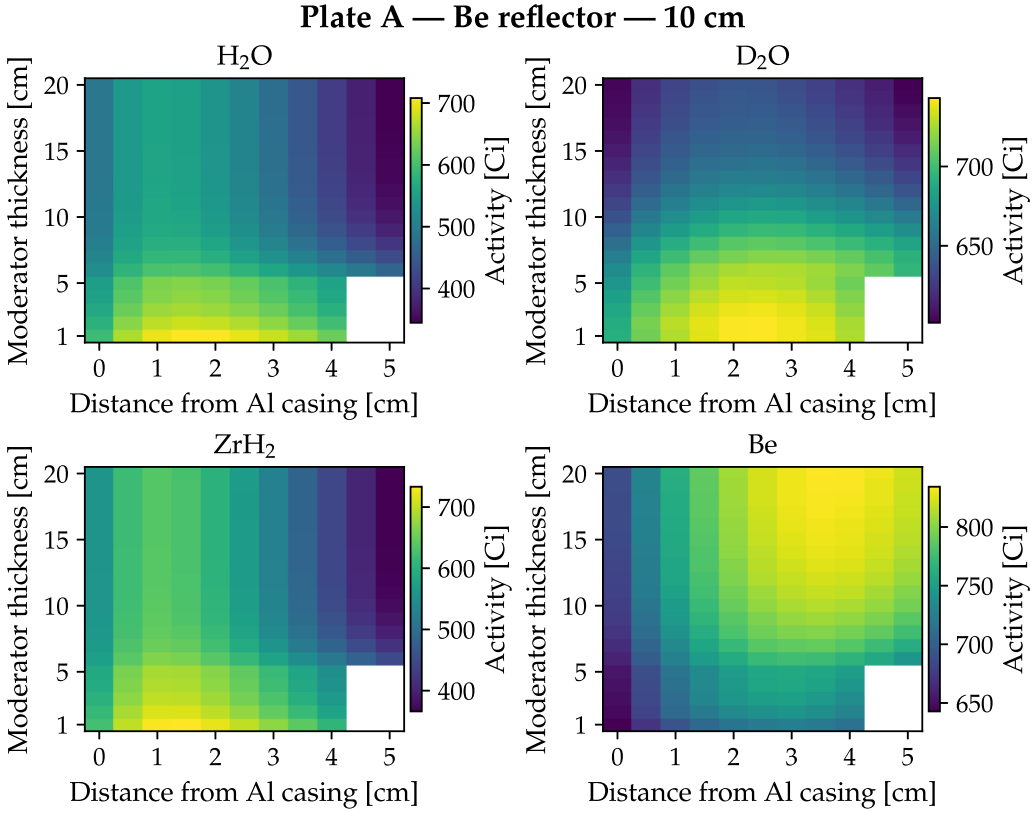

Plate A — MgO reflector — 5 cm
H2O
D2O
ZrH2
Be
Moderator thickness [cm]
Distance from Al casing [cm]
Activity [Ci]

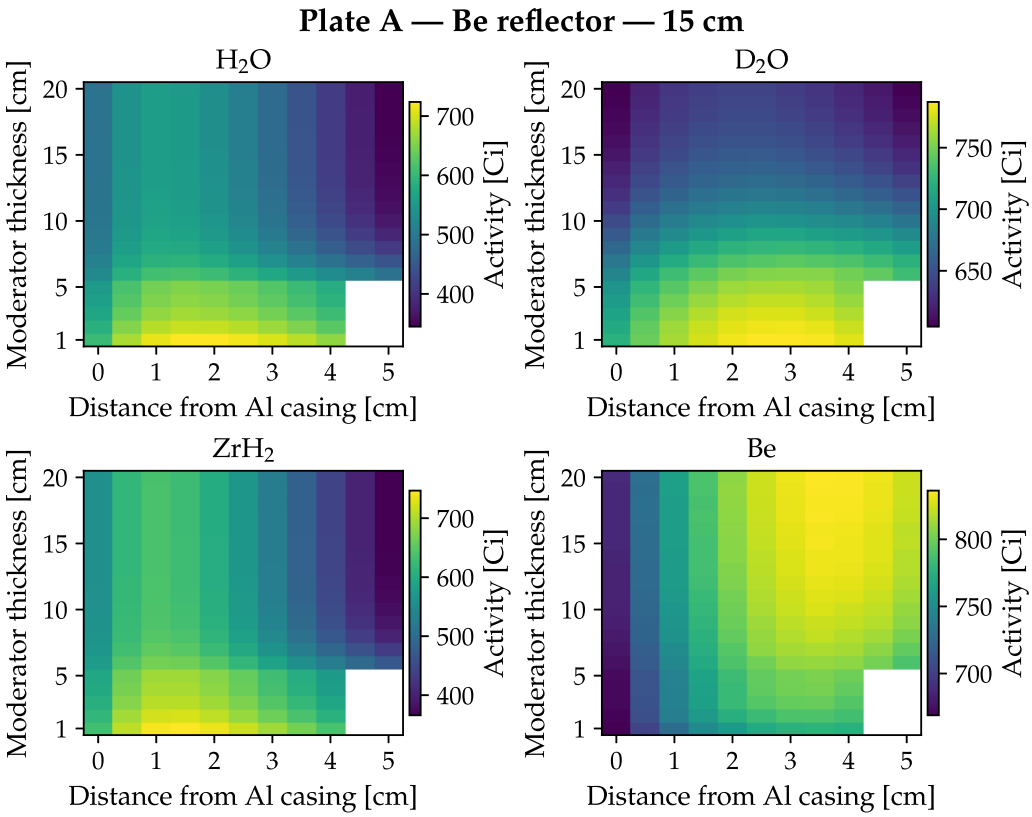

Plate A — MgO reflector — 10 cm
H2O
D2O
ZrH2
Be
Moderator thickness [cm]
Distance from Al casing [cm]
Activity [Ci]

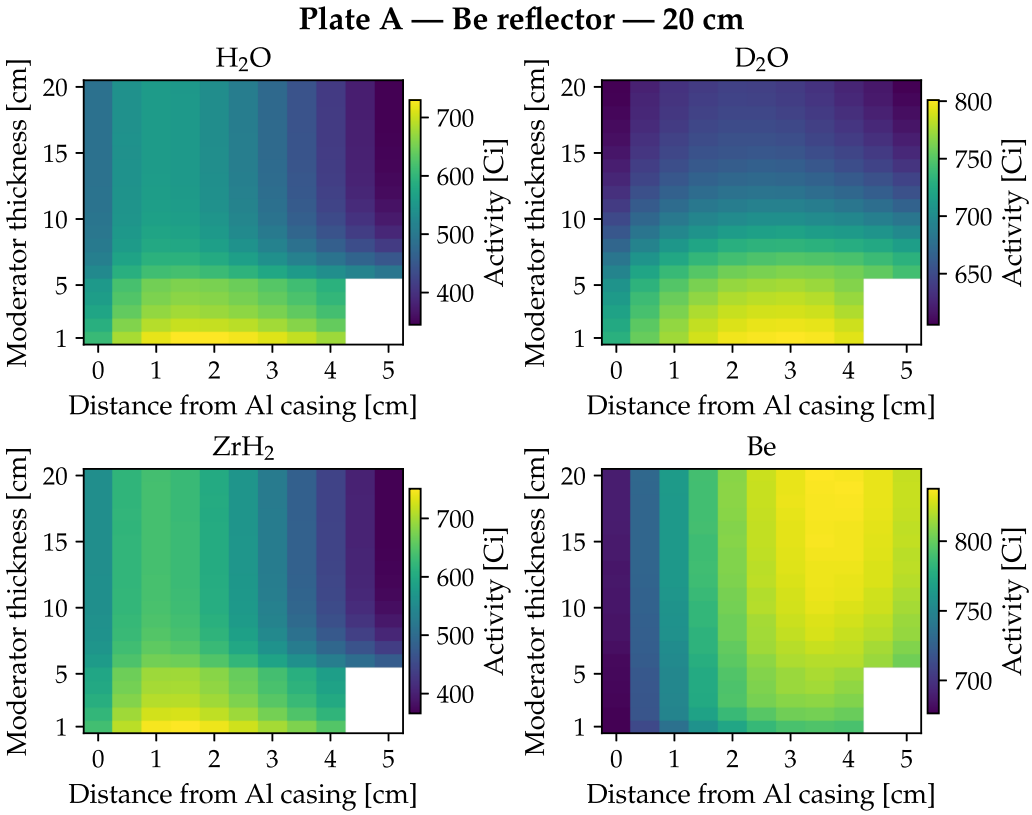

Plate A — MgO reflector — 15 cm
H2O
D2O
ZrH2
Be
Moderator thickness [cm]
Distance from Al casing [cm]
Activity [Ci]

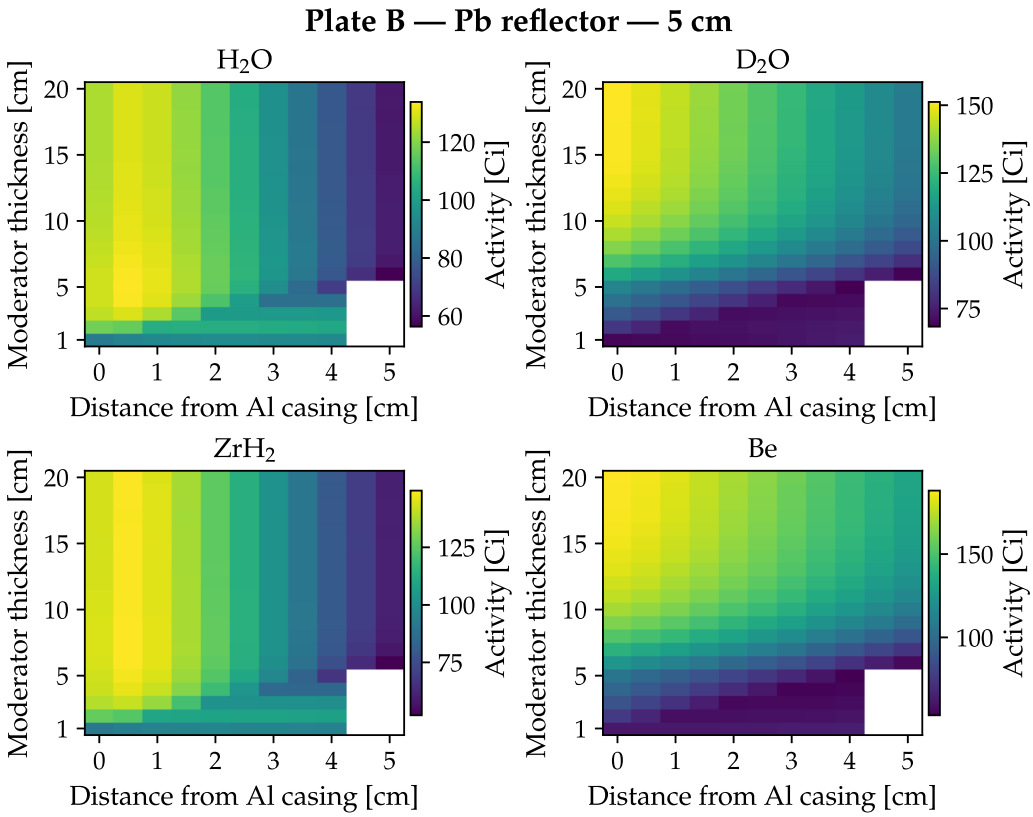

Plate A — MgO reflector — 20 cm
H2O
D2O
ZrH2
Be
Moderator thickness [cm]
Distance from Al casing [cm]
Activity [Ci]

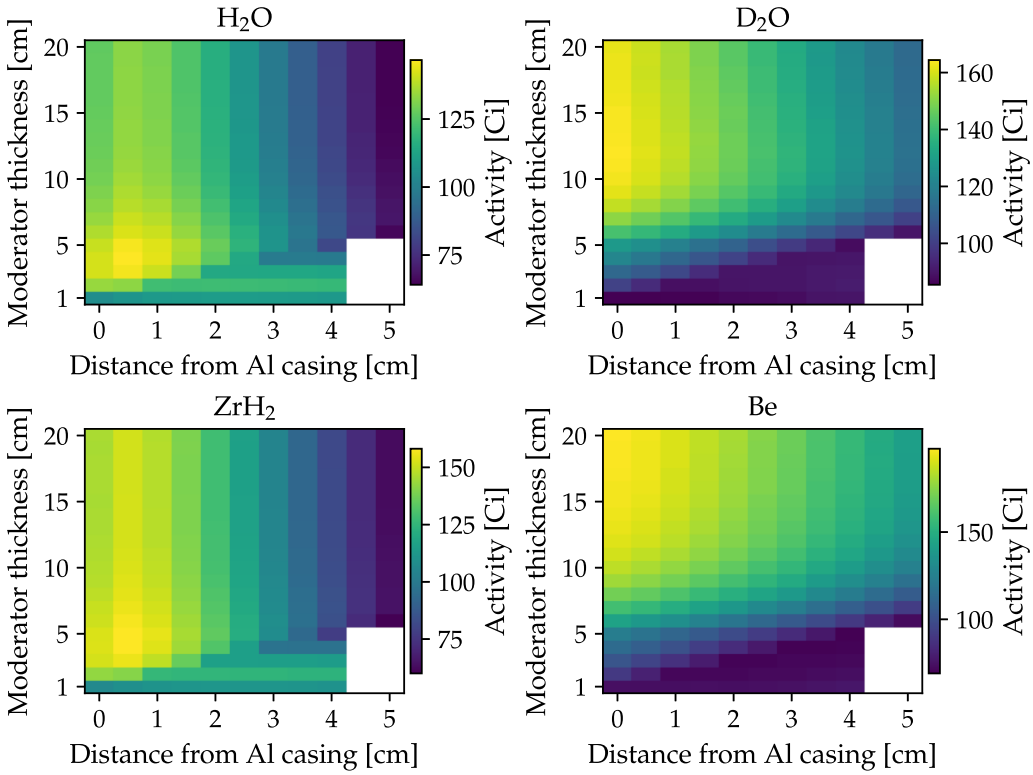

Plate A — Be reflector — 5 cm
H2O
D2O
ZrH2
Be
Moderator thickness [cm]
Distance from Al casing [cm]
Activity [Ci]

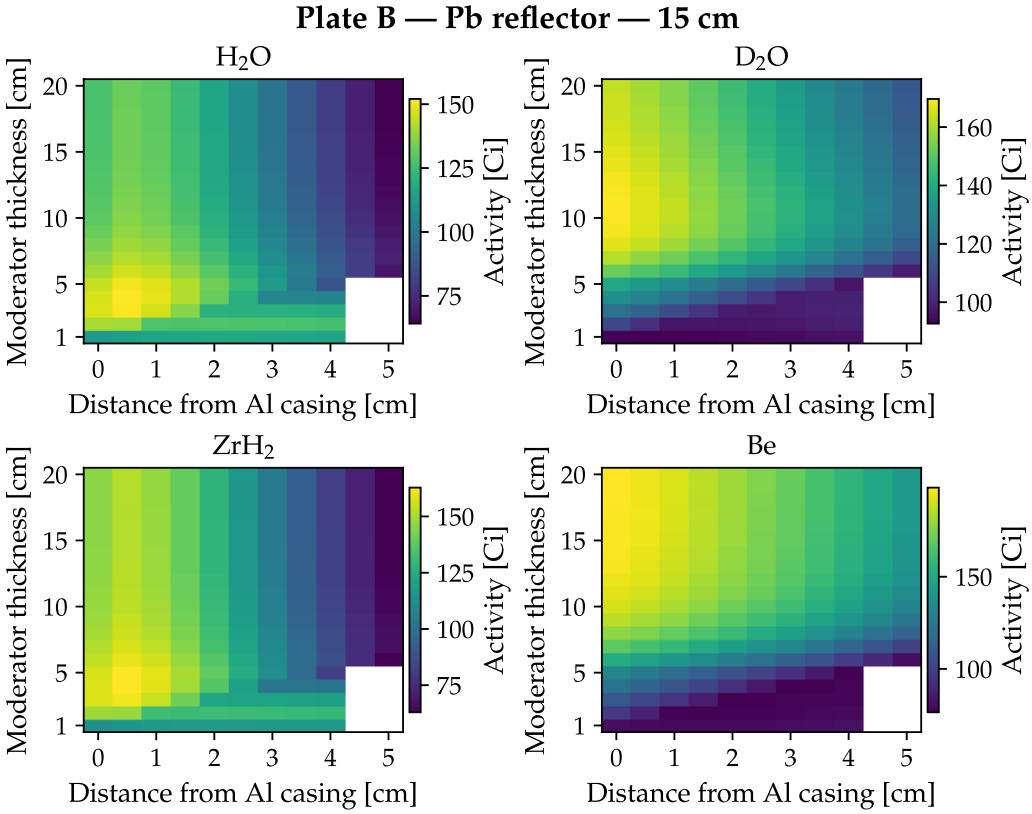

Plate A — Be reflector — 10 cm
H2O
D2O
ZrH2
Be
Moderator thickness [cm]
Distance from Al casing [cm]
Activity [Ci]

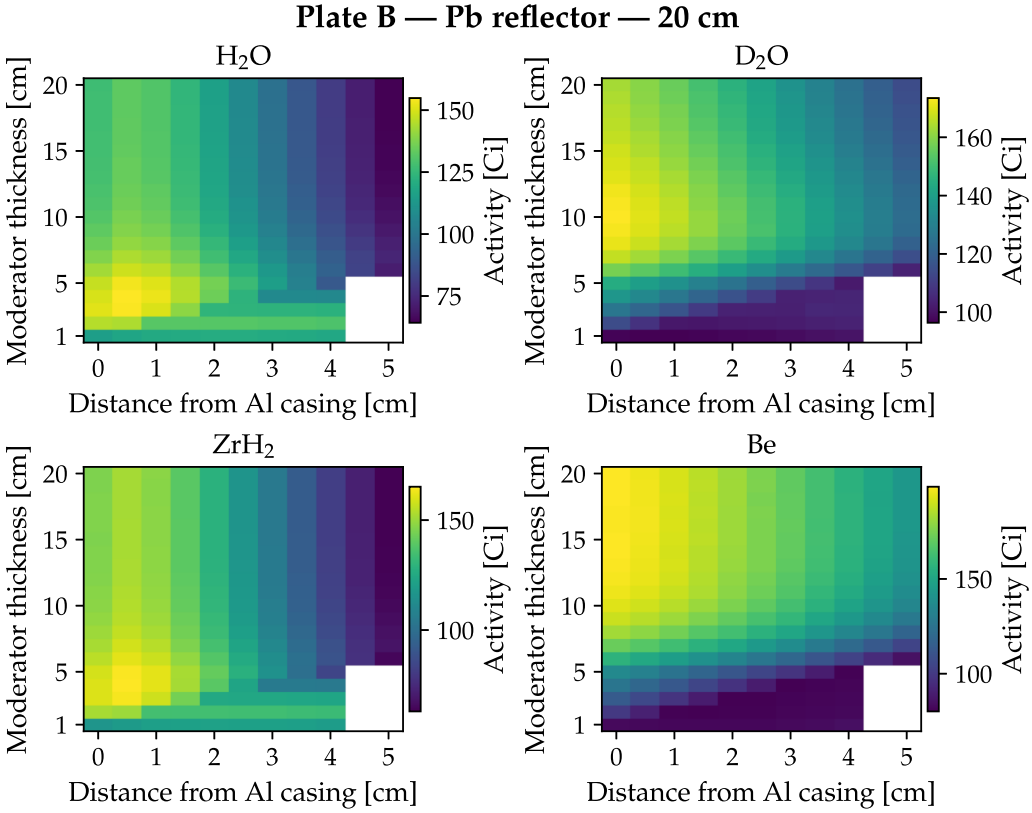

Plate A — Be reflector — 15 cm
H2O
D2O
ZrH2
Be
Moderator thickness [cm]
Distance from Al casing [cm]
Activity [Ci]

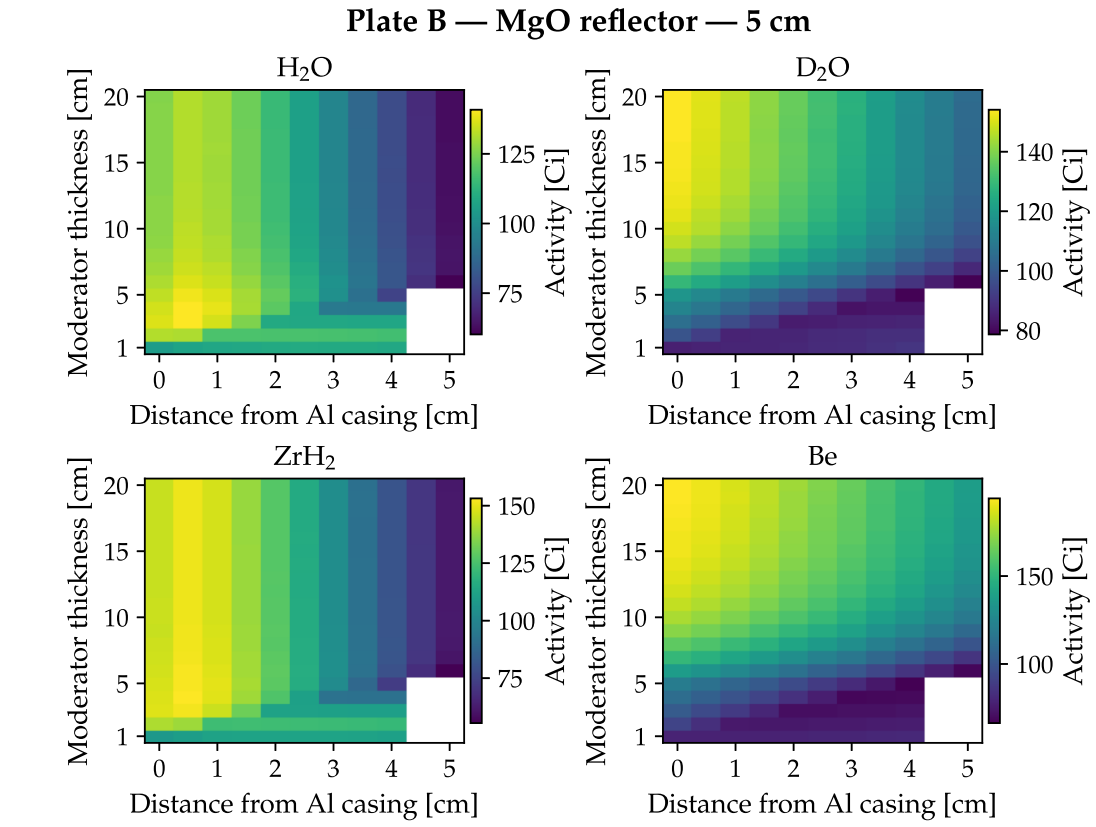

Plate A — Be reflector — 20 cm
H2O
D2O
ZrH2
Be
Moderator thickness [cm]
Distance from Al casing [cm]
Activity [Ci]

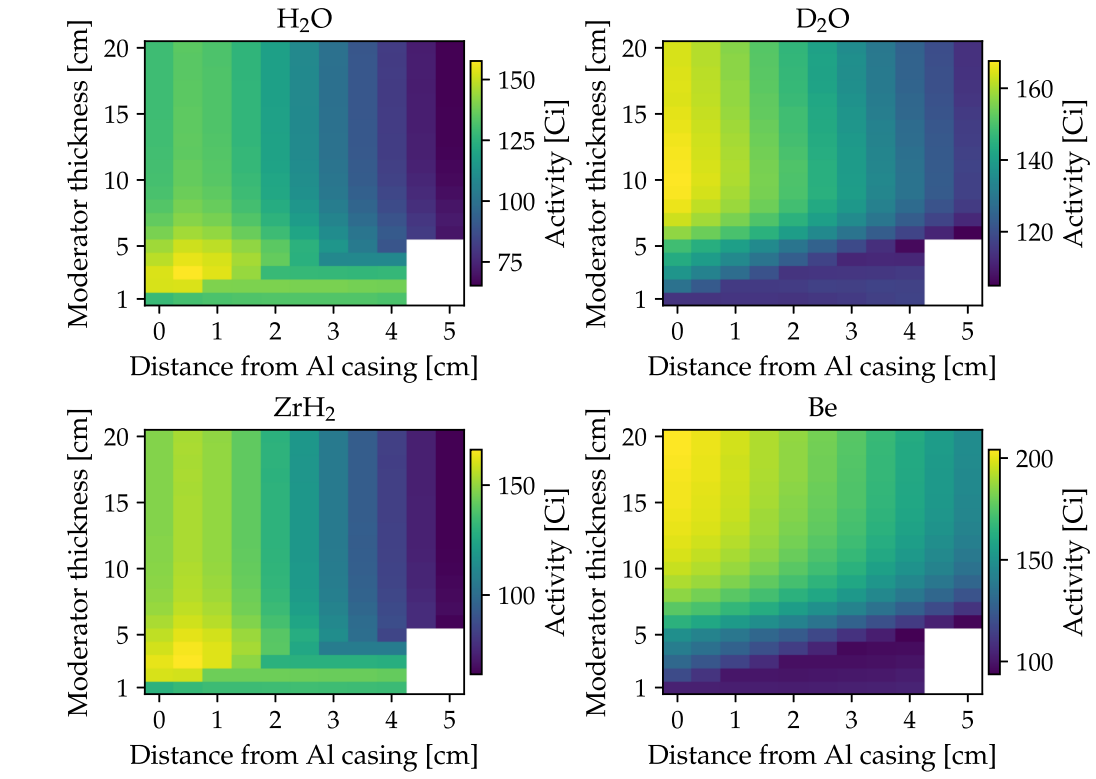

Plate B — Pb reflector — 5 cm
H2O
D2O
ZrH2
Be
Moderator thickness [cm]
Distance from Al casing [cm]
Activity [Ci]

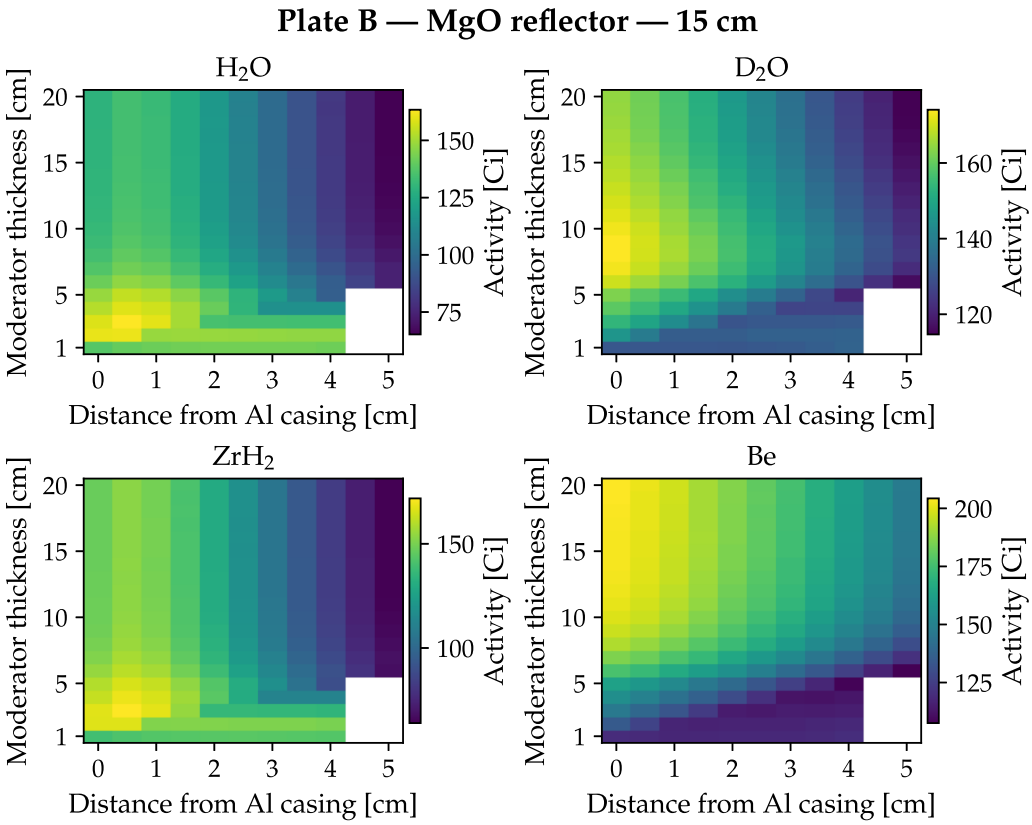

Plate B — Pb reflector — 10 cm
H2O
D2O
ZrH2
Be
Moderator thickness [cm]
Distance from Al casing [cm]
Activity [Ci]

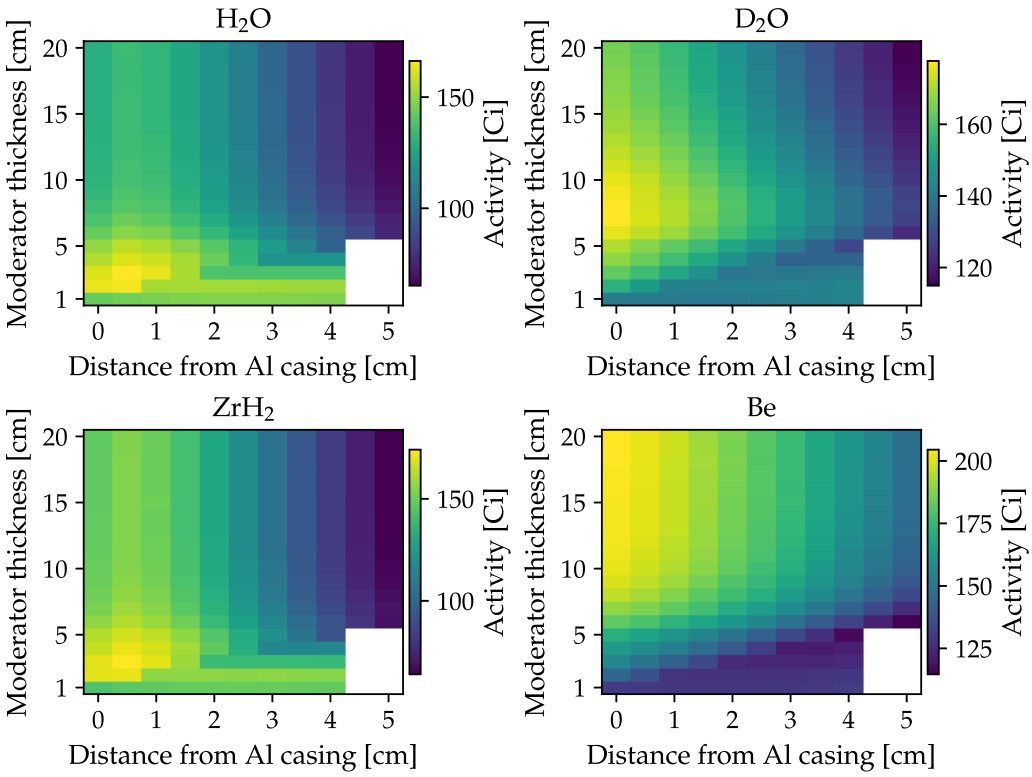

Plate B — Pb reflector — 15 cm
H2O
D2O
ZrH2
Be
Moderator thickness [cm]
Distance from Al casing [cm]
Activity [Ci]

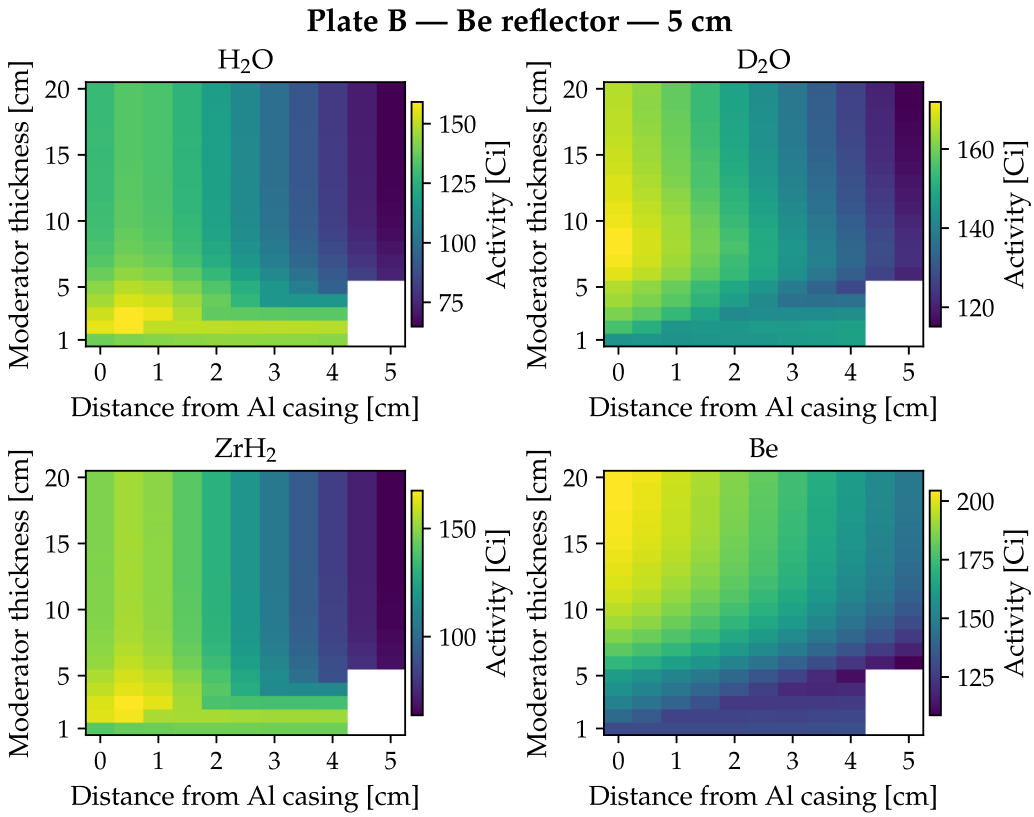

Plate B — Pb reflector — 20 cm
H2O
D2O
ZrH2
Be
Moderator thickness [cm]
Distance from Al casing [cm]
Activity [Ci]

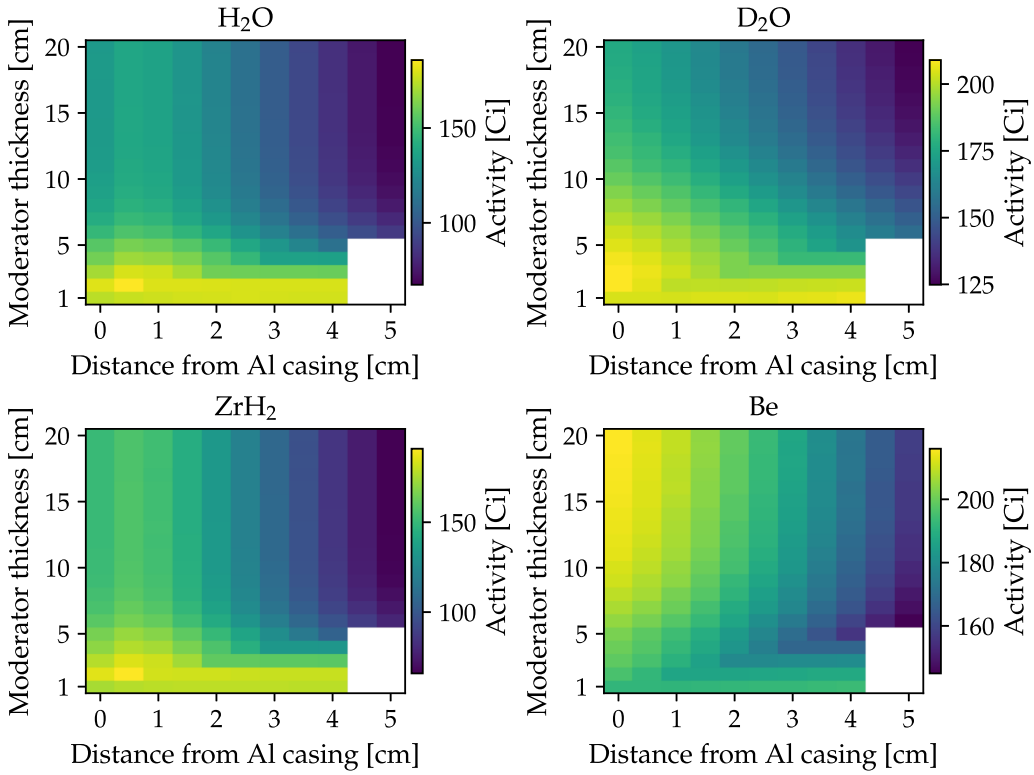

Plate B — MgO reflector — 5 cm
H2O
D2O
ZrH2
Be
Moderator thickness [cm]
Distance from Al casing [cm]
Activity [Ci]

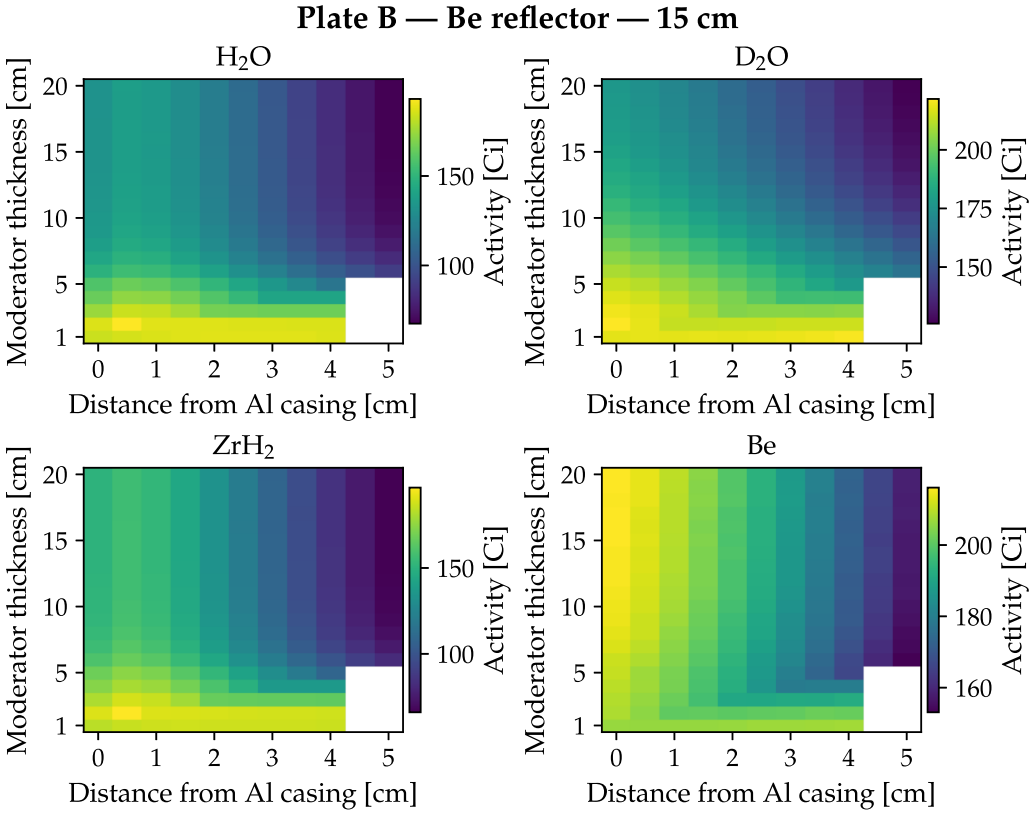

Plate B — MgO reflector — 10 cm
H2O
D2O
ZrH2
Be
Moderator thickness [cm]
Distance from Al casing [cm]
Activity [Ci]

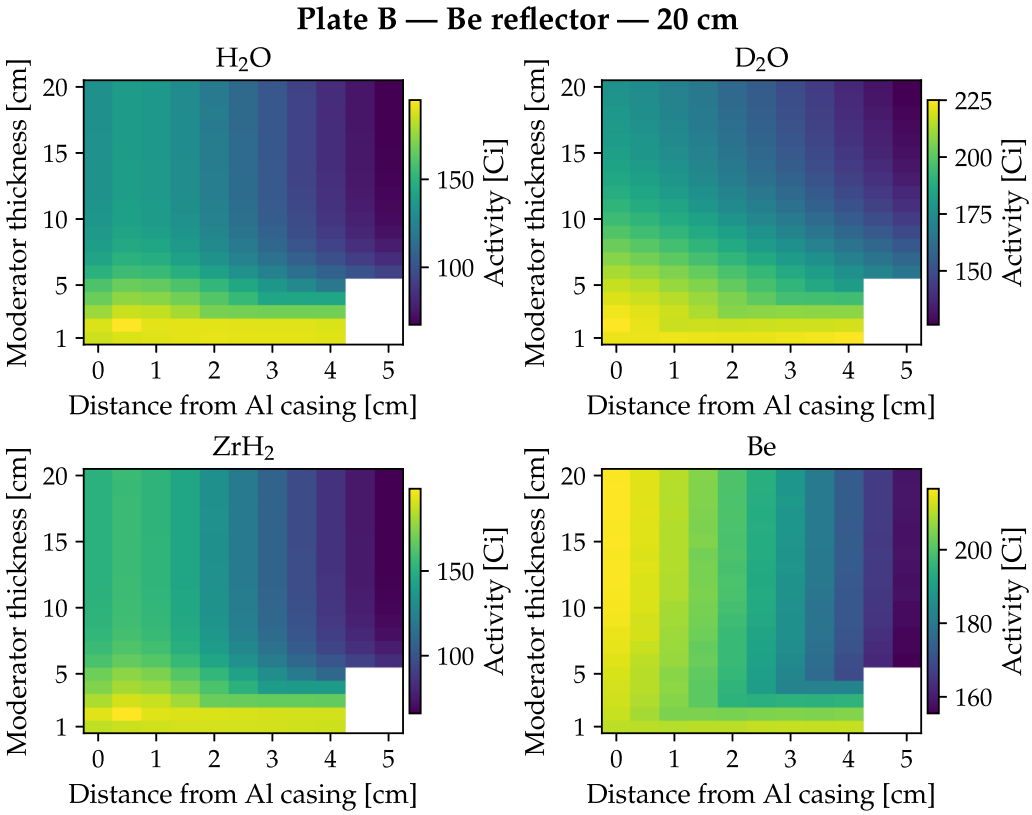

Plate B — MgO reflector — 15 cm
H2O
D2O
ZrH2
Be
Moderator thickness [cm]
Distance from Al casing [cm]
Activity [Ci]

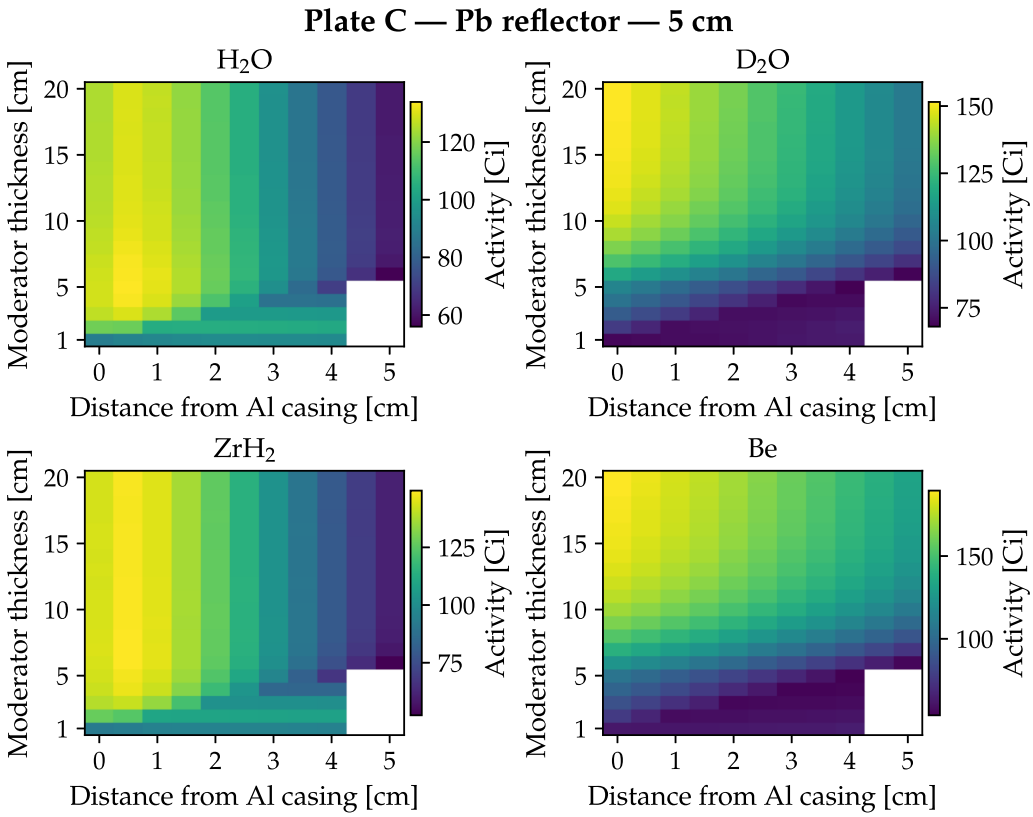

Plate B — MgO reflector — 20 cm
H2O
D2O
ZrH2
Be
Moderator thickness [cm]
Distance from Al casing [cm]
Activity [Ci]

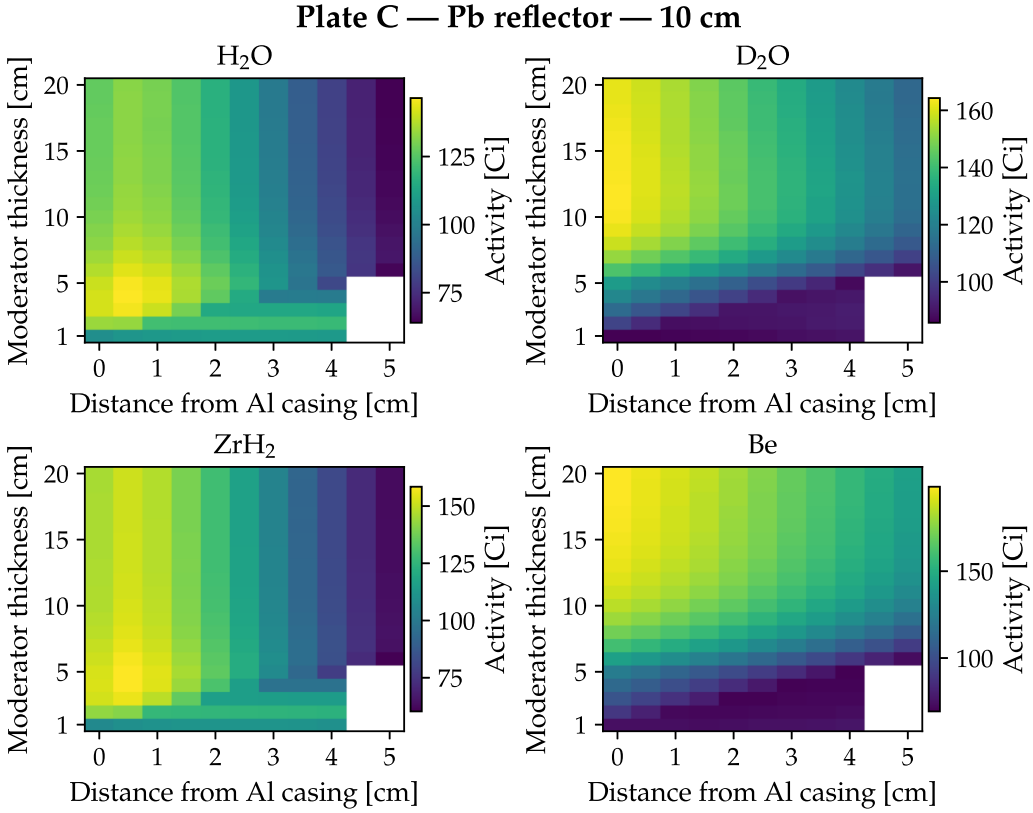

Plate B — Be reflector — 5 cm
H2O
D2O
ZrH2
Be
Moderator thickness [cm]
Distance from Al casing [cm]
Activity [Ci]

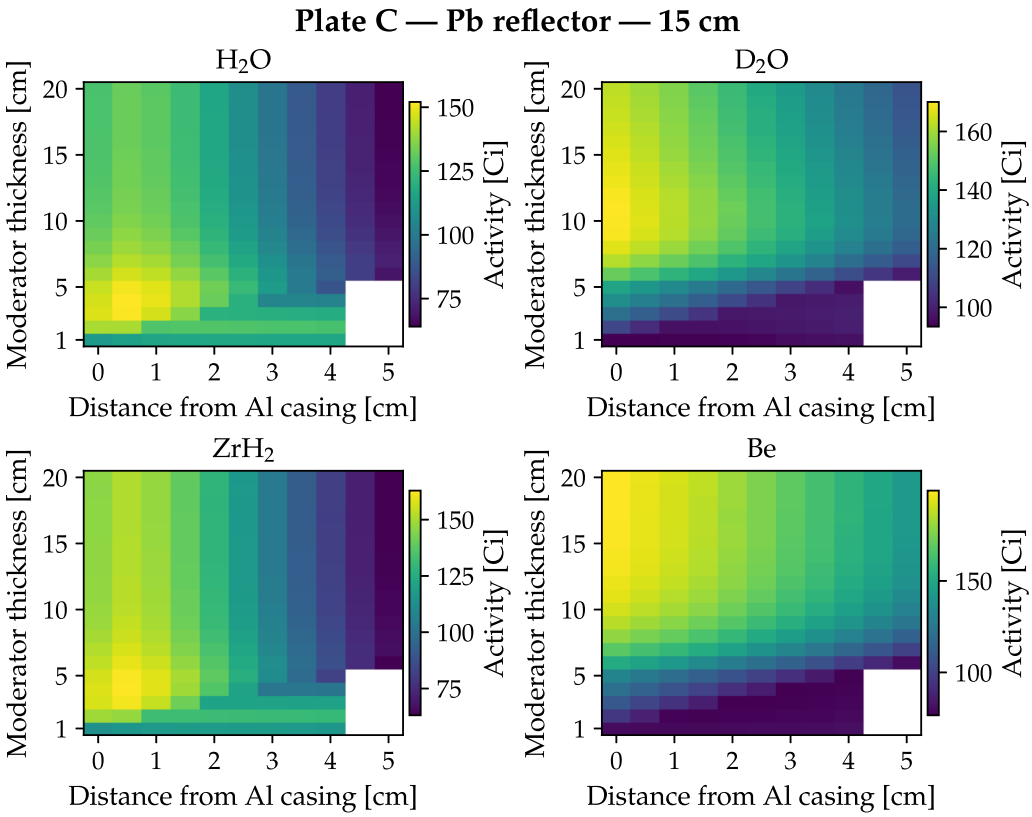

Plate B — Be reflector — 10 cm
H2O
D2O
ZrH2
Be
Moderator thickness [cm]
Distance from Al casing [cm]
Activity [Ci]


Plate B — Be reflector — 15 cm
H2O
D2O
ZrH2
Be
Moderator thickness [cm]
Distance from Al casing [cm]
Activity [Ci]


Plate B — Be reflector — 20 cm
H2O
D2O
ZrH2
Be
Moderator thickness [cm]
Distance from Al casing [cm]
Activity [Ci]


Plate C — Pb reflector — 5 cm
H2O
D2O
ZrH2
Be
Moderator thickness [cm]
Distance from Al casing [cm]
Activity [Ci]


Plate C — Pb reflector — 10 cm
H2O
D2O
ZrH2
Be
Moderator thickness [cm]
Distance from Al casing [cm]
Activity [Ci]


Plate C — Pb reflector — 15 cm
H2O
D2O
ZrH2
Be
Moderator thickness [cm]
Distance from Al casing [cm]
Activity [Ci]

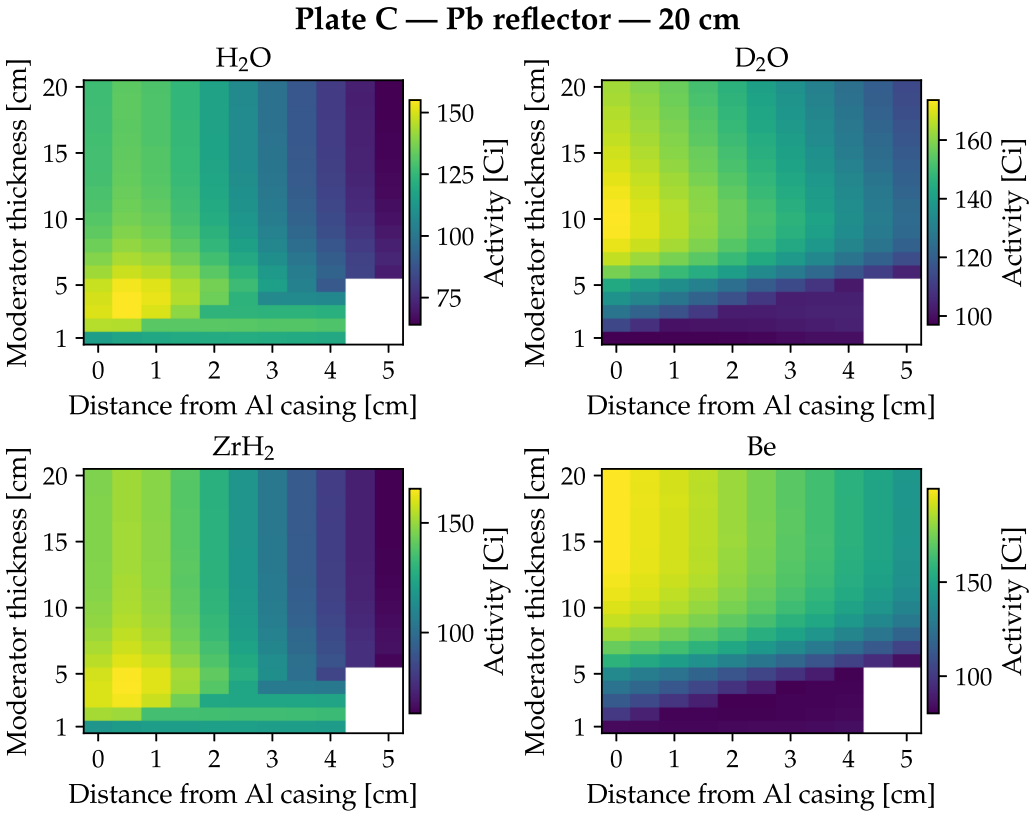

Plate C — Pb reflector — 20 cm
H2O
D2O
ZrH2
Be
Moderator thickness [cm]
Distance from Al casing [cm]
Activity [Ci]

Plate C — MgO reflector — 5 cm

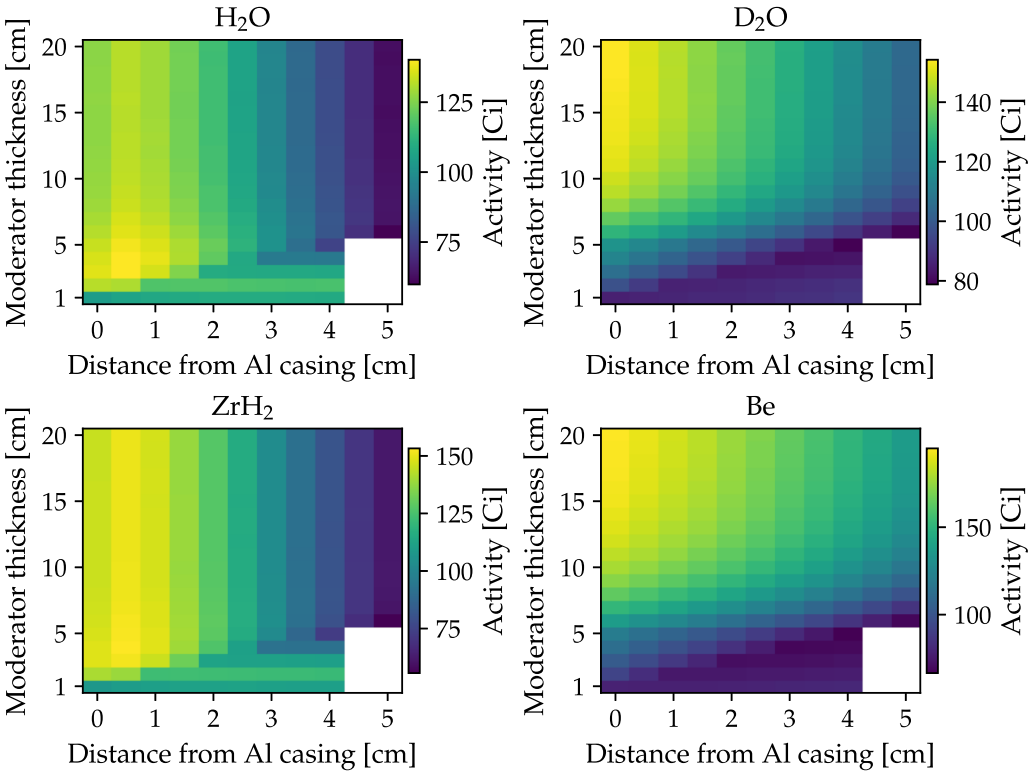
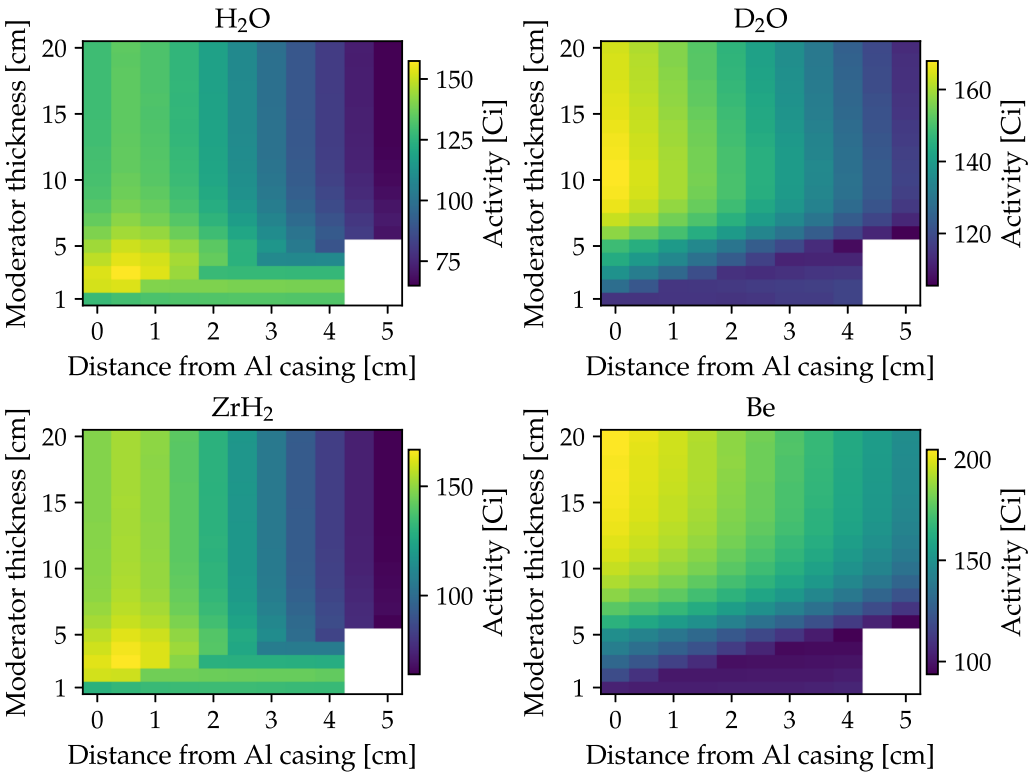
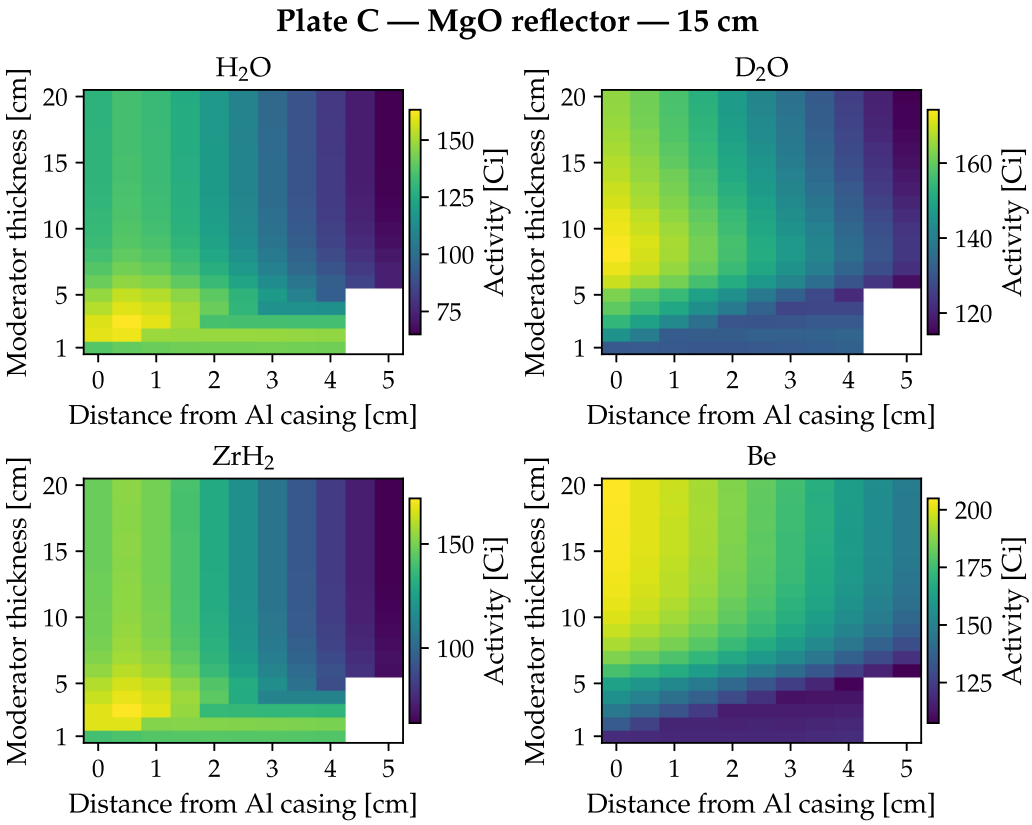
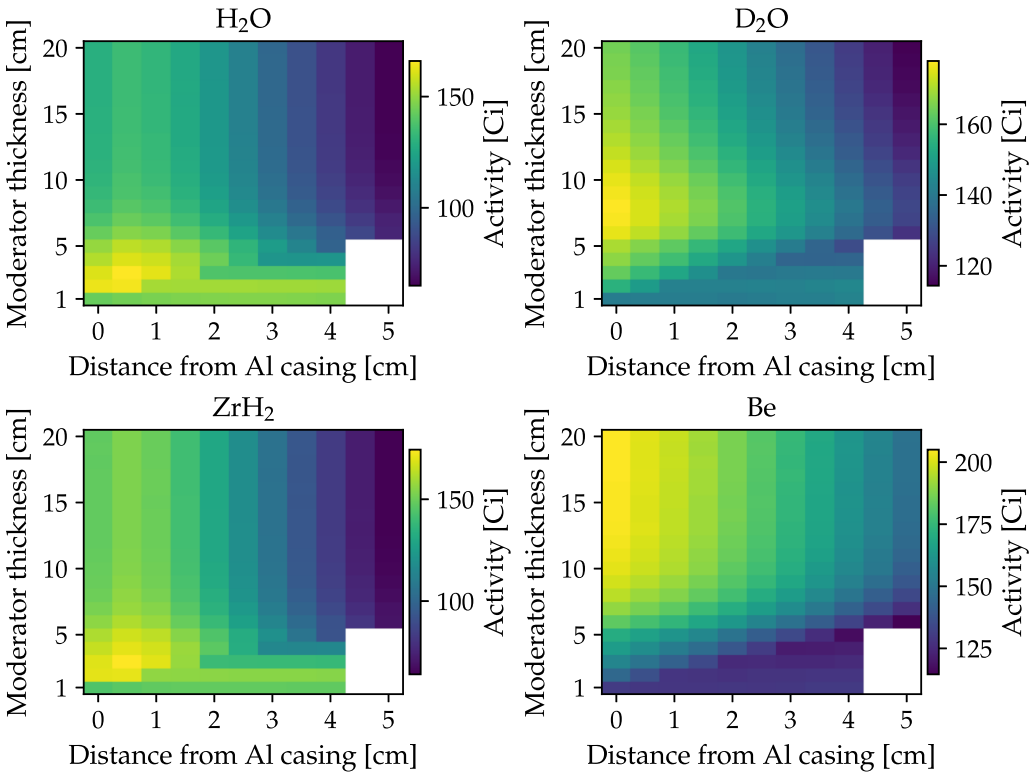
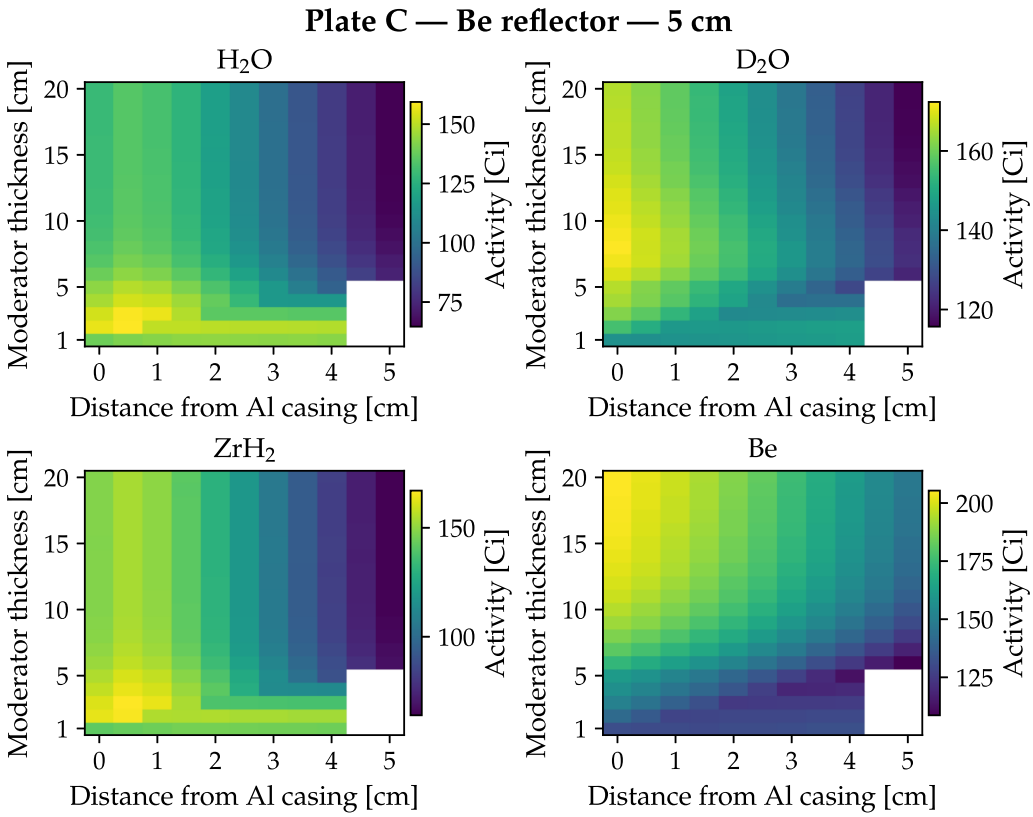


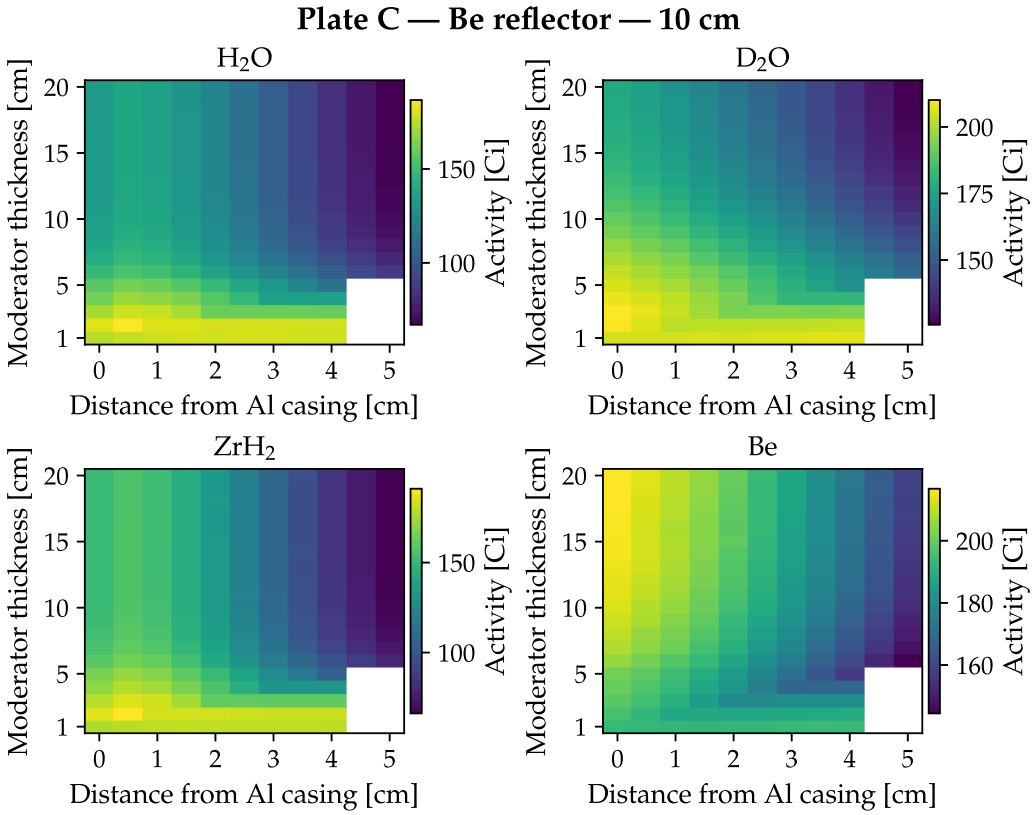
Plate C — MgO reflector — 10 cm

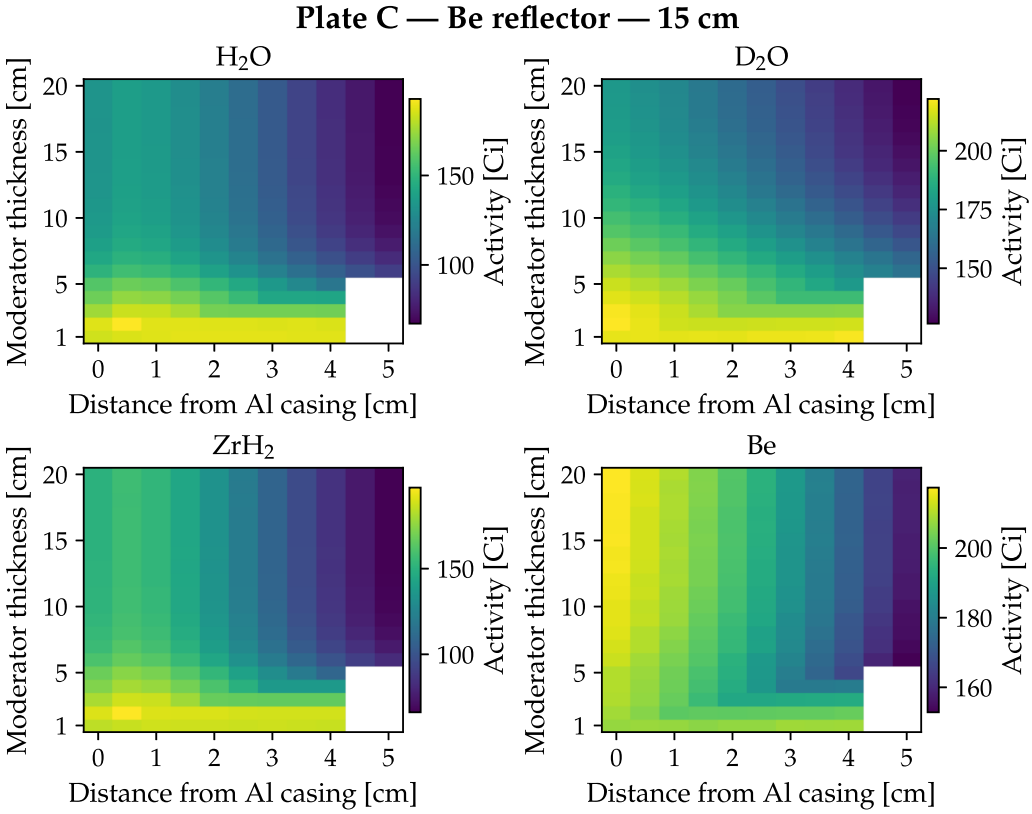


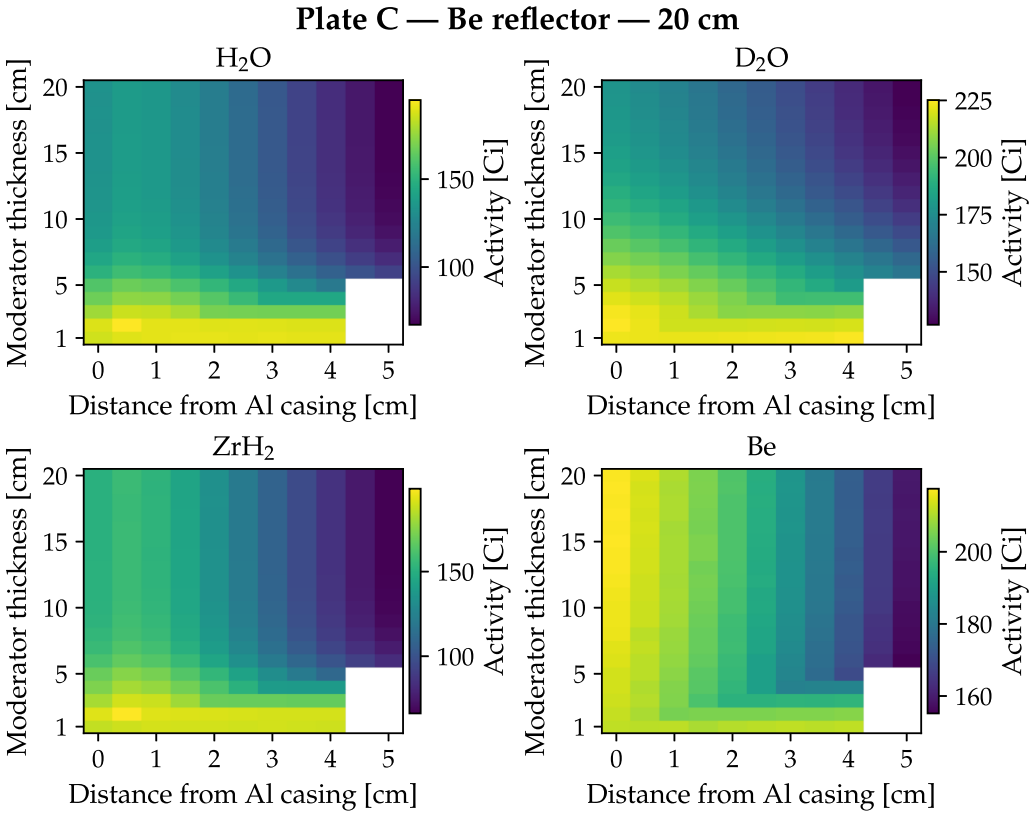

Plate C — MgO reflector — 15 cm
H2O
D2O
ZrH2
Be
Moderator thickness [cm]
Distance from Al casing [cm]
Activity [Ci]

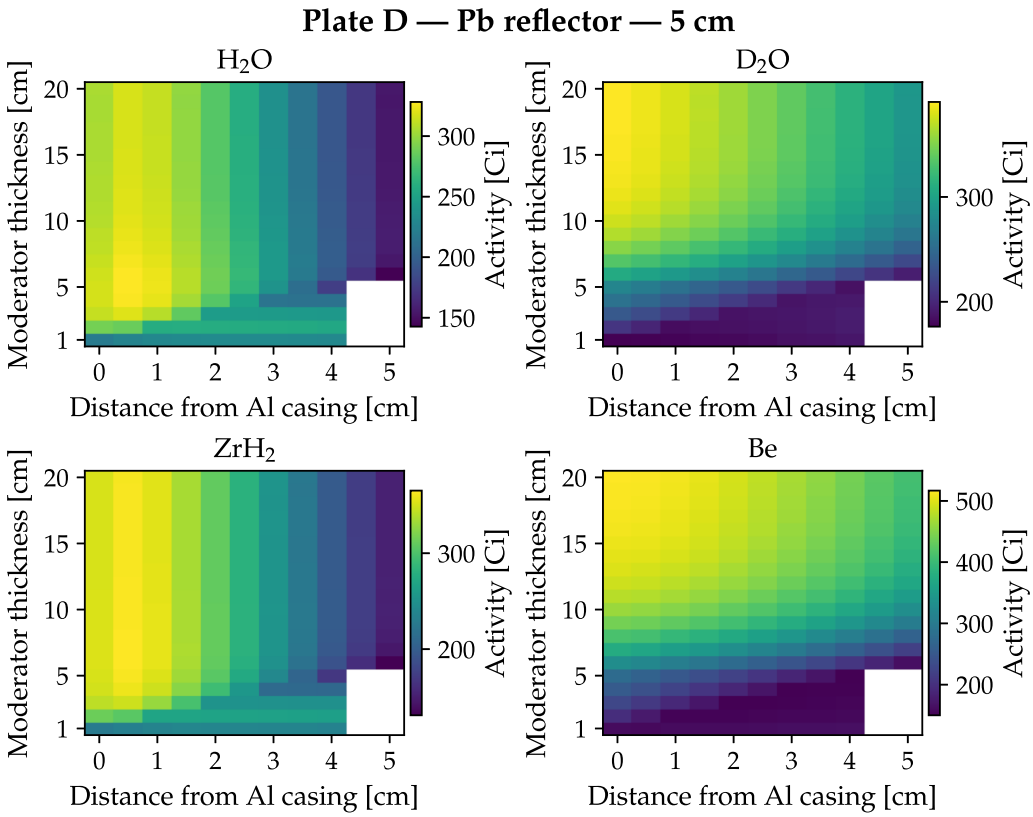

Plate C — MgO reflector — 20 cm
H2O
D2O
ZrH2
Be
Moderator thickness [cm]
Distance from Al casing [cm]
Activity [Ci]

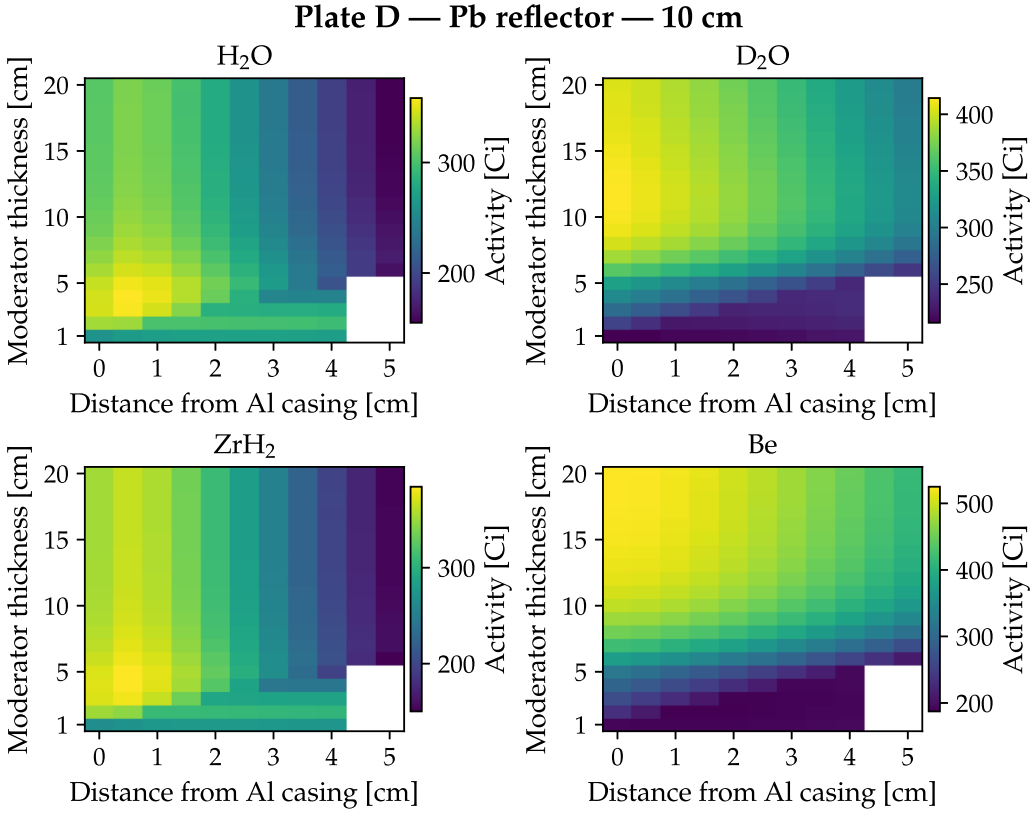

Plate C — Be reflector — 5 cm
H2O
D2O
ZrH2
Be
Moderator thickness [cm]
Distance from Al casing [cm]
Activity [Ci]

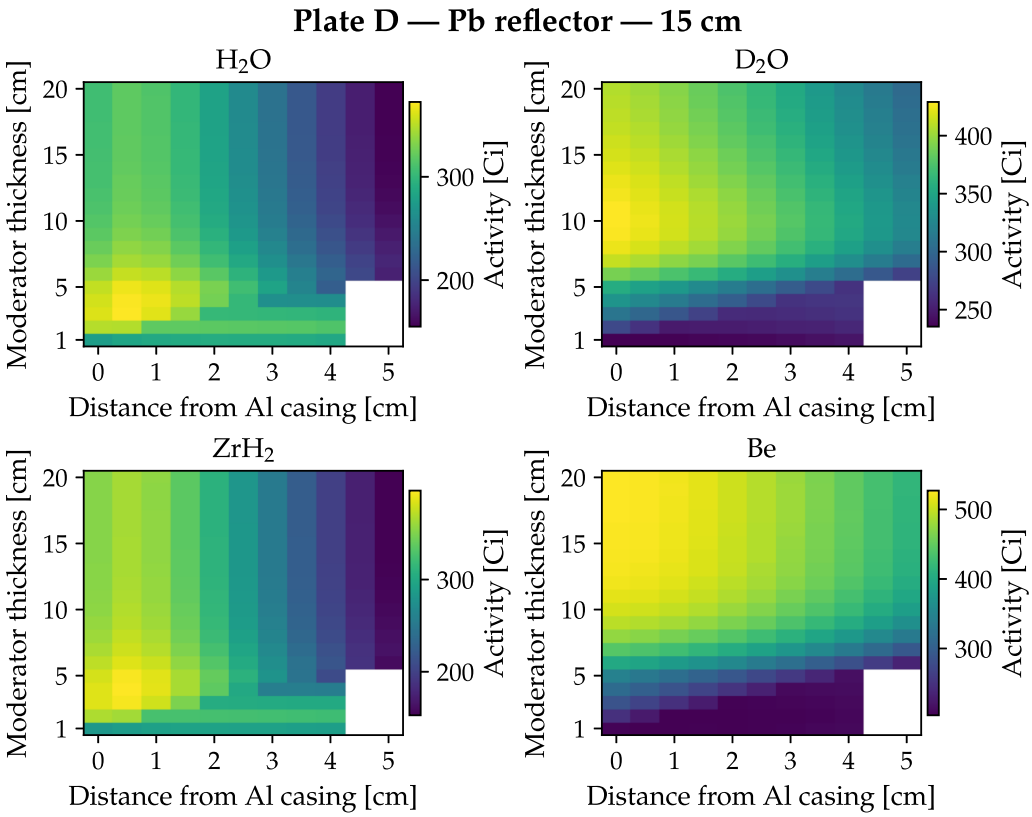

Plate C — Be reflector — 10 cm
H2O
D2O
ZrH2
Be
Moderator thickness [cm]
Distance from Al casing [cm]
Activity [Ci]

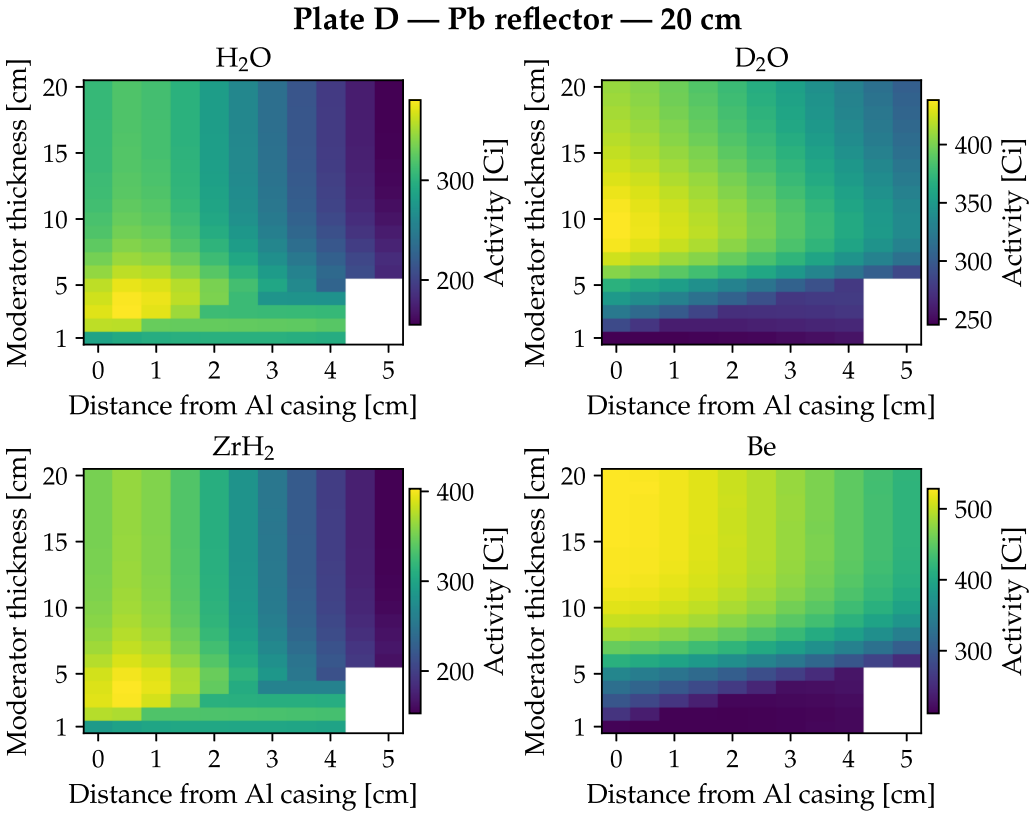

Plate C — Be reflector — 15 cm
H2O
D2O
ZrH2
Be
Moderator thickness [cm]
Distance from Al casing [cm]
Activity [Ci]

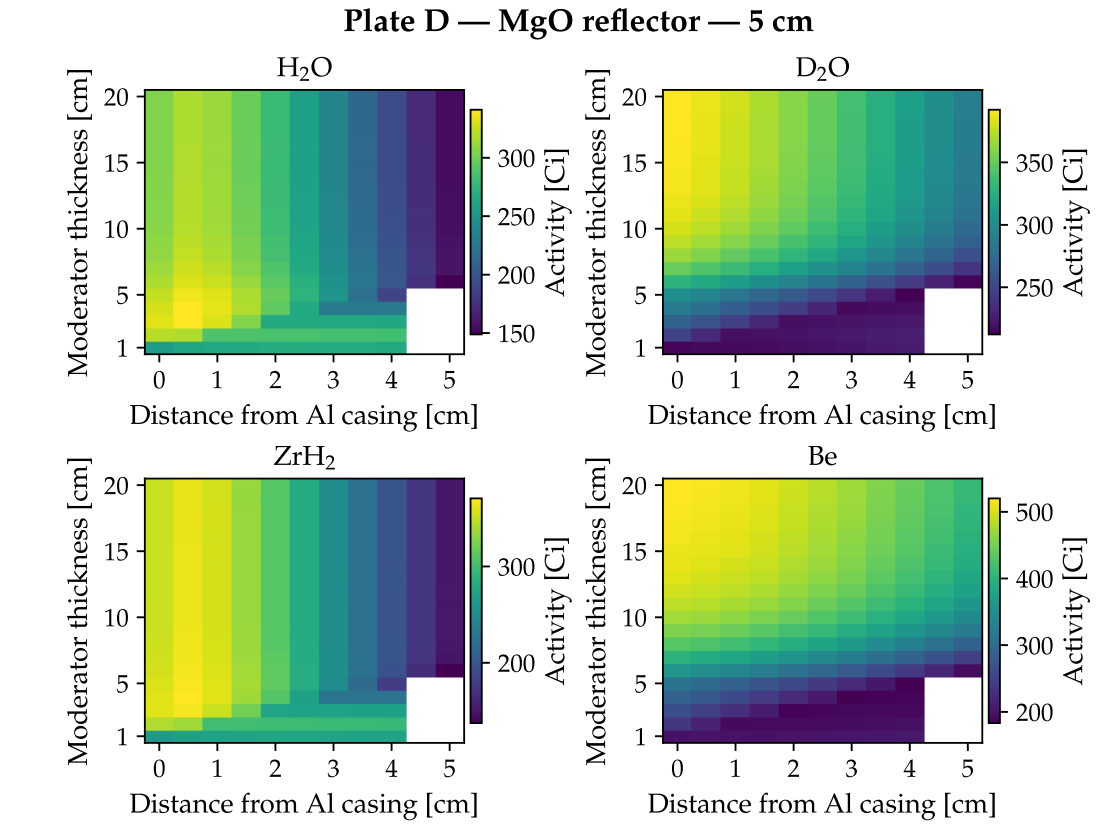

Plate C — Be reflector — 20 cm
H2O
D2O
ZrH2
Be
Moderator thickness [cm]
Distance from Al casing [cm]
Activity [Ci]

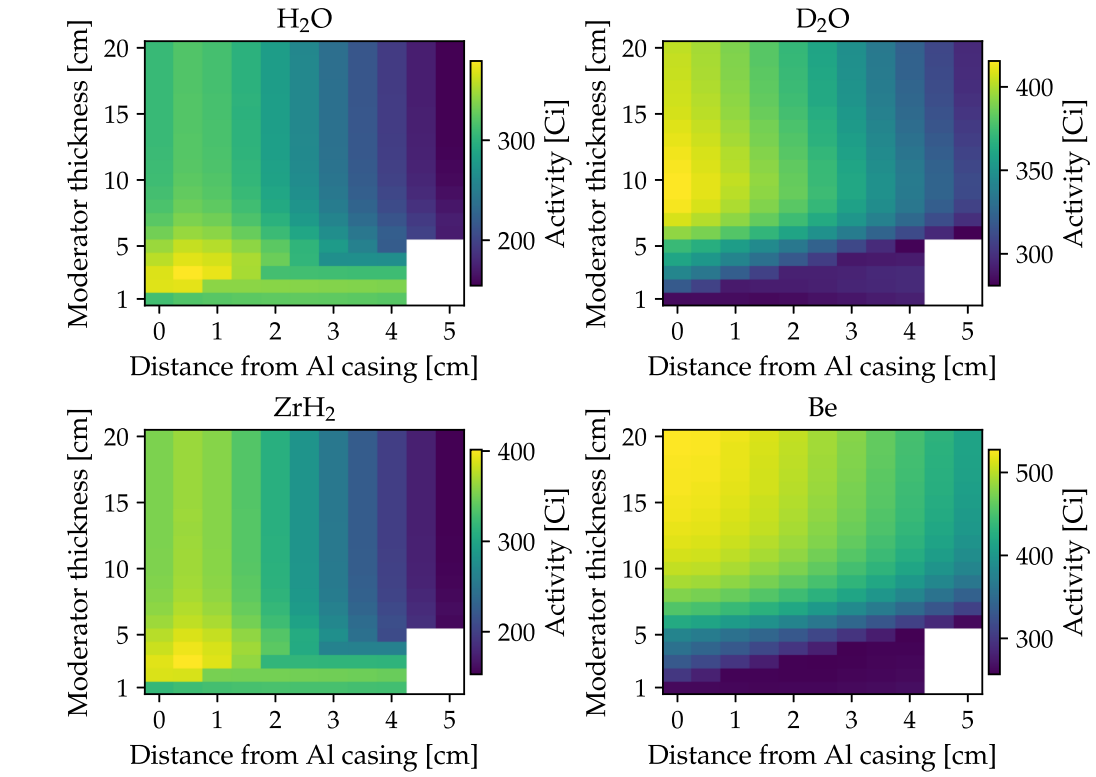

Plate D — Pb reflector — 5 cm
H2O
D2O
ZrH2
Be
Moderator thickness [cm]
Distance from Al casing [cm]
Activity [Ci]

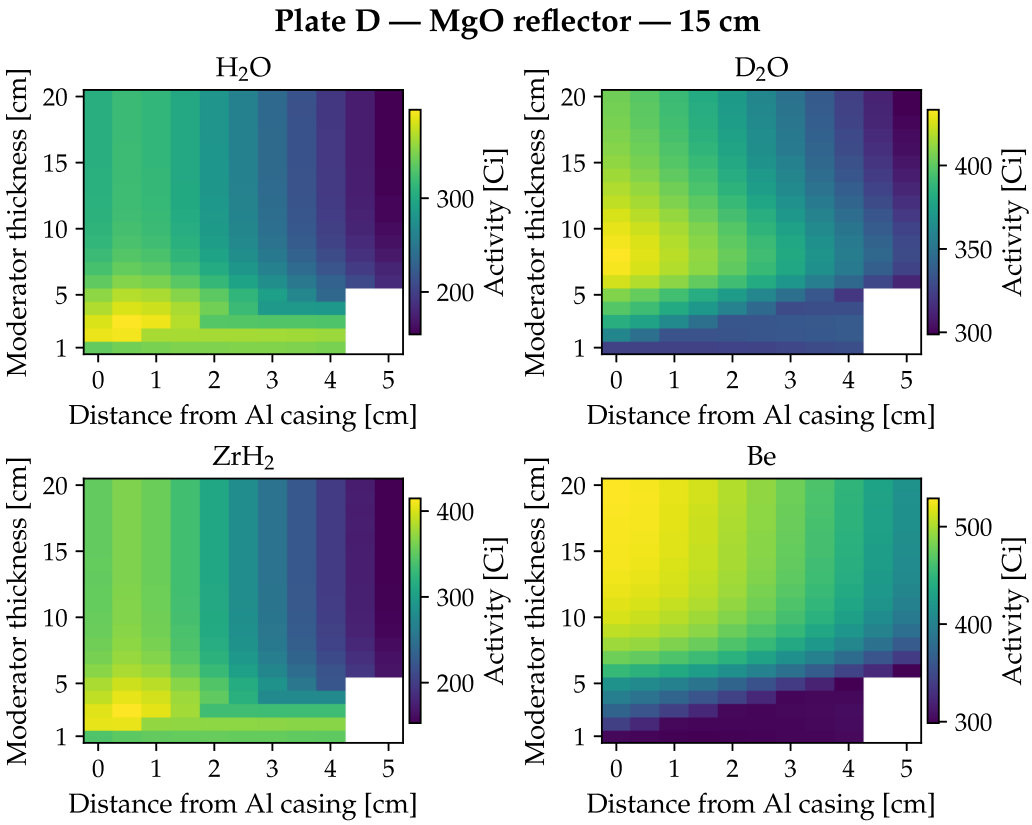

Plate D — Pb reflector — 10 cm
H2O
D2O
ZrH2
Be
Moderator thickness [cm]
Distance from Al casing [cm]
Activity [Ci]

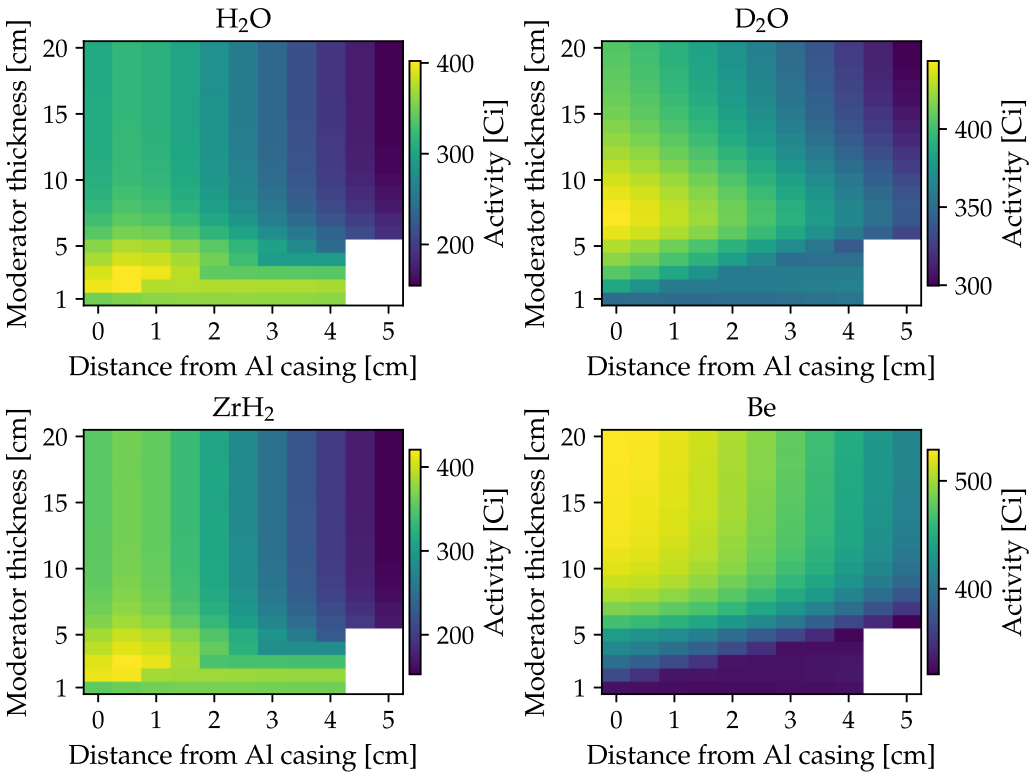

Plate D — Pb reflector — 15 cm
H2O
D2O
ZrH2
Be
Moderator thickness [cm]
Distance from Al casing [cm]
Activity [Ci]

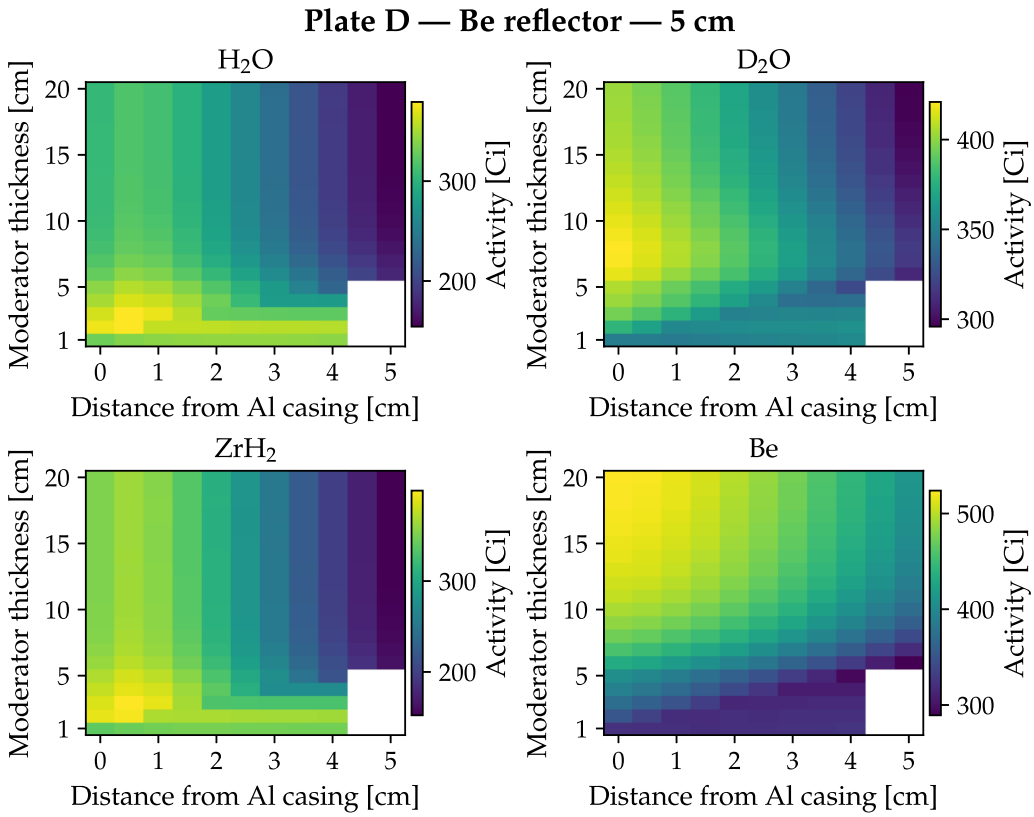

Plate D — Pb reflector — 20 cm
H2O
D2O
ZrH2
Be
Moderator thickness [cm]
Distance from Al casing [cm]
Activity [Ci]

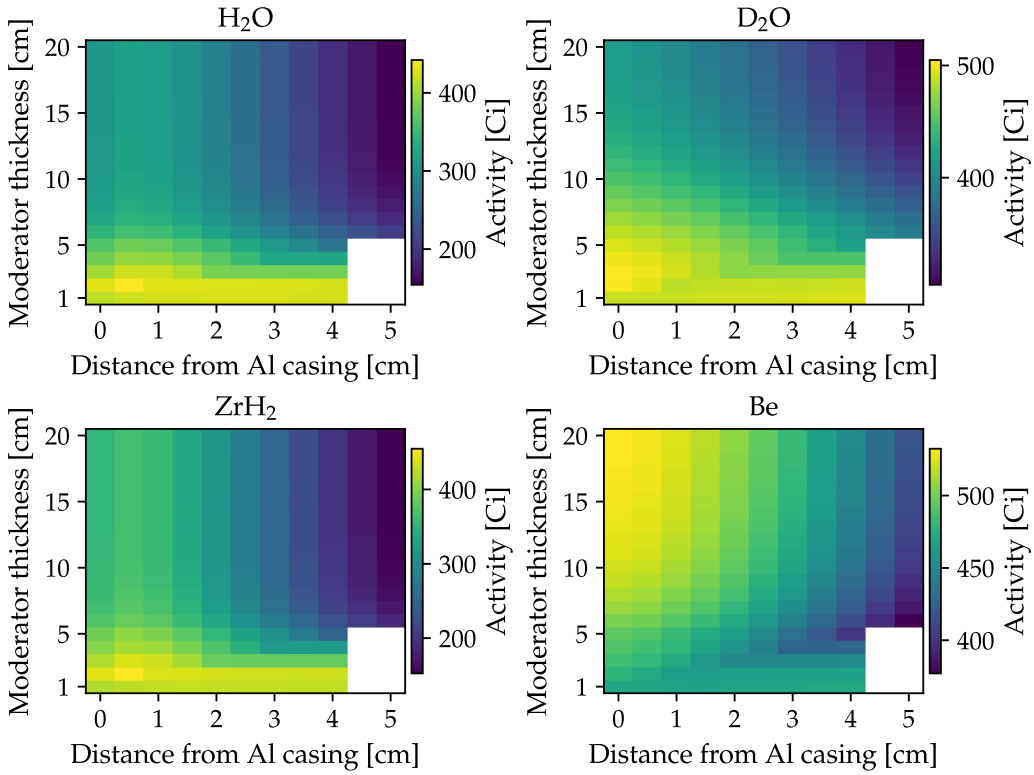

Plate D — MgO reflector — 5 cm
H2O
D2O
ZrH2
Be
Moderator thickness [cm]
Distance from Al casing [cm]
Activity [Ci]

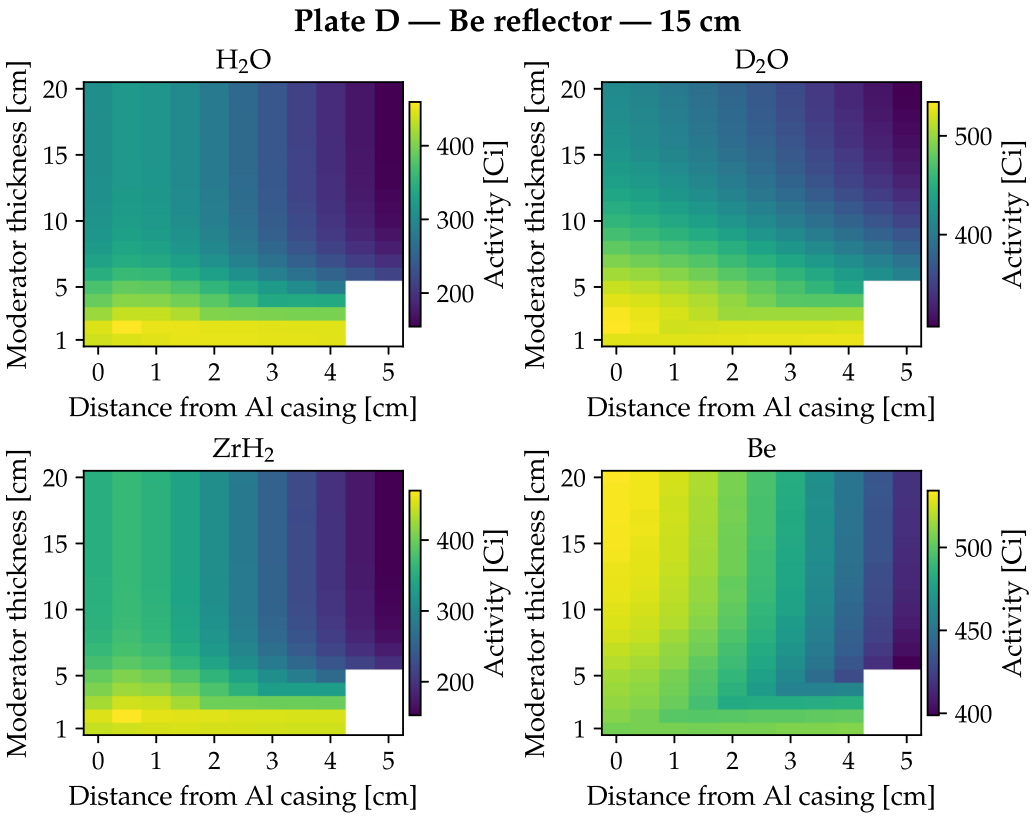

Plate D — MgO reflector — 10 cm
H2O
D2O
ZrH2
Be
Moderator thickness [cm]
Distance from Al casing [cm]
Activity [Ci]

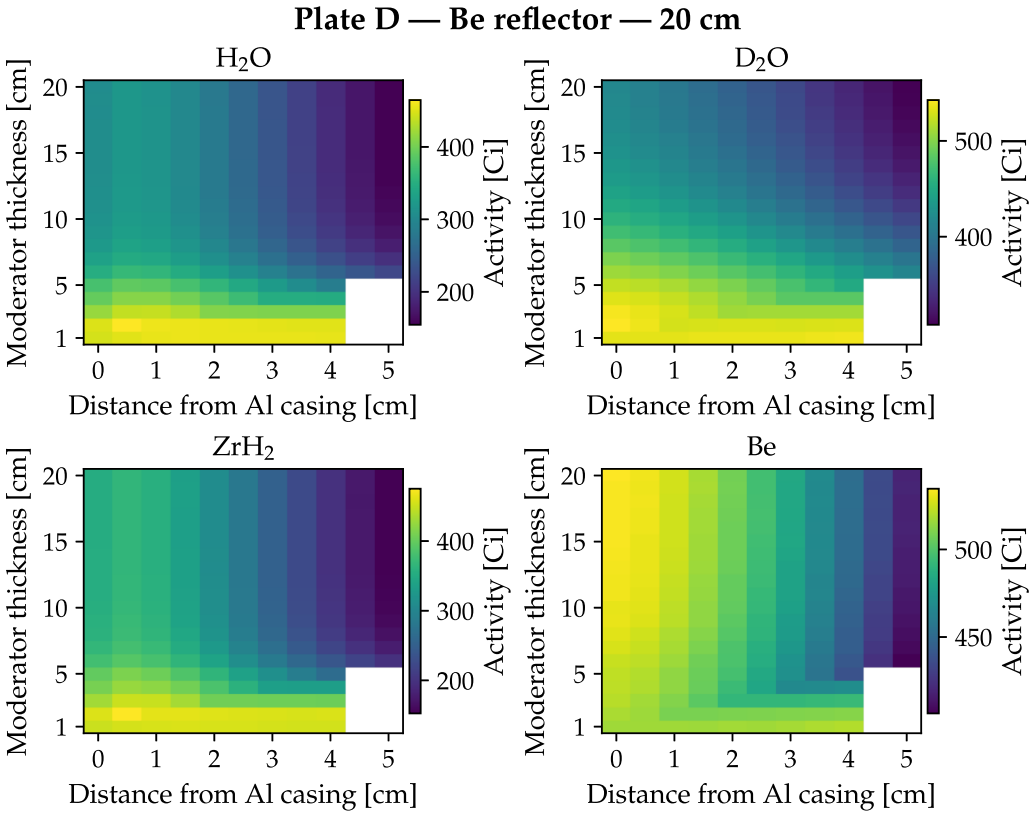

Plate D — MgO reflector — 15 cm
H2O
D2O
ZrH2
Be
Moderator thickness [cm]
Distance from Al casing [cm]
Activity [Ci]


Plate D — MgO reflector — 20 cm
H2O
D2O
ZrH2
Be
Moderator thickness [cm]
Distance from Al casing [cm]
Activity [Ci]


Plate D — Be reflector — 5 cm
H2O
D2O
ZrH2
Be
Moderator thickness [cm]
Distance from Al casing [cm]
Activity [Ci]


Plate D — Be reflector — 10 cm
H2O
D2O
ZrH2
Be
Moderator thickness [cm]
Distance from Al casing [cm]
Activity [Ci]


Plate D — Be reflector — 15 cm
H2O
D2O
ZrH2
Be
Moderator thickness [cm]
Distance from Al casing [cm]
Activity [Ci]


Plate D — Be reflector — 20 cm
H2O
D2O
ZrH2
Be
Moderator thickness [cm]
Distance from Al casing [cm]
Activity [Ci]

D Automation Workflow for PHITS Simulations and Data Analysis

The parameter study presented in this work required the generation, execution, and analysis of a large number of PHITS simulations. The investigated configurations differed in reflector material, reflector thickness, moderator material, moderator thickness, and Mo plate position. Since manual preparation and analysis of all input and output files would have been impractical, a Python-based workflow was developed.
The workflow consisted of three main parts:

1. Generation of PHITS input files
2. Generation of batch files for execution on the computing cluster
3. Parsing, processing, and visualization of the simulation output data

These three steps were implemented in separate Python notebooks. The first notebook was used to generate the PHITS input files, the second notebook was used to generate the cluster batch files, and the third notebook was used to parse the output files, calculate neutron-flux quantities, determine ^{99}Mo activities, and produce the plots used for the comparison of TMR configurations.

D.1 Development of the Reference PHITS Input File

The automation procedure started from a manually written PHITS input file for one reference TMR configuration. This input file contained the complete geometry definition, material definitions, source description, cell definitions, and neutron flux tally. Before any automation was introduced, the geometry was checked using the PHITS geometry plotting functionality. This ensured that the target, moderator, reflector, and Mo plates were positioned correctly.
After the reference geometry was verified, the quantities that needed to be changed during the parameter study were identified. These included the moderator dimensions, reflector dimensions, and Mo plate positions. The corresponding numerical values in the PHITS surface cards were then replaced by Python variables.

D.2 Parameterization of the Geometry

The relevant geometry dimensions were stored as Python variables. These variables represented the boundaries of the aluminium (which separates the moderator from the Ta target and the reflector), moderator, reflector, and Mo plates. Representative examples are shown in D.1.

D.1: Representative geometry variables used for PHITS input generation

```
px_Al_bath = 7.900000
my_Al_bath = -13.9000
py_Al_bath = 13.90000
pz_Al_bath = 7.750000

px_reflector = 12.60000
my_reflector = -18.9000
py_reflector = 18.90000
pz_reflector = 12.75000

mz_Mo = 2.450000
pz_Mo = 3.450000
```

The parameterization allowed the same PHITS template to be reused for all simulation cases. For each moderator thickness and Mo plate position, the script updated the corresponding surface coordinates before writing the input file.

D.3 Generation of PHITS Input Files

The input-generation notebook was used to generate all PHITS input files for one selected reflector material, one selected reflector thickness, and one selected moderator material. For example, the directory

D.2: Example of one input-generation directory

```
/Simulations/Ta_Target_Al_Bath/Big/Pb_Ref/5cm/H2O_mod/
```

corresponds to simulations with a 5 cm thick Pb reflector, and a H_2O moderator. After this set of input files was generated, the reflector thickness was changed from 5 cm to 10 cm, 15 cm, and 20 cm, and the same procedure was repeated. The reflector material was then changed, for example from Pb to MgO or Be, and the full generation procedure was repeated again.
The physical meaning of the folder hierarchy is summarized in D.3.

D.3: Physical meaning of the generated folder hierarchy

```
Pb_Ref              -> reflector material
5cm                 -> reflector thickness
Be_mod              -> moderator material
```

```
4 Thickness_10cm      -> moderator thickness
5 2.5cm.txt           -> Mo plate position
```

For each reflector and moderator configuration, the moderator thickness was varied from 1 to 20 cm. The Mo plate position was varied in steps of 0.5 cm.

D.4: Simplified loop structure for generating moderator thicknesses and plate positions

```
1 for moderator_thickness in range(1, 21):
2
3 create_thickness_directory(moderator_thickness)
4
5 for plate_position in plate_positions:
6
7     update_geometry(moderator_thickness, plate_position)
8     write_phits_input_file()
```

The actual PHITS input file was written from a template string. The template contained the fixed parts of the PHITS model, while the geometry values were inserted from the updated Python variables. A representative example is shown in D.5.

D.5: Representative insertion of variable geometry parameters into the PHITS surface definition

```
1 6  RPP -6.60000 {x_Al_bath} {y_Al_min} {y_Al_max} -5.37500 {z_Al_bath}
2 ...
3 11 RPP -6.00000 6.000000 -12.0000 12.00000 {z_Mo_min} {z_Mo_max}
4 ...
5 15 RPP -11.6000 {x_reflector} {y_ref_min} {y_ref_max} -5.37500 {z_reflector}
```

This approach avoided manual editing of the PHITS surface cards and ensured that all generated geometries were modified consistently.

D.4 Treatment of Molybdenum Plate Positions

The Mo plates were shifted according to the selected plate position. The axial plate position was updated directly along the z direction, while the lateral plate positions were shifted outward according to the available moderator thickness. For thin moderator configurations, the lateral displacement was limited by the moderator thickness. For thicker moderator configurations, the full set of foil positions could be used. This is summarized in D.6.

D.6: Simplified logic for updating Mo plate positions

```
1 for plate_position in plate_positions:
2
3 z_Mo_min = z_Mo_min_reference + plate_position
```

```
z_Mo_max = z_Mo_max_reference + plate_position

if moderator_thickness < 6:
    lateral_offset = min(plate_position, moderator_thickness - 1)
else:
    lateral_offset = plate_position

update_lateral_plate_positions(lateral_offset)
```

This ensured that the Mo plate positions remained consistent with the moderator geometry.

D.5 Generated Directory Structure

The generated directory structure reflected the full hierarchy of the parameter study. A representative example is shown in Listing D.7.

D.7: Representative generated directory structure

```
Pb_Ref
|
|-- 5cm
|   |
|   |-- H2O_mod
|   |   |
|   |   |-- Thickness_1cm
|   |   |   |-- 0.0cm.txt
|   |   |   |-- 0.5cm.txt
|   |   |   |-- ...
|   |   |
|   |   |-- Thickness_2cm
|   |   |-- ...
|   |
|   |-- Be_mod
|   |-- D2O_mod
|   |-- ZrH_mod
|
|-- 10cm
|-- 15cm
|-- 20cm

MgO_Ref
|
|-- 5cm
|-- 10cm
|-- 15cm
|-- 20cm
```

This directory structure allowed each simulation case to be identified directly from its path.

D.6 Generation of Cluster Batch Files

After the PHITS input files had been generated, a separate notebook was used to create batch files for execution on the computing cluster. The script reconstructed the same folder hierarchy and wrote the corresponding `srun` commands for each PHITS input file.

A simplified version of the batch-generation logic is shown in D.8.

D.8: Simplified generation of cluster execution commands

```
def generate_srun_commands(moderator_thickness):

plate_positions = [0.0, 0.5, 1.0, ..., 4.0]

if moderator_thickness >= 6:
    plate_positions += [4.5, 5.0]

for position in foil_positions:
    write_command(f"srun phits.sh {position:.1f}cm.txt")
```

For moderator thicknesses below 6 cm, only foil positions up to 4.0 cm were executed. For moderator thicknesses of 6 cm and above, the full range up to 5.0 cm was included.

The batch file also contained the required SLURM directives and PHITS environment setup.

D.9: Representative structure of the generated cluster batch file

```
#!/bin/sh

#SBATCH --job-name=phits
#SBATCH --cpus-per-task=32
#SBATCH --partition=jcns-d
...
source compiler-select intel
export PATH=/opt/phits322/bin:${PATH}
...
cd Ta_Target_Al_Bath/Big/Pb_Ref/5cm/H2O_mod/Thickness_1cm/
srun /opt/phits322/bin/phits.sh 0.0cm.txt
srun /opt/phits322/bin/phits.sh 0.5cm.txt
...
```

D.7 Parsing of PHITS Output Files

After the simulations are finished, the PHITS output files were processed using a separate data analysis notebook. The script first reconstructed the expected output file paths from the reflector material, reflector thickness, moderator material, moderator thickness, and Mo plate position.

D.10: Simplified generation of PHITS output-file paths for data processing

```
for reflector in reflectors:
for ref_thickness in reflector_thicknesses:
for moderator in moderators:
for mod_thickness in moderator_thicknesses:
for plate_position in plate_positions:

                file_names.append(
                    path_to_output_file(
                        reflector,
                        ref_thickness,
                        moderator,
                        mod_thickness,
                        plate_position
                    )
                )
```

The data of each simulation case were extracted from the file path. The neutron flux spectra were then read from the PHITS tally output. For each scored Mo region, the script extracted the lower and upper energy bin limits, neutron flux, and relative uncertainty.

D.11: Simplified extraction of neutron flux spectra from PHITS output files

```
for file_name in file_names:

metadata = extract_metadata_from_path(file_name)

with open(file_name, "r") as file:

    for line in file:

        if new_region_starts(line):
            region = read_region_number(line)

        if flux_table_starts(line):
            read_flux_values = True

        if read_flux_values:
            e_lower, e_upper, flux, rel_err = read_flux_line(line)

            store_flux_value(metadata, region, e_lower, e_upper, flux,
    rel_err)
```

The extracted values were stored in a structured `pandas` dataframe. This dataframe contained the complete simulation metadata together with the neutron flux spectrum for each Mo plate region.

D.8 Calculation of Neutron Flux Components

The neutron flux spectra were separated into thermal, epithermal, and fast neutron components. The energy limits used in the analysis were

$$E_{\text{th}} < 5.0119 \times 10^{-7}\,\text{MeV} \tag{D.1}$$

$$5.0119 \times 10^{-7}\,\text{MeV} \leq E_{\text{epi}} \leq 1.0 \times 10^{-1}\,\text{MeV} \tag{D.2}$$

$$1.0 \times 10^{-1}\,\text{MeV} \leq E_{\text{fast}} \leq 20\,\text{MeV} \tag{D.3}$$

For each simulation case and Mo region, the neutron flux was summed over the corresponding energy bins. The PHITS flux values were then scaled to the proton current used in the activity calculation.

D.12: Simplified calculation of thermal, epithermal, and fast neutron flux components

```
for case, spectrum in grouped_flux_spectra:

thermal_flux = sum_flux(spectrum, E_upper <= 5.0119e-7)

epithermal_flux = sum_flux(spectrum, 5.0119e-7 <= E_upper <= 1.0e-1)
                    * alpha / (Emin**(-alpha) - Emax**(-alpha))

fast_flux = sum_flux(spectrum,b1.0e-1 <= E_upper <= 2.0e+1)

scale_fluxes_to_beam_current()
```

D.9 Epithermal Spectrum Correction

The epithermal spectrum shape factor α was calculated for each simulation case from the simulated neutron spectrum. As described in Section 3.2.2.1, the epithermal spectrum was fitted using the logarithmic form given in Eq. 3.17.
Therefore, if s is the fitted slope of $\ln(\phi(E)/\Delta E)$ as a function of $\ln(E)$, the spectrum-shape factor is obtained as

$$\alpha = -(s+1) \tag{D.4}$$

The calculated α value was subsequently used both to determine the epithermal flux per unit lethargy and to calculate the α-dependent resonance integral employed in the activity calculation.

D.13: Simplified calculation of α the factor

```
flux_per_energy = epithermal_flux / energy_bin_width

slope, intercept = fit(log(energy),log(flux_per_energy))

alpha = -(slope + 1)
```

The calculated α value was then used to evaluate the α-dependent resonance integral according to Eq. 3.21. A simplified implementation is shown in D.14.

D.14: Simplified calculation of the α-dependent resonance integral

```
resonance_integral = ((
((I_gamma - 0.426 * sigma_th) /
(E_r ** alpha))
+
((0.426 * sigma_th) /
((2 * alpha + 1) *
(E_Cd ** alpha))))
* (E_0 ** alpha) * 1e-24)
```

The factor 10^{-24} converts the resonance integral from barns to cm^2. The resulting resonance integral was subsequently used in the calculation of the epithermal contribution to the ^{99}Mo production rate.

D.10 Flux-Weighted Fast Cross Section

The fast neutron contribution was evaluated using the spectrum-weighted average cross section described in Section 3.2.2.1. For each simulation case, the neutron flux in the fast energy region was obtained from the processed PHITS output files. The energy dependent $^{98}\mathrm{Mo}(n,\gamma)^{99}\mathrm{Mo}$ cross-section data were read from an external data file and interpolated onto the PHITS energy bin structure. The effective fast neutron cross section was then calculated as

$$\frac{\sum_i \phi_i \sigma_i}{\sum_i \phi_i}, \tag{D.5}$$

where ϕ_i is the neutron flux obtained from the PHITS tally in energy bin i, and σ_i is the interpolated microscopic cross section for the same energy bin.
A simplified version of the implementation is shown in D.15.

D.15: Simplified calculation of the flux-weighted fast cross section

```
weighted_sum = 0.0
```

```
fast_flux_sum = 0.0

for energy_bin in fast_energy_bins:

sigma = interpolate_cross_section(energy_bin)
fast_flux  = energy_bin.neutron_flux

weighted_sum += fast_flux * sigma
fast_flux_sum += fast_flux

sigma_fast = weighted_sum / fast_flux_sum
```

This discrete implementation is equivalent to the continuous formulation presented in Section 3.2.2.1, with the integrals evaluated as sums over the PHITS energy bins.

D.11 Calculation of Molybdenum-99 Activity

The activity of each Mo plate was calculated from the thermal, epithermal, and fast neutron contributions. The production rate and EOI were calculated using Eqs. 3.13 and 3.15.
In the implementation, different Mo plate masses were used depending on the scored region. The larger plates corresponded to regions 7 and 10, while the smaller plates corresponded to regions 8 and 9.

D.16: Simplified activity calculation for each molybdenum plate region

```
mass = large_plate_mass if region in [7, 10] else small_plate_mass

production_rate = (thermal_flux * sigma_thermal +
                epithermal_flux * resonance_integral +
                fast_flux * sigma_fast)

activity = ((mass / M) * N_A * abundance_Mo98 *
            production_rate *
            (1 - exp(-lambda_decay * irradiation_time)))
```

The calculated activities were converted from Bq to Ci.

D.12 Summation of Plate Activities

After the activity had been calculated for each Mo plate region, the individual plate activities were summed to obtain the total activity for each TMR configuration.

D.17: Summation of plate activities for each simulation configuration

```
total_activity = activity_data.groupby([
"Reflector",
```

```
3 "Reflector Thickness",
4 "Moderator",
5 "Moderator Thickness",
6 "Foil Position"
7 ])["Activity"].sum()
```

D.13 Visualization and Comparison of Configurations

The processed data were visualized using heatmaps and comparison plots. Heatmaps were used to show the dependence of the calculated activity on moderator thickness and Mo plate position for selected reflector and moderator configurations.

D.18: Simplified generation of activity heatmaps.

```
1 heatmap_data = activity_data.pivot_table(
2 index="Moderator Thickness",
3 columns="Plate Position",
4 values="Total Activity",
5 aggfunc="mean"
6 )
7
8 plot_heatmap(heatmap_data)
```

Additional comparison plots were generated to compare reflector materials, reflector thicknesses, moderator materials, and individual Mo plate regions. These plots formed the basis for identifying the configurations that maximized the calculated ^{99}Mo activity.

D.14 Summary

The automation workflow developed in this work enabled the systematic generation, execution, and analysis of a large PHITS simulation database. The workflow started from a manually verified reference PHITS model. The relevant geometry parameters were then identified, parameterized, and used to generate input files for different reflector materials, reflector thicknesses, moderator materials, moderator thicknesses, and Mo plate positions.
A second notebook generated the batch files required for execution on the computing cluster. After the simulations were completed, a third notebook reconstructed the simulation hierarchy, parsed the PHITS output files, extracted neutron flux spectra, calculated thermal, epithermal, and fast neutron flux components, determined cross sections, and calculated the corresponding ^{99}Mo activities. The resulting structured datasets were used to compare the investigated TMR configurations in Chapter 5.3.